



Tomas Bata University in Zlín
Faculty of Technology

Doctoral Thesis

**Development of polymer systems
suitable for processing *via* advanced
technologies of 3D printing and
electrospinning**

**Vývoj polymerních systémů vhodných pro zpracování
pomocí pokročilých technologií 3D tisku a
elektrostatického zvlákňování**

Author:	Ing. Lenka Vítková
Study program:	P2808/ Chemistry and Technology of Materials
Field of Study:	2808V006/ Technology of Macromolecular Compounds
Supervisor:	prof. Mgr. Aleš Mráček, Ph.D.
Opponents:	doc. Dr. Ing. Vladimír Pavlínek prof. RNDr. Petr Ponížil, Ph.D.

Zlín, 2023

© Lenka Vítková

Klíčová slova: *aditivní výroba, biopolymery, hyaluronan, hydrogely, 3D biotisk, elektrostatické zvlákňování*

Key words: *additive manufacturing, biopolymers, hyaluronan, hydrogels, 3D bioprinting, electrospinning*

The dissertation thesis is available in the Library of TBU in Zlín.

I would like to thank my supervisor, prof. Mgr. Aleš Mráček, Ph.D., for sharing his knowledge and vision, and providing guidance, as well as freedom to explore the fascinating world of materials science throughout my studies. I would also like to thank my consultants Ing. Lenka Musilová, Ph.D. and Ing. Petr Smolka, Ph.D. for offering their expertise and skills during investigation of the problems in this thesis.

Additionally, I want to acknowledge all the co-authors for their keen insights and detailed analysis of the specific aspects of the materials developed throughout the research. Namely, I would like to thank Ing. Roman Kolařík, Ph.D., whom I consider my mentor in the area of rheological evaluation of materials.

I would like to thank the Faculty of Technology of Tomas Bata University in Zlín, the Center of Polymer Systems of Tomas Bata University in Zlín, Experimental Soft Matter Physics group at the University of Luxembourg, and the Chair of Biomaterials at the University of Bayreuth for providing their infrastructure for conducting the necessary experiments.

Additionally, I would like to thank my fellow Ph.D. students for creating a friendly atmosphere and making the sun seem to shine a little brighter every day. I would like to thank my friends and family for their support and patience. Most of all, I would like to thank my husband Pavel for always being there for me, for putting up with me through the late nights and frustrating setbacks, and for believing in me even when I was in doubt.

I want to know why. Why everything. I don't know the answers, but a few days ago I didn't know there were questions.

Terry Pratchett

ABSTRAKT

Tato disertační práce se zabývá fyzikálními aspekty zpracování materiálů na bázi biopolymerů pomocí 3D tisku a elektrostatického zvlákňování, především pak vlivem materiálových vlastností na tyto výrobní procesy. Zvláštní pozornost je věnována tvorbě hydrogelů na bázi biopolymerů pomocí různých metod síťování. Tyto hydrogely mohou dále sloužit jako podklad pro nanovláknenné struktury a být použity jako pokročilé biokompatibilní materiály v biomedicínských aplikacích.

Práce popisuje tvorbu hydrogelů z přírodních polymerů pomocí dynamických polymerních sítí. Hydrogely představují výhodný typ materiálů díky své vnitřní podobnosti s extracelulárním prostředím živočišných buněk. Síťování bylo dosaženo pomocí dynamických kovalentních vazeb, nebo s využitím spontánního vzniku vnitřní podpůrné struktury nanodestiček díky jejich elektrostatickému odpuzování. Optimálního chování pro 3D tisk bylo dosaženo pro několik různých materiálů, které vykazují snížení viskozity se zvyšujícím se smykovým namáháním a poměrně rychlý návrat do původních hodnot viskozity po ukončení smykového namáhání.

Z hlediska elektrostatického zvlákňování polymerních roztoků byly diskutovány vnitřní a vnější faktory ve vztahu k výrobnímu procesu se zvláštním zřetelem na materiálové parametry a jejich návaznost na další aspekty jak procesu, tak podoby získaných vláken. Kromě jednosložkového elektrostatického zvlákňování proběhly experimenty i s koaxiálním zvlákňováním, kdy se navíc projeví jevy na fázovém rozhraní roztoků.

Význam disertační práce přesahuje jednotlivé technologie 3D tisku a elektrostatického zvlákňování, a spočívá především v možnosti jejich kombinace pro vytváření struktur vhodných pro biologické aplikace, včetně tkáňového inženýrství. Přesné makroskopické struktury získané 3D tiskem hydrogelů s nanotopologickými prvky nanovláken vzniklých elektrostatickým zvlákňováním mohou být vytvořeny např. jako 3D tištěné struktury pokryté nanovláknem, vrstvených 3D tištěných/nanovláknenných sendvičových struktur a nanovláknem vyztužených materiálů pro 3D tisk, z nichž každá slibuje různé výhody pro biomedicínské aplikace ve srovnání s komerčně dostupnými materiály.

Výsledky disertační práce z pohledu výroby hydrogelů a nanovláken mohou najít uplatnění v oblasti pokročilých výrobních technologií se zaměřením na biopolymery. Materiály vyvinuté v rámci této disertační práce mohou díky svým unikátním fyzikálním vlastnostem rozšířit využití 3D tisku a elektrostatického zvlákňování nejen pro tkáňové

inženýrství, pro které byly tyto materiály původně zamýšleny.

ABSTRACT

This doctoral dissertation explores the essential physical aspects influencing biopolymers fabrication by 3D printing and electrospinning. The study investigates several polymer system characteristics, and their influence on the respective processes. The focus is directed towards formulation of hydrogel structures *via* various cross-linking methods, which can eventually be decorated with nanofibrous structures and serve as advanced biocompatible materials in biomedical applications.

The work details the enhancement of natural polymers' hydrogel formation using dynamic polymer networks of two kinds - dynamic covalent linkages, and electrostatically driven reinforcement with nanoplatelets. The hydrogels were chosen due to their inherent resemblance to extracellular matrix of a natural tissue. The optimal behavior for 3D printing inks, displaying shear-thinning behavior and swift recovery post shear stress, was achieved for several materials compositions.

In terms of polymer solutions electrospinning, the complex interplay of intrinsic and extrinsic factors was discussed in a relation to the process and its outcomes. The experimental investigation focused on materials parameters and their linking to other electrospinning parameters, as well as the resulting fibres' morphology. Apart from single-solution electrospinning, coaxial electrospinning was explored. In that case, interfacial phenomena had to be considered as well.

Significantly, the dissertation lays the groundwork for combining nanotopological features of electrospun fibrous mats and precise macroscopic structures from 3D printed hydrogels. The results presented in the thesis can be utilized in fabrication of advanced structures eg. in the form of nanofibres decorated 3D printed structures, layered 3D printed-electrospun sandwich structures, and nanofibre-reinforced 3D printing inks, each promising distinct benefits for biomedical applications.

In conclusion, the dissertation provides a thorough exploration of physical factors affecting biopolymers' manufacturing *via* advanced manufacturing technologies, estab-

lishing a substantial base for future advancements in manufacturing of biopolymer based materials.

LIST OF PAPERS

PAPER I

L. MUSILOVÁ, E. ACHBERGEROVÁ, **L. VÍTKOVÁ**, R. KOLAŘÍK, M. MARTÍNKOVÁ, A. MINAŘÍK, A. MRÁČEK*, P. HUMPOLÍČEK and J. PECHA. Cross-Linked Gelatine by Modified Dextran as a Potential Bioink Prepared by a Simple and Non-Toxic Process. *Polymers*. 2022, 14(3). doi:10.3390/polym14030391

PAPER II

L. VÍTKOVÁ, L. MUSILOVÁ*, E. ACHBERGEROVÁ, R. KOLAŘÍK, M. MRLÍK, K. KORPASOVÁ, L. MAHELOVÁ, Z. CAPÁKOVÁ and A. MRÁČEK*. Formulation of Magneto-Responsive Hydrogels from Dually Cross-Linked Polysaccharides: Synthesis, Tuning and Evaluation of Rheological Properties. *International Journal of Molecular Sciences*. 2022, 23(17). doi:10.3390/ijms23179633

PAPER III

L. VÍTKOVÁ, I. SMOLKOVÁ, N. KAZANTSEVA, L. MUSILOVÁ, P. SMOLKA*, K. VALÁŠKOVÁ, K. KOCOURKOVÁ, M. HUMENÍK, A. MINAŘÍK, P. HUMPOLÍČEK and A. MRÁČEK. Magneto-responsive hyaluronan hydrogel for hyperthermia and bio-printing: magnetic, rheological properties and biocompatibility. *APL Bioengineering*. Under review.

PAPER IV

K. KOPECKÁ, **L. VÍTKOVÁ***, Z. KRONEKOVÁ, L. MUSILOVÁ, P. SMOLKA, F. MIKULKA, K. MELÁNOVÁ, P. KNOTEK, M. HUMENÍK, A. MINAŘÍK and A. MRÁČEK*. Synthesis and exfoliation of calcium phosphonates for tailoring rheological properties of sodium alginate solutions: A path towards polysaccharide based bioink. *Biomacromolecules*. Accepted for publication. doi:10.1021/acs.biomac.3c00081

PAPER V

L. VÍTKOVÁ, L. MUSILOVÁ, E. ACHBERGEROVÁ, A. MINAŘÍK, P. SMOLKA, E. WRZECIONKO and A. MRÁČEK*. Electrospinning of Hyaluronan Using Polymer

Coelectrospinning and Intermediate Solvent. *Polymers*. 2019, 11(9).
doi:10.3390/polym11091517

TABLE OF CONTENTS

LIST OF PAPERS	5
1 INTRODUCTION	9
2 STATE OF THE ART	10
3 AIMS OF THE DOCTORAL THESIS	13
4 THEORETICAL BACKGROUND	14
4.1 POLYMERS AND POLYMER SYSTEMS	14
4.1.1 Polymer based scaffolds in tissue engineering	14
4.1.2 Polymer composites in tissue engineering	21
4.2 3D PRINTING	26
4.2.1 Hydrogels for bioprinting	27
4.2.2 Cross-linking strategies of hydrogels for 3D printing	31
4.3 ELECTROFLUIDODYNAMICS	37
4.3.1 Parameters influencing electrospinning	41
4.3.2 Core-shell electrospinning	43
4.3.3 Electric field assisted fabrication of scaffolds	43
5 SUMMARY OF THE PAPERS	45
5.1 SCHIFF-BASE CROSS-LINKING OF NATURAL POLYMERS	45
5.2 RHEOLOGICAL MODIFICATION USING CHARGED NPS	51
5.3 PREPARATION OF BIOPOLYMER-BASED NANOFIBRES BY THE ELECTRO- SPINNING METHOD	55
6 CONTRIBUTION TO RESEARCH AND PRACTICE	60
7 CONCLUSION	62
REFERENCES	64
LIST OF FIGURES	106
LIST OF TABLES	109
LIST OF ABBREVIATIONS	110
PUBLICATIONS OF THE AUTHOR	111
CURRICULUM VITAE	113

LIST OF APPENDICES 115

1 INTRODUCTION

Advanced manufacturing refers to a set of innovative manufacturing processes and techniques that utilize cutting-edge technologies, such as additive manufacturing, nanotechnology or advanced materials manufacturing [1]. These technologies can improve productivity, quality, and flexibility, and can enable manufacturers to produce products faster and more efficiently. Additive manufacturing is often seen as an equivalent of 3D printing, which is an overarching term for various technologies, which make use of computer-aided design to manufacture complex three-dimensional structures in layer-by-layer manner. However, for the purpose of this thesis, the term additive manufacturing will be seen in broader perspective as the opposite of subtractive manufacturing, which typically employs the top-down approach by reshaping a block of material by taking away parts of it. Additive manufacturing utilizing the bottom-up approach has the potential to revolutionize manufacturing by allowing for the creation of complex shapes and structures that would be difficult or impossible to produce using traditional manufacturing methods [2].

3D printing involves the use of a computer-controlled printer to deposit layers of a material (such as plastic, metal, or bioink) to build up a 3D structure. The material is usually supplied in the form of a filament or a liquid, and the printer typically includes a nozzle of various shapes that moves back and forth to deposit the material in a precise pattern [2]. 3D printing produces structures with resolution of thousands to hundreds of micrometers, which are typically highly accurate in shape and dimensions [3, 4, 5].

Electrospinning, on the other hand, involves the use of an electric field to draw a charged polymer solution or melt to produce a fine fibre of hundreds to tens of nanometers in thickness [6]. The electrospinning process itself leads to random nanofibrous meshes, and their orientation has to be ensured by special manufacturing adjustments. These include mainly collecting fibres on rotating drum or cutting a small part of a large mesh exhibiting quasi-uniformity [7, 8]. Electrospinning is a versatile manufacturing method and can be used to create a wide range of 2D or 3D structures.

3D printing and electrospinning are both technologies that can be used to manufacture

3D structures from a variety of materials. Both technologies build up a structure in an additive manner, and both have the potential to produce complex structures with high resolution and accuracy. They have been used in tissue engineering to create scaffolds for cell culture and tissue repair [9]. 3D printing has the advantage of being able to produce complex structures with a high degree of control over their geometry and composition, while electrospinning is faster and can produce fibres with a wider range of diameters and compositions. Furthermore, each technology brings specific qualities influencing the cells behaviour. 3D printed tissue analogues with mechanical and chemical resemblance to extracellular matrix (ECM) provide environment for cell attachment and growth [10]. Cultivation on nanotopographically tuned fibrous scaffolds, on the other hand, guides cell migration and induces orientational growth [11, 12]. Thus, combining 3D printing and electrospinning could be used as biomimetic approach for preparation of structures suitable for tissue engineering or pharmaceutical applications.

2 STATE OF THE ART

The use of advanced technologies brings unbeknown opportunities in almost every aspect of human life, including healthcare [13, 14, 15]. Several medical fields can benefit from advanced fabrication methods, namely drug delivery [16, 17, 18, 19, 20, 21, 22], wound healing [23, 24, 25, 26, 27], tissue engineering [28, 29, 30] and cell scaffold fabrication [31, 32, 33].

Polymer systems designated for use in medical applications have to follow specific requirements, which restrict the available materials platform. Specifically in tissue engineering, the polymer systems should be as close as possible to the properties of native tissue in order to achieve optimal cell stimulation to adhesion and proliferation [34]. These requirements can be divided into several groups: structural, mechanical, chemical, and biological.

Structural requirements include mainly the simulation of functions of ECM - providing support and facilitating communication among cells [1] - which are allowed by high

water content and porosity. These specifications lead to high popularity of hydrogel materials in this area [10]. Furthermore, it has been found that the presence of nanostructures is of immense importance in cell cultivation, as such structures are capable of direct interactions with cells [35]. This approach was used by Li et al., 2023, where hydrogel containing phosphate particles were chosen for material intended for osteocytes cultivation [36]. In another study, Bertels et al., 2021 proved the direct influence of geometry on division rate and morphology of mouse embryonic stem cells [37]. Zhao et al., 2020 observed increased formation of periostum-like tissue when using nanofibrous scaffolds with specific functionalization [38]. De France et al., 2021 proved the capacity of nanostructure to influence the morphology and induce directional growth in mouse myocytes [12]. Nanofibrous scaffolds with controlled topography have been found useful also in guided neuron cultivation [39].

Mechanical properties of various tissue types range from hard cancellous bone (Young's modulus around 25 GPa [40]), muscular tissues (units of MPa for both skeletal and heart muscles [41]), to hundreds of kPa in case of breast tissue [42]. Additionally, many tissue types are highly anisotropic and provide different response with respect to the direction of impulse [41], such as interface tissues [43]. Stanton et al., 2022 successfully mimicked the bone-tendon interface by creating a hydroxyapatite (HAp) gradient in aligned gelatin (Gel) scaffolds, giving mechanical and chemical impulses to achieve desired stem cell differentiation into the interfacial tissue structure [44].

Furthermore, specific tissue types rely on reversible response to mechanical [9, 45] or electric [36, 46, 47] impulses. An emerging approach to cell scaffold fabrication is the use of smart materials, i.e. materials with instant and reversible response to external stimuli [48]. The stimuli range from thermal, electric and magnetic field, to light or humidity. A common feature of many of these materials is shape memory, which is exploited in tissue implants [49, 50]. Díaz-Payno et al., 2023 used combination of hydrogels with different swelling to obtain curvature in a scaffold and induced chondrogenesis in human mesenchymal stromal cells [51]. Similar functionality was obtained by Cui et al., 2020 by selectively adjusting cross-linking density of methacrylated natural polymers, thus affecting their swelling ability [52]. In a different approach, Ko et al., 2020 used superparamagnetic iron oxide particles as a filler for hydrogel-based 3D

printing bioink to obtain magneto-responsive cell scaffolds or drug delivery systems [53]. Shou et al., 2023 used magneto-responsive hydrogels as dynamically mechano-modulable matrices and confirmed induction of mesenchymal stem cells spreading and proliferation [45]. 3D printing of κ -carrageenan yielded electro- and thermo-responsive constructs suitable for on-demand drug release. However, their potential in cell culture and tissue engineering is yet to be confirmed [54]. In a different approach to utilizing smart materials in cell cultivation, Zhao et al., 2023 used electro-stimulation of mouse fibroblasts. They proved enhanced cell proliferation due to electro-stimulation, leading to accelerated wound healing [55]. The combination of advanced additive manufacturing technologies is a way towards 4D printing - 3D printing of structures interchangeable in time, such as studied by Kamperman et al., 2023. In this study, biochemically tunable scaffolds were prepared by utilizing core-shell structured microspheres as building blocks, offering means for spacio-temporal manipulation of cultured cells [56], bringing a different understanding of smart materials.

Cell cultivation on artificial scaffolds relies on specific interactions between the scaffold surface and cell receptors. The biocompatibility of a surface is guided by various material properties, including surface energy, presence of certain chemical groups, topography and mechanical properties [57, 58, 59, 60, 61]. Although the surface properties have an essential role in cell attachment, migration and proliferation, differentiation in 2D cultivation is typically rather poor, and significant changes to morphology can be observed [62]. 3D cell culture allows building conditions *in vivo* by closely resembling the functionality of ECM, and is found to produce more viable tissue analogues. The third dimension has been called the bridge between cell culture and living tissue [63]. The interactions among cells, and cell-ECM interactions are the core of biological communication, and enable the formation of complex, specific tissues. Therefore, the essential concepts of 3D cell cultivation highlight the need to simulate cell-ECM interactions, and allow cell-cell interactions at the same time [64]. Adding cues - both physical, and biochemical - allows guidance of cell growth, proliferation and differentiation, thus expanding the usability of tissue engineering [65].

In a recent study, Fornetti et al., 2023 observed the alignment provided by 3D printing technology in morphogenesis of muscle cells leading to higher orientation of myofibrils

on the 3D printed constructs compared to bulk polymerized scaffolds [66]. Some excellent results in structural guidance of cell proliferation and differentiation have been achieved on scaffolds made of aligned electrospun nanofibres, especially in reconstruction of cardiomyocytes [67, 7, 68] and neural cells [69, 70, 71]. In their study of myocyte behaviour, De France et al., 2021 used the aligned nanofibres in combination with random wrinkling of the foundation [12]. Zhang et al., 2022 reported the ability of nanofibres used as fillers for hydrogel matrices to induce cell alignment [72]. It appears that combining 3D printing and electrospinning technologies holds a great potential for fabrication of cell-instructive scaffolds for tissue engineering applications [9, 73, 74].

3 AIMS OF THE DOCTORAL THESIS

The main focus of the doctoral thesis is the development of natural polymer based systems suitable for processing *via* 3D printing and electrospinning technologies in order to obtain constructs distinctly structured on macro-, micro- and nanolevel. This is achieved through thorough examination and fine tuning of key parameters for the respective techniques. Furthermore, the possibility to utilize composite materials and enhance the polymer matrix performance will be studied. The research objective is directed towards fabrication of scaffolds for cell cultivation. Therefore, it is necessary to be mindful of biocompatibility in each step of the process.

4 THEORETICAL BACKGROUND

4.1 Polymers and polymer systems

Polymers present a group of materials consisting of macromolecules (several millions grams per mol), which are built from repeating units conceptually derived from low-molecular-mass molecules. In general, polymers can be divided into several groups based on their origin (natural or synthetic), primary (homopolymers or copolymers, which can be further divided into subgroups - statistical, alternating, block or graft copolymers) and secondary (linear, branched or cross-linked). The macroscopic behaviour of a polymer is directed by its structure of each level [75]. Alterations in polymer structure, such as changing molecular weight (M_w), polydispersity, linearity etc. can therefore be a useful tool for fine tuning of polymers mechanical [76, 77], rheological [78] or thermal properties [79].

Polymer systems comprise mixtures of polymers with other substances - solvents, fillers (either passive or active), cross-linking agents, other polymers *etc.* [80]. Any given additive influences the behaviour of the polymer chains through physical or chemical interaction. The variety of possible effects leads to almost infinite range of possible polymer systems. For the purposes of the thesis, only certain specific groups of polymer systems essential to the research will be listed.

4.1.1 Polymer based scaffolds in tissue engineering

Tissue engineering is based on three essential building blocks referred to as the tissue engineering triad - a scaffold, cells, and signaling paths between cells. The scaffold is of vital importance to successful growth of artificial tissue replacements [81]. Its primary function is to provide structural support for cells attachment. As such, it must resemble ECM - a matter produced by fibroblast, which is responsible for mechanical support of cell assemblies, nutrient and waste exchange, and support of cellular adhesion, growth and multiplication [1]. ECM is in principle a composite of proteins and

glycosaminoglycans (i.e. anionic polysaccharides) distributed in aqueous environment. It has a fundamental role in determining cell shape, spreading, growth and organization of cytoskeleton, which is guided through physical and chemical stimuli [1]. The ECM environment can be closely simulated by biocompatible hydrogel structures [10]. Therefore, hydrogels are a promising class of materials for fabrication of scaffolds for cell cultivation.

The central characteristic of any scaffold is high porosity, allowing growth of cells inside the pores, as well as flow of liquids through the bulk of the scaffold. The applicability of porous systems is determined mainly by surface area, pore size and pore geometry. Furthermore, functional moieties present on the pore surface tailor the chemical affinity of the material, thus creating a large space for application specific tuning [82]. Many techniques have been developed to fabricate highly porous structures, such as phase separation, gas foaming, solvent casting or freeze drying. The technologies listed here are still popular among researchers due to their ease of use and high yield. However, they suffer from lack of control over pore specifications and overall scaffold geometry [1].

Material designated for tissue engineering must comply to several criteria in order to fulfill their functions. These include biological requirements, namely biodegradability, biocompatibility and non-toxicity, chemical properties, such as presence of biologically active moieties, hydrophilicity, surface charge, and general chemical composition [83]. Both natural and synthetic polymers can be used for this purpose. Natural polymers used in biomedical applications includes proteins, polysaccharides and polynucleotides. Their main advantage is their inherent non-toxicity on account of their chemical structure [84]. However, other common features of natural polymers include the lack of predictability and thermosensitivity, which make their processing into complex shapes challenging [83]. Synthetic polymers, on the other hand, can be produced with high reproducibility, making their processing more straightforward [84]. Unlike natural polymers, the synthetic ones lack cellular adhesive sites and have the risk of cytotoxicity. Therefore, their use as matrix materials for cell growth is conditioned by their functionalization with signaling molecules, such as adhesive peptide sequences [85]. Some specific examples of polymers suitable for tissue engineering are listed

below.

Hyaluronan

Hyaluronan (HA) is a natural part of connective tissue and ECM. It is a linear glycosaminoglycan composed of repeating disaccharide units of N-acetyl-glucosamine and glucuronic acid, see Figure 4.1 (A) [86]. The HA molecule was first isolated in 1934 by Meyer and Palmer [87]. The highest concentrations in human body can be found in umbilical cord, synovial fluid, vitreous body of an eye and dermis. HA solutions show exceptionally high viscosity (10^2 Pa·s for 2% solution of $1.27 \cdot 10^6$ kDa M_w [88]), and shear thinning behaviour [89].

HA is synthesized by an enzymatic biosynthetic reaction catalyzed by HA synthases at the plasma membrane of eukaryotic cells. For commercial use, mainly in biomedical and cosmetic applications, there are three major production methods: (a) extraction from animal tissue, (b) bacterial production, and (c) *in vitro* production [90]. The first option is historically the most established, and is feasible for number of tissues from different animal sources [91, 92]. Even though the water solubility of HA simplifies the extraction, it is difficult to purify the product due to complexing biopolymers, such as proteoglycans. Thus, the HA produced by this method typically induces immunoresponsivity in the host, therefore is not suitable for biomedical applications [93]. The solution to the situation was brought by the bacterial synthesis of HA. Since the molecules produced in bacteria and eucaryotic cells are identical, the bacterial HA can be used in biomedical and cosmetic applications without the possibility of adverse reaction of the host [94]. The foundation of the process is fermentation of *Streptococci* strains, which leads to production of HA of high M_w and low polydispersity in high yields [90].

The function of HA in the ECM is to provide binding sites for proteoglycans, and thus form a template to facilitate ECM assembly and cell migration via interactions with proteoglycans [95]. Its biological effects are strongly dependent on its physical properties and chemical modifications, as well as microenvironment and degradation paths available [96]. Specifically, M_w of HA is crucial for recognition and biologi-

cal function. M_w of HA found in connective tissue varies between $10^5 - 10^7 \text{ g}\cdot\text{mol}^{-1}$ [86]. While high-molecular-weight was found as anti-inflammatory agent and promoting epithelial cells homeostasis and survival [97], fragments of low-molecular-weight HA were observed as pro-inflammatory factor [98]. HA also mediates cell adhesion and motility [99]. It has found use in ophthalmology [100], cosmetics [101], or tissue engineering applications, either as a part of ECM simulating collagen (Col) based hydrogels [102, 103, 104], or isolated [105, 106].

Sodium alginate

Sodium alginate (NaAlg) is a naturally occurring polysaccharide, typically extracted from seaweed by alkaline extraction. In essence, it is a linear copolymer of L-guluronate and D-mannuronate with varying content of the respective monosaccharide units. The monosaccharide units can be organized in blocks, or alternating, but typically they combine both patterns [107]. Based on the extensive research proving cytocompatibility of NaAlg [108, 109, 110], it is approved by the U.S. Food and Drug Administration as a biopolymer for regenerative medicine [111]. Its biocompatibility and ease of tuning of mechanical properties makes it a popular component of materials for tissue engineering [112]. However, as a plant based polymer, it is not degradable by mammalian enzymes, and lacks the adhesive sites for mammalian cells [107]. Therefore, the NaAlg based implants are inert [113]. Derivatization of NaAlg, such as grafting with short peptide chains with specific signaling functions, eg. arginylglycylaspartic acid sequence facilitating cell adhesion [114], is often done to resolve this issue

The prevailing part of commercially produced NaAlg is obtained from wild brown algae. The NaAlg chains form helical structures, combined of double helices formed by mannuronan blocks, and triple helices of guluronan blocks [115]. Its polyanionic character allows gelation in the presence of multivalent ions through formation of guluronan block stable junctions [116]. Additionally, NaAlg forms hydrogen bonds stabilized gels in acidic pH [117].

Collagen and gelatin

The most abundant polymer in mammalian tissue is Col, as it covers 75% of ECM. This protein has found use in tissue engineering in both native and denatured (partially hydrolysed) form – Gel [118]. The triple helical structure of Col makes it extremely stable and helps its function as structural protein [119]. Col is typically extracted from by-products of animal production. The process involves degreasing and removing impurities, followed by acidic, alkalyne or enzymatic treatment [120]. The heating of Col leads to loss of hydrogen and electrostatic interactions among the chains in a triple helix, and allows subsequent breaking of chemical bonds and disintegration of the helical structure [121]. Col is then hydrolyzed by a multistage procedure, involving heating to 40°C, to transform the Col to Gel [122, 123].

The denaturation of Col leads to its solubilization in polar solvents, including water at elevated temperature (30°C - 40°C [124]). Therefore, Gel is processable in mild, biocompatible conditions, making it more suitable for many biomedical applications [125]. Significant potential of Gel based bioinks for 3D printing is well documented in current literature [126, 127, 128]. It was shown that this material is biocompatible, can mimic similar functions as Col for cellular development, is highly soluble and also cheaper in comparison with ECM proteins like Col or fibronectin [127]. The cell adhesion sites from Col, eg. RGD sequence, are preserved in Gel, thus promoting its cytocompatibility, cell adhesion and remodelling [129]. In addition to excellent biocompatibility and biodegradability, aqueous solutions of Gel undergo temperature-dependent physical gelation via transition of peptide coils into helices [130, 131]. However, application of pure Gel in 3D printing is limited by its poor mechanical properties, relatively short degradation time and poor printing resolution. To overcome these drawbacks, Gel can be cross-linked, chemically modified or mixed with other polymers of both synthetic and natural origin [127, 128].

Poly- ϵ -caprolactone

Poly- ϵ -caprolactone (PCL) is a synthetic semi-crystalline aliphatic polyester with melting point of about 60°C. The synthesis is carried out either by polycondensation of

6-hydroxyhexanoic acid, or ring-opening polymerization using ϵ -caprolactone as the starting compound. While polycondensation requires vacuum and continuous removal of water produced during the reaction, the ring-opening polymerization is achieved simply in the presence of metal catalyst. Thus, the latter procedure is more popular [132]. Furthermore, it was found that the ϵ -caprolactone polymerization can be catalyzed by certain enzymes, especially lipases [133]. PCL properties can be tailored through control of M_w , crystallinity, or cross-linking [134]. It is very popular in biological and medical applications on account of its biodegradability and non-toxicity. It can be blended with other polymers bearing hydroxyl groups [135], including biopolymers such as cellulose, chitosan or Gel [136, 137, 138, 139, 140].

Polyethylene oxide

Polyethylene oxide (PEO) is a semicrystalline synthetic polyester soluble in water and organic solvents. It is chemically identical to polyethylene glycol, but as it exceeds M_w of 20,000 kg·mol⁻¹, it is solid until 60-70°C. PEO is commonly synthesized via oxanionic polymerization of epoxides, which is a living polymerization. Therefore, it allows M_w control, and terminating groups can be obtained quantitatively [141]. Its chains are very flexible [142], thus, it is a popular block copolymer providing toughness to more rigid polymers [143, 144, 145]. As a biocompatible polymer, it has been extensively studied for biomedical applications [146], although its rather low mechanical performance leads to its use as an additive, e.g. in polyurethanes or Gel based materials [147]. Also, it is a popular coating of functional nanofillers [148, 149]. Owing to its solubility in water, it can also be used as sacrificial polymer for fabrication of inorganic fibres [150] or hollow structures [151].

Polyvinyl alcohol

Polyvinyl alcohol (PVA) is water soluble semicrystalline polymer. Its structure with many hydroxyl groups allows for hydrogen bonding and forming physical hydrogels [152, 153]. The reactive sites are available for chemical cross-linking as well [154, 155]. The monomer vinyl alcohol is unstable, therefore PVA is produced by partial or

full hydroxylation of polyvinyl acetate [156]. Its melting temperature of 200°C allows its processing via fused filament fabrication [157]. It can be electrospun from aqueous solutions to form nanofibrous mats [158], and has been suggested as a promising material for precision electric-field assisted 3D printing, also known as melt electrowriting [159]. Its biocompatibility and resistance to protein adsorption make it a popular choice in ophthalmic applications or drug delivery [160, 161]. In tissue engineering it is typically used as a mechanical modulator in composite materials, such as hydrogel based [162] or nanofibrous scaffolds [163, 164].

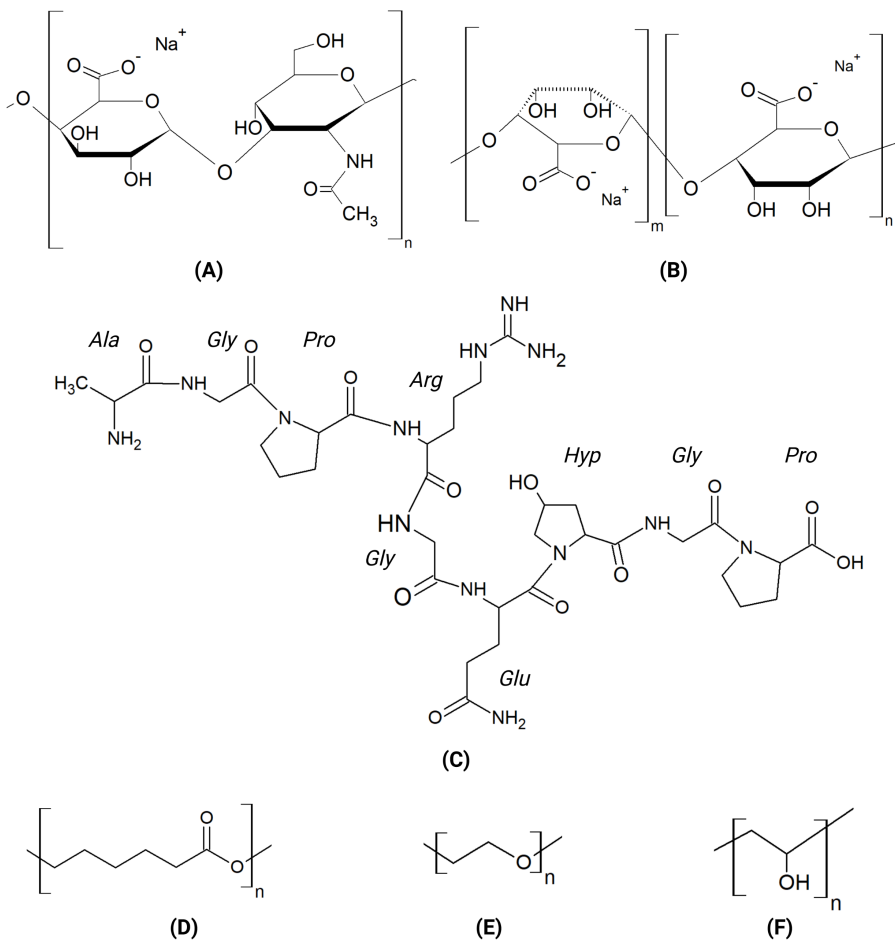


Fig. 4.1 Structural formulas of some polymers significant in tissue engineering: (A) HA, (B) NaAlg, (C) Example of possible Gel structure, (D) PCL, (E) PEO, (F) PVA

4.1.2 Polymer composites in tissue engineering

Despite intensive development in designing single component hydrogels e.g. Gel- and NaAlg-based (bio)ink formulations for 3D printing applications [165, 166], their properties are not suitable for many applications within the field of tissue engineering [167]. Composite materials combine several individual materials in a synergistic manner to enhance desired properties of the components, or provide additional functionality, which is not embedded in the material in the pure form. Precisely structured composite materials geometries yield anisotropic materials with changes of structural characteristics over one or more dimensions [168]. This concept can be used to resolve many issues related to biomedical engineering. Typical example is adding a cell adhesive layer to cell-repellent surface, thus utilizing the advantageous mechanics of one material, but allowing cell attachment and tissue connectivity at the same time, which is seen in a variety of naturally occurring composites [169, 170, 171]. This type of material can also provide platform for stimuli-responsiveness and on-demand modulation, forming smart materials [172].

Using additive manufacturing technologies is a straightforward way to obtain various composite structures. Multimaterial 3D printing offers virtually unlimited possibilities of material combinations and anisotropic domains design, thus allowing application-specific mechanical, chemical and biological characteristics. Popular material combinations in cell scaffold fabrication include PCL or NaAlg as the load-bearing parts, and a peptide or protein, such as Col or bovine serum albumin, to ensure cell adhesion [173, 174, 175, 176]. Modified 3D printing process can yield strands with core-shell geometries. This approach was used by Lian et al., 2021 to print scaffolds mimicking tubular structures found in body, such as hair follicles, or intestinal villus [177]. 3D printing also proves to be a convenient technology for preparing fibre reinforced hydrogel structures [178, 179].

A distinct type of composite structure is the particulate composite, which in general contains a matrix material (usually polymer), and a filler in the form of particles. The outcome is highly dependent, among others, on polymer-filler interface character and properties. If the dimensions of the filler decrease, its specific surface increases, thus

the interfacial effects become more significant. This is the reason for increasing popularity of nanofillers, which provide step change of characteristics at fractions of amount compared to microparticulate fillers [180].

Several types of inorganic particles with different additional functionality were used for such purpose. One of the most common nanofillers are various types of carbon-based nanoparticles (NPs) or bioceramics, especially in bone tissue engineering [181]. Bioceramics include inert silicates [182], but also bioactive materials, which provide not only mechanical reinforcement, but also bioinductivity, namely in case of osteocyte cultivation. Natural bone tissue contains calcium phosphate nanocrystal in the form of HAp [181]. HAp NPs in combination with natural polymers (Col, Gel, chitosan) present promising approach for development of bone tissue scaffolds. It was established that these hybrid materials promote osteoblasts adhesion, migration and differentiation [183, 184, 185]. In addition, hydrogels filled with calcium phosphate NPs should provide advantages from mechanical, chemical and rheological point of view [186]. Moreover, it was found that surface charged disc-like nanoclays, such as Laponite[®], spontaneously form a house-of-cards structure [187, 188]. This structure is characterized by randomly oriented nanoplatelets capable of providing intrinsic structural support to the polymer matrix, as depicted in Figure 4.2. Laponite[®] in association with PEG and NaAlg, acquired improved rheological properties, printability and, at higher clay concentrations, elevated recovery after shear [189, 190]. High shape fidelity of construct was manufactured by Dávila et al., 2019, when Laponite[®]-NaAlg hydrogels were printed [191].

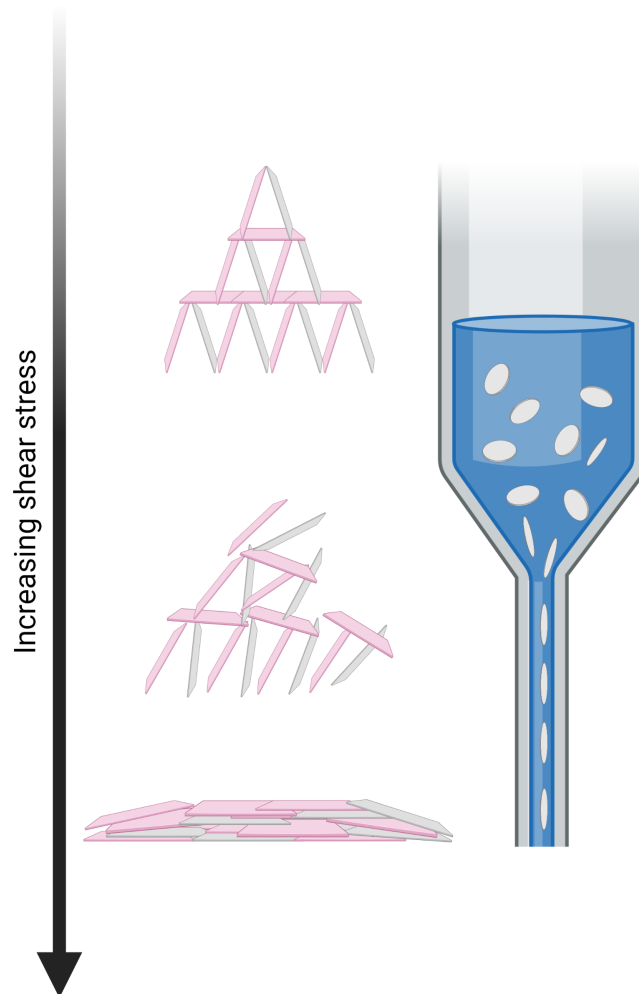


Fig. 4.2 Schematic illustration of the house-of-cards induced printability; Created with BioRender.com

Another possible purpose of incorporating particles in a hydrogel matrix is to introduce stimuli-responsiveness to the material, thus creating so-called smart hydrogels. By choosing magnetically responsive particles as the filler, the obtained hydrogel becomes instantly and reversibly controllable by the application of an external magnetic field. The choice of magnetic material governs both magnitude and character of the response. Two characteristic types of response are significant for the purpose of the thesis and will

be described: a) magneto-rheological effect (MRE), and b) magnetic heating.

Magneto-rheological hydrogels

Magneto-responsivity is a popular means to induce a mechanical response in a hydrogel through the MRE. This refers to the ordering of magnetic dipoles of the filler particles in the direction of an applied magnetic field. The aligned particles effectively create a supportive structure within the carrier medium, increasing the viscosity and strength of the material [192]. The magnitude of the MRE depends on several factors, mainly the saturation magnetization of the particles, their volume fraction, the viscosity of the carrier medium and the magnetic field strength. The magnetic material suitable for this application is soft ferromagnetics typically of micrometers size. The viscosity restrictions lead to generally lower MRE in solid carrier media, such as elastomers or hydrogels [193]. On the other hand, magneto-rheological fluids utilizing low-viscosity media often face the problem of sedimentation, as the density of typical magnetic fillers is high compared to fluid carriers. Nevertheless, careful tuning of rheological behaviour of the matrix can sustain a significant MRE as well as gel-like behaviour. Specifically, Rich et al., 2012 proved that the presence of a yield stress diminishes the viscous hindrance of MRE [194]. Biocompatible magneto-rheological hydrogel have a great potential in a wide variety of biomedical application, such as embolization [195], hard tissue (bone) engineering [196], or dynamic cell mechano-modulation [197].

Magneto-thermally responsive hydrogels

The response of a magneto-responsive hydrogel in a static, and an alternating magnetic field differs greatly. In an alternating magnetic field the magnetic moment is being periodically aligned with the rapidly changing magnetic field, while generating heat. Therefore, placing a magnetic material in an alternating magnetic field results in an increase of temperature, which can be used for a number of applications, including hyperthermia cancer treatment [198], thermal neurostimulation [199], or in combination with thermoresponsive polymer networks targeted drug delivery [200]. The magnetic heating is provided by three mechanisms: hysteresis loss, Brown relaxation and Néel relaxation. Hysteresis loss arises from the domain structure of a ferromagnetic material, and is produced by the domain wall displacement and rotation of magnetic

moment inside a domain. It is given by the area of a hysteresis loop, and is significant especially for hard ferromagnetic materials [201]. Brown relaxation is caused by the viscous drag acting due to physical rotation of the particle in a medium. This mechanism is largely hindered by the viscosity of the medium, and it is negligible in hydrogels [202]. Néel relaxation refers to the phenomenon of magnetic moment rotation without the change of the physical orientation of a particle. This is observed in single-domain or superparamagnetic particles, as the magnetization energy barrier has to decrease for the thermal fluctuations to become significant and allow the spontaneous magnetic moment reversal [198]. For clarity, examples of magnetization curves are depicted in Figure 4.3. The magnetic particle size thus determines the dominant heating mechanism of a magneto-thermally responsive hydrogel, and would also guide the optimal magnetic field characteristics. However, the acceptable alternating magnetic field strength and frequency for medical applications favours the magnetic materials tuning for Néel relaxation maximization as the effective option [203].

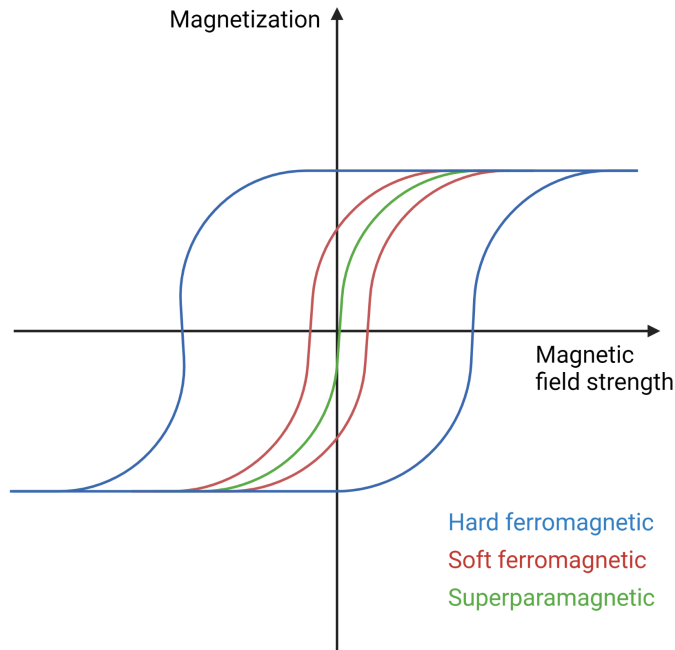


Fig. 4.3 *Typical hysteresis curves of ferromagnetic and superparamagnetic materials; adapted from [204]; Created with BioRender.com*

4.2 3D printing

Since the late 20th century, additive manufacturing technologies began to revolutionize fabrication of man-made products, nowadays entering almost every field of industry. The basic principle of 3D printing is layer-by-layer fabrication of constructs based on a computer model. As such, the technology offers a great versatility in design of the product. Naturally, the technology provides great opportunities also in terms of pharmaceutical research such as temporally programmed drug release and targeted drug delivery [22]. Furthermore, its potential in medical use, especially wound treatment [25] and tissue engineering [205] is abundant.

3D printing for medical applications and specifically bioprinting - i.e. printing of cell-laden biomaterials - draws attention of researchers due to possibility to prepare complex structures with homogeneously distributed cells, thus providing precise tissue analogues [206]. This ability could diminish the shortage of transplantable organs supply [81], as well as allow cruelty-free pharmaceutical research [207, 208].

Materials suitable for tissue engineering can be processed via several techniques respective to their individual properties, as well as desired purpose. The basic options include inkjet printing, extrusion-based printing and laser assisted printing [209].

Inkjet printing

Inkjet printing technology places the ink material dropwise on the predefined location, which is achieved for example by piezoelectric pulses [210], or thermal generation of vapour to pressurize the printhead [211]. The most important characteristic determining the suitability of a material for inkjet printing is surface tension - the measure of cohesive forces at the surface of the liquid. Higher surface tension results in better tendency to form droplets and aids the inkjet printing process [212]. This method requires low viscosity inks, thus the stability of the constructs needs to be ensured by *in situ* cross-linking [213].

Extrusion-based printing

In contrast to inkjet printing, extrusion printing technology generally produces strands of materials, which is placed on the substrate, which leads to lower resolution [214]. On the other hand, the variety of driving systems in this method (pneumatic, piston or screw) extends the range of usable inks to highly viscous materials, as long as they are shear thinning to ensure extrudability. Another advantageous characteristic is self-healing ability, which allows printing at low shear stress due to extreme decrease of viscosity, and immediate gelation upon lifting of the shear stress. This allows more precision of the printing process [213].

Laser assisted printing

The basic principle of laser assisted printing can be likened to inkjet printing, as it also uses placing of small droplets of material to desired position. Conversely to the above listed techniques, laser assisted printing does not use nozzle based printheads, but the printing is realized through a plate composed of donor ribbon (i.e. the printing material), and absorbing layer. The absorbing layer is locally evaporated by a focused laser beam, creating a high-pressure bubble which forces a small droplet of printing material out of the donor ribbon [215]. The high resolution printing is only achieved for materials with rapid gelation, which ensures low spreading [216].

Table 4.1 shows that while the best results in terms of resolution and cell viability can be achieved by laser assisted bioprinting, the high costs prevent its use to expand. Furthermore, like inkjet printing, it is unsuitable for high viscosity materials.

4.2.1 Hydrogels for bioprinting

Polymeric hydrogels, i.e. highly hydrated chemically or physically cross-linked networks, are one of the most advantageous classes of materials for creating 3D porous scaffolds. They provide good shape fidelity as well as simulating ECM and modulating cell fate [217, 218]. These properties are required for the normal development of func-

Printing technology	Advantages	Disadvantages	Ink material
Inkjet	High resolution > 85% cell viability	Low material viscosities (3.5-12 mPa·s) Poor vertical structure Low cell density	NaAlg PEGDMA Col
Extrusion	Wide range of viscosities (30 mPa·s - 10 ⁴ Pa·s) High cell density Good vertical structure	Moderate resolution 40%-80% cell viability	NaAlg GelMA Col
Laser assisted	High resolution > 95% cell viability Good vertical structure Fair cell density	Low viscosity materials (1-300 mPa·s) High cost	Col Matrigel

Tab. 4.1 Comparison of basic 3D printing technologies for tissue engineering [206]

tional tissues [9, 187]. Generally, both synthetic and natural polymers have been used for hydrogels designing [188]. Although synthetic materials provide advantages in terms of tuning of mechanical properties and reproducibility through controlled chemical composition, they also face problems with cellular response due to lack of adhesive sites in their structure. Natural polymers, on the other hand, are considered inherently less risky in terms of cell adhesion and cytotoxicity.

Hydrogels utilizable as bioinks have to fulfill three specifications, which can be denoted as printability, cross-linkability and biocompatibility (Figure 4.4). Printability refers to printing accuracy [219], i.e. the ability to apply precise spacial control over the bioink deposition. The printing process requires certain characteristics related to shear-thinning behaviour, surface tension and surface energy of the bioink-substrate pair, and filament swell due to normal stress at the end of a printing geometry. Hydrogel tuning in terms of printability must therefore address each of these problems.

The second specification, cross-linkability, refers to the necessity of the hydrogel to remain stable for several days during cell cultivation in order to serve as a scaffold [206]. Typical bioink for microextrusion can be characterized as a highly viscous solu-

tion of polymer and cells [213]. Their disadvantage is that it dissolves easily in excess of solvent. Cross-linkability characterizes the ease of stabilization of the printed structure by inducing formation of 3D polymer network. Commonly, this is done by photo [220, 221, 222], chemical [3, 223, 224] or thermal [225] cross-linking. In broader objective, cross-linkability can be seen as long term stability of the scaffold.

Third specification, biocompatibility, can be defined as the ability of a material to coexist with the surrounding tissue without triggering immunogenic reaction [219]. However, in tissue engineering the biological demands are higher, as they include also adhesiveness, support of proliferation and even differentiation in case of stem cell culture [226, 227, 228, 62].

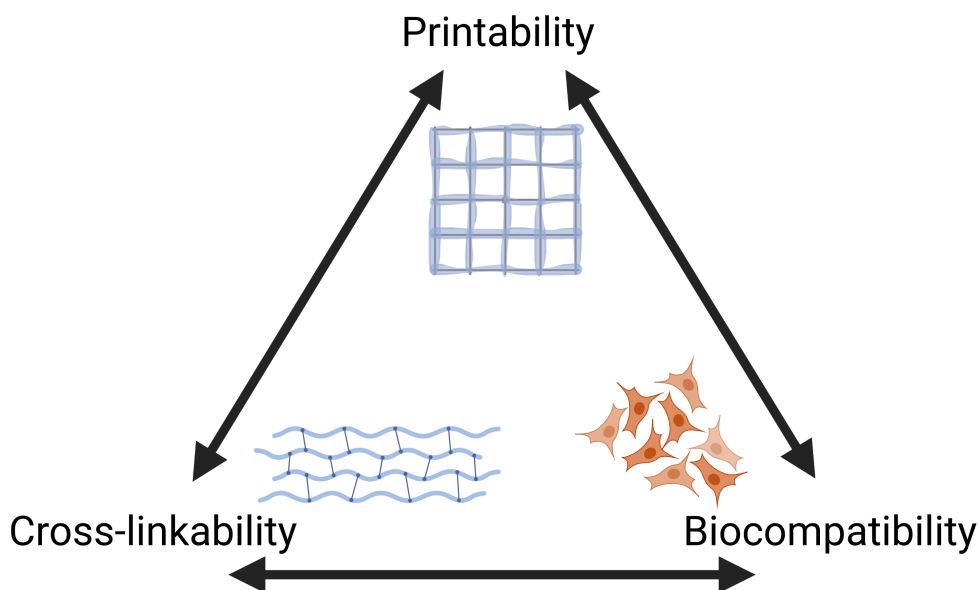


Fig. 4.4 Schematic representation of key characteristics of hydrogels for 3D printing in biological applications; Created with BioRender.com

These key characteristics necessary for obtaining printable hydrogel are interconnected, and must be addressed at the same time. The behaviour to follow includes mainly

- rheological behaviour, influencing printability and biocompatibility (through shear stress induced cell mortality),
- chemistry, influencing cross-linkability and biocompatibility,
- mechanical stability, influenced by cross-linkability (through long term stability) and contributing to biocompatibility (through mechanoresponsiveness),
- morphology, influencing biocompatibility (through structure induced cell guidance).

There appears to be an inversely proportional relationship between printability and cell viability, and printing precision, as illustrated by Figure 4.5. In terms of rheology, it has been found that high shear stress (induced by use of cylindrical needle over conical nozzle, higher extrusion rate or smaller diameter flow domain [229]) increases printability of a material, but it also increases cell mortality and therefore decreases biocompatibility of the printing process [230]. In terms of chemical cross-linking, UV irradiation [231], high temperatures (over 42°C [232]) and large number of commercially available cross-linkers (such as glutaraldehyde or epoxides [233, 234]) are harmful to cells and may cause mutations and cell death.

3D printing, especially bioprinting, is presumed to potentially offer solutions to complex problems in tissue engineering with the need of defined position of matrix and cells along with the vascular network. In this application, hydrogels are of vital importance due to their porous inner structure and high ability of water retention. However, such material may often suffer from severe drawbacks, mainly in terms of mechanical performance, or extrudability. The use of polymer-inorganic nanocomposite is a common approach for improving mechanical properties of hydrogels, while cell viability and fabrication of 3D constructs are supported [237, 238]. Consequently, nanocomposite (bio)inks application in tissue engineering is very promising.

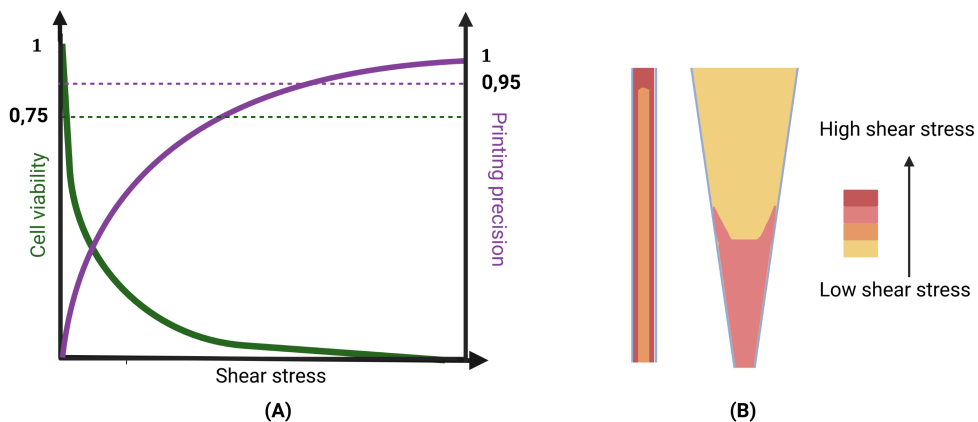


Fig. 4.5 (A) Typical example of the influence of shear stress on printing precision and cell viability in microextrusion 3D printing with marked cell viability (75%) and printing precision (95%) thresholds (inspired by [235]); (B) Schematic representation of shear stress distribution in cylindrical and conical flow channel (adapted from [236]); Created with BioRender.com

4.2.2 Cross-linking strategies of hydrogels for 3D printing

As stated earlier, cross-linkability is an essential quality of a 3D printable hydrogel. There are generally two paths to cross-linking of polymers and thus creating hydrogels - physical and chemical. These two groups differ in the nature of the bonds, where physical hydrogels have a network of non-covalent bonds, while in chemical ones the polymer chains are cross-linked covalently. Some characteristics of physical gels include reversibility and generally lower mechanical performance compared to chemical cross-linking [213]. Nevertheless, both mechanisms are widely used for 3D printable hydrogels.

Physical cross-linking

A typical example of physical cross-linking is utilization of hydrogen bonds, which are a common feature of number of polymers containing polar groups - PVA, Gel, or agarose [153, 124, 239]. These bonds form spontaneously and are thermally reversible

(Gel undergoes transition at around 35°C - 40°C [131], agarose at around 100°C [239]).

Another popular non-covalent cross-linking procedure is metal ion complexation. This strategy is useful in anionic polymers, as they contain readily available binding sites, and the cross-linking upon addition of multivalent metal cations is instantaneous. This phenomenon is very well described and widely used in case of NaAlg [240, 241, 242, 243, 244]. The first proposed mechanism of this type of cross-linking was the egg-box model [245], suggesting polymer chains assembled in the vicinity of Ca^{2+} ions, as can be seen in Figure 4.6. This model predicts increasing strength of the network with increasing number of Ca^{2+} ions until full saturation of the binding sites. It was observed that with increasing ion concentration, the mechanical strength does not reach maximum value, but decreases at some point. This was explained by Donati et al., 2015 as a result of emerging junctions of guluronic acid and mannuronic acid, ultimately causing collapse of the polymer structure [115]. Despite its popularity, use of calcium kation cross-linked NaAlg in cell cultivation and tissue engineering applications suffers from insufficient stability of the hydrogels in cell cultivation media due to exchange of divalent calcium ions and monovalent sodium ions. As a remedy to this drawback, alternative multivalent ions have been tested - e.g. Ba^{2+} , Sr^{2+} or Fe^{3+} [246, 247] - to ensure stronger affinity of the cross-linking ions to the NaAlg chains and thus long-term stability during cultivation. Ionic cross-linking has been described also for pectin [248], chitosan [249, 250, 251], HA [252, 253] or polyurethane [254]. Due to the swift and straightforward mechanism, it is popular also as a complementary cross-linking strategy to more robust chemical bonds [255, 256].

A novel trend of non-covalent cross-linking has emerged with the so-called supramolecular host-guest systems. Such systems consist of a pair of complementary host-guest moieties with unique recognition due to asymmetrical interactions [258, 259]. Such selective relationship have been found for electron-rich and electron-poor units (eg. cucurbiturils or crown ethers and viologen [259, 260]) or hydrophilic and hydrophobic interactions (such as found for dopamine or adamantane and β -cyclodextrin [261, 262, 263]). Host-guest systems utilize the spontaneous self-assembly, weak non-covalent nature of the bonds and selective recognition to produce dynamic networks capable of rapid depleting and self-healing at application of external stimuli. These characteristics

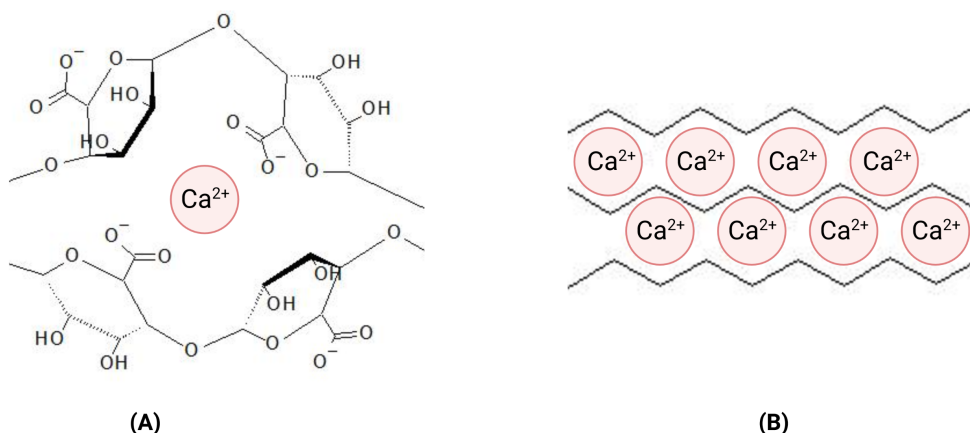


Fig. 4.6 Schematic representation of Ca^{2+} cross-linking of NaAlg: (A) calcium guluronan junction (adapted from [257]), and (B) egg-box model (adapted from [245])

make them promising biomimetic materials for 3D printing in biomedical applications [264, 265].

Chemical cross-linking

The most typical chemical cross-linking involves using low-molecular cross-linking agents, which react with functional groups of the polymer backbone. The most frequently used reactions take place at $-\text{OH}$, $-\text{NH}_2$, or $-\text{COOH}$ groups.

Hydroxyl groups are commonly occurring in both natural and synthetic bicompatible polymers. Due to their reactivity to aldehyde groups, they are often targeted by dialdehyde cross-linkers - glutaraldehyde or glyoxal [266, 267]. However, low-molecular dialdehydes can induce oxidative stress to cells and decrease their viability [233, 234]. Natural derived polyaldehydes have been studied as low-toxicity alternatives [268]. These are commonly obtained by oxidation of saccharide units in polysaccharides [53, 269, 270, 271].

Peptides and proteins, abundant and versatile group of natural polymers, are sequences of amino-acids. As such, they often have accessible $-\text{NH}_2$ groups in their structure,

which can be used for cross-linking or chemical modification. These include for instance Schiff base formation in the presence of aldehydes, such as imine bonds. Schiff bases are so-called dynamic covalent bonds [272], which can be depleted and reformed upon external stimuli, especially pH [273], leading to self-healing and shear-thinning hydrogels [274, 275]. However, it also causes the network to be unstable and vulnerable to presence of free amino-acids, such as found in cell cultivation media. Therefore, their stabilization by reduction can be beneficial [276]. Other possible reaction partners are acid anhydrides which produce peptide bonds [277]. This method is particularly popular for methacrylation of natural polymers, allowing their photocross-linkability [278]. Although cross-linking via reactions of -NH_2 is especially convenient in case of proteins, many researchers introduce these functional groups to other polymer chains via carbodiimide chemistry in order to allow analogous cross-linking [270, 279].

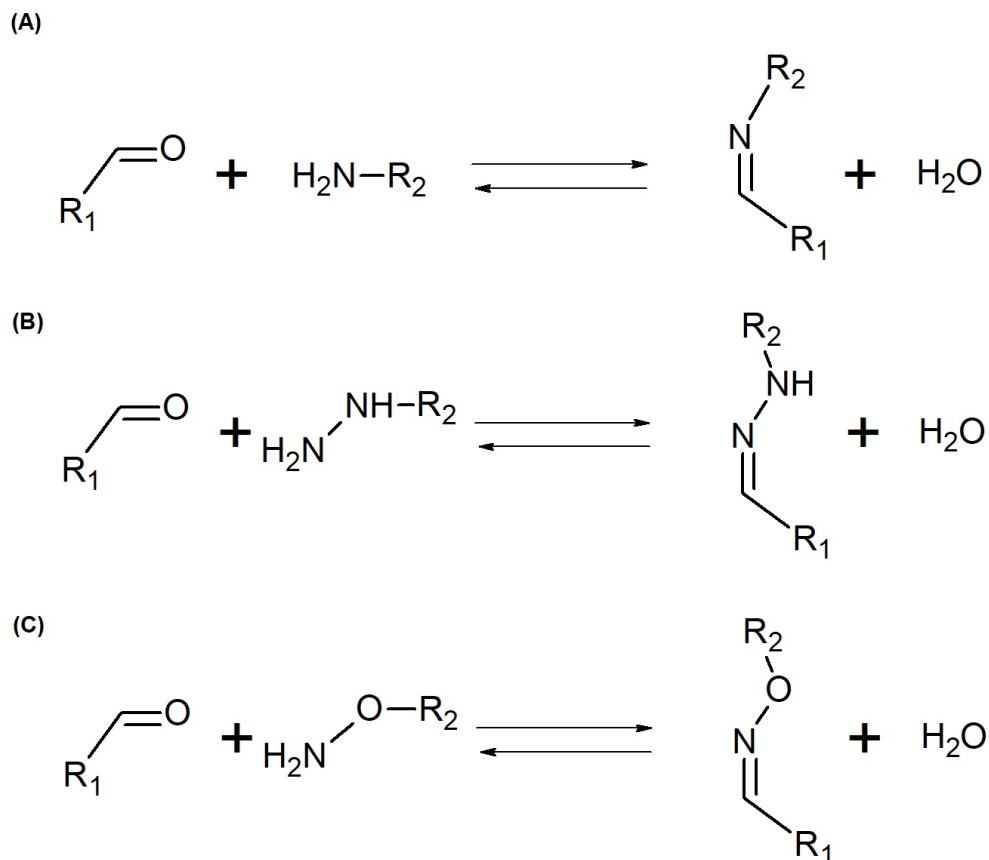


Fig. 4.7 Examples of Schiff bases formation: (A) imine, (B) hydrazone, (C) oxime

The reaction based on carboxyl group of polymers, such as HA or chondroitin sulfate, require activation of the reactive site. A well described activating system employs 1-ethyl-3-(3-dimethyl aminopropyl)carbodiimide (EDC) and N-hydroxysuccinimide (NHS) or 1-hydroxybenzotriazole (HOBT). EDC activation mechanism involves protonation of EDC and formation of unstable *O*-acylurea, which is accessible for other reactants. The presence of nucleophile - NHS or HOBT - prevents reforming of -COOH and urea byproduct in aqueous environment [280]. This activating system is highly versatile, and has been used for various outcomes, including direct cross-linking via esterification of HA [281] or cross-linking of proteins and polysaccharides via amidation [282]. However, the EDC activation is pH sensitive, and yields good results only at acidic

pH [281]. Additionally, carbodiimide chemistry results in part of *O*-acylurea converting to stable *N*-acylurea, which can cause cytocompatibility problems when used in biomedical applications [283]. As an alternative to carbodiimide chemistry, the use of 4-(4,6-Dimethoxy-1,3,5-triazin-2-yl)-4-methylmorpholinium chloride (DMTMM) was proposed. DMTMM is water soluble and produces reactive site, which is not prone to hydrolysis, therefore does not require the presence of a nucleophile. Additionally, D'Este et al., 2014 achieved high efficiency of the activation without adjusting pH [279]. Therefore, DMTMM appears to be a promising alternative to EDC activation of carboxyls in aqueous media.

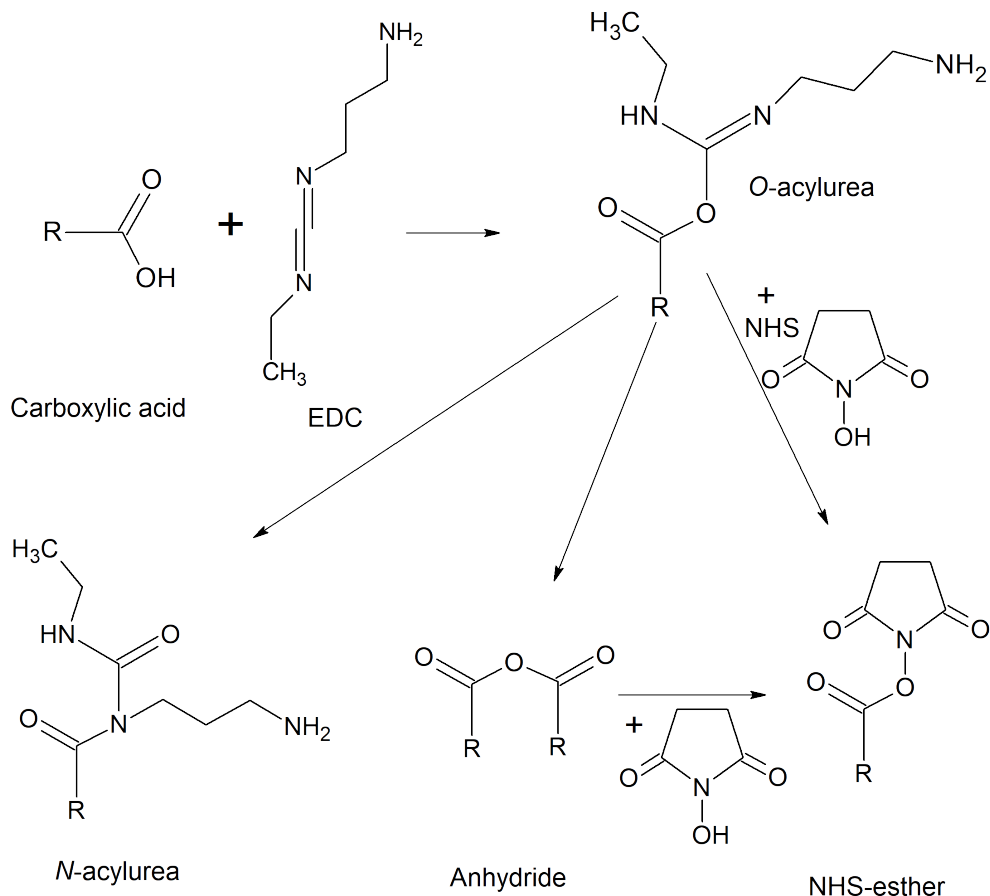


Fig. 4.8 Activation of $-COOH$ group with EDC and NHS system (adapted from [284])

The well described EDC mediated amidation is a convenient means to cross-linking *via* ester bonds, or to introduce other reactive groups to allow two-step cross-linking, such as thiolation [285, 286] producing materials gelling in the presence of oxygen. Another possible outcome is introducing diene and alkyne moieties, thus enabling Diels-Alder cycloaddition to occur [287, 288]. These bonds are thermoreversible and do not require catalysis, although $\text{Cu}^+ \leftrightarrow \text{Cu}^{2+}$ catalytic systems are popular for acceleration of the reaction [289, 290]. In addition to cross-linking and hydrogel formation, these reactions are often sought for grafting polymers with functional molecules, such as dopamine to induce specific cell response [291].

4.3 Electrofluidodynamics

Electrofluidodynamics comprise phenomena occurring when placing a fluid in an external electric field. If the processes are viewed in the most general way, an external electric field causes imbalance of charges in the bulk and on the surface of the liquid, leading to electric pressure. Once the pressure overcomes the capillary forces (i.e. surface tension), the repulsive electrostatic force induces formation of a Taylor cone (Figure 4.9) and subsequently a liquid jet opposite to the direction of electric field gradient [292].

The electric pressure causing the initial instability of the liquid droplet arises from electric force, which can be found as:

$$F_e = \int \left(\frac{1}{2} \varepsilon E^2 \right) ds, \quad (4.1)$$

where ε ($\text{F}\cdot\text{m}^{-1}$) is the permittivity of the environment, and E ($\text{N}\cdot\text{C}^{-1}$) is the electric field intensity. The electric field needs to be strong enough to overcome the capillary forces:

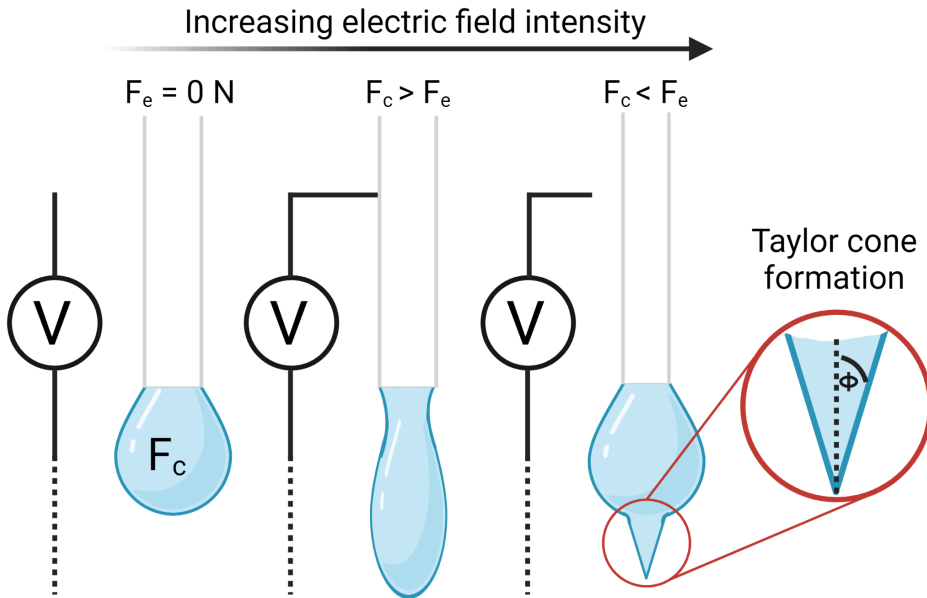


Fig. 4.9 Schematic representation of liquid droplet shape evolution with the increase of electric field intensity and Taylor cone formation (adapted from [6]); Created with BioRender.com

$$F_c = 2\pi r\gamma\cos\theta, \quad (4.2)$$

where γ ($\text{N}\cdot\text{m}^{-1}$) denotes the surface tension and θ is the contact angle between the liquid and the surface [6].

There are three major manufacturing technologies based on the formation of Taylor cones and electrofluidodynamic phenomena following it (Figure 4.10). First, it is the electrospaying technology, which is connected to the early observations of electric instability. These refer to disintegration of the fluid jet into droplets, caused by capillary instability. This behaviour is driven by minimum energy principle, and occurs when the surface tension of individual droplets is lower than that of a fluid cylinder [293]. Electrospaying technology uses this phenomenon to obtain an aerosol of fine liquid

droplets [294].

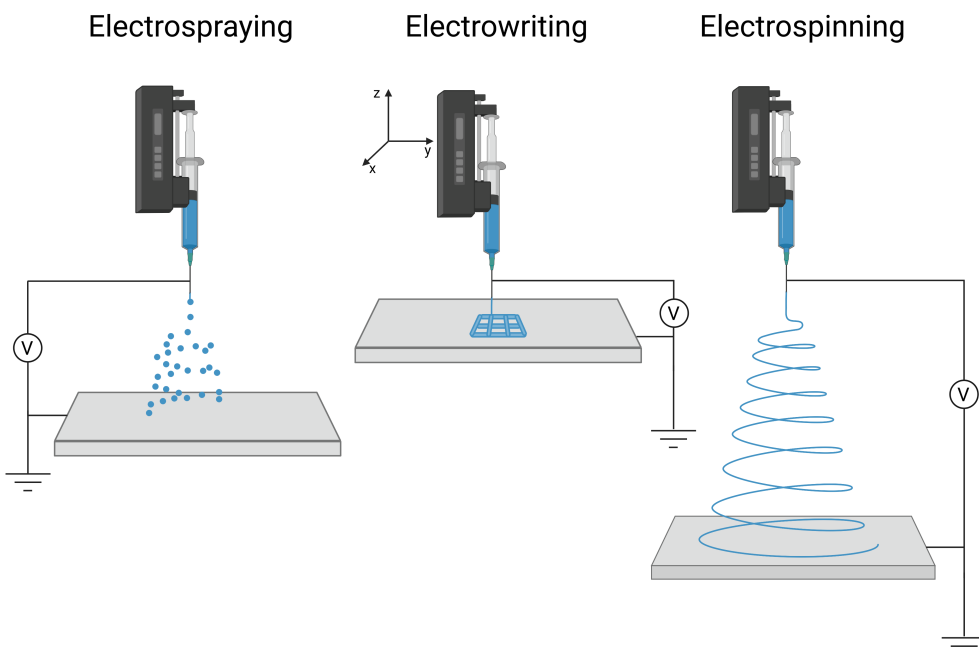


Fig. 4.10 *Technologies based on electrofluidodynamic phenomena; Created with BioRender.com*

Secondly, the electrowriting technology will be described. This technology is based on a stable jet occurrence in the early stage of electrospinning process, while viscoelastic forces prevail over inertia and the jet path is straight. This part of electrospinning process is typically described by rather low elongation rate, and the Trouton ratio (i.e. the ratio of elongation to shear viscosity) is equal to 3 [295]. The electrowriting technology uses precise position of an electrically elongated jet owing to controlled move of the spinneret [296], effectively combining electrofluidodynamics and 3D printing principles. Therefore, keeping the jet in stable spinning region is the key requirement for electrowriting technology. Furthermore, strain hardening due to polymer chain entanglements takes place in this stage of spinning process, providing further stability to the jet. It is argued that stability of the jet can be increased by using branched polymers, or highly polydisperse polymers [297]. Due to short jet path and relatively low elongation, the solvent is unlikely to completely evaporate during electrowriting [295]. It is more favorable to use polymer melts over solutions for this applications, since rather

fast solidification by decrease of temperature can be achieved [298].

Once the polymer jet surpasses the stable region, the main phenomenon to nanofibres fabrication via electrospinning takes place. The charged jet is continuously moving in an external electric field, thus it cannot be in a stable equilibrium according to Earnshaw's theorem. The imbalance of charges causes bending of the jet to occur, which eventually generates an expanding coil [295]. This phenomenon is referred to as whipping instability, and it causes a significant prolongation of jet path, as illustrated in Figure 4.10. The continuous elongation of the jet causes decrease of jet diameter, thus simultaneously increases its specific surface area. This causes rapid evaporation of the solvent in solution spinning and solidification of the fibre [299]. The current thesis is mainly focused on electrospinning technology.

4.3.1 Parameters influencing electrospinning

The electrospinning process as well as other electrofluidodynamic phenomena is influenced by number of parameters. These are usually divided into material, processing and ambient parameters - see Figure 4.11.

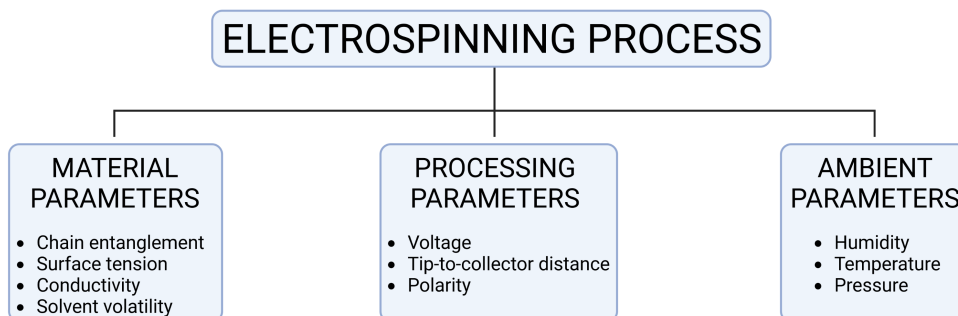


Fig. 4.11 *Parameters influencing electrospinning; Created with BioRender.com*

There are multiple solution parameters, which need to be taken into account in electrospinning process. The most outstanding role can be found for polymer chain entanglement, which involves multiple influences:

- polymer chain rigidity,
- polymer M_w ,
- polymer-solvent interactions,
- polymer chain conformation.

Each of these parameters can be used to influence the outcome of the electrofluidodynamic fabrication. Shenoy et al., 2005 suggested 2,5 entanglements per chain as the minimum for successful electrospinning process. Lower number would yield electro-spraying, while higher number leads to increased fibre diameter [300]. Chain rigidity and M_w are intrinsic characteristics of the polymer. The interactions of the parameters are complex and lead to multiple effects on electrospinning process. The used solvent

influences the polymer chain due to polymer-solvent interactions [301], surface tension [302], and evaporation rate. The gradual solidification of the jet during electrospinning was determined as a means to stabilize the jet, and allow spinning of continuous fibres even at less than 2.5 entanglements per chain [299]. Polymer chain conformation is also influenced by the choice of a solvent through polymer-solvent interactions [303]. Another means to change the conformation, especially in case of polar polymers, is addition of salts [304], which at the same time increases the conductivity of the solution. Higher conductivity leads to polymer jet stabilization against formation of beaded structure [305], and also possibility to form Taylor cones on the surface of emerging fibre, leading to branching [295].

The electric field intensity is directly proportional to the applied voltage, and inversely proportional to electrode - collector distance. Therefore, it is the central characteristic dictated by the processing parameters. However, short distance causes short jet path and limits the elongation zone and evaporation time, causing bead-on-string instabilities, or branching of the electrospun fibres [302, 306, 295, 307]. On the other hand, short jet path is essential for maintaining stable jet path, and allowing electrowriting [298]. The electric field polarity is also reported as an important parameter. While DC positive voltage remains the most popular option, DC negative or AC voltage can facilitate electrospinning as well [308, 309]. Additionally, the voltage polarity have been observed to significantly influence the surface energy of the electrospun fibres [310, 311].

The straightforward understanding of humidity and temperature influence on electrofluidodynamic phenomena lies in their effects on evaporation rate, influencing the fibre diameter [312]. The specific effect are highly dependent on the polymer material, as increased humidity can increase [313] the fibre diameter, and cause the formation of bead-on string instability [314]. Furthermore, electrospinning of water-insoluble polymers in high humidity environment has been used to generate porous fibres *via* vapor-induced phase separation or breath figures method [315].

4.3.2 Core-shell electrospinning

Core-shell electrospun fibres are a typical composite structure composed of inner fibre (core) surrounded by outer material (shell). This method allows tuning mechanical, optical, or biological properties of the fibres, as well as fabrication of hollow fibres and encapsulating low-molecular substances in the fibre core [316]. In general, there are two ways how to achieve this structure: co-axial electrospinning and emulsion electrospinning [317, 318]. Co-axial spinning uses a two-channel spinneret, where the core and shell material flow separately and the Taylor cone is drawn from both. Due to the presence of core-shell interface, shear stress is generated between the spun liquids, and the integrity of the fibre can be disrupted. Therefore, interfacial tension, emerging from the respective fluids miscibility and viscosity difference, has to be maintained at a level, where it prevents blending of the liquids, while at the same time does not cause their separation [319]. Emulsion electrospinning, on the other hand, relies on emulsion of immiscible liquids and can be done from a single spinneret. The rapid stretching of the polymer jet leads to creating long range core-shell fibre. In order to conduct emulsion electrospinning, encapsulation of the core in the shell material is induced by electric field induced phase separation (for oppositely charged phases) [320], or viscosity-driven enveloping [321].

4.3.3 Electric field assisted fabrication of scaffolds

The use of electric force typically yields constructs of small objects with large surface area, high porosity and tunable pore size [1]. In case of fibre fabrication, high aspect ratio needs to be taken into account too. Electrospayed scaffolds are rather less common due to particulate character of the product, which lacks spatial orientation, and their use in biomedical applications is oriented mainly towards drug carriers [322, 323]. They can find use in isotropic tissues (cartilage, fatty tissue) [324], or in combination with other fabrication methods, where it serves to create nanotopography [325, 326]. Electrospinning, on the other hand, can be in principle means to obtain highly oriented structures, as its product is a one dimensional fibre [6, 327]. Nevertheless, the whipping instability typically disrupts the orientation of fibres and results in random fibrous

mesh [328]. To overcome this problem, special collectors are used [329] - static parallel prisms or corrugated collector [8], or rotational drums. Highly oriented fibrous mats are advantageous, especially for muscle and neural tissue scaffolds [67, 69]. The electrowriting method offers means to maintain fibrous structure and precise positioning at the same time. However, the fibre diameter is greater compared to electrospun, and it cannot be used to produce nanotopographical features [330].

Nanofibrous scaffolds combine several characteristics typical for ECM, including tunable porosity and mechanical characteristics, as well as the presence of nanofeatures advantageous in cell guidance [331]. According to the desired use, it is possible to prepare random or directional oriented fibrous scaffolds of various shapes [9, 332]. Oriented nanofibrous structures provide signal paths and lead to the significantly more aligned cytoskeleton of stem cells and also enhance their adhesion [12, 67, 70, 333]. Aside from cellular scaffolds fabrication, nanofibrous constructs may also be used as drug delivery systems [18, 16] or as growth factor delivery mediators [110, 334].

5 SUMMARY OF THE PAPERS

The first 4 papers describe the preparation of natural polymer-based systems suitable for 3D printing. The papers examine the use of dynamic cross-linking in order to achieve a favorable rheological profile for extrusion-based 3D printing [213, 335].

5.1 Schiff-base cross-linking of natural polymers

Dynamic covalent interaction are bonds, which undergo reversible depletion upon introducing an external stimulus. Thus, these bonds lead to self-healing and shear-thinning materials, making them desirable in 3D printing applications. A typical example of this bonds are the Schiff bases, that are the product of reaction of amino-groups and aldehydes (see Figure 5.1). Additionally, hydrazones, a group of bonds in the Schiff base family, are bioorthogonal, and highly desirable in bioprinting and tissue engineering.

The usability of cross-linking *via* Schiff base formation to prepare hydrogels printable by microextrusion is demonstrated in **PAPER I**. The hydrogels are based on Gel, a protein naturally containing $-NH_2$ groups available as reactive sites.

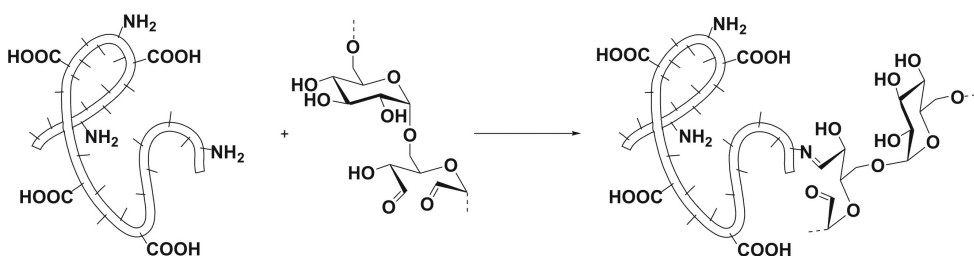


Fig. 5.1 Schematic of a Schiff base formation between Gel and DEX-OX [336]

Polysaccharide-based polyaldehyde obtained by periodate oxidation of dextran was chosen as a substitute to toxic low-molecular bi-functional aldehydes, such as glutaraldehyde [233]. The polysaccharide-based polyaldehydes have been proven as a

low-toxicity cross-linkers in previous studies [268, 269]. The research presented in **PAPER I** studies the influence of Gel origin (bovine, rabbit or chicken) and dextran polyaldehyde (DEX-OX) concentration on reaction kinetics and hydrogel's rheological properties. The reaction kinetics, as followed by the increase of viscosity of the reaction mixture, gives a good fit to the proposed first order reaction model. Additionally, all hydrogel compositions show shear-thinning behavior, which is desirable in terms of extrusion-based 3D printing. The printability evaluation conducted according to the methodology described by Ouyang et al., 2016 [226] shows high correspondence of the printed structure to the model, as the Pr value varies between 0.8-1.5 (the ideal is 1 by the definition of this evaluation method). To conclude, **PAPER I** gives the proof of concept of the usability of Schiff-base cross-linked hydrogels in 3D printing *via* microextrusion.

The successful proof of concept was followed by utilizing the principle of dynamic Schiff-base bonds in smart hydrogels, as described in **PAPER II** and **PAPER III**. Smart hydrogels are a group of materials, which give immediate, macroscopic and reversible response to external stimuli, ranging from temperature, pH, humidity, to electric and magnetic field. **PAPER II** described the use of Schiff-base cross-linked HA hydrogel as a biocompatible matrix suitable for encapsulating carbonyl iron particles (CIPs). The polymer matrix was formed by the reaction of HA modified with adipic acid dihydrazide (HA-ADH), and oxidized HA (HA-OX). The reaction kinetics was followed by the increase of reaction mixture viscosity. In **PAPER I** the reaction rate was proportional to DEX-OX concentration. It was assumed that the reaction rate would follow the same trend of proportionality to the number of reactive sites available. However, the measurement in **PAPER II** showed the highest reaction rate in case of DEX-OX with intermediate degree of oxidation (Figure 5.2). This discrepancy was attributed to larger hydrodynamic diameter of HA-OX coils compared to DEX-OX, which leads to lower diffusion coefficient of HA-OX of either degree of oxidation, thus increasing the gelation time.

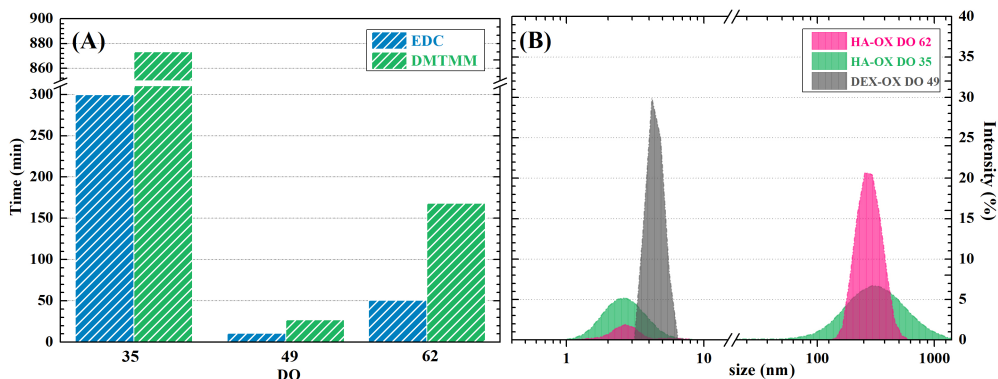


Fig. 5.2 (A) Gelation time of HA hydrogels of HA-ADH modified with EDC (degree of substitution - DS 22 %) and DMTMM (DS 12 %) mediators related to (B) the oxidized polysaccharide hydrodynamic diameter measured by dynamic light scattering - the degree of oxidation (DO) is indicated in the graph [337]

The presence of CIPs described in **PAPER II** leads to the MRE, a phenomenon of considerable stiffening of the material in an external magnetic field. The combination of soft hydrogel matrix and 30 wt.% (approx. 4 vol.%) of CIPs led to 1000 times increased storage modulus of the composite hydrogel reaching 10^4 Pa, as depicted in Figure 5.3 (A) and (C). Such increase is about 50 times higher compared to the highest values found for biocompatible magneto-rheological gels in literature [338].

The character of magnetic response depends largely on the magnetic material used as the responsive filler. The material described in **PAPER II** used soft ferromagnetic CIPs of approx. $3 \mu\text{m}$ in diameter. These particles are widely used as the providers of MRE. Decreasing the particle diameter below a certain threshold, generally tens of nm, leads to transition from ferromagnetic to a single-domain state. The MRE generally decreases with the decrease of magnetic particle size [339]. On the other hand, the low diameter of the particles leads to high energy losses during changes of magnetic field [198].

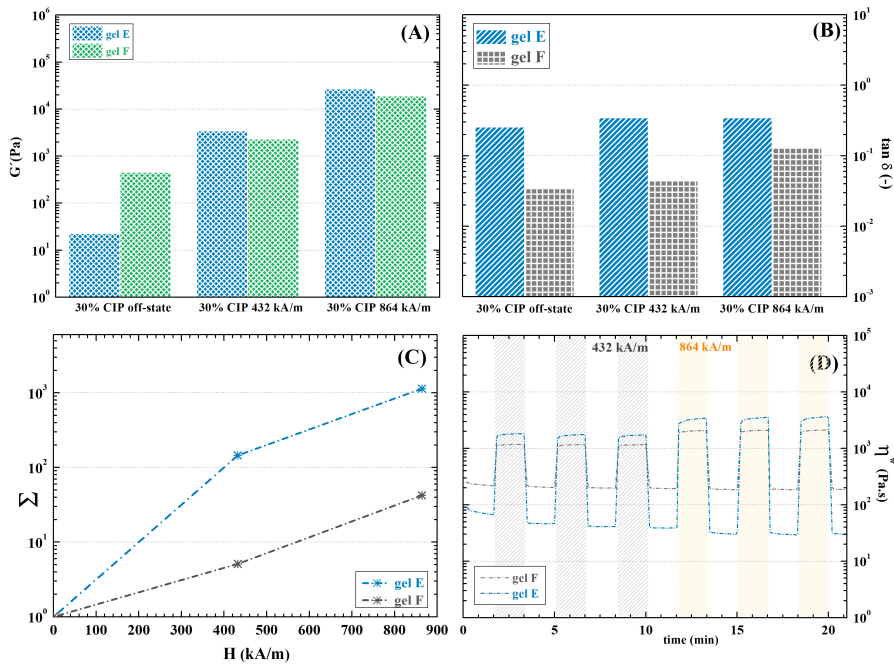


Fig. 5.3 Mechanical characteristics obtained from magneto-rheological measurements of CIP filled Schiff base cross-linked hydrogels in an external magnetic field: (A) Storage modulus; (B) Damping factor; (D) Intensity of MRE expressed as increase in storage modulus related to magnetic field intensity; (E) Cyclic magnetic field exposure

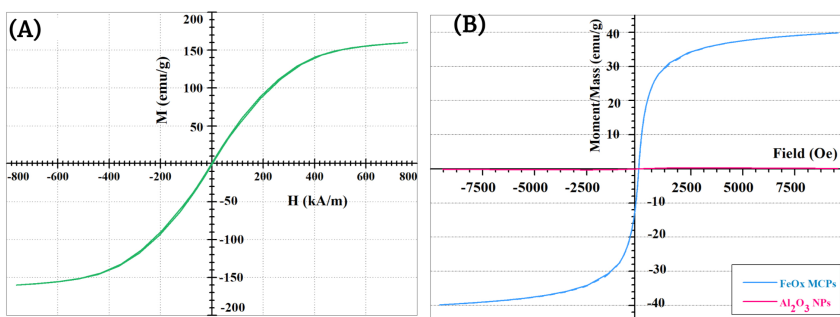


Fig. 5.4 Magnetization curves of (A) soft ferromagnetic CIPs used in **PAPER II** [337] and (B) superparamagnetic iron oxide multicore particles (MCPs) and diamagnetic Al_2O_3 NPs used in **PAPER III**

PAPER III describes the usability of the proposed Schiff-base cross-linked HA hydrogels as efficient magnetic heating mediators in biomedical applications. The superparamagnetic iron oxide MCPs (Figure 5.4) were used as an alternative filler, as these provide significant magneto-thermal response. The hydrogels reached high heating rate of 0.3°C per minute in low-power alternating magnetic field approved for medical applications. Additionally, the positive effect of diamagnetic Al_2O_3 NPs shielding of ferromagnetic FeO_x MCPs on heating efficiency was found both in water dispersions of the particles, as well as in the hydrogel (Figure 5.5). This leads to the conclusion that the shielding affects predominantly the Néel relaxation, i.e. the process of magnetic moment orientation within a MCP.

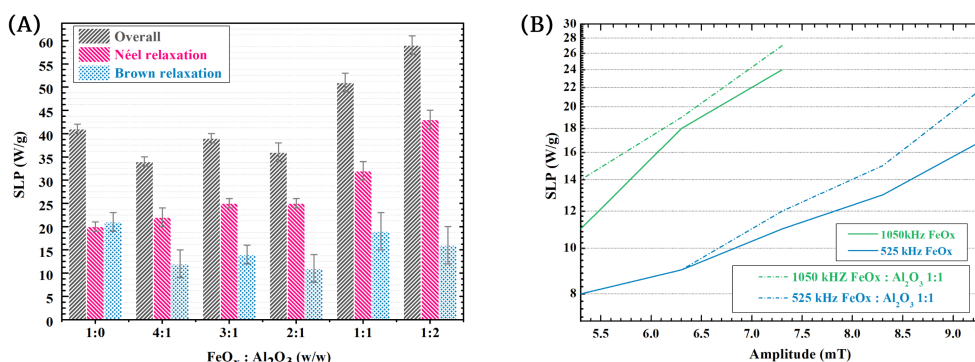


Fig. 5.5 (A) Specific loss power (SLP) of FeO_x dispersions with the increasing amount of Al_2O_3 : Overall denotes the SLP results for water dispersions, where both Brown and Néel relaxation are present; Néel relaxation denotes values obtained by measurement in agar gel; Brown relaxation is the difference between overall SLP (measured in water dispersion), and Néel relaxation induced SLP (measured in agar gel); (B) SLP of magneto-responsive HA hydrogel as a function of AMF amplitude

Moreover, the magneto-responsive hydrogels described in **PAPER III** were used as a biocompatible matrix for encapsulation and 3D bioprinting of BALB/3T3 mouse fibroblasts with cell viability after printing $>85\%$ (Figure 5.6).

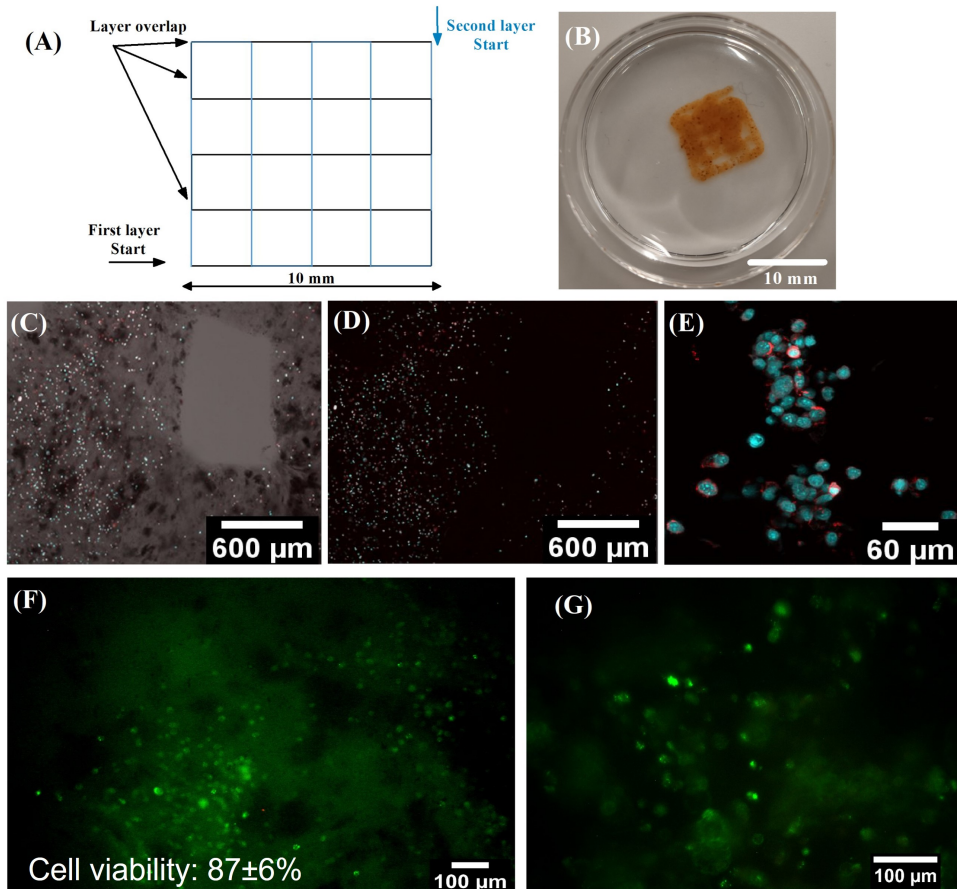


Fig. 5.6 *Bioprinting of BALB/3T3 mouse fibroblasts encapsulated in magneto-responsive HA hydrogel: (A) Printing model; (B) Printed grid photography taken on the 8th day after printing; (C), (D), (E) Confocal imaging of cells distribution within the scaffold in bright field (C) and fluorescence channel (C-E). Cells were stained for cytoskeleton (red) and nucleus (blue); (F), (G) Live/Dead assay of BALB/3T3 fibroblasts. The cells were visualized in fluorescence immediately after the microextrusion.*

An adverse effect of dynamic covalent bonds in biocompatible hydrogels was found through cell cultivation experiments. Despite the fact that Schiff-base cross-linked hydrogels showed good stability in distilled water, 0.1M PBS of physiological pH 7.4, and Dulbecco's Modified Eagle Medium (DMEM) at 37°C, their stability plummeted when calf serum and antibiotics were added to the DMEM. Based on the results, the

following hypothesis was formed: the free amino-acids in calf serum react with the aldehyde groups present on oxidized polysaccharide chains. Thus, the amino-acids are competitive to the aldehyde groups of HA-ADH. The smaller molecules of free amino-acids would bare the advantages of higher concentration of reactive sites, as well as higher diffusivity, shifting the balance towards aldehyde-amino acid bonds over aldehyde-HA-ADH bonds. Interestingly, the hydrogel decay was considerably suppressed in hydrogels containing FeO_x MCPs and Al_2O_3 NPs (see Figure 5.7 (A)), as described in **PAPER III**. These observations might be the result of partial dissociation of Fe^{3+} and Al^{3+} cations and their affinity to the polyanionic HA. These cations would bond to the COO^- groups of HA, and form ionic cross-links in the polymer structure. Following this assumption, the structure of hydrogels was reinforced with Fe^{3+} ionic cross-linking also in **PAPER II**. This treatment led to stiffening of the hydrogel matrix, consequently diminishing, while not completely eradicating the MRE 5.7 (B). It also allowed the matrix to remain stable in cell cultivation conditions for several days, leading to a viable stimuli-responsive material in tissue engineering applications.

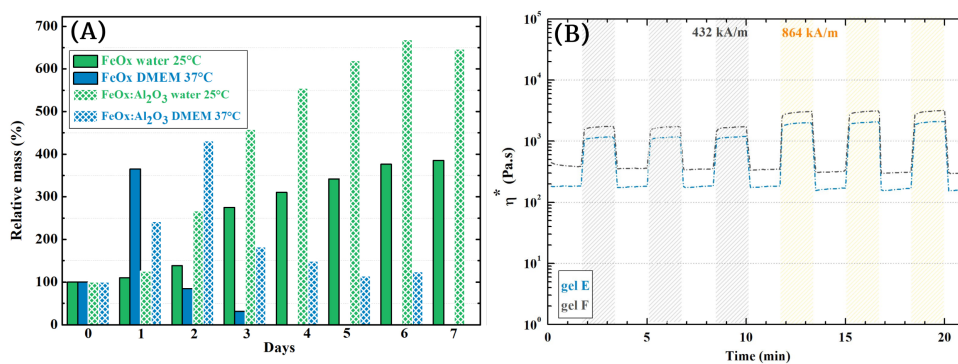


Fig. 5.7 (A) Long-term stability of magneto-responsive HA hydrogels in water and simulated cultivation conditions; (B) Schiff-base and ionically cross-linked CIPs filled HA hydrogel response to cyclic magnetic field exposure [337]

5.2 Rheological modification using charged NPs

In previous studies, inorganic disc-like NPs, specifically Laponite[®], was used as a rheological modifier for various polymer solutions. The rheological modification relies

on electrostatic repulsion of the charged NPs, which consequently leads to formation of a randomly stacked structure within the polymer solution. This structure is known as the "house of cards". The "house of cards" structure provides internal support to the polymer solution, resulting in increased viscosity and gel-like appearance. On the other hand, the weak physical nature of the bonds causes the support to be liable to shear stress. These qualities make the "house of cards" structure an ideal means to achieve 3D printability via microextrusion in low-viscosity polymer solutions. The phenomenon is not selective to Laponite[®], but is rather a common feature of charged nanoplatelets, as proved by [340] and **PAPER IV**. In this paper, a novel layered phenylphosphonate-based nanofillers' efficiency in terms of rheological modification is assessed. The layered NPs prompted considerable thickening in 3 wt.% NaAlg. solutions. The nanoplatelet-NaAlg mixtures also showed shear-thinning behaviour, supporting the hypothesis of "house-of-cards" formation. The random orientation of particles was also observed by AFM, which is consistent with the proposed spontaneous formation of the "house-of-cards" structure. In addition, the rheological behavior was compared to a composite of NaAlg and spherical apatite, as well as partially cross-linked NaAlg containing free Ca²⁺ ions. The experiments were designed to test the alternative hypothesis of partial Ca²⁺ dissociation and subsequent cross-linking of polyanionic NaAlg. The rheological measurement shown in Figure 5.8 (A) confirmed the essential part of the shape of the layered NPs in designing the required shear-thinning profile.

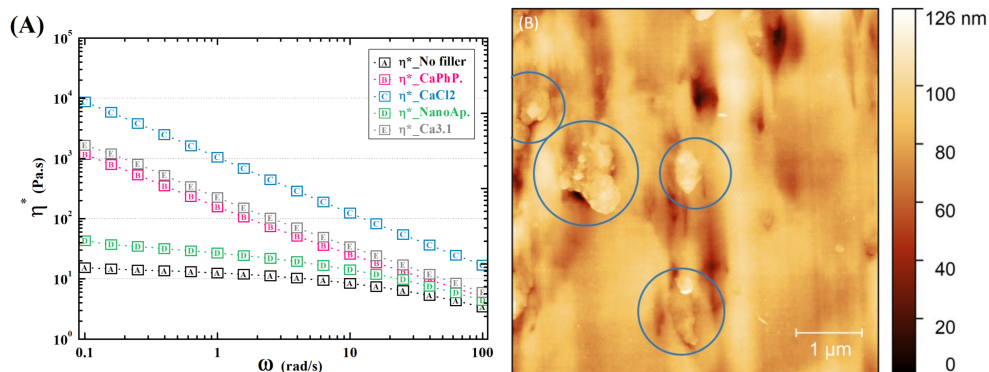


Fig. 5.8 (A) Dependence of viscosity of NaAlg based composites on angular frequency; (B) Atomic force microscopy topography scans of the section of the modified NaAlg hydrogel samples by CaPhP, where randomly oriented aggregates of nanoplatelets are observed [341]

Furthermore, experimental 3D printing showed higher shape fidelity of mixtures with layered NPs compared to the alternative samples. The inherent biocompatibility of NaAlg, as well as readily available low-toxicity cross-linking with multivalent ions (Ca^{2+} , Fe^{3+} , etc.), encouraged the use of the developed materials as a matrix for encapsulating of cells and bioprinting. The favorable rheological profile of the structures led to sufficient cell viability after the printing of mouse fibroblasts encapsulated in the NaAlg modified with layered phenylphosphonate-based NPs >75% confirmed the usability of the house-of-cards modified polymer solutions as potential versatile bioinks (see Figure 5.9).

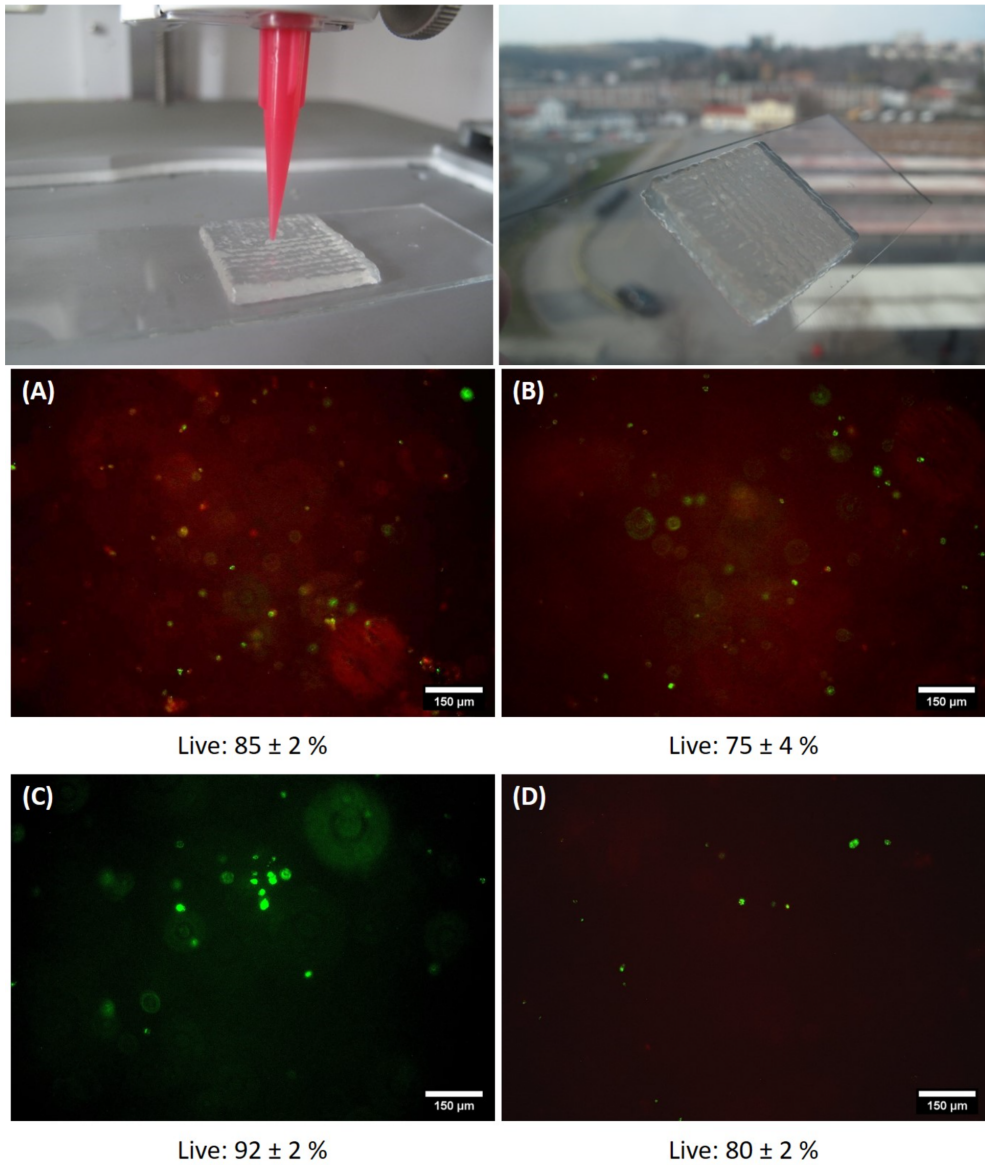


Fig. 5.9 Structures obtained by 3D printing using either nanoplatelets modified NaAlg, and live/dead staining of BALB/3T3 fibroblasts-laden bioinks after 3D printing: (A) 0.52 mm diameter nozzle, (B) 0.52 mm diameter needle, (C) 0.42 mm diameter nozzle, (D) 0.42 mm diameter needle

5.3 Preparation of biopolymer-based nanofibres by the electrospinning method

Fibrous structures are naturally present in a number of tissue types of living organisms, and the positive response to their presence has been reported for several cell lines, eg. myocytes [12], osteocytes [37], or neurons [39]. Fibers are formed naturally from natural polymers, including Col, fibrinogen, or silk fibroin. Artificial formation of fibres from these polymers can, however, be challenging on account of their chemical and thermal sensitivity, and specific physical properties as well. The fifth paper and additional unpublished results communicate the use of electrospinning for preparing nanofibrous structures intended for use in bioapplications.

PAPER V describes electrospinning of HA and the challenges of the process. The fibre solidification process in electrospinning is guided predominantly by rapid solvent evaporation during the polymer jet coiling [295]. The low evaporation rate of water makes it difficult to spin aqueous solutions into solid fibrous mats. However, HA is insoluble or tends to decay in the majority of organic solvents [303]. Additionally, HA displays an exceptional tendency to be solvated by water molecules, leading to extreme viscosity of the solutions among natural polymers, which in turn makes it difficult to achieve critical entanglement concentration [300]. On account of these difficulties, in **PAPER V** was HA spun by exploiting two techniques - co-electrospinning and intermediate solvent solutions. Co-electrospinning is widely acknowledged method for preparing nanofibres from low-spinnable materials, exploiting the viscous drag of highly spinnable polymer acting upon the low spinnable partner. With regards to the potential biomedical use of the prepared materials, biocompatible synthetic polymers - PEO and PVA were used as the highly spinnable component of the polymer mixtures. As both polymers are spinnable in aqueous solutions, the HA can be simply dissolved with the respective co-spinning polymers. In both cases, beaded fibres were formed. This may be the results of an inappropriate elongation viscosity profile. However, the problem requires further investigation.

In the previously described approach, fully miscible solvents were used to prepare composite nanofibres. While this method is advantageous especially due to simplicity, it leads to random fibre structure, and may also result in uneven distribution of respective

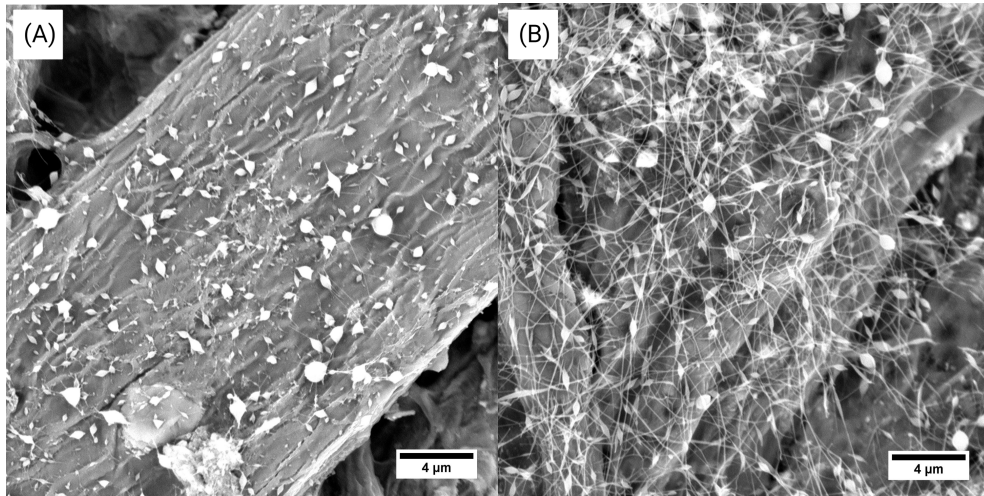


Fig. 5.10 Scanning Electron Microscopy (SEM) micrographs of electrospun structures obtained from (A) HA/PVA blend solution with BEC and (B) HA/PEO blend solution [342]

polymers [343]. Therefore, core-shell fibers are a popular choice of multipolymer composite structure. In this case, complete miscibility of the solvents has adverse effect, and partial miscibility is a necessity for successful core-shell Taylor cone formation [319]. Thus, the water soluble PEO and PVA were replaced by the biocompatible water-insoluble PCL for the core-shell electrospinning using coaxial needle (see Figure 5.11). PCL solution (9 wt.% in mixed chloroform 50 wt.% and EtOH:MeOH in 5:1 volume ratio 50 wt.%) was used as the shell material for electrospinning of core-shell fibers with the core being 2 wt.% HA (M_w 1,18 MDa) in H₂O:EtOH:MeOH 5:5:1 solvent. The core material was chosen due to the possibility to provide defect free fibres, as shown earlier. The shell material was chosen on account of good biocompatibility, as well as high content of alcohol solvents, which would lower the interfacial tension caused by immiscibility of chloroform and H₂O. As found by Vats et al., 2021, partial miscibility of the spinning solutions is needed for successful core-shell spinning process [319]. Unfortunately, the large discrepancy of respective solutions viscosity apparently caused demixing and did not allow core-shell geometry fibres to be formed. Further research is needed in order to obtain HA core-shell fibres.

Alternatively, Col core fibres were spun. Two different solvents of Col were tested:

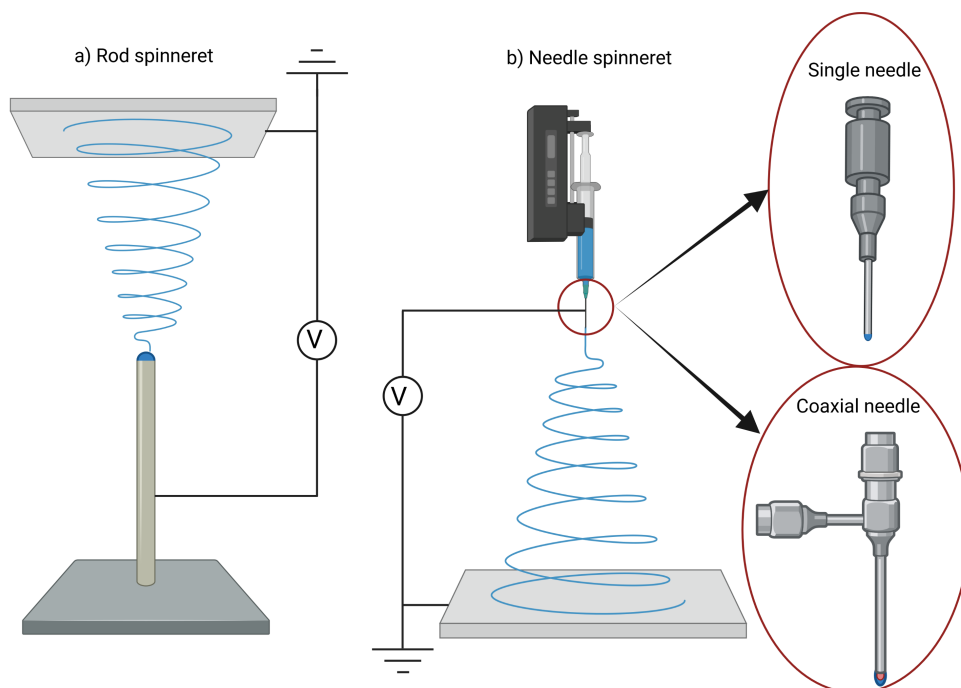


Fig. 5.11 Schematic representation of the various electrospinning setups used for the experiments: upwards electrospinning from rod spinneret, downwards electrospinning from single needle spinneret and downwards electrospinning from coaxial needle spinneret; Created with BioRender.com

50% acetic acid and PBS 20X/EtOH in a 1:1 volume ratio. It was found that 50 wt.% Col solutions in both solvents facilitate the electrospinning of Col fibers at similar conditions. Therefore, PBS 20X/EtOH system was chosen on account of the lower risk of Col degradation, environmental safety, and higher volatility due to EtOH presence. The combination of Col core and PCL shell material (spun from the same mixed solution as in case of HA core) did sustain stable Taylor cones and provided defectless fibers, with evidence of core-shell structure (Figure 5.12).

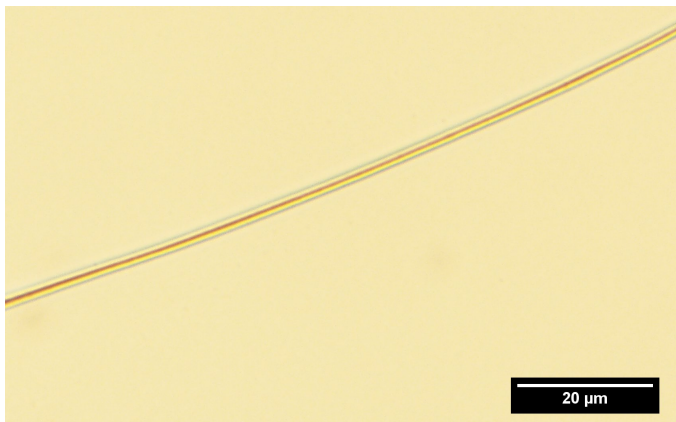


Fig. 5.12 *Electrospun core-shell fiber with Col core and PCL shell; the sample was visualized with polarized light microscopy*

In order to abstain from the use of a second polymer in the HA nanofibers, the method suggested by Malkin et al., 2017 [299] was exercised. This method is based on balancing the Hansen solubility parameters, factoring hydrogen bonding, polar forces and disperse forces, in a manner which promotes the polymer-polymer interactions over the polymer-solvent interactions. **PAPER V** described the use of Teas graph for selecting the intermediate solvent mixtures allowing dissolving of HA, while preserving sufficient polymer-polymer interactions to facilitate polymer chains entanglements. The viscosity measurements shown in Figure 5.13 (B) contradict the popular belief of shear viscosity hindering the electrospinning process. As a pure elongation, electrospinning is unlikely to be influenced by the shear flow behaviour, and the dominant influence would be directed by the elongation properties of the solution.

The intermediate method was successful in preparation of pure HA defectless nanofibres of tens of nanometers in diameter with HA of higher M_w , while lower M_w HA would often result in defects on the fibres, or even electrospaying.

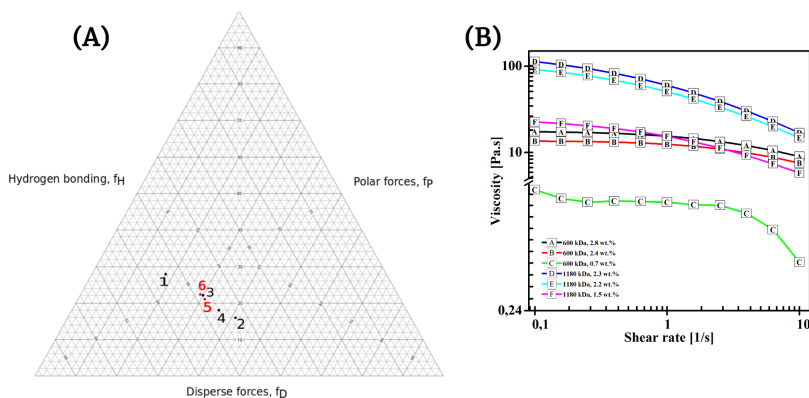


Fig. 5.13 (A) Solvent-mixture representation in Teas graph. 1, H_2O ; 2, IPA; 3, MeOH; 4, EtOH; 5, $H_2O:IPA$ 10:7; 6, $H_2O:EtOH:MeOH$ 5:5:1; (B) Viscosity of HA solutions in $H_2O:EtOH:MeOH$ in 5:5:1 weight ratio solvent mixture as a function of shear rate [342]

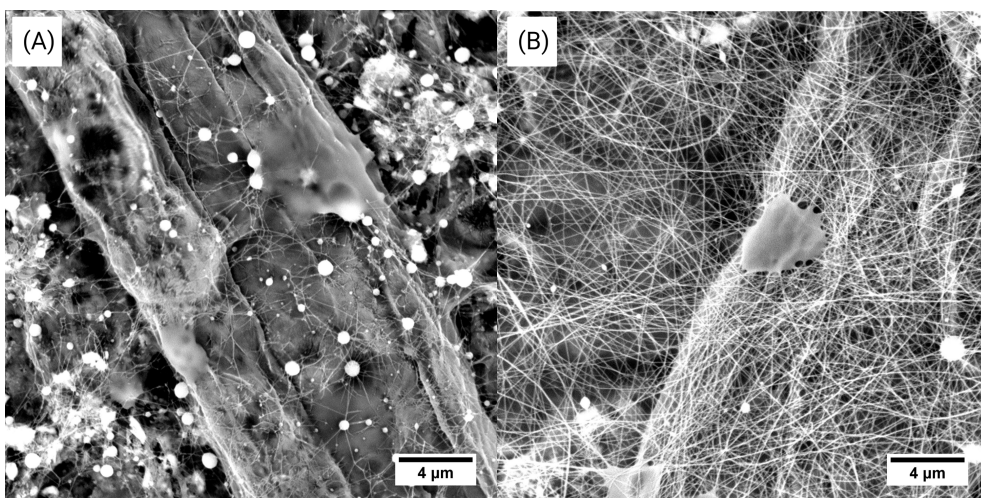


Fig. 5.14 SEM micrographs of electrospun structures obtained from $H_2O:EtOH:MeOH$ in 5:5:1 weight ratio solutions. (A) 2.8 wt.% HA 600 kDa and (B) 1.5 wt.% HA 1180 kDa [342]

6 CONTRIBUTION TO RESEARCH AND PRACTICE

The aim of the work is to understand the physical factors directing the manufacturing of biopolymers by advanced technologies of 3D printing and electrospinning, thus aid the growth of these fields both in research and in practice. These technologies are fundamentally different, as the 3D printing via microextrusion subjects the material predominantly to shear stress, while electrospinning induces elongation flow. Thus, the tuning of materials properties have to be done separately.

The choice of materials for the experimental work was done with regards to the aimed use in cell culture and tissue engineering. Thus, the chosen materials are non-cytotoxic. Furthermore, as successful cell culture and tissue development requires cell adhesion and proliferation, the material needs to provide biochemical and biophysical cues for cellular receptors. Biochemical cues, such as adhesive positively charged functional groups, are inherently present in natural polymers and their derivatives - HA, Gel. Therefore, their use in cell culture is highly advantageous. On the other hand, the natural polymers mechanical performance is often insufficient for efficient mechano-modulation, especially in case of hard tissues, eg. bone tissue. Combining the natural polymers with synthetic ones - PCL, PEO, PVA - can provide better mechanical stiffness and provide close resemblance to natural tissue also from the biophysical point of view.

In terms of 3D printing, the most important characteristic to follow is the rheological profile. The ink materials should be shear-thinning, and display fast recovery upon lifting of the shear stress. This behaviour can be achieved by using dynamic polymer networks - Schiff base cross-linking, or non-covalent interactions. Subjecting such systems to shear stress induces depleting of the bonds and allows flow of the material.

Electrospinning, on the other hand, depends on multiple factors, both intrinsic and extrinsic. The complex relationships are examined in order to achieve better understanding of the electrofluidodynamic phenomena and allow the transfer of the acquired knowledge to practice. In case of core-shell electrospinning, the interfacial phenomena are taken into account too.

The presented doctoral thesis lays the groundwork for preparing scaffolds combining nanotopological features of electrospun fibrous mats, and precise macroscopic structures with high internal porosity provided by the 3D printing of hydrogels. The proposed structures can be further developed into composites with various morphologies. As an example, the following structures are suggested:

1. Nanofibres decorated 3D printed structures. This approach uses the nanofibrous coating of 3D printed structures to introduce attachment sites for cell receptors. This treatment leads to better cell adhesion and promotes proliferation into the bulk of a 3D printed scaffold. It is especially useful for post-printing cell seeding [344, 164].
2. Layered 3D printed (or bioprinted)-electrospun scaffolds. This type of scaffolds mimics the structure of ECM at nanoscale [345]. Such sandwich structures have been described as advantages in biomedical applications [346]. The use of natural polymer fibers, such as HA or Col can provide biochemical cues for enhancing proliferation and migration.
3. Nanofiber-reinforced 3D printing inks (or bioinks). The presence of nanofibres in a bulk of a hydrogel matrix introduces nanofeatures serving as mechanical signals for cell receptors, promoting adhesion, proliferation or morphogenesis [347]. The shear stress imposed on the fibres during 3D printing would presumably induce unidirectional orientation of the fibres to a certain extent, which would benefit highly oriented tissue types, including muscle [12], tendon [347] or bone tissue [348].

Moreover, the materials described here are potentially useful also for other electrofluidynamics based technologies, i.e. electrospraying and electrowriting.

7 CONCLUSION

The research presented in the current thesis aims to provide opportunities to use advanced manufacturing technologies to obtain precisely structured scaffolds with distinct macro-, micro- and nanostructures. To this end, 3D bioprinting *via* microextrusion and solution electrospinning is exploited.

The compilation of the research papers consists of five papers, four of which consider the specific requirements on hydrogels for microextrusion based 3D printing and bioprinting, and one exploring the possibilities to obtain nanofibres from natural polymers by solution electrospinning. The printability of the materials is achieved through tailoring of hydrogels' rheological behaviour to obtain shear-thinning materials. This is achieved by two distinct methods:

- dynamic covalent cross-linking,
- charged nanoplatelets induced rheological modulation.

Dynamic covalent cross-linking, specifically the Schiff base formation, was successfully utilized as a means to prepare hydrogels based on Gel and HA respectively. The rheological measurement confirmed the shear thinning character of the prepared hydrogels, and their printability was demonstrated by experimental microextrusion. Additionally, the Schiff base cross-linked hydrogels can serve as matrices for magneto-responsive particles, making them promising candidates in preparation of smart hydrogels for bioapplications.

Rheological modulation using charged nanoplatelets, on the other hand, is facilitated by the "house of cards" structure formation. The physical character of this phenomenon allows instant change of viscosity upon application of shear stress, which is highly advantageous in 3D printing *via* microextrusion. The rheological experiments also confirm the importance of NPs shape in the desired rheological modification.

Both approaches to hydrogels' rheological modification allow printability of the re-

sulting materials with acceptable shape fidelity. Moreover, the hydrogels allow encapsulation of living cells and their subsequent microextrusion based 3D printing with sufficient cell viability >75%. Therefore, the developed materials have the capacity to form bioinks.

The electrospinning of HA *via* the use of intermediate solvent was found superior to the conventional strategy of polymer co-electrospinning, as it allowed fabrication of smooth fibers of 50-20 nm in diameter. It was also observed that shear viscosity has negligible effect on the electrospinning process and outcome, while polymer's M_w and Hansen solubility parameters are crucial to successful electrospinning. In continuation of this research, core-shell fibers enveloping natural polymer (HA or Gel) in biocompatible PCL were prepared. In core-shell electrospinning, other specific influences, including solvents miscibility and difference of shear viscosity, were identified as potentially significant.

The presented thesis describes several possibilities to utilize advanced manufacturing technologies to prepare biocompatible structures, which can serve as scaffolds in tissue engineering. Furthermore, the respective technologies operate on different level of detail, allowing the combination of precise macroscopic structuring of 3D printing, and presence of nanotopological features provided by electrospun nanofibres. These scaffolds would closely mimic the natural structure of a tissue. Therefore, the presented results have a great potential use in biomedical applications, including precise tissue analogues fabrication and tissue engineering.

REFERENCES

- [1] LAURENCIN, C. and NAIR, L. *Nanotechnology and Regenerative Engineering: The Scaffold - 2. edition*. CRC Press, 2015. ISBN 978-1-138-07658-7.
- [2] PRAKASH, K., NANCHARAIH, T. and RAO, V. S. Additive Manufacturing Techniques in Manufacturing -An Overview. *Materials Today: Proceedings*. 2018, 5, pp. 3873–3882. doi: 10.1016/j.matpr.2017.11.642.
- [3] NOH, I., KIM, N., TRAN, H., LEE, J. and LEE, C. 3D printable hyaluronic acid-based hydrogel for its potential application as a bioink in tissue engineering. *Biomaterials Research*. 2019, 23. doi: 10.1186/s40824-018-0152-8.
- [4] VOZZI, G., FLAIM, C., AHLUWALIA, A. and BHATIA, S. Fabrication of PLGA scaffolds using soft lithography and microsyringe deposition. *Biomaterials*. 2003, 24, pp. 2533–2540. doi: 10.1016/S0142-9612(03)00052-8.
- [5] KAWATA, S., SUN, H., TANAKA, T. and TAKADA, K. Finer features for functional microdevices. *Nature*. 2001, 412, pp. 697–698. doi: 10.1038/35089130.
- [6] LUKÁŠ, D., SARKAR, A., MARTINOVÁ, L., VODSEĎÁLKOVÁ, K., LUBASOVÁ, D., CHALOUPEK, J., POKORNÝ, P., MIKEŠ, P., CHVOJKA, J. and KOMÁREK, M. Physical principles of electrospinning (electrospinning as a nano-scale technology of the twenty-first century). *Text. Prog.* 2009, 41, pp. 59–140. doi: 10.1080/00405160902904641.
- [7] MANCINO, C., HENDRICKSON, T., WHITNEY, L., PARADISO, F., ABASI, S., TASCIOTTI, E., TARABALLI, F. and GUISEPPI-ELIE, A. Electrospun electroconductive constructs of aligned fibers for cardiac tissue engineering. *Nanomedicine: Nanotechnology, Biology and Medicine*. 2022, 44. doi: 10.1016/j.nano.2022.102567.
- [8] PAPAPARASKEVA, G., PAPAGIORGIS, P., ITSKOS, G. and KRASIA-CHRISTOFOROU, T. Highly Aligned Electrospun Polymer Fibers Produced Using a Corrugated Static Collector. *ACS Applied Polymer Materials*. 2022, 4, pp. 586–597. doi: 10.1021/acsapm.1c01435.

- [9] MORI, A. D., FERNÁNDEZ, M. P., BLUNN, G., TOZZI, G. and ROLDO, M. 3D Printing and Electrospinning of Composite Hydrogels for Cartilage and Bone Tissue Engineering. *Polymers*. 2018, 10, pp. 285–311. doi: 10.3390/polym10030285.
- [10] TIBBITT, M. and ANSETH, K. Hydrogels as Extracellular Matrix Mimics for 3D Cell Culture. *Biotechnology and Bioengineering*. 2009, 103. doi: 10.1002/bit.22361.
- [11] CHEN, Z., WANG, P., WEI, B., MO, X. and CUI, F. Electrospun collagen–chitosan nanofiber: A biomimetic extracellular matrix for endothelial cell and smooth muscle cell. *Acta Biomaterialia*. 2010, 6. doi: 10.1016/j.actbio.2009.07.024.
- [12] DE FRANCE, K., F. XU, TOUFANIAN, S., K.J.W. CHAN, S. SAID, T.C. STIMPSON, E. GONZALEZ-MARTINEZ, J.M. MORAN-MIRABAL, E.D. CRANSTON and T. HOARE. Multi-scale structuring of cell-instructive cellulose nanocrystal composite hydrogel sheets via sequential electrospinning and thermal wrinkling. *Acta Biomaterialia*. 2021, 128. doi: 10.1016/j.actbio.2021.04.044.
- [13] NANGARE, S., JADHAV, N., GHAGARE, P. and MUTHANE, T. Pharmaceutical applications of electrospinning. *Pharmaceutiques Françaises*. 2020, 78. doi: 10.1016/j.pharma.2019.07.002.
- [14] REZVANI, G., KHOSRAVI, F., NEISIANY, R., SINGH, S. and RAMAKRISHNA, S. Future of additive manufacturing in healthcare. *Current Opinion in Biomedical Engineering*. 2021, 17. doi: 10.1016/j.cobme.2020.100255.
- [15] DZIEMIDOWICZ, K. et al. Electrospinning for healthcare: recent advancements. *Journal of Materials Chemistry B*. 2021, 9. doi: 10.1039/D0TB02124E.
- [16] MEI, L., WANG, Y., TONG, A. and GUO, G. Facile electrospinning of an efficient drug delivery system. *Expert Opinion on Drug Delivery*. 2016, 13. doi: 10.1517/17425247.2016.1142525.
- [17] JAHANGIRI, A. and ADIBKIA, K. Applications of electrospinning/electrospraying in drug delivery. *BioImpacts*. 2016, 6. doi: 10.15171/bi.2016.08.

- [18] GHOSAL, K., AUGUSTINE, R., ZASZCZYNSKA, A., BARMAN, M., JAIN, A., HASAN, A., KALARIKKAL, N., SAJKIEWICZ, P. and THOMAS, S. Novel drug delivery systems based on triaxial electrospinning based nanofibers. *Reactive and Functional Polymers*. 2021, 163. doi: 10.1016/j.reactfunctpolym.2021.104895.
- [19] TALEBIAN, S., SHIM, I., FOROUGH, J., ORIVE, G., VINE, K. and WALLACE, S. K. G. 3D-Printed Coaxial Hydrogel Patches with Mussel-Inspired Elements for Prolonged Release of Gemcitabine. *Polymers*. 2021, 13. doi: 10.3390/polym13244367.
- [20] AHAMED, F. F. N., HSU, M., WALTON, J., FRISINA, R. and BORKHOLDER, D. A 3D-Printed Modular Microreservoir for Drug Delivery. *Micromachines*. 2020, 11. doi: 10.3390/mi11070648.
- [21] LI, R., ZHANG, L., JIANG, X., LI, L., WU, S., YUAN, X., CHENG, H., JIANG, X. and GOU, M. 3D-printed microneedle arrays for drug delivery. *Journal of Controlled Release*. 2022, 350. doi: 10.1016/j.jconrel.2022.08.022.
- [22] WANG, J., ZHANG, Y., AGHDA, N., PILLAI, A., THAKKAR, R., NOKHODCHI, A. and MANIRUZZAMAN, M. Emerging 3D printing technologies for drug delivery devices: Current status and future perspective. *Advanced Drug Delivery Reviews*. 2021, 174. doi: 10.1016/j.addr.2021.04.019.
- [23] KHAN, A., MORSI, Y., ZHU, T., AHMAD, A., XIE, X., YU, F. and MO, X. Electrospinning: An emerging technology to construct polymer-based nanofibrous scaffolds for diabetic wound healing. *Frontiers of Materials Science*. 2021, 15. doi: 10.1007/s11706-021-0540-1.
- [24] JUNCOS, B., DUNNE, N. and MCCARTHY, H. Electrospinning of natural polymers for the production of nanofibres for wound healing applications. *Materials Science and Engineering: C*. 2020, 114. doi: 10.1016/j.msec.2020.110994.
- [25] CLOHESSY, R., COHEN, D., STUMBRAITE, K., BOYAN, B. and SCHWARTZ, Z. In vivo evaluation of an electrospun and 3D printed cellular delivery device for dermal wound healing. *Journal of Biomedical Materials Research Part B: Applied Biomaterials*. 2020, 108. doi: 10.1002/jbm.b.34587.

- [26] ALIZADEHGIASHI, M., NEMR, C., CHEKINI, M., PINTO, R., MITTAL, N., AHMED, S., KHUU, N., KELLEY, S. and KUMACHEVA, E. Multifunctional 3D-Printed Wound Dressings. *ACS Nano*. 2021, 15. doi: 10.1021/acsnano.1c04499.
- [27] FAYYABAKHSH, F., KHAYAT, J. and LEU, C. 3D-Printed Gelatin-Alginate Hydrogel Dressings for Burn Wound Healing: A Comprehensive Study. *International Journal of Bioprinting*. 2022, 8. doi: 10.18063/ijb.v8i4.618.
- [28] KONG, B., LIU, R., GUO, J., LU, L., ZHOU, Q. and ZHAO, Y. Tailoring micro/nano-fibers for biomedical applications. *Bioactive Materials*. 2023, 19. doi: 10.1016/j.bioactmat.2022.04.016.
- [29] HUANG, Y., LI, X., POUDEL, A., ZHANG, W. and XIAO, L. Hydrogel-based bioinks for 3D bioprinting articular cartilage: A comprehensive review with focus on mechanical reinforcement. *Applied Materials Today*. 2022, 29. doi: 10.1016/j.apmt.2022.101668.
- [30] MARINO, A., BATTAGLINI, M., TAPEINOS, C., LARRANAGA, A. and CIOFANI, G. Innovative nanotechnology tools for the functional control and tracking of human stem cells. *Materials Today Advances*. 2022, 16. doi: 10.1016/j.mtadv.2022.100298.
- [31] CURTI, F., SERAFIM, A., OLARET, E., DINESCU, S., SAMOILA, I., VASILE, B., IOVU, H., LUNGU, A., STANCU, I. and MARINESCU, R. Development of Biocomposite Alginate-Cuttlebone-Gelatin 3D Printing Inks Designed for Scaffolds with Bone Regeneration Potential. *Marine Drugs*. 2022, 20. doi: 10.3390/md20110670.
- [32] MACHOUR, M., HEN, N., GOLDFRACHT, I., SAFINA, D., DAVIDOVICH-PINHAS, M., BIANCO-PELED, H. and LEVENBERG, S. Print-and-Grow within a Novel Support Material for 3D Bioprinting and Post-Printing Tissue Growth. *Advanced Science*. 2022. doi: 10.1002/advs.202200882.
- [33] TALEBI, A., LABBAF, S. and RAHMATI, S. Biofabrication of a flexible and conductive 3D polymeric scaffold for neural tissue engineering applications; physical, chemical, mechanical, and biological evaluations. *Polymers for Advanced Technologies*. 2022. doi: 10.1002/pat.5872.

- [34] GAO, J., YU, X., WANG, X., HE, Y. and DING, J. Biomaterial–Related Cell Microenvironment in Tissue Engineering and Regenerative Medicine. *Engineering*. 2022, 13. doi: 10.1016/j.eng.2021.11.025.
- [35] CHUNG, S. H., SON, S. and MIN, J. The nanostructure effect on the adhesion and growth rates of epithelial cells with well-defined nanoporous alumina substrates. *Nanotechnology*. 2010, 21. doi: 10.1088/0957-4484/21/12/125104.
- [36] LI, C., LI, C., MA, Z., CHEN, H., RUAN, H., DENG, J., WANG, J. and CUI, W. Regulated macrophage immune microenvironment in 3D printed scaffolds for bone tumor postoperative treatment. *Bioactive Materials*. 2023, 19. doi: 10.1016/j.bioactmat.2022.04.028.
- [37] BERTELS, S. et al. Geometrically defined environments direct cell division rate and subcellular YAP localization in single mouse embryonic stem cells. *Scientific Reports*. 2021, 11. doi: 10.1038/s41598-021-88336-y.
- [38] ZHAO, F., C.G. ZHANG, J. LIU, L. LIU, X.D. CAO, X.F. CHEN, B. LEI and L.Q. SHAO. Periosteum structure/function-mimicking bioactive scaffolds with piezoelectric/chem/nano signals for critical-sized bone regeneration. *Chemical Engineering Journal*. 2020, 402. doi: 10.1016/j.cej.2020.126203.
- [39] MARIANO, A., BOVIO, C., CRISCUOLO, V. and SANTORO, F. Bioinspired micro- and nano-structured neural interfaces. *Nanotechnology*. 2022, 33. doi: 10.1088/1361-6528/ac8881.
- [40] SCHAFFLER, M. and BURR, D. Stiffness of compact bone: Effects of porosity and density. *Journal of Biomechanics*. 1988, 21. doi: 10.1016/0021-9290(88)90186-8.
- [41] SINGH, G. and CHANDA, A. Mechanical properties of whole-body soft human tissues: a review. *Biomedical Materials*. 2021, 16. doi: 10.1088/1748-605X/ac2b7a.
- [42] SUTRADHAR, A. and MILLER, M. In vivo measurement of breast skin elasticity and breast skin thickness. *Skin Research and Technology*. 2013, 19. doi: 10.1111/j.1600-0846.2012.00627.x.

- [43] CAI, J., WANG, J., SUN, C., DAI, J. and ZHANG, C. Biomaterials with stiffness gradient for interface tissue engineering. *Biomedical Materials*. 2022, 17. doi: 10.1088/1748-605X/ac8b4a.
- [44] STANTON, A., TONG, X., JING, S., BEHN, A., STORACI, H. and YANG, F. Aligned Gelatin Microribbon Scaffolds with Hydroxyapatite Gradient for Engineering the Bone–Tendon Interface. *Tissue Engineering Part A*. 2022, 28, pp. 712–723. doi: 10.1089/ten.tea.2021.0099.
- [45] SHOU, Y. et al. Mechano-responsive hydrogel for direct stem cell manufacturing to therapy. *Bioactive Materials*. 2023, 24, pp. 387–400. doi: 10.1016/j.bioactmat.2022.12.019.
- [46] DORKHANI, E., NOORAFKAN, Y., SALEHI, Z., GHIASS, M., TAFTI, S., HEIRANI-TABASI, A. and TAVAFOGHI, M. Design and fabrication of polyvinylidene fluoride-graphene oxide/gelatine nanofibrous scaffold for cardiac tissue engineering. *Journal of Biomaterials Science, Polymer Edition*. 2023, pp. 1–22. doi: 10.1080/09205063.2022.2161779.
- [47] APARICIO-COLLADO, J., CONSTANTINO, J. M.-M. T. C., VIDAURRE, A., SALESA, B., SERRANO-AROCA, A. and SERRA, R. S. Pro-Myogenic Environment Promoted by the Synergistic Effect of Conductive Polymer Nanocomposites Combined with Extracellular Zinc Ions. *Biology*. 2022, 11. doi: 10.3390/biology11121706.
- [48] BANDYOPADHYAY, J. and SINHA, R. *Advances in Polymer Nanocomposites, Clay-containing poly(ethylene terephthalate) (PET)-based polymer nanocomposites*. Elsevier, 2012. ISBN 9781845699406.
- [49] WEEMS, A., ARNO, M., YU, W., HUCKSTEPP, R. and DOVE, A. 4D polycarbonates via stereolithography as scaffolds for soft tissue repair. *Nature Communications*. 2021, 12. doi: 10.1038/s41467-021-23956-6.
- [50] DENG, Y., ZHANG, F., JIANG, M., LIU, Y., YUAN, H. and LENG, J. Programmable 4D Printing of Photoactive Shape Memory Composite Structures. *ACS Applied Materials Interfaces*. 2022, 14, pp. 42568–42577. doi: 10.1021/acsami.2c13982.

- [51] DÍAZ-PAYNO, P., KALOGEROPOULOU, M., MUNTZ, I., KINGMA, E., KOPS, N., D'ESTE, M., KOENDERINK, G., FRATILA-APACHITEI, L., OSCH, G. and ZADPOOR, A. Swelling-Dependent Shape-Based Transformation of a Human Mesenchymal Stromal Cells-Laden 4D Bioprinted Construct for Cartilage Tissue Engineering. *Advanced Healthcare Materials*. 2023, 12. doi: 10.1002/adhm.202201891.
- [52] CUI, C., KIM, D., PACK, M., HAN, B., HAN, L., SUN, Y. and HAN, L. 4D printing of self-folding and cell-encapsulating 3D microstructures as scaffolds for tissue-engineering applications. *Biofabrication*. 2020, 12. doi: 10.1088/1758-5090/aba502.
- [53] KO, E., KIM, C., CHOI, Y. and LEE, K. 3D printing of self-healing ferrogel prepared from glycol chitosan, oxidized hyaluronate, and iron oxide nanoparticles. *Carbohydrate Polymers*. 2020, 245. doi: 10.1016/j.carbpol.2020.116496.
- [54] GHOLAMIPOUR-SHIRAZI, A., NORTON, I. and MILLS, T. Dual stimuli-sensitive carrageenan-based formulation for additive manufacturing. *International Journal of Biological Macromolecules*. 2021, 189, pp. 370–379. doi: 10.1016/j.ijbiomac.2021.08.127.
- [55] ZHAO, L., FENG, Z., LYU, Y., YANG, J., LIN, L., BAI, H., LI, Y., FENG, Y. and CHEN, Y. Electroactive injectable hydrogel based on oxidized sodium alginate and carboxymethyl chitosan for wound healing. *International Journal of Biological Macromolecules*. 2023, 230. doi: 10.1016/j.ijbiomac.2023.123231.
- [56] KAMPERMAN, T., WILLEMEN, N., KELDER, C., KOERSELMAN, M., BECKER, M., LINS, L., JOHNBOSCO, C., KAPERIEN, M. and LEIJTEN, J. Steering Stem Cell Fate within 3D Living Composite Tissues Using Stimuli-Responsive Cell-Adhesive Micromaterials. *Advanced Science*. 2023. doi: 10.1002/advs.202205487.
- [57] STEVENS, M. and GEORGE, J. Exploring and engineering the cell surface interface. *Science*. 2005, 310, pp. 1135–1138. doi: 10.1126/science.1106587.
- [58] DISCHER, D., MOONEY, D. and ZANDSTRA, P. Growth factors, matrices, and forces combine and control stem cells. *Science*. 2009, 324, pp. 1673–1677. doi: 10.1126/science.1171643.

- [59] MITRAGOTRI, S. and LAHANN, J. Physical approaches to biomaterial design. *Nature Materials*. 2009, 8, pp. 15–23. doi: 10.1038/nmat2344.
- [60] PLACE, E., EVANS, N. and STEVENS, M. Complexity in biomaterials for tissue engineering. *Nature Materials*. 2009, 8, pp. 457–470. doi: 10.1038/nmat2441.
- [61] NEL, A., MÄDLER, L., VELEGOL, D., XIA, T., HOEK, E., SOMASUNDARAN, P., KLAESSIG, F., CASTRANOVA, V. and THOMPSON, M. Understanding biophysicochemical interactions at the nano–bio interface. *Nature Materials*. 2009, 8, pp. 543–557. doi: 10.1038/nmat2442.
- [62] SONG, Y., ZHANG, Y., QU, Q., ZHANG, X., LU, T., XU, J., MA, W., ZHU, M., HUANG, C. and XIONG, R. Biomaterials based on hyaluronic acid, collagen and peptides for three-dimensional cell culture and their application in stem cell differentiation. *International Journal of Biological Macromolecules*. 2023, 226, pp. 14–36. doi: 10.1016/j.ijbiomac.2022.11.213.
- [63] PAMPALONI, F., REYNAUD, E. and STELZER, E. The third dimension bridges the gap between cell culture and live tissue. *Nature Reviews Molecular Cell Biology*. 2007, 8, pp. 839–845. doi: 10.1038/nrm2236.
- [64] BISSELL, M., RIZKI, A. and MIAN, I. Tissue architecture: the ultimate regulator of breast epithelial function. *Current Opinion in Cell Biology*. 2003, 15, pp. 753–762. doi: 10.1016/j.ceb.2003.10.016.
- [65] ZIELIŃSKI, P., GUDETI, P., RIKMANSPOEL, T. and WŁODARCZYK-BIEGUN, M. 3D printing of bio-instructive materials: Toward directing the cell. *Bioactive Materials*. 2023, 19, pp. 292–327. doi: 10.1016/j.bioactmat.2022.04.008.
- [66] FORNETTI, E. et al. A novel extrusion-based 3D bioprinting system for skeletal muscle tissue engineering. *Biofabrication*. 2023, 15. doi: 10.1088/1758-5090/acb573.
- [67] CHEN, Y., CHAN, J., WU, J., LI, R. and SANTERRE, J. Compatibility and function of human induced pluripotent stem cell derived cardiomyocytes on an electrospun nanofibrous scaffold, generated from an ionomeric polyurethane composite. *Journal of Biomedical Materials Research Part A*. 2022, 110, pp. 1932–1943. doi: 10.1002/jbm.a.37428.

- [68] ADADI, N., YADID, M., GAL, I., ASULIN, M., FEINER, R., EDRI, R. and DVIR, T. Electrospun Fibrous PVDF-TrFe Scaffolds for Cardiac Tissue Engineering, Differentiation, and Maturation. *Advanced Materials Technologies*. 2020, 5. doi: 10.1002/admt.201900820.
- [69] SUMAM, P. and PARAMESWARAN, R. Neuronal cell response on aligned fibroporous electrospun mat generated from silver ion complexed ethylene vinyl alcohol copolymer. *Journal of Biomedical Materials Research Part B: Applied Biomaterials*. 2023, 111, pp. 782–794. doi: 10.1002/jbm.b.35189.
- [70] CHOWDHURY, B. M. F., CHARI, D. and ADAMS, C. Systematic Alignment Analysis of Neural Transplant Cells in Electrospun Nanofibre Scaffolds. *Materials*. 2023, 16. doi: 10.3390/ma16010124.
- [71] PUHL, D., FUNNELL, J., FINK, T., SWAMINATHAN, A., OUDEGA, M., ZHA, R. and GILBERT, R. Electrospun fiber-mediated delivery of neurotrophin-3 mRNA for neural tissue engineering applications. *Acta Biomaterialia*. 2023, 155, pp. 370–385. doi: 10.1016/j.actbio.2022.11.025.
- [72] ZHANG, J., CHERAGA, N. and HUANG, N. Biointerphases. *3D cell/scaffold model based on aligned-electrospun-nanofiber film/hydrogel multilayers for construction of anisotropic engineered tissue*. 2022, 17. doi: 10.1116/6.0002058.
- [73] GONZALEZ-PUJANA, A., CARRANZA, T., SANTOS-VIZCAINO, E., IGARTUA, M., GUERRERO, P., HERNANDEZ, R. and CABA, K. Hybrid 3D Printed and Electrospun Multi-Scale Hierarchical Polycaprolactone Scaffolds to Induce Bone Differentiation. *Pharmaceutics*. 2022, 14. doi: 10.3390/pharmaceutics14122843.
- [74] ALKAISSY, R., RICHARD, M., MORRIS, H., SNELLING, S., PINCHBECK, H., CARR, A. and MOUTHUY, P. Manufacture of Soft-Hard Implants from Electrospun Filaments Embedded in 3D Printed Structures. *Macromolecular Bioscience*. 2022, 22. doi: 10.1002/mabi.202200156.
- [75] MATYJASZEWSKI, K. and MÖLLER, M. *Polymer Science: A Comprehensive Reference*. Elsevier Science, 2012. ISBN 978-0-08-087862-1.

- [76] WISTRAND, A. and ALBERTSSON, A. Tuned mechanical properties achieved by varying polymer structure - Knowledge that generates new materials for tissue engineering. *Chinese Journal of Polymer Science*. 2007, 25. doi: 10.1142/S025676790700190X.
- [77] CZARNECKI, S., ROSSOW, T. and SEIFFERT, S. Hybrid Polymer-Network Hydrogels with Tunable Mechanical Response. *Polymers*. 2016, 8. doi: 10.3390/polym8030082.
- [78] RUYMBEKE, E., LEE, H., CHANG, T., NIKOPOULOU, A., HADJICHRISTIDIS, N., SNIJKERS, F. and VLASSOPOULOS, D. Molecular rheology of branched polymers: decoding and exploring the role of architectural dispersity through a synergy of anionic synthesis, interaction chromatography, rheometry and modeling. *Soft Matter*. 2014, 10. doi: 10.1039/c4sm00105b.
- [79] XU, S., LIU, J. and WANG, X. Thermal Conductivity Enhancement of Polymers via Structure Tailoring. *Journal of Enhanced Heat Transfer*. 2020, 27. doi: 10.1615/JEnhHeatTransf.2020034592.
- [80] RODRIGUEZ, F., COHEN, C., OBER, C. and ARCHER, L. *Principles of Polymer Systems - 6th edition*. CRC Press, 2015. ISBN 78-1-4822-2379-8.
- [81] ABDOLLAHIYAN, P., OROOJALIAN, F. and MOKHTARZADEH, A. The triad of nanotechnology, cell signalling, and scaffold implantation for the successful repair of damaged organs: An overview on soft-tissue engineering. *Journal of Controlled Release*. 2021, 332. doi: 10.1016/j.jconrel.2021.02.036.
- [82] QIU, S. and BEN, T. *Porous Polymers - Design, Synthesis and Applications*. Royal Society of Chemistry, 2016. ISBN 978-1-84973-932-0.
- [83] ADEL, I., ELMELIGY, M. and ELKASABGY, N. Conventional and Recent Trends of Scaffolds Fabrication: A Superior Mode for Tissue Engineering. *Pharmaceutics*. 2022, 14. doi: 10.3390/pharmaceutics14020306.
- [84] OZDIL, D. and AYDIN, H. Polymers for medical and tissue engineering applications. *Journal of Chemical Technology and Biotechnology*. 2014, 89. doi: 10.1002/jctb.4505.

- [85] KATO, R., KAGA, C., KUNIMATSU, M., KOBAYASHI, T. and HONDA, H. Peptide array-based interaction assay of solid-bound peptides and anchorage-dependant cells and its effectiveness in cell-adhesive peptide design. *Journal of Bioscience and Bioengineering*. 2006, 101, pp. 485–495. doi: 10.1263/jbb.101.485.
- [86] FRASER, J., LAURENT, T. and LAURENT, U. Hyaluronan: its nature, distribution, functions and turnover. *Journal of Internal Medicine*. 1997, 242, pp. 27–33. doi: 10.1046/j.1365-2796.1997.00170.x.
- [87] MEYER, K. and PALMER, J. The polysaccharide of the vitreous humor. *The Journal of Biological Chemistry*. 1934, 107, pp. 629–634.
- [88] YU, F., ZHANG, F., LUAN, T., ZHANG, Z. and ZHANG, H. Rheological studies of hyaluronan solutions based on the scaling law and constitutive models. *Polymer*. 2014, 55, pp. 295–301. doi: 10.1016/j.polymer.2013.11.047.
- [89] COMPER, W. and LAURENT, T. Physiological functions of connective tissue polysaccharides. *Physiological Reviews*. 1978, 58, pp. 255–315.
- [90] BOERIU, C., SPRINGER, J., KOOY, F., BROEK, L. and EGGINK, G. Production Methods for Hyaluronan. *Carbohydrate Chemistry*. 2013. doi: 10.1155/2013/624967.
- [91] IGNATOVA, E. and GUROV, A. Principles of extraction and purification of hyaluronic acid (review). *Pharmaceutical Chemistry Journal*. 1990, 24, pp. 211–216. doi: 10.1007/BF00771704.
- [92] AMAGAI, I., TASHIRO, Y. and OGAWA, H. Improvement of the extraction procedure for hyaluronan from fish eyeball and the molecular characterization. *Fisheries Science*. 2009, 75, pp. 805–810. doi: 10.1007/s12562-009-0092-2.
- [93] O'REGAN, M., MARTINI, I., CRESCENZI, F., LUCA, C. D. and LANSING, M. Molecular mechanisms and genetics of hyaluronan biosynthesis. *International Journal of Biological Macromolecules*. 1994, 16, pp. 283–286. doi: 10.1016/0141-8130(94)90056-6.

- [94] THONARD, J., MIGLIORE, S. and BLUSTEIN, R. Isolation of Hyaluronic Acid from Broth Cultures of Streptococci. *The Journal of Biological Chemistry*. 1964, 239, pp. 726–728.
- [95] JOYCE, K., FABRA, G., BOZKURT, Y. and PANDIT, A. Bioactive potential of natural biomaterials: identification, retention and assessment of biological properties. *Signal Transduction and Targeted Therapy*. 2021, 6. doi: 10.1038/s41392-021-00512-8.
- [96] GARANTZIOTIS, S. and SAVANI, R. Hyaluronan biology: A complex balancing act of structure, function, location and context. *Matrix Biology*. 2019, 78-79. doi: 10.1016/j.matbio.2019.02.002.
- [97] MARINHO, A., NUNES, C. and REIS, S. Hyaluronic Acid: A Key Ingredient in the Therapy of Inflammation. *Biomolecules*. 2021, 11. doi: 10.3390/biom11101518.
- [98] ZAKUSILO, F., O'BANIONA, M., GELBARD, H., SELUANOV, A. and GORBUNOVA, V. Matters of size: Roles of hyaluronan in CNS aging and disease. *Ageing Research Reviews*. 2021, 72. doi: 10.1016/j.arr.2021.101485.
- [99] CURTIS, J. and SPATZ, J. Getting a grip: Hyaluronan-mediated cellular adhesion. *Optical Trapping and Optical Micromanipulation*. 2004, 5514. doi: 10.1117/12.560049.
- [100] HUERTA-ANGELES, G. and NEŠPOROVÁ, K. Hyaluronan and its derivatives for ophthalmology: Recent advances and future perspectives. *Carbohydrate Polymers*. 2021, 259. doi: 10.1016/j.carbpol.2021.117697.
- [101] BLANCAS, A., ACOSTA, F. and GRANDE-ALLEN, K. Not just skin deep: cosmetic and medical applications of injectable hyaluronan and fibrin. *Materials Technology*. 2015, 30. doi: 10.1179/17535557B15Y.000000011.
- [102] ANANDAGODA, N., EZRA, D., CHEEMA, U., BAILLY, M. and BROWN, R. Hyaluronan hydration generates three-dimensional meso-scale structure in engineered collagen tissues. *Journal of the Royal Society Interface*. 2012, 9. doi: 10.1098/rsif.2012.0164.

- [103] KESSLER, L., S. GEHRKE, M. WINNEFELD, B. HUBER, WALTER, E., SCHMIDT, R., M. KUCKELHAUS, HIRSCH, M. and JACOBSEN, F. Methacrylated gelatin/hyaluronan-based hydrogels for soft tissue engineering. *Journal of Tissue Engineering*. 2017, 8. doi: 10.1177/2041731417744157.
- [104] OKAWA, M., A. TANABE, S. OHTA, S. NAGATOISHI and ITO, K. Extracellular matrix-inspired hydrogel of hyaluronan and gelatin crosslinked via a Link module with a transglutaminase reactive sequence. *Communications Materials*. 2022, 3. doi: 10.1038/s43246-022-00309-4.
- [105] BAKER, A. et al. Stable oxime-crosslinked hyaluronan-based hydrogel as a biomimetic vitreous substitute. *Biomaterials*. 2021, 271. doi: 10.1016/j.biomaterials.2021.120750.
- [106] AULIN, C., K. BERGMAN, M. JENSEN-WAERN, P. HEDENQVIST, J. HILBORN and T. ENGSTRAND. In situ cross-linkable hyaluronan hydrogel enhances chondrogenesis. *Journal of Tissue Engineering and Regenerative Medicine*. 2011, 5. doi: 10.1002/term.415.
- [107] LEE, K. and MOONEY, D. Alginate: Properties and biomedical applications. *Progress in Polymer Science*. 2012, 37. doi: 10.1016/j.progpolymsci.2011.06.003.
- [108] ZIMMERMANN, U., KLÖCK, G., FEDERLIN, K., HANNIG, K., KOWALSKI, M., BRETZEL, R., HORCHER, A., ENTENMANN, H., SIEBER, U. and ZEKORN, T. Production of mitogen-contamination free alginates with variable ratios of manuronic acid to guluronic acid by free flow electrophoresis. *Electrophoresis*. 1992, 13, pp. 269–274. doi: 10.1002/elps.1150130156.
- [109] ORIVE, G., PONCE, S., HERNANDEZ, R., GASCÓN, A., IGARTUA, M. and PEDRAZ, J. Biocompatibility of microcapsules for cell immobilization elaborated with different type of alginates. *Biomaterials*. 2002, 23. doi: 10.1016/S0142-9612(02)00118-7.
- [110] LEE, K., JEONG, L., KANG, Y., LEE, S. and PARK, W. Electrospinning of polysaccharides for regenerative medicine. *Adv. Drug Deliv. Rev.* 2009, 61, pp. 1020–1032. doi: 10.1016/j.addr.2009.07.006.

- [111] SUN, J. and TAN, H. Alginate-based biomaterials for regenerative medicine applications. *Materials*. 2013, 6. doi: 10.3390/ma6041285.
- [112] SAHOO, D. and BISWAL, T. Alginate and its application to tissue engineering. *SN Applied Sciences*. 2021, 3. doi: 10.1007/s42452-020-04096-w.
- [113] AUGST, A., KONG, H. and MOONEY, D. Alginate hydrogels as biomaterials. *Macromolecular Bioscience*. 2006, 6, pp. 623–633. doi: 10.1002/mabi.200600069.
- [114] TROY, E., TILBURY, M., POWER, A. and WALL, J. Nature-Based Biomaterials and Their Application in Biomedicine. *Polymers*. 2021, 13. doi: 10.3390/polym13193321.
- [115] DONATI, I., HOLTAN, S., MØRCH, Y., BORGOGNA, M., DENTINI, M. and GUDMUND, S.-B. New Hypothesis on the Role of Alternating Sequences in CalciumAlginate Gels. *Biomacromolecules*. 2005, 6, pp. 1031–1040. doi: 10.1021/bm049306e.
- [116] LEE, B., MIN, G. and KIM, T. Preparation and in vitro release of melatonin-loaded multivalent cationic alginate beads. *Archives of Pharmacal Research*. 1996, 19. doi: 10.1007/BF02976241.
- [117] GRASDALEN, H., LARSEN, B. and SMISROD, O. ^{13}C -n.m.r. studies of monomeric composition and sequence in alginate. *Carbohydrate Research*. 1981, 89, pp. 179/191. doi: 10.1016/S0008-6215(00)85243-X.
- [118] S. CHATTOPADHYAY, R. R. and GLICK, G. Collagen-based biomaterials for wound healing. *Biopolymers*. 2014, 8, pp. 821–830. doi: 10.1002/bip.22486.
- [119] SHOULDERS, M. and RAINES, R. Collagen Structure and Stability. *Annual Review of Biochemistry*. 2009, 78. doi: 10.1146/annurev.biochem.77.032207.120833.
- [120] BALAJI, A., PAKALAPATI, H., KHALID, M., WALVEKAR, R. and SIDDIQUI, H. *Biodegradable and Biocompatible Polymer Composites*, Natural and synthetic biocompatible and biodegradable polymers. Elsevier, 2018. ISBN 9780081009703.
- [121] MARIOD, A. and ADAM, H. Review: Gelatin, source, extraction and industrial applications. *Acta Scientiarum Polonorum, Technologia Alimentaria*. 2013, 12, pp. 135–147.

- [122] ZHANG, W., B. ZHANG, Y. WANG, W.P. LU, WANG, J. and Y.C. GUO. Comprehensive physical and chemical characterization highlights the uniqueness of enzymatic gelatin in terms of surface properties. *Green Processing and Synthesis*. 2022, 11. doi: 10.1515/gps-2022-0045.
- [123] MOKREJŠ, P., MRÁZEK, P., ROBERT, R. G. and PAVLAČKOVÁ, J. Biotechnological Preparation of Gelatines from Chicken Feet. *Polymers*. 2019, 11, pp. 1060–1074. doi: 10.3390/polym11061060.
- [124] GUO, L., COLBY, R., LUSIGNAN, C. and HOWE, A. Physical Gelation of Gelatin Studied with Rheo-Optics. *Macromolecules*. 2003, 36, pp. 10009–10020. doi: 10.1021/ma034266c.
- [125] GORGIEVA, S. and KOKOL, V. *Biomaterials Applications for Nanomedicine, Collagen- vs. Gelatine-Based Biomaterials and Their Biocompatibility: Review and Perspectives*. InTech, 2011. ISBN 978-953-307-661-4.
- [126] PANWAR, A. and TAN, L. Current Status of Bioinks for Micro-Extrusion-Based 3D Bioprinting. *Molecules*. 2016, 21. doi: 10.3390/molecules21060685.
- [127] BELLO, A., KIM, D., KIM, D., PARK, H. and LEE, S.-H. Engineering and Functionalization of Gelatin Biomaterials: From Cell Culture to Medical Applications. *Tissue Engineering Part B: Reviews*. 2020, 26, pp. 164–180. doi: 10.1089/ten.teb.2019.0256.
- [128] YU, W., WANG, X., MA, L., LI, H., HE, Z. and ZHANG, Y. Preparation, characterisation and structure of rabbit (Hyla rabbit) skin gelatine. *International Journal of Food Science Technology*. 2016, 51, pp. 574–580. doi: 10.1111/ijfs.13012.
- [129] LUO, C. et al. Biomimetic open porous structured core-shell microtissue with enhanced mechanical properties for bottom-up bone tissue engineering. *Theranostics*. 2019, 9, pp. 4663–4677. doi: 10.7150/thno.34464.
- [130] HSU, S. and JAMIESON, A. Viscoelastic behaviour at the thermal sol-gel transition of gelatin. *Polymer*. 1993, 34. doi: 10.1016/0032-3861(93)90596-3.

- [131] BOHIDAR, H. and JENA, S. Study of sol-state properties of aqueous gelatin solutions. *The Journal of Chemical Physics*. 1994, 100, pp. 6888–6895. doi: 10.1063/1.467004.
- [132] BALAJI, A., PAKALAPATI, H., KHALID, M., WALVEKAR, R. and SIDDIQUI, H. *Biodegradable and Biocompatible Polymer Composites*. Elsevier, 2018. ISBN 9780081009703.
- [133] HUNSEN, M., AZIM, A., MANG, H., WALLNER, S., RONKVIST, A., XIE, W. and GROSS, R. A Cutinase with Polyester Synthesis Activity. *Macromolecules*. 2007, 40, pp. 148–150. doi: 10.1021/ma062095g.
- [134] DHANASEKARAN, N., MUTHUVELU, K. and ARUMUGASAMY, S. *Encyclopedia of Materials: Plastics and Polymers*, Recent Advancement in Biomedical Applications of Polycaprolactone and Polycaprolactone-Based Materials. Elsevier, 2022. ISBN 9780128232910.
- [135] ROHINDRA, D. and KHURMA, J. Miscibility, melting and crystallization of poly(ϵ -caprolactone) and poly (vinyl formal) blend. *The South Pacific Journal of Natural and Applied Sciences*. 2007, 25. doi: 10.1071/SP07009.
- [136] FARZAMFAR, S., ALEAHMAD, M., KOUZEHKONAN, G., SALEHI, M. and NAZERI, N. Polycaprolactone/Gelatin Nanofibrous Scaffolds for Tissue Engineering. *Biointerface Research in Applied Chemistry*. 2021, 11. doi: 10.33263/BRIAC114.1110411115.
- [137] BAI, Y., JIANG, C., WANG, Q. and WANG, T. A novel high mechanical strength shape memory polymer based on ethyl cellulose and polycaprolactone. *Carbohydrate Polymers*. 2013, 96. doi: 10.1016/j.carbpol.2013.04.026.
- [138] GUPTA, A. and MEKONNEN, T. Cellulose nanocrystals enabled sustainable polycaprolactone based shape memory polyurethane bionanocomposites. *Journal of Colloid and Interface Science*. 2022, 611. doi: 10.1016/j.jcis.2021.11.174.
- [139] VAN DER SCHUEREN, L., STEYAERT, I., DE SCHOENMAKER, B. and DE CLERCK, K. Polycaprolactone/chitosan blend nanofibres electrospun from an acetic acid/formic acid solvent system. *Carbohydrate Polymers*. 2012, 88. doi: 10.1016/j.carbpol.2012.01.085.

- [140] EL FAWAL, G., HONG, H., MO, X. and WANG, H. Fabrication of scaffold based on gelatin and polycaprolactone (PCL) for wound dressing application. *Journal of Drug Delivery Science and Technology*. 2021, 63. doi: 10.1016/j.jddst.2021.102501.
- [141] HERZBERGER, J., NIEDERER, K., POHLIT, H., SEIWERT, J., WORM, M., WURM, F. and FREY, H. Polymerization of Ethylene Oxide, Propylene Oxide, and Other Alkylene Oxides: Synthesis, Novel Polymer Architectures, and Bioconjugation. *Chemical Reviews*. 2016, 116. doi: 10.1021/acs.chemrev.5b00441.
- [142] SMITH, G., BEDROV, D. and BORODIN, O. Conformations and Chain Dimensions of Poly(ethylene oxide) in Aqueous Solution: A Molecular Dynamics Simulation Study. *Journal of the American Chemical Society*. 2000, 112. doi: 10.1021/ja001053j.
- [143] LI, S., TIAN, M., WANG, J., DU, F., LI, L. and XUE, Z. Poly (Ethylene Oxide)-Based Block Copolymer Electrolytes Formed via Ligand-Free Iron-Mediated Atom Transfer Radical Polymerization. *Polymers*. 2020, 12. doi: 10.3390/polym12040763.
- [144] PIESOWICZ, E., PASZKIEWICZ, S. and SZYM CZYK, A. Phase Separation and Elastic Properties of Poly(Trimethylene Terephthalate)-block-poly(Ethylene Oxide) Copolymers. *Polymers*. 2016, 8. doi: 10.3390/polym8070237.
- [145] WAGNER, Z., ROENIGK, T. and GOODSON, F. RigidFlexible Alternating Block Copolymers That Contain Poly(p -phenylene) Units of Defined Length as the Rigid Blocks. *Macromolecules*. 2001, 34. doi: 10.1021/ma010406b.
- [146] VISHWAKARMA, A., SHARPE, P., SHI, S. and RAMALINGAM, M. *Stem Cell Biology and Tissue Engineering in Dental Sciences*. Elsevier, 2015. ISBN 978-0-12-397157-9.
- [147] RAHMAN, M., KHNA, M. and TAREQ, S. Preparation and Characterization of Polyethylene Oxide (PEO)/Gelatin Blend for Biomedical Application: Effect of Gamma Radiation. *Journal of Applied Science*. 2010, 117. doi: 10.1002/app.32034.

- [148] PHADATARE, M., KHOT, V., SALUNKHE, A., THORAT, N. and PAWAR, S. Studies on polyethylene glycol coating on NiFe₂O₄ nanoparticles for biomedical applications. *Journal of Magnetism and Magnetic Materials*. 2012, 324. doi: 10.1016/j.jmmm.2011.09.020.
- [149] AL-HARBI, L. and DARWISH, M. Functionalized iron oxide nanoparticles: synthesis through ultrasonic-assisted co-precipitation and performance as hyperthermic agents for biomedical applications. *Heliyon*. 2022, 8. doi: 10.1016/j.heliyon.2022.e09654.
- [150] STARBOVA, K., SPASOVA, M., YORDANOVA, V., STARBOV, N. and RASHKOV, I. Polyethylene oxide assisted synthesis of titania fibers via electrospinning. *Optoelectronics and Advanced Materials - Rapid Communications*. 2007, 1.
- [151] CHEN, Y., TAN, G. and ZHOU, Y. Effects of viscosities and solution composition on core-sheath electrospun polycaprolactone(PCL) nanoporous microtubes. *Polymers*. 2021, 13. doi: 10.3390/polym13213650.
- [152] PERERA, A., JACKSON, R., BRISTOW, R. and WHITE, C. Magnetic cryogels as a shape-selective and customizable platform for hyperthermia-mediated drug delivery. *Scientific Reports*. 2022, 12. doi: 10.1038/s41598-022-13572-9.
- [153] HAYES, J., CURLEY, C., TIERNEY, P. and KENNEDY, J. Biomechanical analysis of a salt-modified polyvinyl alcohol hydrogel for knee meniscus applications, including comparison with human donor samples. *Journal of Mechanical Behavior of Medical Materials*. 2016, 56. doi: 10.1016/j.jmbbm.2015.11.011.
- [154] DENG, S., WANG, L., ZHAO, C., XING, D., LI, H., WANG, B., LI, Z., ZHOU, H. and WU, Y. Low coefficient of friction hydrogels with fast self-healing properties inspired by articular cartilage. *Colloids and Surfaces A: Physicochemical and Engineering Aspects*. 2023, 656. doi: 10.1016/j.colsurfa.2022.130380.
- [155] SERDIUK, V., SCHEVCHUK, O., KOVALENKO, T., BUKARTYK, N. and TOKAREV, V. Synthesis of reactive copolymers with peroxide functionality for cross-linking water-soluble polymers. *Journal of Applied Polymer Science*. 2023, 140. doi: 10.1002/app.53254.

- [156] HAN, F., ZHU, C., CHEN, L., WICKS, J. and LI, B. *Bio-Instructive Scaffolds for Musculoskeletal Tissue Engineering and Regenerative Medicine*. Elsevier, 2017. ISBN 9780128033944.
- [157] SHI, Y., YAN, C., ZHOU, Y., WU, J., WANG, Y., YU, S. and CHEN, Y. *Materials for Additive Manufacturing*, Polymer material for additive manufacturing–filament materials. Elsevier, 2021. ISBN 9780128193020.
- [158] KULA, J., LINKA, A., TUNAK, M. and LUKAS, D. Image analysis of jet structure on electrospinning from free liquid surface. *Applied Physics Letters*. 2014, 104. doi: 10.1063/1.4884597.
- [159] AGARWAL, K., SAHAY, R. and BAJI, A. Tensile Properties of Composite Reinforced with Three-Dimensional Printed Fibers. *Polymers*. 2020, 12. doi: 10.3390/polym12051089.
- [160] SCHMEDLEN, R., MASTERS, K. and WEST, J. Photocrosslinkable polyvinyl alcohol hydrogels that can be modified with cell adhesion peptides for use in tissue engineering. *Biomaterials*. 2002, 23. doi: 10.1016/S0142-9612(02)00177-1.
- [161] YAQOUB, M., JALIL, A. and BERNKOP-SCHNÜRCH, A. *Modeling and Control of Drug Delivery Systems*, Mucoadhesive Polymers: Gateway to Innovative Drug Delivery. Elsevier, 2021. ISBN 9780128211854.
- [162] ELBLBESY, M., HANAFY, T. and KANDIL, B. Effect of gelatin concentration on the characterizations and hemocompatibility of polyvinyl alcohol-gelatin hydrogel. *Bio-medical Materials and Engineering*. 2020, 31. doi: 10.3233/BME-201096.
- [163] ALHOSSEINI, S., MOZTARZADEH, F., MOZAFARI, M., ASGARI, S., DODEL, M., SAMADIKUCHAKSARAEI, A., KARGOZAR, S. and JALALI, N. Synthesis and characterization of electrospun polyvinyl alcohol nanofibrous scaffolds modified by blending with chitosan for neural tissue engineering. *International Journal of Nanomedicine*. 2012, 7. doi: 10.2147/IJN.S25376.
- [164] FARSI, M., ASEFNEJAD, A. and BAHARIFAR, H. A hyaluronic acid/PVA electrospun coating on 3D printed PLA scaffold for orthopedic application. *Progress in Biomaterials*. 2022, 11. doi: 10.1007/s40204-022-00180-z.

- [165] JIA, J. et al. Engineering alginate as bioink for bioprinting. *Acta Biomaterialia*. 2014, 10, pp. 4323–4331. doi: 10.1016/j.actbio.2014.06.034.
- [166] KLOTZ, B., GAWLITTA, D., ROSENBERG, A., MALDA, J. and MELCHELS, F. Gelatin-Methacryloyl Hydrogels: Towards Biofabrication-Based Tissue Repair. *Trends in Biotechnology*. 2016, 34, pp. 394–407. doi: 10.1016/j.tibtech.2016.01.002.
- [167] CHIMENE, D., LENNOX, K., KAUNAS, R. and GAHARWAR, A. Advanced Bioinks for 3D Printing: A Materials Science Perspective. *Annals of Biomedical Engineering*. 2016, 44, pp. 2090–2102. doi: 10.1007/s10439-016-1638-y.
- [168] SOMIYA, S., YOSHIMURA, R. and WATANABE, R. *Sintering '87*. Springer, 1987.
- [169] MISEREZ, A., SCHNEBERK, T., SUN, C., ZOK, F. and WAITE, J. The Transition from Stiff to Compliant Materials in Squid Beaks. *Science*. 2008, 319, pp. 1816–1819. doi: 10.1126/science.1154117.
- [170] POLITI, Y., PRIEWASSER, M., PIPPEL, E., ZASLANSKY, P., HARTMANN, J., SIEGEL, S., LI, C., BARTH, F. and FRATZL, P. A Spider's Fang: How to Design an Injection Needle Using Chitin-Based Composite Material. *Advanced Functional Materials*. 2012, 22, pp. 2519–2528. doi: 10.1002/adfm.201200063.
- [171] WEAVER, J. et al. The Stomatopod Dactyl Club: A Formidable Damage-Tolerant Biological Hammer. *Science*. 2012, 336, pp. 1275–1280. doi: 10.1126/science.1218764.
- [172] ESTELLE, K., BLAIR, D., EVANS, K. and GOZEN, B. Manufacturing of smart composites with hyperelastic property gradients and shape memory using fused deposition. *Journal of Manufacturing Processes*. 2017, 28, pp. 500–507. doi: 10.1016/j.jmapro.2017.04.018.
- [173] SONG, Y., HU, Q., LIU, Q., LIU, S., WANG, Y. and ZHANG, H. Design and fabrication of drug-loaded alginate/hydroxyapatite/collagen composite scaffolds for repairing infected bone defects. *Journal of Materials Science*. 2023, 58, pp. 911–926. doi: 10.1007/s10853-022-08053-3.

- [174] HASSAN, S. et al. Tunable and Compartmentalized Multimaterial Bioprinting for Complex Living Tissue Constructs. *ACS Applied Materials Interfaces*. 2022, 14. doi: 10.1021/acsami.2c12585.
- [175] HU, Q., WU, J., ZHANG, H., DONG, W., GU, Y. and LIU, S. Designing Double-Layer Multimaterial Composite Patch Scaffold with Adhesion Resistance for Hernia Repair. *Macromolecular Bioscience*. 2022, 22. doi: 10.1002/mabi.202100510.
- [176] ABDULMAGED, A., SOON, C., TALIP, B., ZAMHURI, S., MOSTAFA, S. and ZHOU, W. Characterization of Alginate–Gelatin–Cholesteryl Ester Liquid Crystals Bioinks for Extrusion Bioprinting of Tissue Engineering Scaffolds. *Polymers*. 2022, 14. doi: 10.3390/polym14051021.
- [177] LIAN, L. et al. Uniaxial and Coaxial Vertical Embedded Extrusion Bioprinting. *Advanced Healthcare Materials*. 2022, 11. doi: 10.1002/adhm.202102411.
- [178] SUN, W., TASHMAN, J., SHIWARSKI, D., FEINBERG, A. and WEBSTER-WOOD, V. Long-Fiber Embedded Hydrogel 3D Printing for Structural Reinforcement. *ACS Biomaterials Science Engineering*. 2022, 8, pp. 303–313. doi: 10.1021/acsbiomaterials.1c00908.
- [179] SUN, W., FEINBERG, A. and WEBSTER-WOOD, V. Continuous fiber extruder for desktop 3D printers toward long fiber embedded hydrogel 3D printing. *HardwareX*. 2022, 11. doi: 10.1016/j.ohx.2022.e00297.
- [180] CAI, Y., CHANG, S., GAN, S., MA, S., LU, W. and YEN, C. Nanocomposite bioinks for 3D bioprinting. *Acta Biomaterialia*. 2022, 151, pp. 45–69. doi: 10.1016/j.actbio.2022.08.014.
- [181] BHATTACHARYYA, A., JANARTHANAN, G. and NOH, I. Nano-biomaterials for designing functional bioinks towards complex tissue and organ regeneration in 3D bioprinting. *Additive Manufacturing*. 2021, 37. doi: 10.1016/j.addma.2020.101639.
- [182] CIDONIO, G., COOKE, M., GLINKA, M., DAWSON, J., GROVER, L. and ORFFO, R. Printing bone in a gel: using nanocomposite bioink to print functionalised bone scaffolds. *Materials Today Bio*. 2019, 4. doi: 10.1016/j.mtbio.2019.100028.

- [183] LI, Q., LEI, X., WANG, X., CAI, Z., LYU, P. and ZHANG, G. Hydroxyapatite/Collagen Three-Dimensional Printed Scaffolds and Their Osteogenic Effects on Human Bone Marrow-Derived Mesenchymal Stem Cells. *Tissue Engineering Part A*. 2019, 25, pp. 1261–1271. doi: 10.1089/ten.tea.2018.0201.
- [184] GUO, Y.-P., GUAN, J.-J., YANG, J., WANG, Y., ZHANG, C.-Q. and KE, Q.-F. Hybrid nanostructured hydroxyapatite–chitosan composite scaffold: bioinspired fabrication, mechanical properties and biological properties. *Journal of Materials Chemistry B*. 2015, 3, pp. 4679–4689. doi: 10.1039/C5TB00175G.
- [185] VOZZI, G., CORALLO, C., CARTA, S., FORTINA, M., GATTAZZO, F., GALLETTI, M. and GIORDANO, N. Collagen-gelatin-genipin-hydroxyapatite composite scaffolds colonized by human primary osteoblasts are suitable for bone tissue engineering applications: In vitro evidences. *Journal of Biomedical Materials Research Part A*. 2014, 102, pp. 1415–1421. doi: 10.1002/jbm.a.34823.
- [186] KISHORE, S., CHEN, Y., RAVINDRA, P. and BHATIA, S. The effect of particle-scale dynamics on the macroscopic properties of disk-shaped colloid–polymer systems. *Colloids and Surfaces A: Physicochemical and Engineering Aspects*. 2015, 482, pp. 585–595. doi: 10.1016/j.colsurfa.2015.06.056.
- [187] JABBARI, E., LEIJTEN, J., XU, Q. and KHADEMHOSEINI, A. The matrix reloaded: the evolution of regenerative hydrogels. *Materials Today*. 2016, 19, pp. 190–196. doi: 10.1016/j.mattod.2015.10.005.
- [188] SMITHMYER, M., SAWICKI, L. and KLOXIN, A. Hydrogel scaffolds as in vitro models to study fibroblast activation in wound healing and disease. *Biomaterials Science*. 2014, 2, pp. 634–650. doi: 10.1039/C3BM60319A.
- [189] PEAK, C., STEIN, J., GOLD, K. and GAHARWAR, A. Nanoengineered Colloidal Inks for 3D Bioprinting. *Langmuir*. 2018, 34, pp. 917–925. doi: 10.1021/acs.langmuir.7b02540.
- [190] HONG, S., SYCKS, D., CHAN, H., LIN, S., GUILAK, G. L. F., LEONG, K. and ZHAO, X. 3D Printing of Highly Stretchable and Tough Hydrogels into Complex, Cellularized Structures. *Advanced Materials*. 2015, 27, pp. 4035–4040. doi: 10.1002/adma.201501099.

- [191] DÁVILA, J. and D'ÁVILA, M. Rheological evaluation of Laponite/alginate inks for 3D extrusion-based printing. *The International Journal of Advanced Manufacturing Technology*. 2019, 101, pp. 675–686. doi: 10.1007/s00170-018-2876-y.
- [192] BOSSIS, G., VOLKOVA, O., LACIS, S. and MEUNIER, A. *Ferrofluids. Lecture Notes in Physics*, Magnetorheology: Fluids, Structures and Rheology. Springer: Berlin, Germany, 2022.
- [193] MORILLAS, J. and DE VINCENTE, J. Magnetorheology: A review. *Soft Matter*. 2020, 16, pp. 9614–9642.
- [194] RICH, J., MCKINLEY, G. and DOYLE, P. Arrested Chain Growth During Magnetic Directed Particle Assembly in Yield Stress Matrix Fluids. *Langmuir*. 2012, 28.
- [195] LIU, J., FLORES, G. A. and SHENG, R. In-vitro investigation of blood embolization in cancer treatment using magnetorheological fluids. *Journal of Magnetism and Magnetic Materials*. 2001, 225, pp. 209–217. doi: 10.1016/S0304-8853(00)01260-9.
- [196] BODA, S., THRIVIKRAMAN, G. and BASU, B. Magnetic field assisted stem cell differentiation - role of substrate magnetization in osteogenesis. *Journal of Materials Chemistry B*. 2015, 3, pp. 3150–3168. doi: 10.1039/c5tb00118h.
- [197] TAY, A., SOHRABI, A., POOLE, K., SEIDLITS, S. and CARLO, D. D. A 3D magnetic hyaluronic acid hydrogel for magnetomechanical neuromodulation of primary dorsal root ganglion neurons. *Advanced Materials*. 2018, 30. doi: 10.1002/adma.201800927.
- [198] DUTZ, S. and HERGT, R. Magnetic particle hyperthermia—a promising tumour therapy? *Nanotechnology*. 2014, 25. doi: 10.1088/0957-4484/25/45/452001.
- [199] CHEN, R., ROMERO, G., CHRISTIANSEN, M., MOHR, A. and ANIKEEVA, P. Wireless magnetothermal deep brain stimulation. *Science*. 2015, 347. doi: 10.1126/science.1261821.

- [200] VANGIJZEGEM, T., STANICKI, D. and LAURENT, S. Magnetic iron oxide nanoparticles for drug delivery: applications and characteristics. *Expert Opinion on Drug Delivery*. 2019, 16. doi: 10.1080/17425247.2019.1554647.
- [201] SHARMA, S., SHRIVASTAVA, N., ROSSI, F., TUNG, L. and THANH, N. Nanoparticles-based magnetic and photo induced hyperthermia for cancer treatment. *Nano Today*. 2019, 29. doi: 10.1016/j.nantod.2019.100795.
- [202] OTA, S. and TAKEMURA, Y. Characterization of Néel and Brownian Relaxations Isolated from Complex Dynamics Influenced by Dipole Interactions in Magnetic Nanoparticles. *The Journal of Physical Chemistry C*. 2019, 123. doi: 10.1021/acs.jpcc.9b06790.
- [203] WELLS, J. et al. Challenges and recommendations for magnetic hyperthermia characterization measurements. *International Journal of Hyperthermia*. 2021, 38. doi: 10.1080/02656736.2021.1892837.
- [204] SEZER, N., ARI, I., BICER, Y. and KOC, M. Superparamagnetic Nanoarchitectures: Multimodal Functionalities and Applications. *Journal of Magnetism and Magnetic Materials*. 2021, 538. doi: 10.1016/j.jmmm.2021.168300.
- [205] BELLEGHEM, S. V., TORRES, L., SANTORO, M., MAHADIK, B., WOLFAND, A., KOFINAS, P. and FISHER, J. Hybrid 3D Printing of Synthetic and Cell-Laden Bioinks for Shape Retaining Soft Tissue Grafts. *Advanced Functional Materials*. 2019, 30. doi: 10.1002/adfm.201907145.
- [206] MANDRYCKY, C., WANG, Z., KIM, K. and KIM, D.-H. 3D bioprinting for engineering complex tissues. *Biotechnology Advances*. 2016, 34, pp. 422–434. doi: 10.1016/j.biotechadv.2015.12.011.
- [207] CAUSA, F., NETTI, P. and AMBROSIO, L. A multi-functional scaffold for tissue regeneration: The need to engineer a tissue analogue. *Biomaterials*. 2007, 28, pp. 5093–5099. doi: 10.1016/j.biomaterials.2007.07.030.
- [208] LAROCHELLE, E., STREETER, S., LITTLER, E. and RUIZ, A. 3D-Printed Tumor Phantoms for Assessment of In Vivo Fluorescence Imaging Analysis Methods. *Molecular Imaging and Biology*. 2023, 25, pp. 212–220. doi: 10.1007/s11307-022-01783-5.

- [209] JIANG, Z., DIGGLE, B., TAN, M., VIKTOROVA, J., BENNET, C. and CONNALL, L. Extrusion 3D Printing of Polymeric Materials with Advanced Properties. *Advanced Science*. 2020, 7. doi: 10.1002/advs.202001379.
- [210] GANTUMUR, E., KIMURA, M., TAYA, M., HORIE, M., NAKAMURA, M. and SAKAI, S. Inkjet micropatterning through horseradish peroxidase-mediated hydrogelation for controlled cell immobilization and microtissue fabrication. *Biofabrication*. 2020, 12. doi: 10.1088/1758-5090/ab3b3c.
- [211] WANG, W., ZHU, X., LI, L., QIAN, B. and XIE, Y. Characterization of thermal inkjet droplets jitter. *Journal of Physics D: Applied Physics*. 2019, 52. doi: 10.1088/1361-6463/ab1e33.
- [212] XU, C., ZHENG, M., HUANG, Y., OGALE, A., FU, J. and MARKWALD, R. Study of droplet formation process during drop-on-demand inkjetting of living cell-laden bioink. *Langmuir*. 2014, 30, pp. 9130–9138. doi: 10.1021/la501430x.
- [213] HÖLZL, K., LIN, S., TYTGAT, L., VLIERBERGHE, S. V., GU, L. and OVSIANIKOV, A. Bioink properties before, during and after 3D bioprinting. *Biofabrication*. 2016, 8, pp. 032002–032020. doi: 10.1088/1758-5090/8/3/032002.
- [214] OZBOLAT, I. and HOSPODIUK, M. Current advances and future perspectives in extrusion-based bioprinting. *Biomaterials*. 2016, 76, pp. 321–343. doi: 10.1016/j.biomaterials.2015.10.076.
- [215] GUILLOTIN, B. et al. Laser assisted bioprinting of engineered tissue with high cell density and microscale organization. *Biomaterials*. 2010, 31, pp. 7250–7256. doi: 10.1016/j.biomaterials.2010.05.055.
- [216] GUILLEMOT, F. et al. High-throughput laser printing of cells and biomaterials for tissue engineering. *Acta Biomaterialia*. 2010, 6, pp. 2494–2500. doi: 10.1016/j.actbio.2009.09.029.
- [217] JANG, T.-S., JUNG, H.-D., PAN, H., HAN, W., CHEN, S. and SONG, J. 3D printing of hydrogel composite systems: Recent advances in technology for tissue engineering. *International Journal of Bioprinting*. 2018, 4. doi: 10.18063/ijb.v4i1.126.

- [218] LEIJTEN, J. et al. Spatially and temporally controlled hydrogels for tissue engineering. *Materials Science and Engineering: R: Reports*. 2017, 119, pp. 1–35. doi: 10.1016/j.mser.2017.07.001.
- [219] MURPHY, S. and ATALA, A. 3D bioprinting of tissues and organs. *Nature Biotechnology*. 2014, 32, pp. 773–785. doi: 10.1038/nbt.2958.
- [220] PETTA, D., ARMIENTO, A., GRIJMA, D., ALINI, M., EGLIN, D. and D'ESTE, M. 3D bioprinting of a hyaluronan bioink through enzymatic-and visible light-crosslinking. *Biofabrication*. 2018, 10, pp. 044104–044114. doi: 10.1088/1758-5090/aadf58.
- [221] DOBOS, A. et al. Thiol–Gelatin–Norbornene Bioink for Laser-Based High-Definition Bioprinting. *Advanced Healthcare Materials*. 2019, pp. 1900752–1900761. doi: 10.1002/adhm.201900752.
- [222] KAJAVE, N., SCHMITT, T., NGUYEN, T.-U. and KISHORE, V. Dual crosslinking strategy to generate mechanically viable cell-laden printable constructs using methacrylated collagen bioinks. *Materials Science and Engineering: C*. 2020, 107, pp. 110290–110301. doi: 10.1016/j.msec.2019.110290.
- [223] PUERTAS-BARTOLOMÉ, M., WŁODARCZYK-BIEGUN, M., CAMPO, A., VÁZQUEZ-LASA, B. and ROMÁN, J. S. 3D Printing of a Reactive Hydrogel Bio-Ink Using a Static Mixing Tool. *Polymers*. 2020, 12. doi: 10.3390/polym12091986.
- [224] XU, J., LIN, Y. and HSU, S. Hydrogels Based on Schiff Base Linkages for Biomedical Applications. *Molecules*. 2019, 24. doi: 10.3390/molecules24163005.
- [225] SINGH, Y., BANDYOPADHYAY, A. and MANDAL, B. 3D Bioprinting Using Cross-Linker-Free Silk–Gelatin Bioink for Cartilage Tissue Engineering. *ACS Applied Materials Interfaces*. 2019, 11, pp. 33684–33696. doi: 10.1021/acsami.9b11644.
- [226] OUYANG, L., YAO, R., ZHAO, Y. and SUN, W. Effect of bioink properties on printability and cell viability for 3D bioplotting of embryonic stem cells. *Biofabrication*. 2016, 8, pp. 035020–035033. doi: 10.1088/1758-5090/8/3/035020.

- [227] LI, Z., HUANG, S., LIU, Y., YAO, B., HU, T., SHI, H., XIE, J. and FU, X. Tuning Alginate-Gelatin Bioink Properties by Varying Solvent and Their Impact on Stem Cell Behavior. *Scientific Reports*. 2018, 23, pp. 8020–8028. doi: 10.1038/s41598-018-26407-3.
- [228] POTTER, C., LAO, K., ZENG, L. and XU, Q. Role of Biomechanical Forces in Stem Cell Vascular Lineage Differentiation. *Arteriosclerosis, Thrombosis, and Vascular Biology*. 2014, 34, pp. 2184–2190. doi: 10.1161/ATVBAHA.114.303423.
- [229] LEMARIÉ, L., ANANDAN, A., PETIOT, E., MARQUETTE, C. and COURTIAL, E. Rheology, simulation and data analysis toward bioprinting cell viability awareness. *Bioprinting*. 2021, 21. doi: 10.1016/j.bprint.2020.e00119.
- [230] BLAESER, A., CAMPOS, D. D., PUSTER, U., RICHTERING, W., STEVENS, M. and FISCHER, H. Controlling Shear Stress in 3D Bioprinting is a Key Factor to Balance Printing Resolution and Stem Cell Integrity. *Advanced Healthcare Materials*. 2016, 5, pp. 326–333. doi: 10.1002/adhm.201500677.
- [231] URUSHIBARA, A., KODAMA, S. and YOKOYA, A. Induction of genetic instability by transfer of a UV-A-irradiated chromosome. *Mutation Research/Genetic Toxicology and Environmental Mutagenesis*. 2014, 766. doi: 10.1016/j.mrgentox.2014.02.005.
- [232] GILCHRIST, R., MEDAL, R., SHOREY, W., HANSELMAN, R., PARROTT, J. and TAYLOR, C. Selective Inductive Heating of Lymph Nodes. *Annals of Surgery*. 1957, 146, pp. 596–606. doi: 10.1097/00000658-195710000-00007.
- [233] SHANGARI, N. and O'BRIEN, P. The cytotoxic mechanism of glyoxal involves oxidative stress. *Biomedical Pharmacology*. 2004, 68, pp. 1433–1442. doi: 10.1016/j.bcp.2004.06.013.
- [234] CLAIR, M., BERMUDEZ, E., GROSS, E., BUTTERWORTH, B., RECIO, L. and CARRANO, A. Evaluation of the genotoxic potential of glutaraldehyde. *Environmental and Molecular Mutagenesis*. 1991, 18, pp. 113–119. doi: 10.1002/em.2850180206.

- [235] SCHWAB, A., LEVATO, R., D'ESTE, M., PILUSO, S., EGLIN, D. and MALDA, J. Printability and Shape Fidelity of Bioinks in 3D Bioprinting. *Chemical Reviews*. 2020, 120, pp. 11028–11055. doi: 10.1021/acs.chemrev.0c00084.
- [236] REINA-ROMO, E., MANDAL, S., AMORIM, P., BLOEMEN, V., FERRARIS, E. and GERIS, L. Towards the Experimentally-Informed In Silico Nozzle Design Optimization for Extrusion-Based Bioprinting of Shear-Thinning Hydrogels. *Frontiers in Bioengineering and Biotechnology*. 2021, 9. doi: 10.3389/fbioe.2021.701778.
- [237] LEE, M., BAE, K., GUILLON, P., CHANG, J., ARLOV, O. and ZENOBI-WONG, M. Exploitation of Cationic Silica Nanoparticles for Bioprinting of Large-Scale Constructs with High Printing Fidelity. *ACS Applied Materials Interfaces*. 2018, 10, pp. 37820–37828. doi: 10.1021/acsami.8b13166.
- [238] FARAHANI, R., DUBÉ, M. and THERRIAULT, D. Three-Dimensional Printing of Multifunctional Nanocomposites: Manufacturing Techniques and Applications. *Advanced Materials*. 2016, 28, pp. 5794–5821. doi: 10.1002/adma.201506215.
- [239] GHEBREMEDHIN, M., SEIFFERT, S. and VILGIS, T. Physics of agarose fluid gels: Rheological properties and microstructure. *Current Research in Food Science*. 2021, 4, pp. 436–448. doi: 10.1016/j.crfs.2021.06.003.
- [240] JEJURIKAR, A., LAWRIE, G., MARTIN, D. and GRØNDAHL, L. A novel strategy for preparing mechanically robust ionically cross-linked alginate hydrogels. *Biomedical Materials*. 2011, 6. doi: 10.1088/1748-6041/6/2/025010.
- [241] DUTTA, S., HEXIU, J., PATEL, D., GANGULY, K. and LIM, K. 3D-printed bioactive and biodegradable hydrogel scaffolds of alginate/gelatin/cellulose nanocrystals for tissue engineering. *International Journal of Biological Macromolecules*. 2021, 167, pp. 644–658. doi: 10.1016/j.ijbiomac.2020.12.011.
- [242] SULTAN, S. and MATHEW, A. 3D printed scaffolds with gradient porosity based on a cellulose nanocrystal hydrogel. *Nanoscale*. 2018, 10, pp. 4421–4431. doi: 10.1039/C7NR08966J.

- [243] ROH, H., KIM, H., KIM, C. and LEE, K. 3D Printing of Polysaccharide-Based Self-Healing Hydrogel Reinforced with Alginate for Secondary Cross-Linking. *Biomedicines*. 2021, 9. doi: 10.3390/biomedicines9091224.
- [244] AHMAD, R., NAWAWI, W. W. and NASARUDDIN, R. Alginate and alginate composites for biomedical applications. *Asian Journal of Pharmaceutical Sciences*. 2021, 16, pp. 280–306. doi: 10.1016/j.ajps.2020.10.001.
- [245] GRANT, T., MORRIS, E., REES, D., SMITH, P. and THOM, D. Biological interactions between polysaccharides and divalent cations: The egg-box model. *FEBS Letters*. 1973, 32, pp. 195–198.
- [246] MØRCH, , DONATI, I., STRAND, B. and SKJÅK-BRÆK, G. Effect of Ca^{2+} , Ba^{2+} , and Sr^{2+} on Alginate Microbeads. *Biomacromolecules*. 2006, 7, pp. 1471–1480. doi: 10.1021/bm060010d.
- [247] MASSANA, R., OTHMAN, A., MELMAN, A. and KATZ, E. Iron(III)-cross-linked alginate hydrogels: a critical review. *Materials Advances*. 2022, 3, pp. 1849–1873. doi: 10.1039/D1MA00959A.
- [248] CERNENCU, A., LUNGU, A., STANCU, I., SERAFIM, A., HEGGSET, E., SYVERUD, K. and IOVU, H. Bioinspired 3D printable pectin-nanocellulose ink formulations. *Carbohydrate Polymers*. 2019, 220, pp. 12–21. doi: 10.1016/j.carbpol.2019.05.026.
- [249] TANG, S., JIANG, L., JIANG, Z., MA, Y., ZHANG, Y. and SU, S. Improving the mechanical, degradation properties and biocompatibility of nano-hydroxyapatite/chitosan composite scaffold by the introduction of carboxylated bamboo fiber. *Cellulose*. 2023, 30, pp. 1585–1597. doi: 10.1007/s10570-022-05001-x.
- [250] DOUSTDAR, F., OLAD, A. and GHORBANI, M. Effect of glutaraldehyde and calcium chloride as different crosslinking agents on the characteristics of chitosan/cellulose nanocrystals scaffold. *International Journal of Biological Macromolecules*. 2022, 208, pp. 912–924. doi: 10.1016/j.ijbiomac.2022.03.193.

- [251] OLFAT, N., GOLCHIN, A., FATHI, M. and NAKHLBAND, A. Designing robust chitosan-based hydrogels for stem cell nesting under oxidative stress. *BioImpacts*. 2021. doi: 10.34172/bi.2021.23831.
- [252] JONIDI, S., SOLOUK, A., BAGHERI, K., BONAKDAR, S. and MIRZADEH, H. Injectable and reversible preformed cryogels based on chemically crosslinked gelatin methacrylate (GelMA) and physically crosslinked hyaluronic acid (HA) for soft tissue engineering. *Colloids and Surfaces B: Biointerfaces*. 2021, 203. doi: 10.1016/j.colsurfb.2021.111725.
- [253] MÖRÖ, A., SAMANTA, S., HONKAMÄKI, L., RANGASAMI, V., PUISTOLA, P., KAUPPILA, M., NARKILAHTI, S., MIETTINEN, S., OOMMEN, O. and SKOTTMAN, H. Hyaluronic acid based next generation bioink for 3D bioprinting of human stem cell derived corneal stromal model with innervation. *Biofabrication*. 2022, 15. doi: 10.1088/1758-5090/acab34.
- [254] CHAN, J., BATTISTON, K. and SANTERRE, J. Synthesis and characterization of electrospun nanofibrous tissue engineering scaffolds generated from in situ polymerization of ionomeric polyurethane composites. *Acta Biomaterialia*. 2019, 96, pp. 161–174. doi: 10.1016/j.actbio.2019.06.046.
- [255] WANG, Y., HE, Y., YU, J., LI, H., LI, S. and TIAN, S. A freestanding dual-cross-linked membrane with robust anti-crude oil-fouling performance for highly efficient crude oil-in-water emulsion separation. *Colloids and Surfaces A: Physicochemical and Engineering Aspects*. 2022, 654. doi: 10.1016/j.colsurfa.2022.130117.
- [256] ZHENG, Z., GUO, Z., ZHONG, F., WANG, B., LIU, L., MA, W., YU, C. and WEI, H. A dual crosslinked hydrogel-mediated integrated peptides and BMSC therapy for myocardial regeneration. *Journal of Controlled Release*. 2022, 347, pp. 127–142. doi: 10.1016/j.jconrel.2022.04.010.
- [257] HU, T. and LO, A. Y. Collagen–Alginate Composite Hydrogel: Application in Tissue Engineering and Biomedical Sciences. *Polymers*. 2021, 13. doi: 10.3390/polym13111852.

- [258] WANG, L., CHENG, L., LI, G., LIU, K., ZHANG, Z., LI, P., DONG, S., YU, W., HUANG, F. and YAN, X. A Self-Cross-Linking Supramolecular Polymer Network Enabled by Crown-Ether-Based Molecular Recognition. *Journal of the American Chemical Society*. 2020, 142, pp. 2051–2058. doi: 10.1021/jacs.9b12164.
- [259] ZHENG, B., WANG, F., DONG, S. and HUANG, F. Supramolecular polymers constructed by crown ether-based molecular recognition. *Chemical Society Reviews*. 2012, 41, pp. 1621–1636. doi: 10.1039/C1CS15220C.
- [260] BARROW, S., KASERA, S., ROWLAND, M., BARRIO, J. and SCHERMAN, O. Cucurbituril-Based Molecular Recognition. *Chemical Reviews*. 2015, 115. doi: 10.1021/acs.chemrev.5b00341.
- [261] UEDA, C. et al. Behavior of supramolecular cross-links formed by host-guest interactions in hydrogels responding to water contents. *Supramolecular Materials*. 2022, 1. doi: 10.1016/j.supmat.2021.100001.
- [262] LI, Y. et al. Enhancing cartilage repair with optimized supramolecular hydrogel-based scaffold and pulsed electromagnetic field. *Bioactive Materials*. 2023, 22, pp. 312–324. doi: 10.1016/j.bioactmat.2022.10.010.
- [263] MUROI, R., SUGANE, K. and SHIBATA, M. Self-healing thiol-ene networks based on cyclodextrin-adamantane host-guest interactions. *Polymer*. 2019, 185. doi: 10.1016/j.polymer.2019.121990.
- [264] DAS, M., PARATHODIKA, A., MAJI, P. and NASKAR, K. Dynamic chemistry: The next generation platform for various elastomers and their mechanical properties with self-healing performance. *European Polymer Journal*. 2023, 186. doi: 10.1016/j.eurpolymj.2023.111844.
- [265] MORGAN, F., MORONI, L. and BAKER, M. Dynamic Bioinks to Advance Bio-printing. *Advanced Healthcare Materials*. 2020, 9. doi: 10.1002/adhm.201901798.
- [266] BATA-MPOUMA, J., KANDHOLA, G., SAKON, J. and KIM, J. Covalent Crosslinking of Colloidal Cellulose Nanocrystals for Multifunctional Nanostructured Hydrogels with Tunable Physicochemical Properties. *Biomacromolecules*. 2022, 23, pp. 4085–4096. doi: 10.1021/acs.biomac.2c00417.

- [267] HOEMANN, C., CHENITE, A., SUN, J., HURTIG, M., SERRECI, A., LU, Z., ROSSOMACHA, E. and BUSCHMANN, M. Cytocompatible gel formation of chitosan-glycerol phosphate solutions supplemented with hydroxyl ethyl cellulose is due to the presence of glyoxal. *Journal of Biomedical Materials Research Part A*. 2007, 83, pp. 521–529. doi: 10.1002/jbm.a.31365.
- [268] KRISTIANSEN, K., POTTHAST, A. and CHRISTENSEN, B. Periodate oxidation of polysaccharides for modification of chemical and physical properties. *Carbohydrate Research*. 2010, 345, pp. 1264–1271. doi: 10.1016/j.carres.2010.02.011.
- [269] MAIA, J., CARVALHO, R., COELHO, J., SIMOES, P. and GIL, M. Insight on the Periodate Oxidation of Dextran and Its Structural Vicissitudes. *Polymer*. 2011, 52, pp. 258–265. doi: 10.1016/j.polymer.2010.11.058.
- [270] LUO, X., GUO, Z., HE, P., CHEN, T., LI, L., DING, S. and LI, H. Study on structure, mechanical property and cell cytocompatibility of electrospun collagen nanofibers crosslinked by common agents. *International Journal of Biological Macromolecules*. 2018, 113. doi: 10.1016/j.ijbiomac.2018.01.179.
- [271] DING, W., ZHOU, J., ZENG, Y., WANG, Y. and SHI, B. Preparation of oxidized sodium alginate with different molecular weights and its application for crosslinking collagen fiber. *Carbohydrate Polymers*. 2017, 157, pp. 1650–1656. doi: 10.1016/j.carbpol.2016.11.045.
- [272] UMAN, S., DHAND, A. and BURDICK, J. Recent advances in shear-thinning and self-healing hydrogels for biomedical applications. *Journal of Applied Polymer Science*. 2020, 137. doi: 10.1002/app.48668.
- [273] TANG, Y., SUN, MA, J. and YAN, Q. Mussel-inspired self-healing hydrogel based on gelatin and oxidized tannic acid for pH-responsive controlled drug release. *Journal Journal of Biomaterials Science, Polymer Edition*. 2023. doi: 10.1080/09205063.2023.2182577.
- [274] KIM, S., KIM, D., ROH, H., KIM, H., LEE, J. and LEE, K. Three-Dimensional Bioprinting of Cell-Laden Constructs Using Polysaccharide-Based Self-Healing Hydrogels. *Biomacromolecules*. 2019, 20, pp. 1860–1866. doi: 10.1021/acs.biomac.8b01589.

- [275] LI, S., PEI, M., WAN, T., YANG, H., GU, S., TAO, Y., LIU, X., ZHOU, Y., XU, W. and XIAO, P. Self-healing hyaluronic acid hydrogels based on dynamic Schiff base linkages as biomaterials. *Carbohydrate Polymers*. 2020, 250. doi: 10.1016/j.carbpol.2020.116922.
- [276] BILLMAN, J. and DIESING, A. Reduction of Schiff Bases with Sodium Borohydride. *The Journal of Organic Chemistry*. 1957, 22. doi: 10.1021/jo01360a019.
- [277] HE, J., HORIE, K., YOKOTA, R. and HE, F. Preparation of end-crosslinked polyimide gels with high moduli. *Polymer*. 2001, 42, pp. 4063–4072. doi: 10.1016/S0032-3861(00)00803-X.
- [278] BULCKE, A. V. D., BOGDANOV, B., ROOZE, N. D., SCHACHT, E., CORNELISSEN, M. and BERGHAMS, H. Structural and Rheological Properties of Methacrylamide Modified Gelatin Hydrogels. *Biomacromolecules*. 2000, 1, pp. 31–38. doi: 10.1021/bm990017d.
- [279] D'ESTE, M., EGLIN, D. and ALINI, M. A systematic analysis of DMTMM vs EDC/NHS for ligation of amines to hyaluronan in water. *Carbohydrate Polymers*. 2014, 108, pp. 239–246. doi: 10.1016/j.carbpol.2014.02.070.
- [280] CAMMARATA, C., HUGHES, M. and OFNER, C. Carbodiimide Induced Cross-Linking, Ligand Addition, and Degradation in Gelatin. *Molecular Pharmaceutics*. 2015, 12, pp. 783–793. doi: 10.1021/mp5006118.
- [281] MUSILOVÁ, L., MRÁČEK, A., KOVALCIK, A., SMOLKA, P., MINAŘÍK, A., HUMPOLÍČEK, P., VÍCHA, R. and PONÍŽIL, P. Hyaluronan hydrogels modified by glycinated Kraft lignin: Morphology, swelling, viscoelastic properties and biocompatibility. *Carbohydrate Polymers*. 2018, 181, pp. 394–403. doi: 10.1016/j.carbpol.2017.10.048.
- [282] PIEPER, J., WACHEM, P., LUYN, M., BROUWER, L., HAFMANS, T., VEERKAMP, J. and KUPPEVELT, T. Attachment of glycosaminoglycans to collagenous matrices modulates the tissue response in rats. *Biomaterials*. 2000, 21, pp. 1689–1699. doi: 10.1016/S0142-9612(00)00052-1.
- [283] SOLINAS, A., FAURE, H., ROUDAUT, H., TRAIFFORT, E., SCHOENFELDER, A., MANN, A., MANETTI, F., TADDEI, M. and RAUT, M. Acylthiourea, Acylurea,

- and Acylguanidine Derivatives with Potent Hedgehog Inhibiting Activity. *Journal of Medicinal Chemistry*. 2012, 55, pp. 1559–1571. doi: 10.1021/jm2013369.
- [284] PALAZON, F., BENAVIDES, C. M., LÉONARD, D., SOUTEYRAND, E., CHEVOLOT, Y. and CLOAREC, J. Carbodiimide/NHS Derivatization of COOH-Terminated SAMs: Activation or Byproduct Formation? *Langmuir*. 2014, 30, pp. 4545–4550. doi: 10.1021/la5004269.
- [285] CAI, S., LIU, Y., ZHENG, S. and PRESTWICH, G. Injectable glycosaminoglycan hydrogels for controlled release of human basic fibroblast growth factor. *Biomaterials*. 2005, 26, pp. 6054–6067. doi: 10.1016/j.biomaterials.2005.03.012.
- [286] HORN, E., BEAUMONT, M., SHU, X., HARVEY, A., PRESTWICH, G., HORN, K., GIBSON, A., PREUL, M. and PANITCH, A. Influence of cross-linked hyaluronic acid hydrogels on neurite outgrowth and recovery from spinal cord injury. *Journal of Neurosurgery: Spine*. 2007, 6, pp. 133–140. doi: 10.3171/spi.2007.6.2.133.
- [287] GARCÍA-ASTRAIN, C., GANDINI, A., PEÑA, C., ALGAR, I., ECEIZA, A., CORCUERA, M. and GABILONDO, N. Diels–Alder “click” chemistry for the cross-linking of furfuryl-gelatin-polyetheramine hydrogels. *RSC Advances*. 2014, 4, pp. 2046–2069. doi: 10.1039/C4RA06122E.
- [288] MADL, C. and HEILSHORN, S. Rapid Diels–Alder Cross-linking of Cell Encapsulating Hydrogels. *Chemistry of Materials*. 2019, 31, pp. 8035–8043. doi: 10.1021/acs.chemmater.9b02485.
- [289] GOLAS, P. and MATYJASZEWSKI, K. Marrying click chemistry with polymerization: expanding the scope of polymeric materials. *Chem. Soc. Rev.* 2010, 39, pp. 1338–1354. doi: 10.1039/B901978M.
- [290] BI, B., MA, M., LV, S., ZHUO, R. and JIANG, X. In-situ forming thermosensitive hydroxypropyl chitin-based hydrogel crosslinked by Diels–Alder reaction for three dimensional cell culture. *Carbohydrate Polymers*. 2019, 212, pp. 368–377. doi: 10.1016/j.carbpol.2019.02.058.
- [291] PIRMORADIAN, M., HOOSHMAND, T., NAJAFI, F., HAGHBIN, N. and DAVAIE, S. Design, synthesis, and characterization of a novel dual cross-linked gelatin-

- based bioadhesive for hard and soft tissues adhesion capability. *Biomedical Materials*. 2022, 17. doi: 10.1088/1748-605X.
- [292] SPIVAK, A., DZENIS, Y. and RENEKER, D. A model of steady state jet in the electrospinning process. *Mechanics Research Communications*. 2000, 27, pp. 37–42. doi: 10.1016/S0093-6413(00)00060-4.
- [293] FRAGKOPOULOS, A., ELLIS, P. and FERNANDEZ-NIEVES, A. Teaching Rayleigh–Plateau instabilities in the laboratory. *European Journal of Physics*. 2015, 36. doi: 10.1088/0143-0807/36/5/055023.
- [294] JAWOREK, A. and SOBczyk, A. Electrospaying route to nanotechnology: An overview. *Journal of Electrostatics*. 2008, 66, pp. 197–219. doi: 10.1016/j.elstat.2007.10.001.
- [295] RENEKER, D. and YARIN, A. Electrospinning jets and polymer nanofibers. *Polymer*. 2008, 49, pp. 2387–2425. doi: 10.1016/j.polymer.2008.02.002.
- [296] REIZABAL, A., TANDON, B., LANCEROS-MENDEZ, S. and DALTON, P. Electrohydrodynamic 3D Printing of Aqueous Solutions. *Small*. 2023, 19. doi: 10.1002/sml.202205255.
- [297] PALANGETIC, L., REDDY, N., SRINIVASAN, S., COHEN, R. E., MCKINLEY, G. H. and CLASEN, C. Dispersity and spinnability: Why highly polydisperse polymer solutions are desirable for electrospinning. *Polymer*. 2014, 55, pp. 4920–4931. doi: 10.1016/j.polymer.2014.07.047.
- [298] BROWN, T., DALTON, P. and HUTMACHER, D. Direct Writing By Way of Melt Electrospinning. *Advanced Materials*. 2011, 23, pp. 5651–5658. doi: 10.1002/adma.201103482.
- [299] MALKIN, A., SEMAKOV, A., SKVORTSOV, I., ZATONSKIKH, P., KULICHIKHIN, V., SUBBOTIN, A. and SEMENOV, A. Spinnability of Dilute Polymer Solutions. *Macromolecules*. 2017, 50, pp. 8231–8244. doi: 10.1021/acs.macromol.7b00687.
- [300] SHENOY, S., BATES, W., FRISH, H. and WNEK, G. Role of chain entanglements on fiber formation during electrospinning of polymer solutions: good solvent, no-

- specific polymer-polymer interaction limit. *Polymer*. 2005, 46, pp. 3372–3384. doi: 10.1016/j.polymer.2005.03.011.
- [301] LIU, T., LIU, L., DING, F. and LI, Y. A Machine Learning Study of Polymer-Solvent Interactions. *Chinese Journal of Polymer Science*. 2022, 40, pp. 834–842. doi: 10.1007/s10118-022-2716-2.
- [302] DEITZEL, J., KLEINMEYER, J., HARRIS, D. and TAN, N. The effect of processing variables on the morphology of electrospun nanofibers and textiles. *Polymer*. 2001, 42, pp. 261–272. doi: 10.1016/S0032-3861(00)00250-0.
- [303] KUTALKOVA, E., INGR, M., KOLAŘÍKOVÁ, A., HRNČIŘÍK, J., WITASEK, R., HERMANOVÁ, M., ŠTRYMPL, O. and HUERTA-ÁNGELES, G. Structure and dynamics of the hyaluronan oligosaccharides and their solvation shell in water: organic mixed solvents. *Carbohydrate Polymers*. 2023, 304. doi: 10.1016/j.carbpol.2022.120506.
- [304] KOLAŘÍKOVÁ, A., KUTÁLKOVÁ, E., BUŠ, V., WITASEK, R., HRNČIŘÍK, J. and INGR, M. Salt-dependent intermolecular interactions of hyaluronan molecules mediate the formation of temporary duplex structures. *Carbohydrate Polymers*. 2022, 286. doi: 10.1016/j.carbpol.2022.119288.
- [305] ANGAMANNA, C. and JAYARAM, S. Investigation of the Optimum Electric Field for a Stable Electrospinning Process. *IEEE Transactions on Industry Applications*. 2012, 48, pp. 808–815. doi: 10.1109/TIA.2011.2180010.
- [306] DEMIR, M., YILGOR, I., YILGOR, E. and ERMAN, B. Electrospinning of polyurethane fibers. *Polymer*. 2002, 43, pp. 3303–3309. doi: 10.1016/S0032-3861(02)00136-2.
- [307] GHELICH, R., RAD, M. K. and YOUZBASHI, A. Study on Morphology and Size Distribution of Electrospun NiO-GDC Composite Nanofibers. *Journal of Engineered Fibers and Fabrics*. 2015, 10. doi: 10.1177/155892501501000102.
- [308] TONG, H. and WANG, M. Negative Voltage Electrospinning and Positive Voltage Electrospinning of Tissue Engineering Scaffolds: A Comparative Study and Charge Retention on Scaffolds. *Nano LIFE*. 2012, 2. doi: 10.1142/S1793984411000384.

- [309] SIVAN, M., MADHESWARAN, D., HAUZEROVA, S., NOVOTNY, V., HEDVIČAKOVA, V., JENCOVA, V., KOSTAKOVA, E., SCHINDLER, M. and LUKAS, D. AC electrospinning: impact of high voltage and solvent on the electrospinnability and productivity of polycaprolactone electrospun nanofibrous scaffolds. *Materials Today Chemistry*. 2022, 26. doi: 10.1016/j.mtchem.2022.101025.
- [310] STACHEWICZ, U., STONE, C., WILLIS, C. and BARBER, A. Charge assisted tailoring of chemical functionality at electrospun nanofiber surfaces. *Journal of Materials Chemistry*. 2012, 22. doi: 10.1039/C2JM33807F.
- [311] JIRKOVEC, R., KALOUS, T. and CHVOJKA, J. The modification of the wetting of polycaprolactone nanofibre layers via alternating current spinning. *Materials & Design*. 2021, 210. doi: 10.1016/j.matdes.2021.110096.
- [312] SZEWCZYK, P. and STACHEWICZ, U. The impact of relative humidity on electrospun polymer fibers: From structural changes to fiber morphology. *Advances in Colloid and Interface Science*. 2020, 286. doi: 10.1016/j.cis.2020.102315.
- [313] ICOGLU, H. and OGULATA, R. Effect of ambient parameters on morphology of electrospun polyetherimide (PEI) fibers. *Tekstil ve Konfekslyon*. 2013, 23.
- [314] HARIDAS, A., SHARMA, C., SRITHARAN, V. and RAO, T. Fabrication and surface functionalization of electrospun polystyrene submicron fibers with controllable surface roughness. *RSC Advances*. 2014, 4. doi: 10.1039/C3RA44170A.
- [315] MARINO, T., RUSSO, F. and FIGOLI, A. The Formation of Polyvinylidene Fluoride Membranes with Tailored Properties via Vapour/Non-Solvent Induced Phase Separation. *Membranes*. 2018, 8. doi: 10.3390/membranes8030071.
- [316] LI, D. et al. Fabrication and Applications of Multi-Fluidic Electrospinning Multi-Structure Hollow and Core-Shell Nanofibers. *Engineering*. 2022, 13, pp. 116–127. doi: 10.1016/j.eng.2021.02.025.
- [317] SCHELSKI, K., REYES, C., PSCHYKLENK, L., KAUL, P. and LAGERWALL, J. Quantitative volatile organic compound sensing with liquid crystal core fibers. *Cell Reports Physical Sciences*. 2021, 2. doi: 10.1016/j.xcrp.2021.100661.

- [318] ZHOU, Z., WU, X., DING, Y., YU, M., ZHAO, Y., JIANG, L., XUAN, C. and SUN, C. Needleless Emulsion Electrospinning for Scalable Fabrication of Core-Shell Nanofibers. *Journal of Applied Polymer Science*. 2014, 131. doi: 10.1002/APP.40896.
- [319] VATS, S., ANYFANTAKIS, M., HONAKER, L., BASOLI, F. and LAGERWALL, J. Stable Electrospinning of Core-Functionalized Coaxial Fibers Enabled by the Minimum-Energy Interface Given by Partial Core-Sheath Miscibility. *Langmuir*. 2021, 37, pp. 13265–13277. doi: 10.1021/acs.langmuir.1c01824.
- [320] MA, H., CHEN, G., ZHANG, J., LIU, Y., NIE, J. and MA, G. Facile fabrication of core-shell polyelectrolyte complexes nanofibers based on electric field induced phase separation. *Polymer*. 2017, 110, pp. 80–86. doi: 10.1016/j.polymer.2016.12.062.
- [321] DEDE, S., SADAK, O., DIDIN, M. and GUNASEKARAN, S. Basil oil-loaded electrospun biofibers: Edible food packaging material. *Journal of Food Engineering*. 2022, 319. doi: 10.1016/j.jfoodeng.2021.110914.
- [322] MA, J. et al. Enhanced viability of probiotics encapsulated within synthetic/natural biopolymers by the addition of gum arabic via electrohydrodynamic processing. *Food Chemistry*. 2023, 413. doi: 10.1016/j.foodchem.2023.135680.
- [323] JAYAPRAKASH, P., MAUDHUIT, A., GAIANI, C. and DESOBRY, S. Encapsulation of bioactive compounds using competitive emerging techniques: Electro-spraying, nano spray drying, and electrostatic spray drying. *Journal of Food Engineering*. 2023, 339. doi: 10.1016/j.jfoodeng.2022.111260.
- [324] KORNMULLER, A., COOPER, T., JANI, A., LAJOIE, G. and FLYNN, L. Probing the effects of matrix-derived microcarrier composition on human adipose-derived stromal cells cultured dynamically within spinner flask bioreactors. *Journal of Biomedical Materials Research Part A*. 2023, 111, pp. 415–434. doi: 10.1002/jbm.a.37459.
- [325] KLICOVA, M. et al. Biomimetic hierarchical nanofibrous surfaces inspired by superhydrophobic lotus leaf structure for preventing tissue adhesions. *Materials & Design*. 2022, 217. doi: 10.1016/j.matdes.2022.110661.

- [326] KIM, J., KIM, D., LIM, K., SEONWOO, H., PARK, S., KIM, Y., KIM, Y., CHOUNG, Y., CHOUNG, P. and CHUNG, J. Charged Nanomatrices as Efficient Platforms for Modulating Cell Adhesion and Shape. *Tissue Engineering Part C: Methods*. 2012, 18, pp. 913–923. doi: 10.1089/ten.tec.2011.0731.
- [327] LIU, S., WHITE, K. and RENEKER, D. Electrospinning Polymer Nanofibers With Controlled Diameters. *IEEE Transactions on Industry Applications*. 2019, 55, pp. 5239–5243. doi: 10.1109/TIA.2019.2920811.
- [328] THOMPSON, C., CHASE, G. and D.H. RENEKER, A. Y. Effects of parameters on nanofiber diameter determined from electrospinning model. *Polymer*. 2007, 48, pp. 6913–6922. doi: 10.1016/j.polymer.2007.09.017.
- [329] SUBRAHMANYA, T. M., ARSHAD, A., LIN, P., WIDAKDO, J., H.K. MAKARI, H. A., HU, C., LAI, J. and HUNG, W. A review of recent progress in polymeric electrospun nanofiber membranes in addressing safe water global issues. *RSC Advances*. 2021, 11, pp. 9638–9663. doi: 10.1039/D1RA00060H.
- [330] WARREN, P., DAVIS, Z. and FISHER, M. Parametric control of fiber morphology and tensile mechanics in scaffolds with high aspect ratio geometry produced via melt electrowriting for musculoskeletal soft tissue engineering. *Journal of the Mechanical Behavior of Biomedical Materials*. 2019, 99, pp. 153–160. doi: 10.1016/j.jmbbm.2019.07.013.
- [331] BUSKERMOLLEN, A., SURESH, H., SHISHVAN, S., VIGLIOTTI, A., DESIMONE, A., KURNIAWAN, N., BOUTEN, C. and DESHPANDE, V. Entropic Forces Drive Cellular Contact Guidance. *Biophysical Journal*. 2019, 116, pp. 1994–2008. doi: 10.1016/j.bpj.2019.04.003.
- [332] BAZRAFSHAN, Z. and GEORGE, G. S. One-Step Fabrication of Three-Dimensional Fibrous Collagen-Based Macrostructure with High Water Uptake Capability by Coaxial Electrospinning. *Nanomaterials*. 2018, 8. doi: 10.3390/nano8100803.
- [333] PRABHAKARAN, M., VENUGOPAL, J. and RAMAKRISHNA, S. Mesenchymal stem cell differentiation to neuronal cells on electrospun nanofibrous substrates for

- nerve tissue engineering. *Biomaterials*. 2009, 30. doi: 10.1016/j.biomaterials.2009.05.057.
- [334] CASPER, C., YANG, W., FARACH-CARSON, M. and RABOLT, J. Coating Electrospun Collagen and Gelatin Fibers with Perlecan Domain I for Increased Growth Factor Binding. *Biomacromolecules*. 2007, 8. doi: 10.1021/bm061003s.
- [335] L., O., J.P.K., A., Q., C., Y., L. and M.M., S. Void-Free 3D Bioprinting for In Situ Endothelialization and Microfluidic Perfusion. *Advanced Functional Materials*. 2019, 30, pp. 1908349–1908358. doi: 10.1002/adfm.201908349.
- [336] MUSILOVÁ, L., ACHBERGEROVÁ, E., VÍTKOVÁ, L., KOLAŘÍK, R., MARTÍNKOVÁ, M., MINAŘÍK, A., MRÁČEK, A., HUMPOLÍČEK, P. and PECHA, J. Cross-Linked Gelatine by Modified Dextran as a Potential Bioink Prepared by a Simple and Non-Toxic Process. *Polymers*. 2022, 1. doi: 10.3390/polym14030391.
- [337] VÍTKOVÁ, L., MUSILOVÁ, L., ACHBERGEROVÁ, E., KOLAŘÍK, R., MRLÍK, M., KORPASOVÁ, K., MAHELOVÁ, L., CAPÁKOVÁ, Z. and MRÁČEK, A. Formulation of Magneto-Responsive Hydrogels from Dually Cross-Linked Polysaccharides: Synthesis, Tuning and Evaluation of Rheological Properties. *International Journal of Molecular Sciences*. 2022, 23. doi: 10.3390/ijms23179633.
- [338] TRAN, K. A., KRAUS, E., CLARK, A. T., BENNETT, A., POGODA, K., CHENG, X., CEBERS, A., A.JANMEY, P. and GALIE, P. A. Dynamic Tuning of Viscoelastic Hydrogels with Carbonyl Iron Microparticles Reveals the Rapid Response of Cells to Three-Dimensional Substrate Mechanics. *ACS Applied Materials Interfaces*. 2021, 13, pp. 20947–20959. doi: 10.1021/acsami.0c21868.
- [339] WINGER, J., SCHÜMANN, M., KUPKA, A. and ODENBACH, S. Influence of the particle size on the magnetorheological effect of magnetorheological elastomers. *Journal of Magnetism and Magnetic Materials*. 2019, 481, pp. 176–182. doi: 10.1016/j.jmmm.2019.03.027.
- [340] REICH, H., DIJKSTRA, M., ROIJ, R. and SCHMIDT, M. Entropic Wetting and the Free Isotropic-Nematic Interface of Hard Colloidal Platelets. *Journal of Physical Chemistry B*. 2007, 111. doi: 10.1021/jp068870b.

- [341] KOPECKÁ, K. et al. Synthesis and Exfoliation of Calcium Organophosphonates for Tailoring Rheological Properties of Sodium Alginate Solutions: A Path toward Polysaccharide-Based Bioink. *Biomacromolecules*. 2023. doi: 10.1021/acs.biomac.3c00081.
- [342] VÍTKOVÁ, L., MUSILOVÁ, L., ACHBERGEROVÁ, E., MINAŘÍK, A., SMOLKA, P., WRZECIONKO, E. and MRÁČEK, A. Electrospinning of Hyaluronan Using Polymer Coelectrospinning and Intermediate Solvent. *Polymers*. 2019, 11. doi: 10.3390/polym14030391.
- [343] EWALDZ, E. and BRETTMANN, B. Molecular Interactions in Electrospinning: From Polymer Mixtures to Supramolecular Assemblies. *ACS Applied Polymer Materials*. 2019, 1, pp. 298–308. doi: 10.1021/acsapm.8b00073.
- [344] ZHU, M., TAN, J., LIU, L., TIAN, J., LI, L., LUO, B., ZHOU, C. and LU, L. Construction of biomimetic artificial intervertebral disc scaffold via 3D printing and electrospinning. *Materials Science Engineering C*. 2021, 128. doi: 10.1016/j.msec.2021.112310.
- [345] WANG, Z., WANG, H., XIONG, J., LI, J., MIAO, X., LAN, X., LIU, X., WANG, W., CAI, N. and TANG, Y. Fabrication and *in vitro* evaluation of PCL/gelatin hierarchical scaffolds based on melt electrospinning wiring and solution electrospinning for bone regeneration. *Materials Science Engineering C*. 2021, 128. doi: 10.1016/j.msec.2021.112287.
- [346] FANG, Y., LIU, Z., WANG, H., LUO, X., XU, Y., CHAN, H., LV, S., TAO, Y. and LI, M. Implantable Sandwich-like Scaffold/Fiber Composite Spatiotemporally Releasing Combretastin A4 and Doxorubicin for Efficient Inhibition of Postoperative Tumor Recurrence. *Applied Materials Interfaces*. 2022, 14, pp. 27525–27537. doi: 10.1021/acsami.2c02103.
- [347] CALEJO, I., LABRADOR-RACHED, J., GOMEZ-FLORIT, M., REIS, R., DOMINGUES, R. and GOMES, M. Bioengineered 3D Living Fibers as In Vitro Human Tissue Models of Tendon Physiology and Pathology. *Advanced Healthcare Materials*. 2022, 11. doi: 10.1002/adhm.202102863.

- [348] HERRERA-RUIZ, A., TOVAR, B., GARCIA, R., TAMEZ, M. and MAMIDI, N. Nanomaterials-Incorporated Chemically modified Gelatin Methacryloyl-Based Biomedical Composites: A Novel Approach for Bone Tissue Engineering. *Pharmaceutics*. 2022, 14. doi: 10.3390/pharmaceutics14122645.

LIST OF FIGURES

4.1	Structural formulas of some polymers significant in tissue engineering: (A) HA, (B) NaAlg, (C) Example of possible Gel structure, (D) PCL, (E) PEO, (F) PVA	20
4.2	Schematic illustration of the house-of-cards induced printability; Created with BioRender.com	23
4.3	Typical hysteresis curves of ferromagnetic and superparamagnetic materials; adapted from [204]; Created with BioRender.com	25
4.4	Schematic representation of key characteristics of hydrogels for 3D printing in biological applications; Created with BioRender.com	29
4.5	(A) Typical example of the influence of shear stress on printing precision and cell viability in microextrusion 3D printing with marked cell viability (75%) and printing precision (95%) thresholds (inspired by [235]); (B) Schematic representation of shear stress distribution in cylindrical and conical flow channel (adapted from [236]); Created with BioRender.com	31
4.6	Schematic representation of Ca^{2+} cross-linking of NaAlg: (A) calcium guluronan junction (adapted from [257]), and (B) egg-box model (adapted from [245])	33
4.7	Examples of Schiff bases formation: (A) imine, (B) hydrazone, (C) oxime	35
4.8	Activation of -COOH group with EDC and NHS system (adapted from [284])	36
4.9	Schematic representation of liquid droplet shape evolution with the increase of electric field intensity and Taylor cone formation (adapted from [6]); Created with BioRender.com	38
4.10	Technologies based on electrofluidodynamic phenomena; Created with BioRender.com	39
4.11	Parameters influencing electrospinning; Created with BioRender.com	41
5.1	Schematic of a Schiff base formation between Gel and DEX-OX [336]	45

- 5.2 (A) Gelation time of HA hydrogels of HA-ADH modified with EDC (degree of substitution - DS 22 %) and DMTMM (DS 12 %) mediators related to (B) the oxidized polysaccharide hydrodynamic diameter measured by dynamic light scattering - the degree of oxidation (DO) is indicated in the graph [337] 47
- 5.3 Mechanical characteristics obtained from magneto-rheological measurements of CIP filled Schiff base cross-linked hydrogels in an external magnetic field: (A) Storage modulus; (B) Damping factor; (D) Intensity of MRE expressed as increase in storage modulus related to magnetic field intensity; (E) Cyclic magnetic field exposure . 48
- 5.4 Magnetization curves of (A) soft ferromagnetic CIPs used in **PAPER II** [337] and (B) superparamagnetic iron oxide multicore particles (MCPs) and diamagnetic Al₂O₃ NPs used in **PAPER III** . . . 48
- 5.5 (A) Specific loss power (SLP) of FeO_x dispersions with the increasing amount of Al₂O₃: Overall denotes the SLP results for water dispersions, where both Brown and Néel relaxation are present; Néel relaxation denotes values obtained by measurement in agar gel; Brown relaxation is the difference between overall SLP (measured in water dispersion), and Néel relaxation induced SLP (measured in agar gel); (B) SLP of magneto-responsive HA hydrogel as a function of AMF amplitude 49
- 5.6 Bioprinting of BALB/3T3 mouse fibroblasts encapsulated in magneto-responsive HA hydrogel: (A) Printing model; (B) Printed grid photography taken on the 8th day after printing; (C), (D), (E) Confocal imaging of cells distribution within the scaffold in bright field (C) and fluorescence channel (C-E). Cells were stained for cytoskeleton (red) and nucleus (blue); (F), (G) Live/Dead assay of BALB/3T3 fibroblasts. The cells were visualized in fluorescence immediately after the microextrusion. 50
- 5.7 (A) Long-term stability of magneto-responsive HA hydrogels in water and simulated cultivation conditions; (B) Schiff-base and ionically cross-linked CIPs filled HA hydrogel response to cyclic magnetic field exposure [337] 51

5.8	(A) Dependence of viscosity of NaAlg based composites on angular frequency; (B) Atomic force microscopy topology scans of the section of the modified NaAlg hydrogel samples by CaPhP, where randomly oriented aggregates of nanoplatelets are observed [341] . . .	53
5.9	Structures obtained by 3D printing using either nanoplatelets modified NaAlg, and live/dead staining of BALB/3T3 fibroblasts-laden bioinks after 3D printing: (A) 0.52 mm diameter nozzle, (B) 0.52 mm diameter needle, (C) 0.42 mm diameter nozzle, (D) 0.42 mm diameter needle	54
5.10	Scanning Electron Microscopy (SEM) micrographs of electrospun structures obtained from (A) HA/PVA blend solution with BEC and (B) HA/PEO blend solution [342]	56
5.11	Schematic representation of the various electrospinning setups used for the experiments: upwards electrospinning from rod spinneret, downwards electrospinning from single needle spinneret and downwards electrospinning from coaxial needle spinneret; Created with BioRender.com	57
5.12	Electrospun core-shell fiber with Col core and PCL shell; the sample was visualized with polarized light microscopy	58
5.13	(A) Solvent-mixture representation in Teas graph. 1, H ₂ O; 2, IPA; 3, MeOH; 4, EtOH; 5, H ₂ O:IPA 10:7; 6, H ₂ O:EtOH:MeOH 5:5:1; (B) Viscosity of HA solutions in H ₂ O:EtOH:MeOH in 5:5:1 weight ratio solvent mixture as a function of shear rate [342]	59
5.14	SEM micrographs of electrospun structures obtained from H ₂ O:EtOH:MeOH in 5:5:1 weight ratio solutions. (A) 2.8 wt.% HA 600 kDa and (B) 1.5 wt.% HA 1180 kDa [342]	59

LIST OF TABLES

4.1	Comparison of basic 3D printing technologies for tissue engineering [206]	28
-----	--	----

LIST OF ABBREVIATIONS

ADH	adipic acid dihydrazide
CaPhP	calcium phenylphosphonate
CIP	carbonyl iron microparticle
Col	collagen
DEX-OX	dextran polyaldehyde
DMEM	Dulbecco's Modified Eagle Medium
DMTMM	4-(4,6-Dimethoxy-1,3,5-triazin-2-yl)-4-methylmorpholinium chloride
DO	degree of oxidation
DS	degree of substitution
ECM	extracellular matrix
EDC	1-ethyl-3-(3-dimethyl aminopropyl)carbodiimide
EtOH	ethanol
ff-Ca	mixed calcium phenylphosphonate-phosphate
Gel	gelatin
HA	hyaluronan
HA-ADH	adipic acid dihydrazide grafted hyaluronan
HA-OX	hyaluronan polyaldehyde
HAp	hydroxyapatite
HOBt	1-hydroxybenzotriazole
M_w	molecular weight
MCP	multicore particle
MeOH	methanol
MRE	magneto-rheological effect
NaAlg	sodium alginate
NHS	N-hydroxysuccinimide
NP	nanoparticle
PCL	poly- ϵ -caprolactone
PEO	polyethylene oxide
PVA	polyvinyl alcohol
SLP	specific loss power

PUBLICATIONS OF THE AUTHOR

- [P.1] I.S. Smolkova*, N.E. Kazantseva, **L. Vitkova**, V. Babayan, J. Vilcakova and P. Smolka *Size Dependent Heating Efficiency of Multicore Iron Oxide Particles in Low-Power Alternating Magnetic Fields*. Acta Physica Polonica A, 2017, 131(4). <https://doi.org/10.12693/APhysPolA.131.663>.
- [P.2] **L. Vitkova**, L. Musilova, E. Achbergerova, A. Minarik, P. Smolka, E. Wrzecionko and A. Mracek* *Electrospinning of Hyaluronan Using Polymer Coelectrospinning and Intermediate Solvent*. Polymers, 2019, 11(1517). <https://doi.org/10.3390/polym11091517>.
- [P.3] L. Musilova, E. Achbergerova, **L. Vitkova**, R. Kolarik, M. Martinkova, A. Minarik, A. Mracek*, P. Humpolicek and J. Pecha *Cross-Linked Gelatine by Modified Dextran as a Potential Bioink Prepared by a Simple and Non-Toxic Process*. Polymers, 2021, 1(391). <https://doi.org/10.3390/polym14030391>
- [P.4] **L. Vitkova**, L. Musilova*, E. Achbergerova, R. Kolarik, M. Mrlik, K. Korpasova, L. Mahelova, Z. Capakova and A. Mracek* *Formulation of Magneto-Responsive Hydrogels from Dually Cross-Linked Polysaccharides: Synthesis, Tuning and Evaluation of Rheological Properties*. International Journal of Molecular Sciences, 2022, 23(9633). <https://doi.org/10.3390/ijms23179633>
- [P.5] M. Jurtik, B. Greskova, Z. Pruckova, M. Rouchal, L. Dastychova, **L. Vitkova**, K. Valaskova, E. Achbergerova and R. Vicha* *Assembling a supramolecular 3D network with tuneable mechanical properties using adamantylated cross-linking agents and β -cyclodextrin-modified hyaluronan*. Carbohydrate Polymers, 2023, 313. <https://doi.org/10.1016/j.carbpol.2023.120872>
- [P.6] K. Kopecka, **L. Vitkova***, Z. Kronekova, L. Musilova, P. Smolka, F. Mikulka, K. Melanova, P. Knotek, M. Humenik, A. Minarik and A. Mracek* *Synthesis and Exfoliation of Calcium Organophosphonates for Tailoring Rheological Properties of Sodium Alginate Solutions: A Path toward Polysaccharide-Based Bioink*. Biomacromolecules, 2023, *Accepted for publication*. <https://doi.org/10.1021/acs.biomac.3c00081>

- [P.7] **L. Vitkova**, I. Smolkova, N. Kazantseva, L. Musilova, P. Smolka*, K. Valaskova, K. Kocourkova, M. Humenik, A. Minarik, P. Humpolicek and A. Mracek *Magneto-responsive hyaluronan hydrogel for hyperthermia and bioprinting: magnetic, rheological properties and biocompatibility*. APL Bio-engineering, *Under review*.
- [P.8] S. Emebu*, R.O. Ogunleye, E. Achbergerová, **L. Vítková**, P. Ponížil, C. Menodza-Martinez* *Review and proposition for model-based multivariable-multiobjective optimisation of extrusion-based bioprinting*. Applied Materials Today, *Submitted*.

CURRICULUM VITAE

EDUCATION

Tomas Bata University in Zlín

9/2019-Currently

Ph.D. studies in Technology of Macromolecules

Tomas Bata University in Zlín

9/2014 - 6/2019

Bachelor's and Master's degree in Materials Engineering

INTERNATIONAL EXPERIENCE

University of Luxembourg

9/2021-10/2021 (8 weeks)

An internship in the group of Experimental Soft Matter Physics led by prof. Jan Lagerwall.

University of Bayreuth

11/2022-12/2022 (3 weeks)

An internship at the Chair of Biomaterials led by prof. Thomas Scheibel. The internship was supervised by assoc. prof. Martin Humenik.

PROJECT PARTICIPATION

IGA/FT/2023/006: Study and design of new processing procedures of polymer-based materials for advanced additive manufacturing

Team member

IGA/FT/2022/009: Hyaluronic acid and protein-based materials for 3D printing from theoretical and applied chemistry perspectives

Lead investigator

IGA/FT/2021/010: Preparation of advanced biopolymer systems

Team member

JUNG-2020-007: Development of biopolymer-based hydrogels for microextrusion

Lead investigator

IGA/FT/2020/005: Preparation of structured materials based on biopolymers

Team member

IGA/FT/2019/012: Preparation of structured biomaterials

Team member

LIST OF APPENDICES

APPENDIX A: Full texts of PAPERS I-V

APPENDIX A: FULL TEXTS OF PAPERS I-V

PAPER I: L. Musilova, E. Achbergerova, L. Vitkova, R. Kolarik, M. Martinkova, A. Minarik, A. Mracek*, P. Humpolicek and J. Pecha *Cross-Linked Gelatine by Modified Dextran as a Potential Bioink Prepared by a Simple and Non-Toxic Process*. *Polymers*, 2021, 1(391). <https://doi.org/10.3390/polym14030391>

PAPER II: L. Vitkova, L. Musilova*, E. Achbergerova, R. Kolarik, M. Mrlik, K. Korpasova, L. Mahelova, Z. Capakova and A. Mracek* *Formulation of Magneto-Responsive Hydrogels from Dually Cross-Linked Polysaccharides: Synthesis, Tuning and Evaluation of Rheological Properties*. *International Journal of Molecular Sciences*, 2022, 23(9633). <https://doi.org/10.3390/ijms23179633>

PAPER III: L. Vitkova, I. Smolkova, N. Kazantseva, L. Musilova, P. Smolka*, K. Valaskova, K. Kocourkova, M. Humenik, A. Minarik, P. Humpolicek and A. Mracek *Magneto-responsive hyaluronan hydrogel for hyperthermia and bioprinting: magnetic, rheological properties and biocompatibility*. *APL Bioengineering*, *Under review*.










PAPER IV: K. Kopecka, L. Vitkova*, Z. Kronekova, L. Musilova, P. Smolka, F. Mikulka, K. Melanova, P. Knotek, M. Humenik, A. Minarik and A. Mracek* *Synthesis and Exfoliation of Calcium Organophosphonates for Tailoring Rheological Properties of Sodium Alginate Solutions: A Path toward Polysaccharide-Based Bioink*. *Biomacromolecules*, 2023, *Accepted for publication*. <https://doi.org/10.1021/acs.biomac.3c00081>

PAPER V: L. Vitkova, L. Musilova, E. Achbergerova, A. Minarik, P. Smolka, E. Wrzcionko and A. Mracek* *Electrospinning of Hyaluronan Using Polymer Coelectrospinning and Intermediate Solvent*. *Polymers*, 2019, 11(1517). <https://doi.org/10.3390/polym11091517>.

,

Article

Cross-Linked Gelatine by Modified Dextran as a Potential Bioink Prepared by a Simple and Non-Toxic Process

Lenka Musilová ^{1,2} , Eva Achbergerová ³ , Lenka Vítková ¹ , Roman Kolařík ² , Martina Martínková ² , Antonín Minařík ^{1,2} , Aleš Mráček ^{1,2,*} , Petr Humpolíček ^{1,2}  and Jiří Pecha ³ 

- ¹ Department of Physics and Materials Engineering, Faculty of Technology, Tomas Bata University in Zlín, Vavreckova 275, 760 01 Zlín, Czech Republic; lmusilova@utb.cz (L.M.); vitkova@utb.cz (L.V.); minarik@utb.cz (A.M.)
 - ² Centre of Polymer Systems, Tomas Bata University in Zlín, tř. Tomáše Bati 5678, 760 01 Zlín, Czech Republic; rkolarik@utb.cz (R.K.); martinkova@utb.cz (M.M.); humpolicek@utb.cz (P.H.)
 - ³ CEBlA-Tech, Faculty of Applied Informatics, Tomas Bata University in Zlín, Nad Stráněmi 4511, 760 05 Zlín, Czech Republic; achbergerova@utb.cz (E.A.); pecha@utb.cz (J.P.)
- * Correspondence: mracek@utb.cz

Abstract: Essential features of well-designed materials intended for 3D bioprinting via microextrusion are the appropriate rheological behavior and cell-friendly environment. Despite the rapid development, few materials are utilizable as bioinks. The aim of our work was to design a novel cytocompatible material facilitating extrusion-based 3D printing while maintaining a relatively simple and straightforward preparation process without the need for harsh chemicals or radiation. Specifically, hydrogels were prepared from gelatines coming from three sources—bovine, rabbit, and chicken—cross-linked by dextran polyaldehyde. The influence of dextran concentration on the properties of hydrogels was studied. Rheological measurements not only confirmed the strong shear-thinning behavior of prepared inks but were also used for capturing cross-linking reaction kinetics and demonstrated quick achievement of gelation point (in most cases < 3 min). Their viscoelastic properties allowed satisfactory extrusion, forming a self-supported multi-layered uniformly porous structure. All gelatin-based hydrogels were non-cytotoxic. Homogeneous cells distribution within the printed scaffold was confirmed by fluorescence confocal microscopy. In addition, no disruption of cells structure was observed. The results demonstrate the great potential of the presented hydrogels for applications related to 3D bioprinting.

Keywords: gelatine-dextran; hydrogel; 3D printing; microextrusion; rheology; cell distribution



Citation: Musilová, L.; Achbergerová, E.; Vítková, L.; Kolařík, R.; Martínková, M.; Minařík, A.; Mráček, A.; Humpolíček, P.; Pecha, J. Cross-Linked Gelatine by Modified Dextran as a Potential Bioink Prepared by a Simple and Non-Toxic Process. *Polymers* **2022**, *1*, 391. <https://doi.org/10.3390/polym14030391>

Academic Editor: Sidi A. Bencherif

Received: 20 December 2021

Accepted: 14 January 2022

Published: 19 January 2022

Publisher's Note: MDPI stays neutral with regard to jurisdictional claims in published maps and institutional affiliations.



Copyright: © 2022 by the authors. Licensee MDPI, Basel, Switzerland. This article is an open access article distributed under the terms and conditions of the Creative Commons Attribution (CC BY) license (<https://creativecommons.org/licenses/by/4.0/>).

1. Introduction

Nowadays, 3D bioprinting has become one of the lead technologies in tissue engineering. Compared to the traditional preparation of cell-seeded scaffolds, the 3D bioprinting via microextrusion process enables the incorporation of selected cells within the printed material prior to or directly during the printing process. The major advantage of this technology is that cells, biomaterials, and biomolecules can be spatially defined. Therefore, more homogeneous cell distribution through the material could be achieved using this technique [1]. In addition, 3D bioprinting is more straightforward, less prone to human error, and gives an opportunity to precisely fabricate complex structures [2,3]. The technique relies on well-designed materials, so-called bioinks, which are essential for 3D-bioprinted scaffolds in tissue engineering [4]. Despite the rapid development, the discipline still has a shortage of materials utilizable as bioinks [5–7].

Materials for microextrusion in biological applications need to fulfill several criteria, concerning both cellular response to the ink and mechanical response to printing-induced stress. Good cytocompatibility and a suitable micro- and nanostructure serve to facilitate cell proliferation and growth [8–10]. Regarding the physical behavior during printing, their

rheological properties present the main contribution. They have to be tailored in a way that allows uninterrupted flow of the material in the nozzle and provides stability to the printed structure at the same time. In addition, the bioink should help minimize the shear stress during printing in order to avoid the risk of cell destruction [11,12]. In addition to suitable rheology, sufficient layer adhesion is needed to ensure stable structures [13,14]. From the described point of view, hydrogels hold a great promise as potential bioinks [15]. Those formed from biopolymers such as hyaluronan (HA), collagen, or gelatine (Gel) are especially useful due to their ability to mimic the cellular environment [16].

Hydrogels generally consist of a cross-linked polymer network. The cross-linking can be facilitated either by non-covalent interactions or covalent (chemical) interactions. A typical feature of the former is the reversibility of bonds under specific conditions, which offers an opportunity in terms of rheology tuning [17,18]. The downside to this characteristic is the sensitivity to changes of thermodynamic conditions. It can also result in poor mechanical properties of the hydrogels [13,19,20]. In contrast, covalent bonds are less dynamic, but they provide the material with long-term stability in various environments. Furthermore, hydrogels cross-linked by this type of bond show superior durability under mechanical stress compared to non-covalent ones [17,21,22], which is desired for printed products [20].

To date, several chemically cross-linked hydrogels based on biopolymers for 3D bioprinting have been reported. Photocross-linking using UV irradiation was performed for modified natural polymers, such as HA [23] or in combination with modified polypeptides [16,24]. Although UV-initiated polymerization is popular due to its effectivity and predictability, this approach is also associated with the potential risk of inducing chromosomal and genetic instabilities in cells and subsequent cell mortality. The weaknesses of UV light were omitted when HA and Gel, both modified by phenolic hydroxyl moieties, were photocross-linked by irradiation from a visible spectrum. However, a disadvantage of this hydrogel preparation was the employment of a ruthenium/ammonium persulfate system [25]. Regarding other methods of bioink preparation, Gel–norbornene hydrogels were synthesized by two-photon polymerization [26], or modified HA, Gel, and acrylate cross-linked via radical polymerization [27] have been reported. Nevertheless, both mentioned methods required the complex chemical modification of used biopolymers before hydrogels preparation.

In a different approach, a dual cross-linking mechanism employing enzymatic reaction and photocross-linking [28,29] or photo- with chemical cross-linking [30] was utilised for bioink preparation [28–30]. Although the dual cross-linking strategies were developed to improve the mechanical and degradation properties of bioink while maintaining their printability and cell viability, this approach involves multi-step bioink preparation processes, especially when it is compared to much more straightforward simple methods utilizing UV irradiation [16,23,24]. On the other hand, the combined methods may allow avoiding the harmful effect of high-energy light by shifting the UV irradiation prior to embedding the cells in the material [29].

The aim of our work was to design a novel bipolymer-based hydrogel using chemical cross-linking hydrogels that allows microextrusion printing while maintaining a relatively simple and straightforward preparation process. Specifically, three types of Gel were examined: bovine (Gel-B)—a source of Gel often used in biomedical application—and two promising alternative sources—rabbit (Gel-R) and chicken (Gel-C) gelatines. The advantages of Gel-R and Gel-C are that they do not suffer from concerns about bovine spongiform encephalopathy or religious limitations [31,32]. All three gelatines were combined with dextran polyaldehyde (Dex-Ox) providing firm hydrogels. To the best of our knowledge, this presents a unique approach to using the described hydrogels (Gel-Dex-Ox) as a convenient material for 3D printing bearing the potential to be combined with living cells in a direct and simple procedure, thus creating a bioink.

Prepared printing materials were thoroughly investigated, and their performance in microextrusion-based 3D printing was evaluated. The study comprises hydrogels reaction kinetics, a detailed characterization of hydrogel rheological and swelling behavior, porosity,

and printability, which are discussed with respect to Gel origin and the amount of cross-linking agent used throughout the study.

Die swell, a parameter closely connected to printing precision in microextrusion [14,33], is, to our best knowledge, underrepresented in case of biopolymer-based hydrogel 3D printing. Die swell is a result of normal stress induced by the sudden change in diameter of the flow channel [34]. Although the mechanical stress-induced cell mortality is primarily connected to tangential forces [35], evidence of normal stress affecting cell viability during printing have been found as well [36]. Consequently, the performed analysis also includes the issue of die swell.

Regarding the hydrogels performance in biomedical application, cytotoxicity assay was performed on the materials. Finally, fluorescently labeled mouse fibroblasts were added to the gels and printed so that the cell distribution could be evaluated. The prepared hydrogels proved to be shear thinning and suitable for 3D printing applications as well as showing good cytocompatibility and negligible deformation of cells during printing.

2. Materials and Methods

2.1. Chemicals

Gel-B (dry content 91.3%, $M_w = 209,600 \text{ g}\cdot\text{mol}^{-1}$) and Gel-R (dry content 86.5%, $M_w = 157,800 \text{ g}\cdot\text{mol}^{-1}$) were obtained from Tanex Vladislav, a.s. Gel-C (dry content 92.7%, $M_w = 190,900 \text{ g}\cdot\text{mol}^{-1}$) was prepared according to a patented biotechnological process [37], which is described in detail in Mokrejš et al., 2019 [38] and Gál et al., 2020 [39]. Dextran (Dex) $M_w = 40,400 \text{ g}\cdot\text{mol}^{-1}$, sodium periodate, and phosphate-buffered saline sterile solution (PBS), pH 7.4, were obtained from Sigma Aldrich. Demineralized (DEMI) water was prepared using Milipore Q System. Ammonia solution, 30 vol% was purchased from Penta and diluted to 25 vol%. $\text{Na}_2\text{HPO}_4\cdot 12\text{H}_2\text{O}$ and $\text{NaH}_2\text{PO}_4\cdot 2\text{H}_2\text{O}$, used for the preparation of PBS pH 7, were obtained from Lach-Ner.

2.2. Dextran Oxidation

The oxidation of Dex was performed according to the previously described method [40]. Briefly, to the 13 wt % water solution of Dex and a 0.4 molar fold of NaIO_4 pre-dissolved in 5 mL of DEMI water was added. The reaction was stirred for 4 h at room temperature. Subsequently, the reaction mixture was diluted with DEMI water and put into a dialysis tube (membrane cut-off $12,000 \text{ g}\cdot\text{mol}^{-1}$). The crude product was purified via dialysis against DEMI water for 3 days. Then, the solution was casted in a glass mold and frozen first at $-18 \text{ }^\circ\text{C}$ for 24 h followed by freeze drying in a freeze-dryer (ALPHA1-2 LD plus, M. Christ, Osterode am Harz, Germany). The pure product was obtained in yield 90%, and its M_w was $7700 \text{ g}\cdot\text{mol}^{-1}$. The number of aldehyde groups per 100 glucose subunits was determined using hydroxylamine hydrochloride method [41]. Automatic titrator T50 (Metler Toledo, Greifensee, Switzerland) was used for the measurements.

2.3. Polymers Characterisation

Proton Nuclear Magnetic Resonance (^1H NMR) spectra were recorded on a machine JEOL ECZ 400 (JEOL Ltd., Tokyo, Japan) operating at ^1H frequency of 399.78 MHz at $60 \text{ }^\circ\text{C}$. The samples were dissolved in D_2O at concentration of $10 \text{ mg}\cdot\text{mL}^{-1}$ for the analysis. The water signal was used as reference and was set at 4.75 ppm.

The average molecular weight and distribution curve of the initial biopolymers were determined by means of the size exclusion chromatography (SEC) method performed on a high-performance liquid chromatograph (HPLC) system Shimadzu Prominence equipped with UV-Vis and RI detectors (Shimadzu Prominence, LC-20 series, Shimadzu corporation, Kyoto, Japan). The conditions for analysis of polysaccharides were following: 0.1M PBS solution of pH equal to 7.4, flow $0.8 \text{ mL}\cdot\text{min}^{-1}$, oven temperature $30 \text{ }^\circ\text{C}$, columns PL aquagel-OH 60 μm , $300 \times 7.5 \text{ mm}$ and PL aquagel-OH 40 μm , $300 \times 7.5 \text{ mm}$ were connected in series. Pullulan standards were used for molecular weight calibration, analysis was based on RI data. Conditions for analysis of proteins were as follows: 0.15 M PBS

solution of pH equal to 7.0, flow $0.35 \text{ mL}\cdot\text{min}^{-1}$, oven temperature $30 \text{ }^\circ\text{C}$, column Agilent Bio SEC-5, $5 \text{ }\mu\text{m}$, $150 \text{ }\text{Å}$, $300 \times 4.6 \text{ mm}$. Protein standards were used for molecular weight calibration; analysis was based on UV data gained at 210 nm .

2.4. Hydrogels Preparation and Characterization

Hydrogels were prepared in the following manner: 2 wt % solution of Dex-Ox in PBS (0.1 M, pH 7.4) was mixed with 15 wt % solution of Gel dissolved in PBS (0.1 M, pH 7.4). Three volume ratios of the solutions were examined—Gel:Dex-Ox 1:1, 2:1, and 3:1. After that, 25 vol % ammonia solution was added in concentration $50 \text{ }\mu\text{L}$ per 1 mL of Gel solution, and all the reactants were mixed.

Rheological measurements of the prepared fresh mixture of biopolymer solutions (2 mL) were performed on a rotational rheometer Anton-Paar MCR 502 (Graz, Austria) at $30 \text{ }^\circ\text{C}$ under normal pressure in an air atmosphere. In case of the reaction kinetics measurement, time sweep experiments were performed using a 50 mm parallel-plate measuring system oscillating at constant 10% deformation with a constant angular frequency of $10 \text{ rad}\cdot\text{s}^{-1}$. Fundamental rheological data, i.e., complex viscosity η , storage (G'), and loss (G'') moduli, were followed in a 40 min time sweep. It should be noted that the sample preparation caused a 1 min delay between the reaction start and first data obtained.

On the other hand, the rheology of fully cross-linked hydrogels was performed using a 25 mm parallel-plate measuring system oscillating at constant 10% deformation with angular frequency sweep increasing from 0.1 to $10 \text{ rad}\cdot\text{s}^{-1}$ at $35 \text{ }^\circ\text{C}$. The frequency sweep measurement in a descending direction was carried out as well, without any change in rheological behavior. It is important to note that before such measurement was started, the hydrogel samples were prepared 12 h before in the form of circular plates with a diameter of 30 mm and a thickness of 2 mm.

As a 3D Printing instrument, Cellink BioX (Gothemburg, Sweden) was used with the following specifications: a polypropylene conical nozzle— 0.41 mm diameter, 3 mL polypropylene syringe, microextrusion syringe pump printhead, and microscope glass slide printbed. The printhead speed was $2 \text{ mm}\cdot\text{s}^{-1}$, and the extrusion rate was $1.5 \text{ }\mu\text{L}\cdot\text{s}^{-1}$. During printing, both the printhead and printbed were kept at room temperature. Optical analysis of the printing performance was carried out using a Dino-Lite AM4815ZT optical microscope and evaluated with the aid of ImageJ software. The shape fidelity was characterized using the method described by Ouyang et al. [42], i.e., determining the printability (Pr) as the similitude of a gap between printed strands to a square in the top layer of a multi-layered $10 \times 10 \text{ mm}$ rectilinear patterned grid. The distance between strand centers in a single layer had to be adjusted to 3.3 mm due to the strong die swell of the material. The layer height was set to 0.6 mm in order to account for the die swell as well as to ensure good adhesion between layers. To calculate Pr, the following formula was used: $\text{Pr} = L^2/16A$, where L denotes the perimeter (mm) and A the area of a gap (mm^2). Moreover, an uninterrupted flow of material was recorded, and the die swell was measured at the perceived distance between the printbed and nozzle, i.e., 0.5 mm . Additionally, a model specifically designed for the materials examined in the current study was developed in the following way: The overall dimensions were $10 \times 10 \times 5 \text{ mm}$, the layer height was 1 mm , the material extrusion was continuous, and the speed of the printhead was monotonous throughout the printing.

The shape and porosity of printed structures before and after freeze drying was analyzed using X-ray computed micro-tomography (CT) with the help of SkyScan (Model 1174, Bruker, Billerica, MA, USA). The printed structures were obtained using the material-specific model described earlier. The device was equipped with the X-ray source, (voltage of $20\text{--}50 \text{ kV}$, maximum power of 40 W) and the X-ray detector. The CCD 1.3 Mpix was coupled to the scintillator by a lens with 1:6 zoom range. The projection images were recorded at angular increments of 0.5° or 1° using tube voltage and tube current of 35 kV and $585 \text{ }\mu\text{A}$, respectively. The exposure time was set to 15 s without using any filter. The 3D reconstructions, surface, and volume analysis were performed via built-in CT image

analysis software (version 1.16.4.1, Bruker, USA). The results, in terms of images with different X-ray adsorption, 2D cross-sections, and 3D models were exported from DataViewer and CTvox software. Prior to CT characterization, the printed hydrogels were placed in a closed sample holder with increased humidity so that the analyzed scaffold does not dry out.

The inner porosity of the material was assessed via scanning electron microscopy (SEM) imaging of freeze-dried samples in vertical sections using a Phenom Pro instrument at an accelerating voltage of 10 kV. The samples were sputtered with a gold/palladium layer prior to imaging. The pore size and total pore area were statistically evaluated with the aid of ImageJ software.

The swelling behavior of hydrogels was determined gravimetrically as follows: weighed lyophilized samples were immersed in PBS (0.1 M pH 7.4) to gradually reach swelling equilibrium. The equilibrium buffer uptake, $S(e)(\%)$, of hydrogels was determined by taking the swollen samples from buffer solutions at selected time intervals of 1, 2, 6, 15, 30, 60, 120, 240, 360, and 1440 min, wiping with tissue paper and weighing. The presented results are expressed as an average values of 4 measurements. The samples were conditioned to 37 °C throughout the measurement in order to meet the requirements of testing for biological use.

2.5. Cytotoxicity

Cytotoxicity was tested using a mouse embryonic fibroblast cell line (ATCC CRL-1658 NIH/3T3). Testing was performed according to ISO 10993 standard concretely by testing of extracts from freeze-dried hydrogel samples. Extracts were prepared according to ISO standard 10993-12 with modifications; the extraction ratio was 0.02 g per 1 mL of culture medium (which is a lower amount than according to the ISO, which is due to the swelling properties of lyophilized samples). The ATCC-formulated Dulbecco's Modified Eagle's Medium (PAA Laboratories, Inc., Etobicoke, ON, Canada) containing 10% of calf serum (BioSera, Nuaille, France) and 100 U mL⁻¹ penicillin/streptomycin (GE 209 Healthcare HyClone, Hyclone Ltd., Cramlington, UK) was used as the culture medium. Tested samples were extracted in culture medium for 24 h at 37 °C under stirring. Subsequently, the extracts were filtered using a syringe filter with a pore size of 0.22 µm. Then, the parent extracts (100%) were diluted in culture medium to obtain a series of dilutions with concentrations of 75, 50, 25, 10, and 5%. Cells were proceeded in concentration of 10⁵ per 1 mL and cultivated for 24 h at 37 °C in 5% CO₂ in humidified air. Then, the medium was removed after the pre-cultivation and replaced by individual extracts. Cell viability was evaluated after 24 h of exposure using ATP assay (ATP Determination Kit A22066, ThermoFisher Scientific, Waltham, MA, USA). The results are presented as the relative cell viability compared to the reference (cells cultivated without extracts), where the reference corresponding to 1 means 100% cell viability. The presented data are from three experiments, each performed in triplicate.

2.6. Cell Distribution within 3D-Printed Structure

Before the test, the cells were fixed and counterstained. The 4% formaldehyde (Penta chemicals, Prague, Czech Republic) was used to fix the cells within the suspension. After 15 min of exposure, the cell suspension was centrifugated (1.5 RPM for 2 min) and supernatant was aspirated. Then, the cells were washed with PBS, and after centrifugation (1.5 RPM for 2 min), 0.5% Triton x-100 (Merck Group, Darmstadt, Germany) was added for 5 min followed by centrifugation and three washes with PBS. Then, the cells nuclei were counterstained by Hoechst 3325 ($\lambda_{ex} = 355$ nm, $\lambda_{em} = 465$ nm) and the cytoskeleton was counterstained by ActinRed 555 ($\lambda_{ex} = 540$ nm and $\lambda_{em} = 665$ nm) according to the protocol of the producer (both Sigma Aldrich). The stained fibroblasts were mixed with hydrogel in concentration of 5·10⁵ cells per 1 mL of hydrogel. These mixtures were printed (using the same procedure as describe before) and observed by the means of confocal microscopy using an Olympus FLUOVIEW FV3000 (Olympus corporation, Laser Scanning

Confocal Microscope (LSCM) in order to determine the homogeneity of cells distribution. The Plan-Apochromat objective with magnification $10\times$ and numerical aperture $NA = 0.8$ or $4\times$ and $NA = 0.4$, respectively, were used for analysis. The figures were obtained as three-dimensional reconstruction from confocal images in the z-axis ($4\times$ magnification—10 images with $10\ \mu\text{m}$ steps, $10\times$ magnification—10 images with $5\ \mu\text{m}$ steps).

3. Results and Discussion

3.1. Polysaccharide Oxidation and Hydrogel Formation

In order to develop printable hydrogels as potential bioinks based on a chemically cross-linked polymeric matrix, modified Dex and Gels were utilized. Bovine, rabbit, and chicken gelatines, hydrolyzed forms of collagens, were chosen in order to achieve close resemblance of the scaffold to extracellular matrix [43], thus maximizing the potential to produce material which may ensure sufficient viability, adhesion, and proliferation of fibroblasts [44]. Note that the source of gelatine and method of its preparation affect the ultimate mechanical and functional properties of final hydrogels [45], and consequently, the present study shall facilitate comparison of these Gel sources as a matrix of printable hydrogel.

Oxidized dextran (Dex-Ox) was used as a cross-linking agent so that high-energy light irradiation, toxic chemicals [46–48], or free radicals formation [29] was avoided. Initially, Dex was oxidized by sodium periodate [40,49], forming Dex-Ox with approximately 50 aldehyde groups per 100 units of the biopolymer chain. Comparing the ^1H NMR spectrum of unmodified Dex to the spectrum of Dex-Ox (see Figure S1 in Supplement), in ^1H NMR of Dex-Ox, several characteristic peaks were observed in the region of 6.0–4.4 ppm. These signals, which were assigned to protons of hemiacetals formed from aldehyde groups, confirmed the successful oxidation of Dex [40]. Subsequently, the hydrogels were obtained when Gels of bovine, rabbit, or chicken origin were chemically cross-linked by Dex-Ox, expecting Schiff base formation between Dex-Ox and amino groups present in Gel [50], as presented in Figure 1. The chosen manner of hydrogel preparation is characterized by mild conditions, avoiding the presence of harmful chemicals or radiation, which could be favorable for the intended application with respect to cell compatibility and viability.

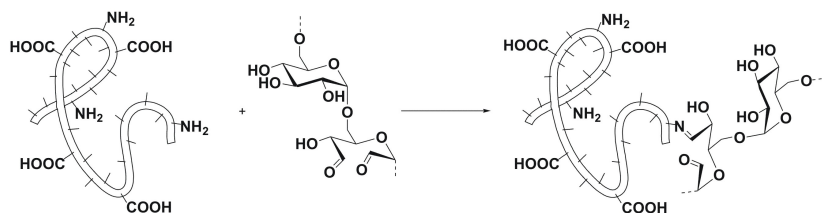


Figure 1. Schematic illustration of the cross-linking reaction between Dex-Ox and Gel.

3.2. Reaction Kinetics

Rheological experiments were designed to determine the kinetics of cross-linking reaction of Gels with Dex-Ox and a time of sol–gel transition, i.e., gelation point. A basic kinetics model of the first order was employed to fit the experimental rheological data and determine the reaction rates in order to facilitate reasonable kinetic data comparison (details of the data processing procedure are given in Supplementary Information). Table 1 summarizes the evaluated reaction rate coefficients together with the corresponding coefficients of determination. As can be seen, the reaction rates of a cross-linking reaction of Gel-B and Gel-R with Dex-Ox are similar; all were found to be in the range of $7\text{--}12\ \text{h}^{-1}$. In contrast, the cross-linking reaction of Gel-C was significantly slower with reaction rates in the range of $1.0\text{--}2.5\ \text{h}^{-1}$. The differences in reaction rates between Gel-B and Gel-R versus Gel-C can be most probably attributed to the different manufacturing procedures of the gelatines and resulting different properties of the used protein material. The rate coefficients show that conversion of cross-linking reaction equal to 75% is achieved in a time shorter than 10 min in case of Gel-B and Gel-R, while it took more than 30 min to

reach this conversion in case of Gel-C. From a practical point of view, it is advantageous to print the hydrogel after reaching such conversion of cross-linking reaction in order to ensure the relatively stable properties of ink during printing.

Table 1. Dependence of reaction rate coefficient on reaction mixture composition

Gel:Dex-Ox Solution Ratio	Reaction Rate Coefficient (h ⁻¹)	Coefficient of Determination (1)	Gelation Point (min)
		Gel-B	
1:1	11.6	0.998	<1
2:1	8.3	0.990	2
3:1	10.6	0.986	2
		Gel-R	
1:1	11.1	0.993	<1
2:1	7.6	0.994	2
3:1	8.7	0.990	2.5
		Gel-C	
1:1	2.0	0.997	2
2:1	1.2	0.999	13
3:1	2.4	0.994	>30

We should note that in some cases, a short initial “lag” period was observed. This lag period can be attributed to the cross-linking reaction complexity. Despite this not being described by a first-order kinetic model, the overall fit was good, as is documented by the values of coefficients of determination and similar values of reaction rate coefficients of each type of Gel. As a result, even a simple model of the first order was able to acceptably describe the course of this reaction.

Another significant characteristic obtained in this measurement is the gelation point, which describes the solidification of the material and therefore can be found as the time when the crossing of storage and loss moduli occurs [51]. From that point, elastic forces begin to overcome the viscous ones, and the substance is defined as solid. The gelation point was not recorded in case of 1:1 polymer solution ratio for neither Gel-B nor Gel-R-based hydrogel (see Table 1) as the storage modulus is higher than the loss modulus; therefore, it is safe to assume that it is lower than 1 min, and gelation took place during the sample preparation. In case of Gel-C, the gelation point was detected after 2 min of reaction. When the proportion of Gel was increased, the gelation point increased as well to approximately 2 min. Curiously, no difference was detected between the Gel-B:Dex 2:1 and 3:1 solution ratios. However, Gel-R exhibits an additional 30 s increase in gelation time with each decrease of Dex-Ox content. Gel-C based gels exhibit the highest increase in gelation time. Despite this, all of the hydrogels solidify within 1 hour, which is rapid enough for their utilization in practice.

3.3. Rheology

Knowledge of hydrogels’ rheological behavior is of great importance in terms of printability and shape fidelity [52]. Cell viability can be ensured by minimizing the shear stress arising from the process [12]. A typical means of achieving this goal is to utilize a wider flow geometry [11]. However, this approach directly opposes precise positioning of the materials, which is the great advantage of 3D printing. Another way to reduce the shear stress during an ink flow is to reduce the viscosity [52]. However, during printing, a material with high viscosity and a significant difference between the loss and storage moduli is desirable due to the quickly achievable solid state. Other characteristics, such as brittleness of the extruded strand, also play an important role in the final appearance of the printed structure [42,52]. The above-mentioned requirements regarding the rheological behavior of gels indicate that the objectives of this work are to prepare a highly shear-thinning material with a fast sol–gel transition at various angular frequencies. For this

purpose, the rheological properties of fully cross-linked hydrogels were characterized in the region of increasing angular frequency, simulating 3D-printing conditions.

To this end, the linear viscoelastic region (LVE) on a fully formed gel-like structure was checked at 35 °C. Thus, strain sweep oscillatory measurements were performed with a constant angular frequency of 10 rad·s⁻¹ for Gel:Dex-Ox 1:1 and 3:1 hydrogels (see Supplementary Information Figure S2). The LVE region was identified in the range where modulus G' or G'' is independent of the applied deformation from 0.1% to 100%. Thus, 10% deformation was used for the following frequency sweep oscillatory measurements. It is clear that besides Gel-R:Dex-Ox 3:1 and Gel-B:Dex-Ox 3:1, the storage modulus, G' , is the significant one describing a gel-like state.

This fact is also followed in the case of performed frequency sweep oscillatory measurements describing loss and storage modulus dependence on printing speed expressed by angular frequency. As can be seen in Figure 2, a strong shear-thinning behavior of the prepared hydrogels is observed. In case of all Gel-C:Dex-Ox solutions, the highest viscosities are reached as well as gel-like structure. It is clear that Gel-R:Dex-Ox solutions reach the lowest viscosity values. Moreover, in case of Gel-R:Dex-Ox 2:1; 3:1, and Gel-B:Dex-Ox 3:1 when the gelation point is taken into account, the sol-like structure is observed when complex viscosity is lower than 0.3 Pa·s. This means that the angular frequency at which the gelation point occurs depends on both Gel origin and biopolymer ratio. It should be mentioned that reverse measurements (from 10 to 0.1 rad·s⁻¹) performed on the same sample achieved identical results as in the original measurements. Thus, any changes occurring in the material are reversible, even though such behavior is atypical in chemical hydrogels. Nevertheless, Khorsidi et al. [53] have found a growing number of amine-aldehyde cross-links to correlate with the increased shear-thinning character of hydrogels. Another research found that similar material compositions to the ones examined in the current study can be printed by microextrusion; therefore, a certain level of shear-thinning behavior can be assumed [54].

This described rheological characterization proves that the prepared hydrogels are suitable materials for 3D printing by microextrusion due to their shear flow and stability after stress relaxation. Based on experiments performed from prepared hydrogels composed of different gels and biopolymer ratios, it should be noted that these materials can be used in a variety of applications for 3D printing with specific rheological properties.

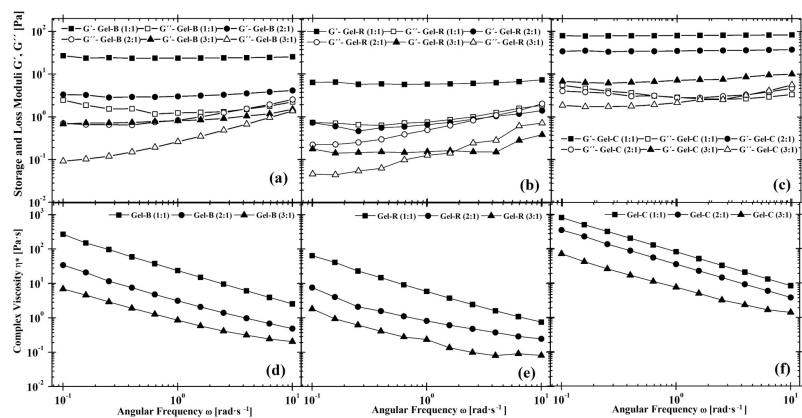


Figure 2. The angular frequency-dependent viscoelastic moduli (a–c) and complex viscosity (d–f) for Gel-based hydrogels: (a,d) Gel-B, (b,e) Gel-R, and (c,f) Gel-C for all examined Gel:Dex-Ox ratios.

3.4. 3D Printing

Printability of the materials was practically assessed in microextrusion printing experiments. Two contributions to printing precision were measured—die swell and shape

fidelity. Die swell is a parameter that affects the printing resolution, pore size, and layer height [14,55]. Several studies, both theoretical and experimental, have confirmed the significance of the phenomenon on the process of 3D printing [33,56–61]. Nevertheless, it is often omitted in the research of biopolymer based hydrogels as materials for microextrusion.

As is apparent from Table 2, all hydrogels examined in the current study experience a non-negligible die swell, reaching up to 3.3 times increase of the strand diameter. That is a clear indication of significant normal stress being built up in the material during shearing [14]. The die swell is notably lower in case of Gel-C:Dex-Ox 1:1 hydrogel. Some differences are found in the relative standard deviation (RSD) of die swell corresponding to different origins of Gel. The higher RSD suggests fluctuations in strand diameter, which are especially prominent in Gel-B-based materials and would consequently lead to lower printing precision. It can also indicate the phenomenon of over-gelation being present [42]. Based on this information, the highest printing precision is expected from Gel-C-based hydrogel. No significant difference caused by variation in Dex-Ox content was found, regardless of the Gel origin. It is possible that large fluctuations masked the influence of cross-linking agent amount on die swell.

The shape fidelity was characterized using the so-called printability (Pr) parameter, which was evaluated following a simple procedure described in [42]. This parameter reflects the precision of printing square-shaped pores. It is closely connected to the phenomenon of under- and over-gelation, and to a certain extend, it is able to describe the smoothness of the strand as well as hydrogel stability after removal of shear stress. The Pr values of most hydrogels are close to 1, as can be seen in Table 2, which encourages the possibility of using these materials for precise printing. Only Gel-B:Dex-Ox 3:1 exhibited insufficient mechanical strength of the strand, which caused the material to be completely fused and prevented the measurement. No significant difference in Pr with respect to neither Dex-Ox content nor Gel origin was observed.

Table 2. Printing characteristics of Gel-based hydrogels.

Gel:Dex-Ox Solution Ratio	Die Swell (1)	Relative Standard Deviation (RSD) of Die Swell (%)	Printability (Pr) (1)
Gel-B			
1:1	3.0	13	1.0 ± 0.2
2:1	3.2	11	1.0 ± 0.2
3:1	3.0	14	/
Gel-R			
1:1	2.9	10	0.90 ± 0.09
2:1	3.3	6	0.873 ± 0.009
3:1	3.2	10	0.90 ± 0.07
Gel-C			
1:1	2.4	7	1.0 ± 0.1
2:1	2.6	9	1.0 ± 0.2
3:1	2.7	8	0.92 ± 0.09

Moreover, the printing of 5 layers of material proved that hydrogels presented in the current study provide self-supporting structures, i.e., those that do not collapse due to their own weight, in the 3D printing process. These structures were further used in the study of printing-induced porosity and hydrogel inner porosity.

To investigate the shape and pore distribution in the printed scaffold, the selected sample (Gel-C:Dex-Ox 1:1) was analyzed using CT (Figure 3). Due to the limited resolution of the CT used—SkyScan 1174 (6–30 µm per voxel), a special printing model was created for these purposes (Figure 3a left). In addition, it was necessary to create a special closed box for the hydrogel to prevent it from drying out during a 60-min CT scan (Figure 3a right). Figure 3b,c compares the scaffold in the hydrated state and after freeze drying. A

comparison of these figures shows that the shape of the printed structure corresponds to the desired model both in the hydrated and dry state. The hydrated structure is larger than the freeze-dried structure and does not contain pores inside printed layers, detectable air bubbles, or other large defects. The printed hydrogel occupies 59% of the volume (299 mm^3) with a surface area of 722 mm^2 . After lyophilization, the volume of the printed structure decreases to 63 mm^3 (13% of space), while its surface increases to 1061 mm^2 due to the formation of open pores. The analyzed space was $11.1 \times 11.1 \times 4.1 \text{ mm}^3$ (505 mm^3). From X-ray adsorption images for two different angles (0° and 90°), it is clear that the printed material is accumulating in accordance with the printing model.

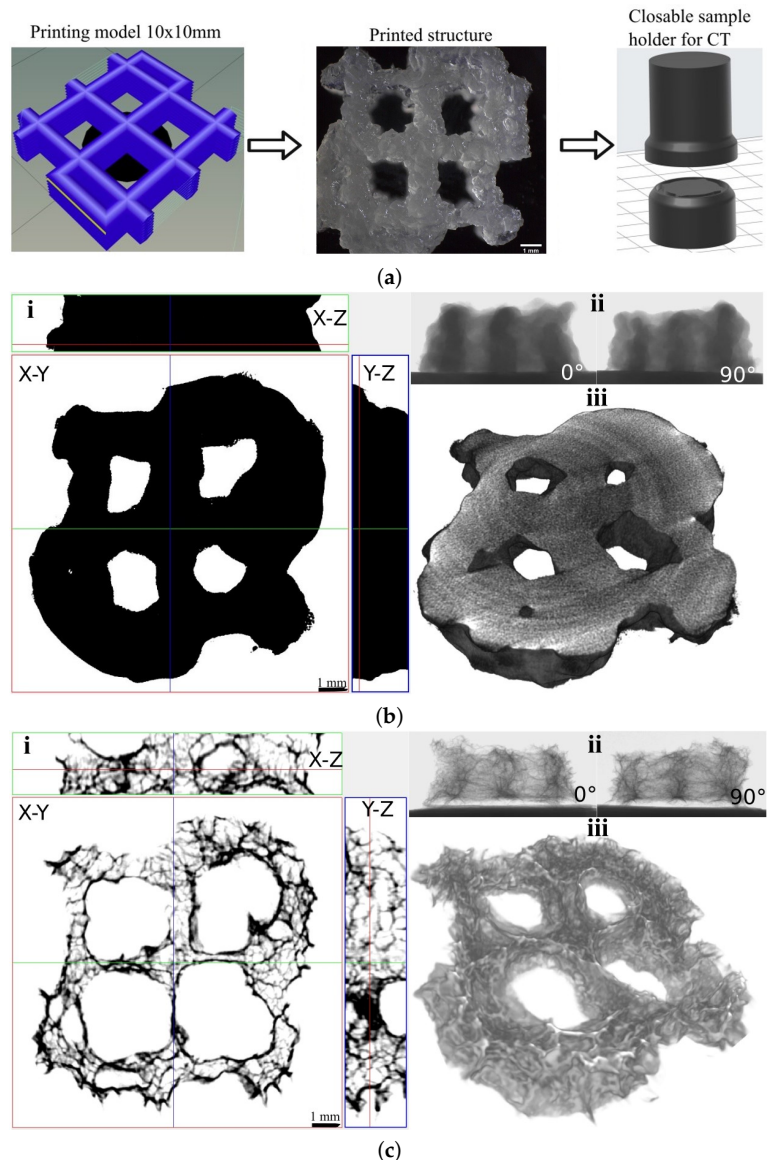


Figure 3. CT analysis of printed structures; (a) Scheme of sample preparation, (b) As-printed structure, (c) Lyophilized structure: i—2D cross-sections in respective planes, ii—X-ray adsorption for either 0° or 90° , and iii—3D model.

3.5. Swelling Tests

Swelling is defined as the amount of buffer or water bound into a hydrogel. It is considered to be a crucial characteristic of hydrogels, as it gives an initial view of their hydrophilicity and cross-linking density. In general, rigid networks lead to lower water uptake [62]. Moreover, the swelling characterization is useful in the hydrogel preparation procedure as an insight into the possibility of cell proliferation or to determine hydrogel stability over time. Figure 4 shows the equilibrium swelling of prepared hydrogels at different ratios of Gel and Dex-Ox. The only observed difference between used Gels is the speed of PBS uptake, being notably lower in the case of Gel-C in comparison. Meanwhile, both Gel-B and Gel-R displayed similar swelling behavior. These results could refer to different network rigidity. This assumption was supported by rheology results (see Figure 2). Statistical analysis of the swelling test results proved that the concentration of the cross-linking agent has a minimal impact on swelling, and the observed differences correspond to the measurement deviation. Thus, the mechanical characteristics and rheology of the prepared hydrogel can be tailored without any impact on swelling, which is advantageous in the case of the cell proliferation.

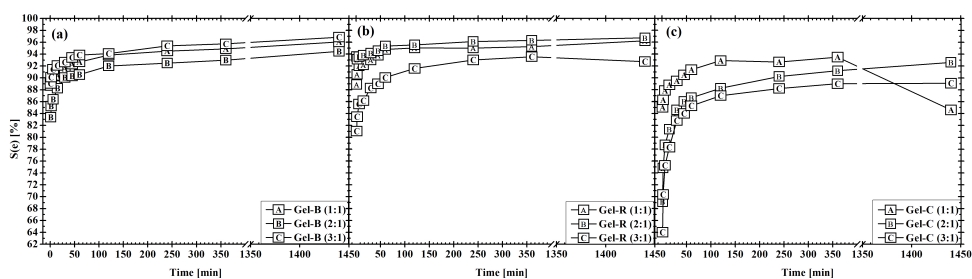


Figure 4. Swelling of Gel-based hydrogels: (a) Gel-B, (b) Gel-R, and (c) Gel-C.

3.6. Inner Porosity

SEM micrographs of the printed products after freeze drying revealed the highly porous inner structure of the materials. Table 3 presents the results of the average pore diameter in the cross-section. In addition, the relative pore area was determined in the cross-section in order to assess the porosity of the hydrogel. The pores are interconnected (see Supplementary Information Figure S2) and fall approximately in the range 50–100 μm in diameter [63]. The pore size remains practically constant regardless of both the Gel origin and the amount of Dex-Ox.

Table 3. Evaluation of pore size and porosity of hydrogels after shear strain and subsequent lyophilization.

Gel:Dex-Ox Solution Ratio	Average Pore Size (mm^2)	Relative Pore Area (%)
Gel-B		
1:1	0.014 ± 0.009	40–70
2:1	0.017 ± 0.005	45–80
3:1	0.020 ± 0.009	60–75
Gel-R		
1:1	0.017 ± 0.006	40–80
2:1	0.011 ± 0.003	35–65
3:1	0.009 ± 0.004	35–50
Gel-C		
1:1	0.010 ± 0.004	35–45
2:1	0.036 ± 0.008	45–50
3:1	0.04 ± 0.02	30–50

3.7. Cytotoxicity

Due to their natural origin, the chosen biopolymers—Gel and Dex—are generally characterized by low toxicity [26,64–66], which makes them especially advantageous for scaffold preparation. However, the presence of highly reactive aldehyde groups raises the concerns over the biocompatibility of Dex-Ox [66,67]. Additionally, the cytotoxicity of Dex-Ox has been observed to increase with the decrease of M_w [68]. In order to address this issue, the cytotoxicity of the here-prepared hydrogels was tested. Samples with the highest amount of potentially cytotoxic component, i.e., those with a solution ratio of 1:1, were chosen for the test. The results are presented in Figure 5. As can be seen, Gel-B and Gel-C were non-cytotoxic in a whole range of concentrations. A non-significant decrease in cell viability is observed in the case of Gel-R for a concentration of extract above 50%. However, the viability does not decrease below 70%, which is the limit of cytotoxicity potential. It can be concluded that all tested hydrogels do not express cytotoxicity potential. These results are highly encouraging in terms of using the proposed hydrogels, especially Gel-B and Gel-C-based ones, as bioinks for the preparation of scaffolds.

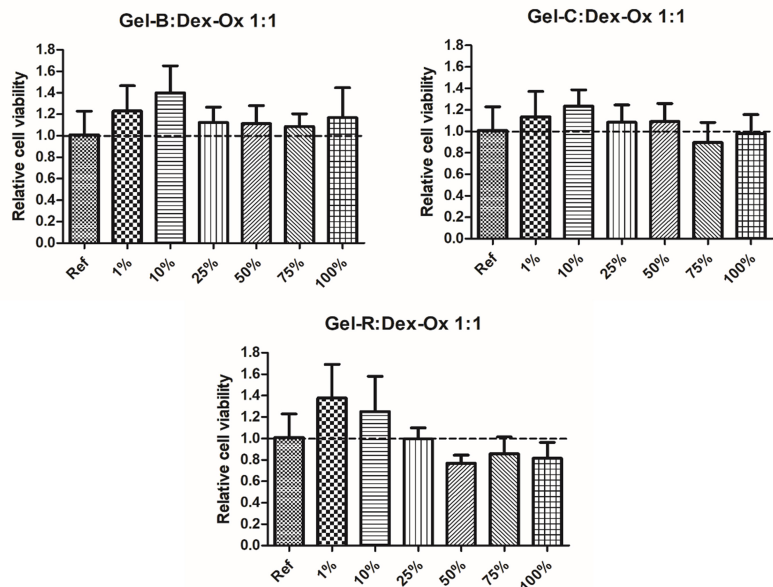


Figure 5. Cell viability determined by ATP assay performed on extracts from Gel:Dex-Ox 1:1 hydrogels.

3.8. Cell Distribution within 3D-Printed Structure Evaluation

The homogeneity of cell distribution within the structure of scaffolds is a critical parameter for their applicability. This parameter is not ideal in case of the standard procedure of cell seeding into the scaffolds (e.g., by forcing the cells through a scaffold by either internal pressure or external vacuum pressure). The direct printing of cells within the material allows overcoming this problem. Thus, the effect of microextrusion on mouse fibroblasts distribution was observed by the means of LSCM. As can be seen in Figure 6, 3D printing ensured a homogeneous distribution of cells within the printed material. In addition, the overlay (Figure 6) demonstrated that cell nuclei were located inside undisturbed cells; thus, fibroblasts were not destroyed during 3D printing. The results are promising in terms of considering the presented biopolymers-based hydrogels as bioinks.

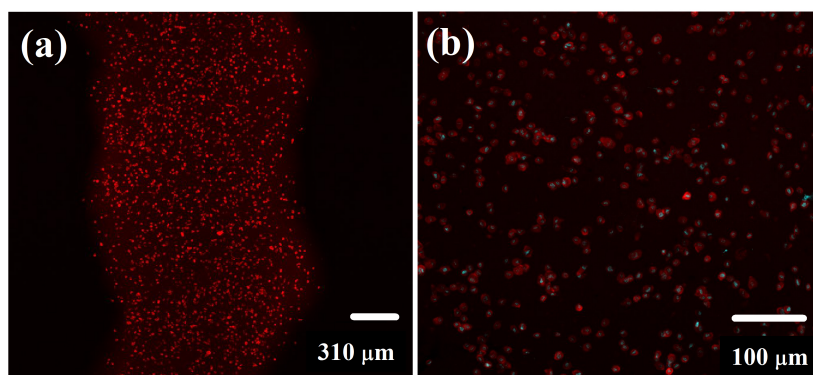


Figure 6. Microextruded Gel-B:Dex-Ox strand with incorporated mouse fibroblasts observed by the means of fluorescence confocal microscopy—(a) 4× magnification—image of cytoskeleton and (b) 10× magnification—overlay of cell nuclei and cytoskeleton images.

4. Conclusions

A series of hydrogels, which may potentially serve as bioinks, formed from Gel of different origin (bovine, rabbit, and chicken) cross-linked with various ratios of Dex-Ox were prepared by means of a simple and rapid method. Even though there are differences in Gel behavior depending on its origin, 3D-printing studies usually focus on bovine or porcine Gel, while research of rabbit and chicken Gel is rather scarce in this field. Study of the rheological behavior of the materials upon application of shear stress proved that the all investigated hydrogels were able to flow in shear, while they remain stable after stress relaxation and consequently are well suited for utilization in microextrusion. Additionally, die swell was significant, reaching a threefold increase in strand diameter in case of Gel-R and Gel-B samples. From the printing precision point of view, Gel-C was the most promising with the lowest die swell. Measurements confirmed that the complex viscosity of the hydrogels increased with the higher amount of cross-linking agent—Dex-Ox. In addition, rheology facilitated the study of reaction kinetics. This confirmed that the cross-linking reaction followed kinetics of the first order, and the gelation point was reached later as the amount of Dex-Ox solution decreased.

All the investigated hydrogels were able to form self-supporting structures in several layers, despite their various rheological properties. Moreover, the CT analysis confirmed that it is possible to produce constructs with continuous macroscopic pores throughout the structure via microextrusion processing of the hydrogels. In addition, the constructs remained stable even after freeze drying, and their highly porous inner structure was proved by means of CT and SEM measurements.

Optical imaging revealed that fluorescent-labeled mouse fibroblasts encapsulated within the polymeric matrix were of uniform distribution throughout the printed materials, and no cell disruption was observed. Finally, the printed constructs displayed no cytotoxicity in case of all tested materials. Thus, 3D-printable hydrogels with a potential to serve as bioinks have been successfully developed in the current study.

Supplementary Materials: The following are available at <https://www.mdpi.com/article/10.3390/polym1010391/s1>, Figure S1: ¹H NMR spektra of dextran (Dex) and dextran after oxidation (Dex-Ox), Figure S2: Linearity sweep for hydrogels with different amount of cross-linking agent, Figure S3: SEM micrograph of lyophilized hydrogels in cross section

Author Contributions: Conceptualization, L.M., E.A., L.V., J.P. and A.M. (Aleš Mráček); methodology, L.M., E.A., L.V., J.P., P.H., M.M., A.M. (Anotnín Minařík) and R.K.; validation, L.M., E.A., L.V., J.P., P.H., M.M., A.M. (Anotnín Minařík) and R.K.; formal analysis, L.M., E.A., L.V., J.P., P.H., M.K., A.M. (Anotnín Minařík) and R.K.; investigation, L.M., E.A., L.V., J.P., P.H., M.M., A.M. (Aleš Mráček) and

R.K.; writing—original draft preparation, L.M., J.P., E.A., P.H. and L.V.; writing—review and editing, L.M., J.P., E.A., L.V., A.M. (Aleš Mráček); visualization L.M., E.A., L.V., J.P., M.M., A.M. (Anotnín Minařík) and R.K.; supervision, A.M. (Aleš Mráček); project administration, A.M. (Aleš Mráček); funding acquisition, A.M. (Aleš Mráček). All authors have read and agreed to the published version of the manuscript.

Funding: The work of authors L.M., A.M. (Aleš Mráček), A.M. (Anotnín Minařík) and R.K. was financially supported by the Ministry of Education, Youth and Sports of the Czech republic—DKRVO (RP/CPS/2022/003). Author LV gratefully acknowledge the project OP RDE Junior Grants of TBU in Zlín, Reg. No. CZ.02.2.69/0.0/0.0/19_073/0016941. Authors EA and JP received financial supports from CEBIA-Tech Instrumentation (Project No. CZ.1.05/2.1.00/19.0376). Authors PH and MM thank the project funded by Czech Science Foundation (Project No. 20-28732S) and project funded by Ministry of Education, Youth and Sports of the Czech Republic – DKRVO (RP/CPS/2022/001).

Institutional Review Board Statement: Not applicable.

Informed Consent Statement: Not applicable.

Data Availability Statement: The data presented in this study are available on request from the corresponding author.

Conflicts of Interest: The authors declare no conflict of interest.

References

- Wei, L.; Jovina, T.; Wai, Y.; May, W. Proof-of-concept: 3D bioprinting of pigmented human skin constructs. *Biofabrication* **2018**, *10*, 1758–5090. [[CrossRef](#)]
- Billiet, T.; Vandenhoute, M.; Schelfhout, J.; Vlierberghe, S.V.; Dubruel, P. A review of trends and limitations in hydrogel-rapid prototyping for tissue engineering. *Biomaterials* **2012**, *33*, 6020–6041. [[CrossRef](#)] [[PubMed](#)]
- Gopinathan, J.; Noh, I. Recent trends in bioinks for 3D printing. *Biomater. Res.* **2018**, *22*, 11. [[CrossRef](#)] [[PubMed](#)]
- Ashammakhi, N.; Ahadian, S.; Xu, C.; Montazerian, H.; Ko, H.; Nasiri, R.; Barros, N.; Khademhosseini, A. Bioinks and bioprinting technologies to make heterogeneous and biomimetic tissue constructs. *Mater. Today Bio* **2019**, *1*, 100008. [[CrossRef](#)] [[PubMed](#)]
- Gungor-Ozkerim, P.; Inci, I.; Zhang, Y.; Khademhosseini, S.; Dokmeci, M. Bioinks for 3D bioprinting: An overview. *Biomater. Sci.* **2018**, *6*, 915–946. [[CrossRef](#)] [[PubMed](#)]
- Dorishetty, P.; Dutta, N.; Choudhury, N. Bioprintable tough hydrogels for tissue engineering applications. *Adv. Colloid Interface Sci.* **2020**, *281*, 102163. [[CrossRef](#)] [[PubMed](#)]
- Chimene, D.; Kaunas, R.; Gaharwar, A. Hydrogel Bioink Reinforcement for Additive Manufacturing: A Focused Review of Emerging Strategies. *Adv. Mater.* **2020**, *32*, 1902026–1902048. [[CrossRef](#)]
- Chung, S.H.; Son, S.; Min, J. The nanostructure effect on the adhesion and growth rates of epithelial cells with well-defined nanoporous alumina substrates. *Nanotechnology* **2010**, *21*, 125104. [[CrossRef](#)]
- Ermis, M.; Antmen, E.; Hasirci, V. Micro and Nanofabrication methods to control cell-substrate interactions and cell behavior: A review from the tissue engineering perspective. *Bioact. Mater.* **2018**, *3*, 355–369. [[CrossRef](#)]
- Buskermolen, A.; Suresh, H.; Shishvan, S.; Vigliotti, A.; DeSimone, A.; Kurniawan, N.; Bouten, C.; Deshpande, V. Entropic Forces Drive Cellular Contact Guidance. *Biophys. J.* **2019**, *116*, 1994–2008. [[CrossRef](#)]
- Smith, C.; Stone, A.; Parkhill, R.; Stewart, R.; Simpkins, M.; Kachurin, A.; Warren, W.; Williams, S. Three-Dimensional BioAssembly Tool for Generating Viable Tissue-Engineered Constructs. *Tissue Eng.* **2004**, *10*, 1566–1576. [[CrossRef](#)]
- Blaeser, A.; Campos, D.D.; Puster, U.; Richtering, W.; Stevens, M.; Fischer, H. Controlling Shear Stress in 3D Bioprinting is a Key Factor to Balance Printing Resolution and Stem Cell Integrity. *Adv. Healthc. Mater.* **2016**, *5*, 326–333. [[CrossRef](#)]
- Hölzl, K.; Lin, S.; Tytgat, L.; Vlierberghe, S.V.; Gu, L.; Ovsianikov, A. Bioink properties before, during and after 3D bioprinting. *Biofabrication* **2016**, *8*, 032002–032020. [[CrossRef](#)]
- Mackay, M. The importance of rheological behavior in the additive manufacturing technique material extrusion. *J. Rheol.* **2018**, *62*, 1549–1561. [[CrossRef](#)]
- Mori, A.D.; Fernández, M.P.; Blunn, G.; Tozzi, G.; Roldo, M. 3D Printing and Electrospinning of Composite Hydrogels for Cartilage and Bone Tissue Engineering. *Polymers* **2018**, *10*, 285. [[CrossRef](#)] [[PubMed](#)]
- Mazzocchi, A.; Devarasetty, M.; Huntwork, R.; Soker, S.; Skardal, A. Optimization of collagen type I-hyaluronan hybrid bioink for 3D bioprinted liver microenvironments. *Biofabrication* **2019**, *11*, 015003–015014. [[CrossRef](#)] [[PubMed](#)]
- Caló, E.; Khutoryanskiy, V. Biomedical applications of hydrogels: A review of patents and commercial products. *Eur. Polym. J.* **2015**, *65*, 252–267. [[CrossRef](#)]
- Gründelová, L.; Gregorova, A.; Mráček, A.; Vicha, R.; Smolka, P.; Minařík, A. Viscoelastic and mechanical properties of hyaluronan films and hydrogels modified by carbodiimide. *Carbohydr. Polym.* **2015**, *119*, 142–148. [[CrossRef](#)]
- Dababneh, A.; Ozbolat, I. Bioprinting Technology: A Current State-of-the-Art Review. *J. Manuf. Sci. Eng.* **2014**, *136*, 061016. [[CrossRef](#)]

20. Jungst, T.; Smolan, W.; Schacht, K.; Scheibel, T.; Groll, J. Strategies and Molecular Design Criteria for 3D Printable Hydrogels. *Chem. Rev.* **2016**, *116*, 1496–1539. [[CrossRef](#)]
21. Khunmanee, S.; Jeong, Y.; Park, H. Crosslinking method of hyaluronic-based hydrogel for biomedical applications. *J. Tissue Eng.* **2017**, *8*, 2041731417726464–2041731417726479. [[CrossRef](#)] [[PubMed](#)]
22. Musilová, L.; Mráček, A.; Kovalcik, A.; Smolka, P.; Minařík, A.; Humpolíček, P.; Vícha, R.; Ponížil, P. Hyaluronan hydrogels modified by glycinated Kraft lignin: Morphology, swelling, viscoelastic properties and biocompatibility. *Carbohydr. Polym.* **2018**, *181*, 394–403. [[CrossRef](#)] [[PubMed](#)]
23. Poldervaart, M.; Goversen, B.; de Ruijter, M.; Abbadessa, A.; Melchels, F.; Öner, F.; Dhert, W.; Vermonden, T.; Alblas, J.; Yamamoto, M. 3D bioprinting of methacrylated hyaluronic acid (MeHA) hydrogel with intrinsic osteogenicity. *PLoS ONE* **2017**, *12*, e0177628. [[CrossRef](#)]
24. Skardal, A.; Zhang, J.; McCoard, L.; Xu, X.; Oottamasathien, S.; Prestwich, G. Photocrosslinkable Hyaluronan-Gelatin Hydrogels for Two-Step Bioprinting. *Tissue Eng. Part A* **2010**, *16*, 2675–2685. [[CrossRef](#)] [[PubMed](#)]
25. Sakai, S.; Ohi, H.; Taya, M. Gelatin/Hyaluronic Acid Content in Hydrogels Obtained through Blue Light-Induced Gelation Affects Hydrogel Properties and Adipose Stem Cell Behaviors. *Biomolecules* **2019**, *9*, 342. [[CrossRef](#)]
26. Dobos, A.; Hoorick, J.V.; Steiger, W.; Gruber, P.; Markovic, M.; Andriotis, O.; Rohatschek, A.; Dubrue, P.; Thurner, P.; Vlierberghe, S.V.; et al. Thiol–Gelatin–Norbornene Bioink for Laser-Based High-Definition Bioprinting. *Adv. Healthc. Mater.* **2019**, *9*, 1900752–1900761. [[CrossRef](#)] [[PubMed](#)]
27. Noh, I.; Kim, N.; Tran, H.; Lee, J.; Lee, C. 3D printable hyaluronic acid-based hydrogel for its potential application as a bioink in tissue engineering. *Biomater. Res.* **2019**, *23*, 3. [[CrossRef](#)]
28. Mehrotra, S.; Melo, B.; Hirano, M.; Keung, W.; Li, R.; Mandal, B.; Shin, S. Nonmulberry Silk Based Ink for Fabricating Mechanically Robust Cardiac Patches and Endothelialized Myocardium-on-a-Chip Application. *Adv. Funct. Mater.* **2020**, *30*, 1907436. [[CrossRef](#)] [[PubMed](#)]
29. Petta, D.; Armiento, A.; Grijpma, D.; Alini, M.; Eglín, D.; D’Este, M. 3D bioprinting of a hyaluronan bioink through enzymatic-and visible light-crosslinking. *Biofabrication* **2018**, *10*, 044104–044114. [[CrossRef](#)] [[PubMed](#)]
30. Kajave, N.; Schmitt, T.; Nguyen, T.U.; Kishore, V. Dual crosslinking strategy to generate mechanically viable cell-laden printable constructs using methacrylated collagen bioinks. *Mater. Sci. Eng. C* **2020**, *107*, 110290–110301. [[CrossRef](#)]
31. Yu, J.H.; Fridrikh, S.V.; Rutledge, G.C. The role of elasticity in the formation of electrospun fibers. *Polymer* **2006**, *47*, 4789–4797. [[CrossRef](#)]
32. Angel Martinez-Ortiz, M.; Delia Hernandez-Fuentes, A.; Pimentel-Gonzalez, D.J.; Campos-Montiel, R.G.; Vargas-Torres, A.; Aguirre-Alvarez, G. Extraction and characterization of collagen from rabbit skin: partial characterization. *CYTA-J. Food* **2015**, *13*, 253–258. [[CrossRef](#)]
33. Yousefi, A.M.; Smucker, B.; Naber, A.; Wyrick, C.; Shaw, C.; Bennett, K.; Szekely, S.; Focke, C.; Wood, K. Controlling the extrudate swell in melt extrusion additive manufacturing of 3D scaffolds: A designed experiment. *J. Biomater. Sci.* **2017**, *29*, 195–216. [[CrossRef](#)]
34. Tanner, R. A theory of die-swell. *J. Polym. Sci. Part A-2 Polym. Phys.* **1970**, *8*, 2067–2078. [[CrossRef](#)]
35. Emmermacher, J.; Spura, D.; Czioommer, J.; Kilian, D.; Wollborn, T.; Fritsching, U.; Steingroewer, J.; Walther, T.; Gelinsky, M.; Lode, A. Engineering considerations on extrusion-based bioprinting: interactions of material behavior, mechanical forces and cells in the printing needle. *Biofabrication* **2020**, *12*, 025022. [[CrossRef](#)] [[PubMed](#)]
36. Ning, L.; Yang, B.; Mohabatpour, F.; Betancourt, N.; Sarker, M.; Papagerakis, P.; Chen, X. Process-induced cell damage: Pneumatic versus screw-driven bioprinting. *Biofabrication* **2020**, *12*, 025011. [[CrossRef](#)] [[PubMed](#)]
37. Mokrejš, P.; Gál, R.; Mrázek, P. Biotechnology-Based Production of Food Gelatine from Poultry by-Products. Patent number: CZ 307665, 16 May 2019.
38. Mokrejš, P.; Mrázek, P.; Robert, R.G.; Pavlačková, J. Biotechnological Preparation of Gelatines from Chicken Feet. *Polymers* **2019**, *11*, 1060. [[CrossRef](#)]
39. Gál, R.; Mokrejš, P.; Mrázek, P.; Pavlačková, J.; Janáčková, D.; Orsavová, J. Chicken Heads as a Promising By-Product for Preparation of Food Gelatins. *Molecules* **2020**, *25*, 494. [[CrossRef](#)]
40. Maia, J.; Carvalho, R.; Coelho, J.; Simoes, P.; Gil, M. Insight on the Periodate Oxidation of Dextran and Its Structural Vicissitudes. *Polymer* **2011**, *52*, 258–265. [[CrossRef](#)]
41. Zhao, H.; Heindel, N. Determination of Degree of Substitution of Formyl Groups in Polyaldehyde Dextran by the Hydroxylamine Hydrochloride Method. *Pharm. Res.* **1991**, *8*, 400–402. [[CrossRef](#)]
42. Ouyang, L.; Yao, R.; Zhao, Y.; Sun, W. Effect of bioink properties on printability and cell viability for 3D bioplotting of embryonic stem cells. *Biofabrication* **2016**, *8*, 035020–035033. [[CrossRef](#)] [[PubMed](#)]
43. Chattopadhyay, S.; Raines, R. Collagen-based biomaterials for wound healing. *Biopolymers* **2014**, *8*, 821–830. [[CrossRef](#)] [[PubMed](#)]
44. Eisenbarth, E. Biomaterials for Tissue Engineering. *Adv. Eng. Mater.* **2007**, *9*, 1051–1060. [[CrossRef](#)]
45. Young, A.T.; White, O.C.; Daniele, M.A. Rheological Properties of Coordinated Physical Gelation and Chemical Crosslinking in Gelatin Methacryloyl (GelMA) Hydrogels. *Macromol. Biosci.* **2020**, *20*, 2000183. [[CrossRef](#)] [[PubMed](#)]
46. Draye, J.P.; Delaey, B.; de Voorde, A.V.; Bulcke, A.V.D.; Reu, B.D.; Schacht, E. In vitro and in vivo biocompatibility of dextran dialdehyde cross-linked gelatin hydrogel films. *Biomaterials* **1998**, *19*, 1677–1687. [[CrossRef](#)]

47. Balakrishnan, B.; Jayakrishnan, A. Self-cross-linking biopolymers as injectable in situ forming biodegradable scaffolds. *Biomaterials* **2005**, *26*, 3941–3951. [[CrossRef](#)]
48. Kristiansen, K.; Potthast, A.; Christensen, B. Periodate oxidation of polysaccharides for modification of chemical and physical properties. *Carbohydr. Res.* **2010**, *345*, 1264–1271. [[CrossRef](#)] [[PubMed](#)]
49. Liu, Z.; Li, Y.; Li, W.; Lian, W.; Kemell, M.; Hietala, S.; Figueiredo, P.; Li, L.; Mäkilä, E.; Ma, M.; et al. Close-loop dynamic nanohybrids on collagen-ark with in situ gelling transformation capability for biomimetic stage-specific diabetic wound healing. *Mater. Horiz.* **2019**, *6*, 385–393. [[CrossRef](#)]
50. Nonsuwan, P.; Matsugami, A.; Hayashi, F.; Hyon, S.H.; Matsumura, K. Controlling the degradation of an oxidized dextran-based hydrogel independent of the mechanical properties. *Carbohydr. Polym.* **2019**, *204*, 131–141. [[CrossRef](#)]
51. Winter, H. Chapter Physical and Chemical Gelation. In *Encyclopedia of Materials: Science and Technology*; Elsevier: Amsterdam, The Netherlands, 2001.
52. Wu, D.; Yu, Y.; Tan, J.; Huang, L.; Luo, B.; Lu, L.; Zhou, C. 3D bioprinting of gellan gum and poly (ethylene glycol) diacrylate based hydrogels to produce human-scale constructs with high-fidelity. *Mater. Des.* **2018**, *160*, 486–495. [[CrossRef](#)]
53. Khorshidi, S.; Karkhaneh, A.; Bonakdar, S.; Omidian, M. High-strength functionalized pectin/fibroin hydrogel with tunable properties: A structure–property relationship study. *J. Appl. Polym. Sci.* **2019**, *137*, 48859–48872. [[CrossRef](#)]
54. Zehnder, T.; Freund, T.; Demir, M.; Detsch, R.; Boccaccini, A. Fabrication of Cell-Loaded Two-Phase 3D Constructs for Tissue Engineering. *Materials* **2016**, *9*, 887. [[CrossRef](#)]
55. McIlroy, C.; Olmsted, P. Deformation of an amorphous polymer during the fused-filament-fabrication method for additive manufacturing. *J. Rheol.* **2017**, *61*, 379–397. [[CrossRef](#)]
56. Comminal, R.; Serdeczny, M.; Pedersen, D.; Spangenberg, J. Numerical modeling of the strand deposition flow in extrusion-based additive manufacturing. *Addit. Manuf.* **2018**, *20*, 68–76. [[CrossRef](#)]
57. Serdeczny, M.; Comminal, R.; Pedersen, D.; Spangenberg, J. Experimental validation of a numerical model for the strand shape in material extrusion additive manufacturing. *Addit. Manuf.* **2018**, *24*, 145–153. [[CrossRef](#)]
58. Xia, H.; Lu, J.; Tryggvason, G. A numerical study of the effect of viscoelastic stresses in fused filament fabrication. *Comput. Methods Appl. Mech. Eng.* **2019**, *346*, 242–259. [[CrossRef](#)]
59. Hebda, M.; McIlroy, C.; Whiteside, B.; Caton-Rose, F.; Coates, P. A method for predicting geometric characteristics of polymer deposition during fused-filament-fabrication. *Addit. Manuf.* **2019**, *27*, 99–108. [[CrossRef](#)]
60. Coogan, T.; Kazmer, D. Modeling of interlayer contact and contact pressure during fused filament fabrication. *J. Rheol.* **2019**, *63*, 655–672. [[CrossRef](#)]
61. Gopi, S.; Kontopoulou, M. Investigation of thermoplastic melt flow and dimensionless groups in 3D bioplotting. *Rheol. Acta* **2020**, *59*, 83–93. [[CrossRef](#)]
62. Ahmed, E. Hydrogel: Preparation, characterization, and applications. *J. Adv. Res.* **2015**, *6*, 105–121. [[CrossRef](#)]
63. Trautmann, A.; Rütth, M.; Lemke, H.D.; Walther, T.; Hellmann, R. Two-photon polymerization based large scaffolds for adhesion and proliferation studies of human primary fibroblasts. *Opt. Laser Technol.* **2018**, *106*, 474–480. [[CrossRef](#)]
64. Choksakulnimitr, S.; Masuda, S.; Tokuda, H.; Takakura, Y.; Hashida, M. In vitro cytotoxicity of macromolecules in different cell culture systems. *J. Control. Release* **1995**, *34*, 233–241. [[CrossRef](#)]
65. Groot, C.D.; Luyn, M.V.; Dijk-Wolthuis, W.V.; Cadee, J.; Plantinga, J.; Otter, W.D.; Hennink, W. In vitro biocompatibility of biodegradable dextran-based hydrogels tested with human fibroblasts. *Biomaterials* **2001**, *22*, 1197–1203. [[CrossRef](#)]
66. Poursamar, S.; Hatami, J.; Lehner, A.; da Silva, C.; Ferreira, F.; Antunes, A. Gelatin porous scaffolds fabricated using a modified gas foaming technique: Characterisation and cytotoxicity assessment. *Mater. Sci. Eng. C* **2015**, *48*, 63–70. [[CrossRef](#)] [[PubMed](#)]
67. Pronina, E.; Vorotnikov, Y.; Pozmogova, T.; Solovieva, A.; Miroshnichenko, S.; Plyusnin, P.; Pishchur, D.; Eltsov, I.; Edeleva, M.; Efremova, M.S.O. No Catalyst Added Hydrogen Peroxide Oxidation of Dextran: An Environmentally Friendly Route to Multifunctional Polymers. *ACS Sustain. Chem. Eng.* **2020**, *8*, 5371–5379. [[CrossRef](#)]
68. Artzi, N.; Shazly, T.; Crespo, C.; Ramos, A.; Chenault, H.; Edelman, E. Characterization of Star Adhesive Sealants Based on PEG/Dextran Hydrogels. *Macromol. Biosci.* **2009**, *9*, 754–765. [[CrossRef](#)]



Article

Formulation of Magneto-Responsive Hydrogels from Dually Cross-Linked Polysaccharides: Synthesis, Tuning and Evaluation of Rheological Properties

Lenka Vítková¹, Lenka Musilová^{1,2,*} , Eva Achbergerová³, Roman Kolařík², Miroslav Mrlík² ,
Kateřina Korpasová¹, Leona Mahelová², Zdenka Capáková² and Aleš Mráček^{1,2,*}

- ¹ Department of Physics and Materials Engineering, Faculty of Technology, Tomas Bata University in Zlin, Vavrečkova 275, 760 01 Zlin, Czech Republic
² Centre of Polymer Systems, Tomas Bata University in Zlin, tř. Tomáše Bati 5678, 760 01 Zlin, Czech Republic
³ CEBIA-Tech, Faculty of Applied Informatics, Tomas Bata University in Zlin, Nad Stráněmi 4511, 760 05 Zlin, Czech Republic
* Correspondence: lmusilova@utb.cz (L.M.); mracek@utb.cz (A.M.)

Abstract: Smart hydrogels based on natural polymers present an opportunity to fabricate responsive scaffolds that provide an immediate and reversible reaction to a given stimulus. Modulation of mechanical characteristics is especially interesting in myocyte cultivation, and can be achieved by mechanically controlled stiffening. Here, hyaluronan hydrogels with carbonyl iron particles as a magnetic filler are prepared in a low-toxicity process. Desired mechanical behaviour is achieved using a combination of two cross-linking routes—dynamic Schiff base linkages and ionic cross-linking. We found that gelation time is greatly affected by polymer chain conformation. This factor can surpass the influence of the number of reactive sites, shortening gelation from 5 h to 20 min. Ionic cross-linking efficiency increased with the number of carboxyl groups and led to the storage modulus reaching 10^3 Pa compared to 10^1 Pa– 10^2 Pa for gels cross-linked with only Schiff bases. Furthermore, the ability of magnetic particles to induce significant stiffening of the hydrogel through the magnetorheological effect is confirmed, as a 10^3 -times higher storage modulus is achieved in an external magnetic field of $842 \text{ kA} \cdot \text{m}^{-1}$. Finally, cytotoxicity testing confirms the ability to produce hydrogels that provide over 75% relative cell viability. Therefore, dual cross-linked hyaluronan-based magneto-responsive hydrogels present a potential material for on-demand mechanically tunable scaffolds usable in myocyte cultivation.

Keywords: hyaluronan; smart hydrogels; magnetorheology; Schiff base; hydrodynamic radius; tissue engineering



Citation: Vítková, L.; Musilová, L.; Achbergerová, E.; Kolařík, R.; Mrlík, M.; Korpasová, K.; Mahelová, L.; Capáková, Z.; Mráček, A.

Formulation of Magneto-Responsive Hydrogels from Dually Cross-Linked Polysaccharides: Synthesis, Tuning and Evaluation of Rheological Properties. *Int. J. Mol. Sci.* **2022**, *23*, 9633. <https://doi.org/10.3390/ijms23179633>

Academic Editor: Yi Cao

Received: 30 July 2022

Accepted: 23 August 2022

Published: 25 August 2022

Publisher's Note: MDPI stays neutral with regard to jurisdictional claims in published maps and institutional affiliations.



Copyright: © 2022 by the authors. Licensee MDPI, Basel, Switzerland. This article is an open access article distributed under the terms and conditions of the Creative Commons Attribution (CC BY) license (<https://creativecommons.org/licenses/by/4.0/>).

1. Introduction

Hydrogels, i.e., 3D cross-linked, high-water-content networks, have been used in many biomedical applications [1], e.g., fabrication of scaffolds for cell cultivation [2] and tissue engineering [3], drug delivery [4], and wound dressing [5], as well as industrial applications such as soft electronics [6], water treatment [7,8], food applications [9,10], etc. Each of these applications requires a tailored hydrogel with desired characteristics. Basic properties of 3D networks are given by their chemistry as well as the incorporation of other components. Tissue engineering application in particular require close resemblance to native tissue in terms of morphology, as well as functionality, which often includes sudden and reversible changes of properties. In the case of smart hydrogels, their composition enables them to respond to external stimuli (pH, ionic strength, temperature, or electric or magnetic fields), and thus their properties can be advantageously dynamically changed. Namely, magnetorheological (MR) materials can rapidly and reversibly alter the mechanical properties of hydrogels under a magnetic field due to the magnetorheological effect (MRE) [11].

MRE refers to a highly non-linear mechanical response of a material to the presence of an external magnetic field. This is commonly achieved in multi-phase systems containing magnetically active filler (e.g., iron oxide-based nanoparticles Fe_3O_4 (magnetite) or $\gamma\text{-Fe}_2\text{O}_3$ (maghemite) [12]; superparamagnetic iron-oxide particles (SPIONs) [13]; or CoFe_2O_4 [14]) dispersed in a non-magnetic matrix [15]. Iron-based magnetic fillers are advantageous in biological applications due to their degradability in vivo [16] through a biotransformation mechanism whereby the magnetic material is converted into nontoxic iron species within acidic intracellular lysosomes [17]. Further, carbonyl iron particles have been found to be nontoxic to living cells [18,19], and their hydrogels based on Poly(2-oxazolines) show very promising magneto-responsive and noncytotoxic behaviour [11]. Applying an external magnetic field induces magnetic dipoles in the filler particles, causing the particles to be in order, effectively forming a network and thus leading to material stiffening [20]. This allows on-demand reversible modulation of mechanical properties. The magnitude of MRE is given by the magnetization saturation and the volume fraction of the magnetic filler, and the viscous dissipation of carrier medium [15,21]. Due to viscosity restrictions, MRE is generally greater in liquid carrier media [22]. Nevertheless, significant stiffening has been achieved in solid matrices such as hydrogel [23–25] as well. Furthermore, it has been shown that complex rheological tuning of the carrier medium, specifically its yield stress, may produce a solid system with virtually unaffected MR efficiency [26]. In terms of life sciences and tissue engineering, this can be exploited for arterial embolization in cancer treatment [27,28] or mechanical stimulation of cells via an external stimulus [29,30].

Cross-linked hydrogel matrix can be made from both synthetic and natural polymers. In most cases, synthetic polymers present a challenge in terms of biological response and biodegradability, making them less favourable in biomedical applications despite their possibility to be precisely tailored and thus achieve high reproducibility [31]. Natural polymers, on the other hand, are not cytotoxic and are mostly good candidates for cell adhesion and proliferation [32]. Several examples of naturally derived polymers used as the matrix material for MR hydrogels can be found in the literature, including proteins—gelatin [33–35], artificial polypeptides [36], polysaccharides—agarose [37,38], alginate [22,24,39–41], and carrageenan [38,42,43].

Hyaluronan (HA), a linear glycosaminoglycan (GAG) composed of D-glucuronic acid and N-acetyl-D-glucosamine linked by alternating $\beta(1\rightarrow3)$ and $\beta(1\rightarrow4)$ glycosidic bonds, is an excellent candidate for hydrogel formation. It is also the most abundant GAG occurring in the extracellular matrix (ECM). As such, it is largely responsible for the ECM's physical properties and for modulating cellular behaviour [44]. Due to relatively available reactive functional groups (hydroxyl, carboxyl), HA is often chemically modified to allow hydrogel formation. Common approaches to cross-linking include methacrylation [45–47] or tyramine modification [48] followed by photocross-linking. Alternatively, thiol modification combined with enzymatic or chemical cross-linking [49–51] as well as amination [52] have been described.

However, the aforementioned modifications lead to non-reversible covalent cross-linking, which limits the possibility for further shape alterations. Dynamic cross-linking, such as Schiff base formation, is a convenient means to obtain pliable hydrogels exhibiting yield stress [53]. Such an approach, combined with photocross-linking, was used, e.g., by Wang et al., 2018 to obtain a non-cytotoxic hydrogel designed for scaffold fabrication [54].

HA- and iron-based particle composites present great potential in a wide variety of bioapplications. Numerous studies on magnetically responsive HA-based hydrogels can be found in the literature, describing materials suitable for magnetic heating [55,56], magnetic resonance imaging contrast agents [57], magnetomechanical neuromodulation [58], and controlled drug release [59]. In terms of MR hydrogels, Tran et al., 2021 reported collagen-HA hydrogels with added carbonyl iron particles (CIPs) to significantly alter the biological response through MRE [60]. Furthermore, it has been demonstrated that self-healing printable gels can show macroscopic and reversible change in dimensions in the presence of a magnetic field and thus may be potentially useful in 4D printing [61]. A similar

phenomenon was observed in dynamically cross-linked self-healing ferrogel containing SPIONs [62]. Moreover, the presence of iron particles enhanced cell proliferation [61].

The literature review listed above presents several hypotheses for next steps in MR hydrogels for bioapplications:

1. The use of dynamic cross-linking is more favourable compared to non-reversible covalent cross-linking, as it provides pliable materials that can exhibit yield stress [53,63]. Such behaviour is advantageous in terms of materials processing, namely injectability and extrudability, but also promises a possibility to achieve significant MRE [26,64].
2. Iron-based magnetic fillers are non-toxic and biodegradable on account of biotransformation mechanisms [16,17]. The use of CIPs provides more-pronounced MRE compared to iron oxide microparticles or SPIONs due to higher saturation magnetization values [20].
3. Purely HA-based hydrogel matrices are rather scarce in the literature even though they may find use in tissue engineering, scaffold fabrication, and on-demand cell stimulation through an external impulse [22].

Nevertheless, natural polymer-based magneto-responsive hydrogels are seldom reported in the literature. Furthermore, their use is mainly focused on magnetic heating [65] or magnetic guidance in targeted drug delivery systems [66] rather than MR-induced changes to hydrogel mechanics. Even when MRE is described in a natural-based hydrogel, the matrix does not purely utilize polysaccharides [60]. Therefore, our study can bring benefits to the field of magnetorheology by extending the utilizable materials to natural-based polymers, and thus find use in bioapplications.

In the present study, we describe a straightforward method for preparing a dynamically cross-linked MR hydrogel based on modified HA and CIPs. In order to obtain HA functionalised with adipic acid dihydrazide (ADH), traditional carbodiimide chemistry and 4-(4,6-Dimethoxy-1,3,5-triazin-2-yl)-4-methylmorpholinium chloride (DMTMM) mediated reactions are used. This ADH-modified HA is used as a precursor for Schiff base-linked hydrogels in combination with polysaccharide-based polyaldehydes. The dynamic character of cross-links provides a soft, shear-thinning matrix for preparation of MR hydrogel, which supposedly could lead to diminishing viscous restriction of the MR effect [26]. As the magnetically responsive filler, commercially available CIPs are used. The mechanical performance of the hydrogel is reversibly enhanced via an external magnetic field, as well as permanently by application of dual cross-linking. Finally, cytocompatibility is tested.

2. Results and Discussion

2.1. Polysaccharide Modification

Hydrogel preparation was preceded by two different biopolymer (HA and dextran) modifications. The first approach was based on covalent bonding of ADH to HA chains via two different activators of HA carboxyl groups. Initially, HA derivatization was carried out by the well-established carbodiimide-based activation of the HA carboxyl group using 1-ethyl-3-(3-dimethylaminopropyl)carbodiimide hydrochloride (EDC) and 1-hydroxybenzotriazole hydrate (HOBt) [67], as illustrated in Figure 1. Unfortunately, the reaction is strictly pH-dependent and also suffers from the creation of side products. Namely, bonding of N-acylurea to HA carboxyl groups makes the removal of the byproduct quite difficult [49]. Therefore, in order to synthesize ADH-modified HA (HA-ADH), an alternative coupling agent, DMTMM, was employed (Figure 1). Subsequently, the carboxyl group activators used, EDC and DMTMM, were compared and evaluated. Using either EDC or DMTMM, the desired product (HA-ADH) was successfully synthesized. Further, HA-ADH with different degrees of substitution (DS) was obtained depending on the activating agents. EDC provided HA-ADH with higher DS (22%) compared to DMTMM (DS 12%). Regarding reactions mediated by DMTMM, it was not possible to produce HA-ADH with higher DS because increasing reactant molar ratios led to undesirable in situ cross-linking of HA-ADH. On the other hand, the advantages of DMTMM include the reaction not being so strongly pH-dependent, and providing the product without

side products, as was observed when using EDC. Despite the different DS, all prepared HA-ADHs were successfully employed for hydrogel preparation.

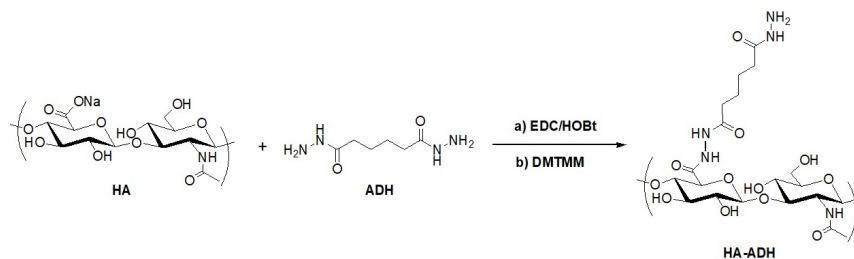


Figure 1. Synthesis of HA modified with ADH using (a) EDC/HOBt and (b) DMTMM.

The second type of polysaccharide modification consisted of HA (Figure 2) and dextran oxidation. For this purpose, reactions mediated by NaIO_4 were carried out [67,68], leading to polysaccharide polyaldehydes. Oxidized HA (HA-OX) and oxidized dextran (DEX-OX) were prepared with different degrees of oxidation (DO)—35 and 62 for HA-OX, and 49 for DEX-OX. The molecular weight of the polymers decreased to 7.5 kDa–9.0 kDa due to oxidation. The presence of formed carbonyl groups in biopolymer chains further enabled utilisation of HA-OX and DEX-OX for hydrogel formation after reaction with HA-ADH.

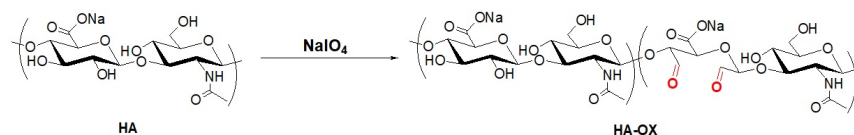


Figure 2. Oxidation of HA.

2.2. Schiff Base Formation-Induced Gelation

The hydrogels were obtained when HA-ADH was chemically cross-linked by polysaccharide polyaldehydes (Figure 3), resulting in Schiff base formation between aldehyde and amino groups present in polymer chains [69]. Table 1 gives the specifications of the hydrogel compositions. Hydrogel formation was evident by the significant increase in viscosity and mechanical stability over time. These changes in rheology were used to quantify the reaction rate by determination of gelation time.

In order to examine the effect of DO on gelation time, three polysaccharide polyaldehydes with different DO (i.e., HA-OX with DO 35 or 62 and DEX-OX with DO 49) were compared (Figure 4). The molecular weights of both HA-OX and DEX-OX were kept in the same range, so that DO could be followed as an independent factor. It is evident from Figure 4A that in HA-OX, the gelation time directly corresponds to differences in DO, i.e., the number of reactive sites available. However, when comparing HA-OX with DO 62 to DEX-OX with DO 49, the shortest gelation time was observed in DEX-OX, despite its lower DO. Therefore, the gelation time is not dependent only on the number of aldehyde groups that participate in gelation, but may be also influenced by biopolymer properties such as polymer chain conformation. This quality is reflected in polymers' hydrodynamic size, which can be characterized by the z-average diameters of the polymer coils in a solution [70]. Observed variation of the z-average diameter can be seen in Figure 4B. Based on this, it can be stated that the mean diameter of DEX-OX with DO 49 shows a very small value (4.36 ± 0.44 nm), and the resultant particle size distribution is narrow and monomodal, indicating the occurrence of one population of particles. On the other hand, the particle size distributions for both HA-OX samples are bimodal, which means the samples contain two different particle-size populations. HA-OX with DO 35 has a rather broad bimodal distribution that contains two particle-size fractions (2.80 ± 0.02 nm and 360 ± 50 nm).

HA-OX with DO 62 has a rather narrow bimodal distribution that contain two size fractions (2.6 ± 0.4 nm and 280 ± 10 nm). This also confirms the generally accepted finding that HA in salt solutions has an expanded random-coil conformation, as would be expected for a flexible polyelectrolyte [71]. Moreover, the size of a polymer coil is proportional to its diffusion coefficient; thus, a smaller hydrodynamic radius benefits from fast diffusion through the sample [72]. Therefore, smaller particles of DEX-OX DO 49 move through the solvent more easily and accelerate the formation of Schiff bases [73]. The results indicate the complexity of chemical reactions among polymer chains and highlight the necessity of thorough evaluation of the macromolecules in order to accurately predict the outcomes.

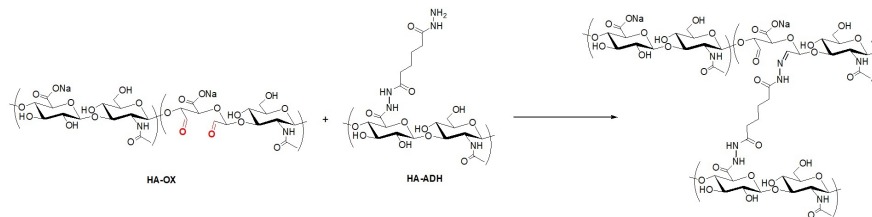


Figure 3. Schiff base formation between HA-OX and HA-ADH.

Table 1. List of prepared hydrogel samples and their compositions as indicated by the checkmarks at respective components.

Sample Name	HA-ADH (EDC)	HA-ADH (DMTMM)	HA-OX DO 35	HA-OX DO 62	DEX-OX DO 49
gel A	✓		✓		
gel B	✓			✓	
gel C	✓				
gel D		✓	✓		✓
gel E		✓		✓	
gel F		✓			✓

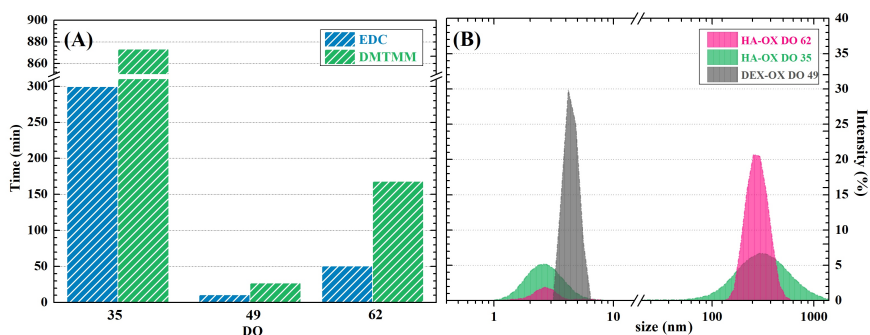


Figure 4. (A) Gelation times of HA gel formulations; (B) Hydrodynamic radius of oxidized polysaccharides.

2.3. Dual Cross-Linking of Hydrogels

A Schiff base as a dynamic bond can be easily depleted in some environments based on pH, ionic strength, and/or the presence of competitive agents capable of forming the same type of bonds. Thus, in order to achieve sufficient stability of the obtained hydrogels, ionic cross-linking with Fe^{3+} ions was additionally chosen as a simple and non-toxic option. Figure 5 shows a schematic of Schiff-base and dual cross-linked hydrogel preparation with the optional addition of a magnetoresponsive filler. Ionic bath treatment led to significant

improvement of hydrogel structural integrity in cultivation conditions from less than 12 h to several days. We observed that hydrogels containing HA-OX (gels A, B, D, and E) were more stable (lasting 5 days in simulated cultivation conditions) compared to DEX-OX containing gels (C and F; lasting 2 days in simulated cultivation conditions) in the presence of Fe^{3+} . Unlike dextran, HA contains free carboxyl groups in its structure, even in the oxidized form. As ionic cross-linking is fundamentally related to the reaction of multivalent ions and polar, typically carboxyl groups, it is reasonable to expect a more-pronounced effect in a system rich in the desired groups. A study conducted by Zellermann et al., 2013 [74] confirmed a significant effect of barium ions on behaviour of HA, while dextran, as an uncharged polysaccharide, was intact with the Ba^{2+} presence. Analogous behaviour can be expected in the presence of Fe^{3+} ions. This is also reflected in the possibility of using Fe^{3+} ions for obtaining HA-based hydrogels [75].

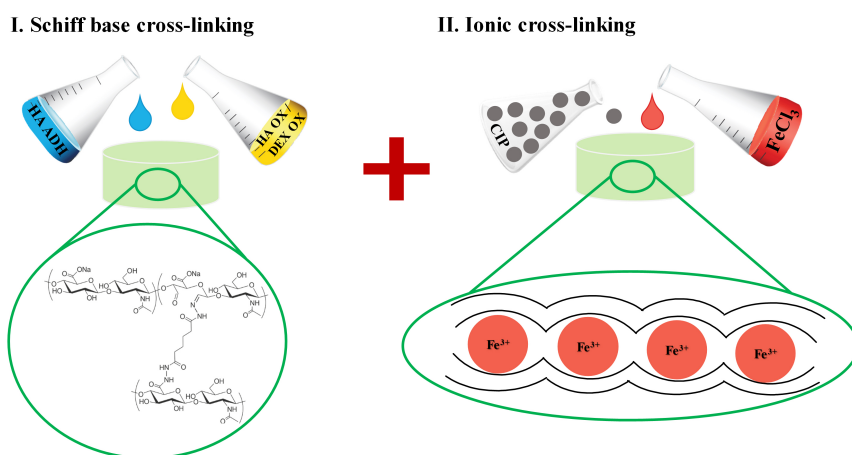


Figure 5. Schematic representation of (I) Schiff base cross-linking and (II) subsequent ionic cross-linking of prepared hydrogels with optional incorporation of magnetoresponsive filler CIPs.

2.4. Rheology

2.4.1. Schiff-Base Cross-Linked Hydrogels

Oscillation rheometry was chosen as the primary tool to evaluate hydrogel mechanics, as it can characterize steady shear flow viscoelastic behaviour as well as be approximated to steady-state characterization. The measurements reveal that HA-ADH with higher DS (gels A-C) leads to stronger hydrogel structures (storage modulus differs as much as three times compared to their respective gel D-F counterparts; see Figure 6A). A similar trend is observed for shear stress (Figure 7C,D). Furthermore, the dynamic character of the Schiff base linkages allows shear-thinning behaviour, as displayed in the decreasing viscosity with increasing shear rate (Figure 7A,B), which makes the hydrogels promising in terms of injectability and extrudability, qualities which are essential in medical applications and additive manufacturing [64,76]. The damping factor, on the hand, shows the opposite trend, confirming lower elasticity of hydrogels D–F (Figure 6B). It can be assumed that the lower DS achieved in DMTMM-mediated reactions leads to lower cross-linking density, thus weakening the structure.

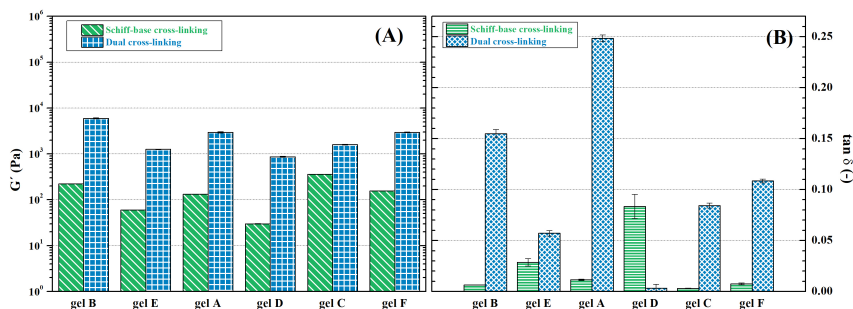


Figure 6. Comparison of (A) storage modulus and (B) damping factor of hydrogels cross-linked via Schiff bases and dually.

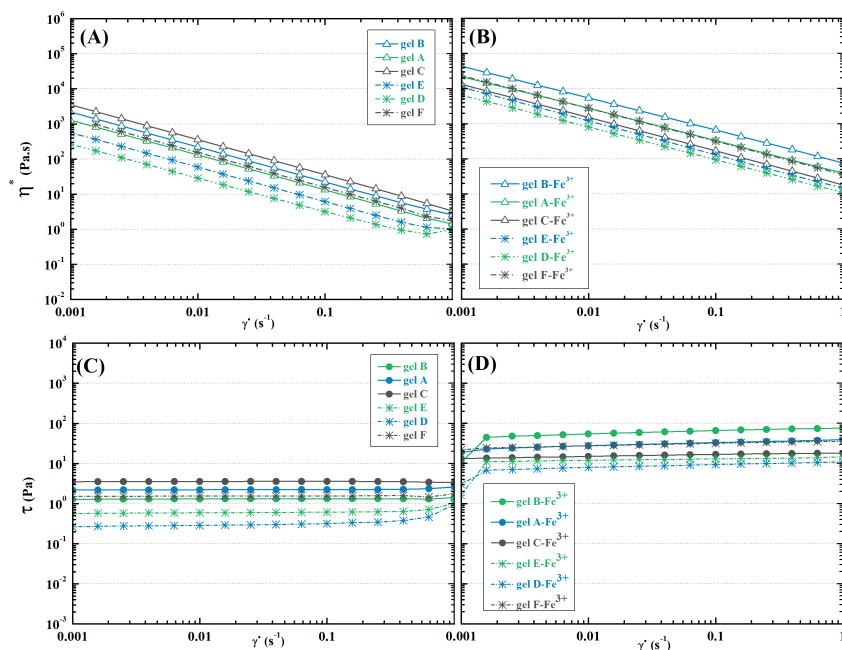


Figure 7. Rheological characterisation of the hydrogels: (A) Complex viscosity–shear rate curves of Schiff base cross-linked and (B) dually cross-linked hydrogels; (C) Shear stress–shear rate curves of Schiff base cross-linked and (D) dually cross-linked hydrogels.

Similar to gelation time, strength of hydrogels is not dependent solely on the DO of oxidized polysaccharides, although it is clearly a factor, as can be observed from comparison of storage moduli of hydrogels A and B and hydrogels D and E, as well as the generated shear stress. Nevertheless, the highest mechanical stability, reflected in storage modulus, viscosity, and shear stress (See Figures 6A and 7), was found for hydrogels C and F containing DEX-OX with DO 49. Given the lower hydrodynamic radius of DEX-OX chains, as discussed earlier, it is possible to assume a more-compact polymer network was formed, which increased overall mechanical strength [77]. Thus, tuning of hydrogel rheological behaviour needs to account for the complex behaviour of polymer chains in order to successfully achieve desired properties.

2.4.2. Dually Cross-Linked Hydrogels

Application of dual cross-linking leads to significant stiffening of the hydrogels. Shear stress increases as much as 10^2 (Figure 7C,D), and storage modulus increases by a factor of 10^3 (Figure 6A). This enhancement of mechanical stability allows easier manipulation of the compact hydrogel, and it increases endurance against mechanical stress, which is desirable for tissue analogue or replacement applications [78]. Nevertheless, the ionic cross-links lack the dynamic character of Schiff bases, which is documented by the milder slope of the viscosity–shear rate curve seen in Figure 7A,B. This confirms the necessity of subsequently applying the second cross-linking strategy in manufacturing in order to avoid material breakage while forming specific shapes [79]. Moreover, the damping factor increased in addition to the other rheological characteristics. Although it does not exceed one in any case (Figure 6B), proving that the hydrogels maintain their solid-like character, it also signals a rather significant increase in loss modulus, i.e., dissipated energy during mechanical stress. This unusual behaviour of hydrogels has been observed previously for polydimethylsiloxane hydrogels [80]. It may protect the components (particles, cells, etc.) enclosed in the hydrogel matrix during vibration or flow, and bring the overall behaviour closer to that of the native tissue.

2.5. Cytotoxicity

Cytotoxicity tests were performed on dually cross-linked HA-based hydrogels in order to establish the most suitable compositions for cell cultivation. The results can be found in Figure 8. All hydrogels based on EDC-modified HA were cytotoxic at 100% concentration. Presumably, this is the result of residual low-molecular-weight by-products from the modification reaction. Gel E was the only formulation that proved to be non-toxic in any concentration. It can be assumed that HA-OX with DO 35 gives very weakly bound hydrogels (gel A and D), which can easily deplete and thus release unreacted aldehyde groups, which are known for their cytotoxicity [81]. DEX-OX with DO 49 was less stable in cultivation medium than its HA-OX cross-linked counterparts. It appears that the reason for increased cytotoxicity is the same as in the previous case, i.e., the exposure of aldehyde groups. The lower stability of DEX-OX with DO 49 hydrogels may be associated with the inefficiency of additional stabilization mechanisms caused by the lower quantity of carboxyl groups available for ionic cross-linking due to the different structure of dextran compared to HA, as discussed in Section 3.3.

2.6. Swelling

Swelling ability is a core characteristic of hydrogels. It mainly depends on the material's chemical nature, cross-linking density, solvent, and temperature [82]. Due to presumed utilization of the proposed hydrogels in bioapplications, the solvent and temperature were chosen to simulate biological conditions (PBS pH 7.4, 37 °C). We found that in such conditions, all of the hydrogel compositions reached equilibrium swelling within one hour. The differences are within measurement uncertainty; therefore, it appears that the individual specifics of the compositions have very little impact on swelling behaviour. Furthermore, all hydrogels except for gel D seemed stable for the whole time period (see Figure 9B). Gel D began to fall apart after two hours of swelling. This was likely due to a weak Schiff base network, which was insufficient even in the presence of secondary ionic cross-linking.

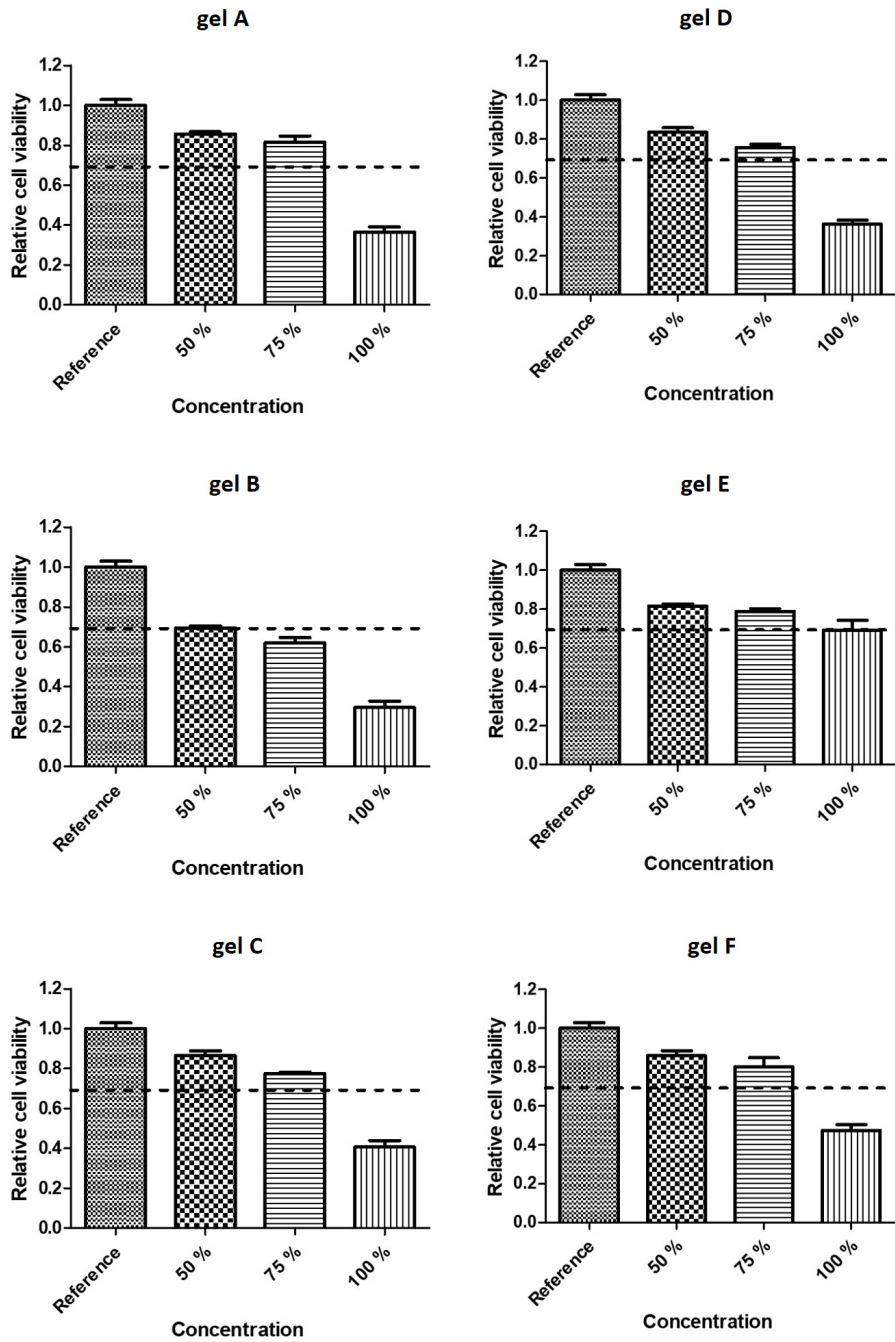


Figure 8. Cytotoxicity of dually cross-linked hydrogels.

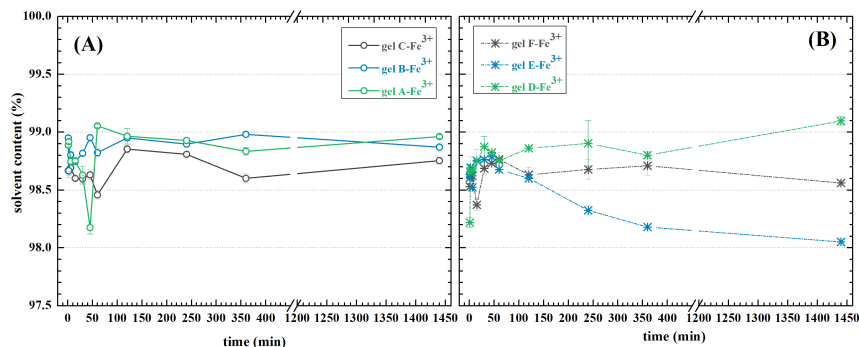


Figure 9. Swelling of dually cross-linked hydrogels. (A) Hydrogels based on HA-ADH modified using EDC; (B) Hydrogels based on HA-ADH modified using DMETMM.

2.7. Mr Hydrogel Preparation

The tests conducted on hydrogels without CIPs were used as indicators to select materials best-suited for fabrication of scaffolds potentially utilizable in cell cultivation. In accordance with the aim of the study, only such materials were subjected to magneto-sensitising and characterisation of magneto-responsiveness. Hydrogels A–C were deemed unsuitable on account of cytotoxicity. Furthermore, the stability of gel D was not sufficient to be useful in cell cultivation applications (Figure 9). Despite the unfavourable cytotoxicity results of gel F, this hydrogel was used for further testing. Assuming the cytotoxicity was caused by the unstable part of the hydrogel, it would still be possible for cells to proliferate in the stable portion of the material. Therefore, two hydrogel compositions were chosen for MR experiments: gels E and F.

CIPs Characterization

Size, volume fraction, and magnetic properties are essential in understanding MR behaviour of the composite as a whole. Therefore, they need to be addressed individually as well as in the material. The used CIPs show saturation magnetization of $15.7 \text{ emu} \cdot \text{g}^{-1}$ and coercivity of 23 Oe (Figure 10A). Their magnetization is approximately 10 times lower and coercivity 20 times higher than that of carbonyl iron powder [83]. The most likely explanation is higher content of impurities, which are known to negatively affect magnetic properties of iron. Additionally, morphological analysis shows a spherical shape of the particles with a rather broad size distribution, as can be seen in Figure 10B,C.

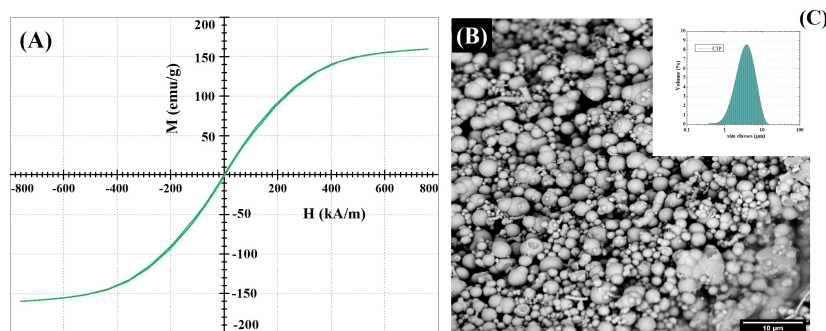


Figure 10. Characterization of CIPs used in MR hydrogels: (A) Magnetization hysteresis curve of CIPs; (B) SEM micrograph of CIPs; (C) CIP size distribution.

2.8. CIP-Filled Hydrogel Magnetic Properties

CIPs, being hard inorganic particles, may induce stiffening of a hydrogel matrix due to their unyielding character. This effect is strongly connected to the particle volume fraction; specifically, non-linear growth begins at approximately 5 vol.% [84]. Due to high density of CIPs, it is possible to use significant weight fractions of particles as fillers, as their volume fraction is rather low. In the current study, we worked with CIPs at 30% weight fraction, thus reaching approximately 4% volume fraction. This amount of CIPs was chosen in order to obtain significant MRE while minimising the effects of hard filler particles. Additionally, it has been shown that higher filling of hydrogels (approx. 30 wt.%) diminishes shear-induced structural disintegration [85], which is desirable for injection and extrusion.

MRE is highly dependent on a material's saturation magnetization. It has been found that dispersing CIPs in HA hydrogels leads to lowering of saturation magnetization compared to bare particles, as is apparent from Figure 11. Saturation magnetization was inversely proportional to hydrogel viscosity. It can be assumed that CIPs' interparticle magnetic interactions are hindered in high-viscosity media. This also corresponds to the widely acknowledged inverse relationship between viscosity and MRE magnitude [15]. Coercivity—being dependent on the properties of a magnetic material, especially particle size [86]—remains unchanged, as the CIPs only serve as a filler and are not chemically changed during Schiff base formation.

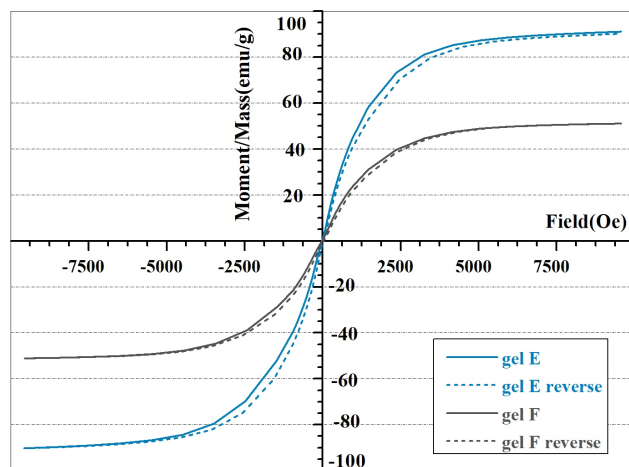


Figure 11. Magnetization hysteresis curves of Schiff base cross-linked HA gels containing 30% CIPs.

2.9. Magnetorheology

2.9.1. Schiff Base Cross-Linked MR Hydrogels

Using CIPs as a magneto-responsive filler induced several effects in hydrogel behaviour. Firstly, an interesting disproportion was found in the shear-flow behaviour without a magnetic field with respect to the polysaccharide polyaldehyde type. The presence of DEX-OX with DO 49 in gel F-CIP caused the storage modulus to increase with the addition of CIPs behaviour may be related to the formation of complexes between dextran and iron-containing particles [87]. Furthermore, the rapid gelation of DEX-OX with DO 49 would likely lead to more homogeneous distribution of CIPs, thus providing mechanical stiffening due to the content of hard particles [84]. This effect was not observed in gel E-CIP. Viscosity curves (Figure 12) confirm the shear-thinning character of hydrogels, as was described in the hydrogels without CIPs.

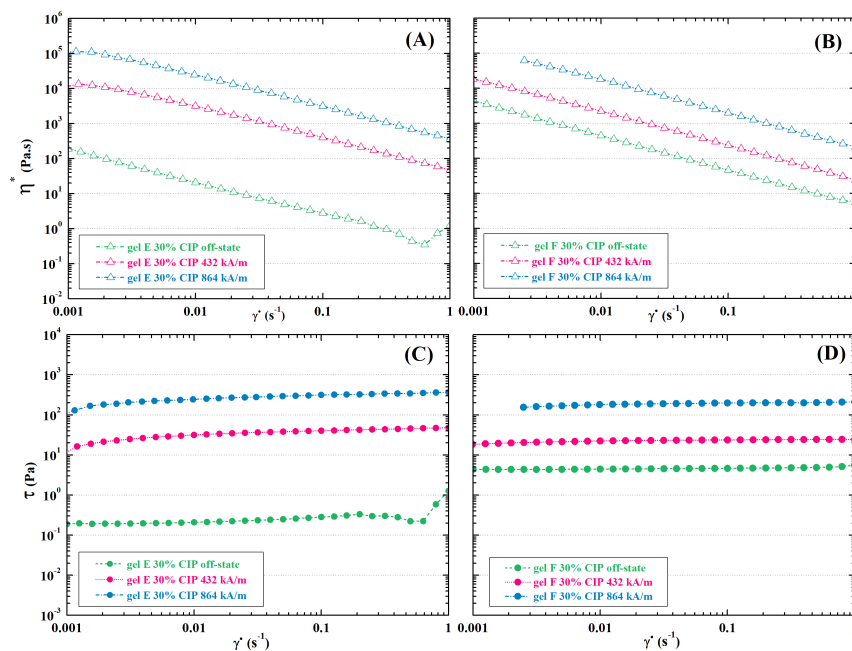


Figure 12. Shear-flow characterisation of CIP-filled Schiff base cross-linked gels: (A,B) Complex viscosity–shear rate curves and (C,D) shear stress–shear rate curves of gel E-CIP (A,C) and gel F-CIP (B,D) in an external magnetic field.

Damping factor shows the opposite trend, which corresponds to the expected shifting towards liquid-like or solid-like character of the respective hydrogels. In case of gel E-CIP, $\tan \delta$ is close to 1, meaning that the viscous behaviour of the mixture is more pronounced than in gel E without CIPs (see Figure 13B). This may cause problems with manipulation in hydrogel applications. However, as long as sufficient viscosity is maintained, certain manufacturing techniques can be applied (e.g., casting or free-form fabrication) [64].

The main reason for incorporating magnetic filler is to induce magneto-sensitivity to the hydrogel, and thus obtain an MR material. In such a material, an external magnetic field induces (partial) alignment of CIPs. The filler thus creates chain-like clusters that provide internal mechanical support to the structure [20]. By comparing rheological characteristics—viscosity, shear stress, and storage modulus—it is clear that this effect is present in both of the examined hydrogel compositions. In order to quantify the magnitude of the MRE, we utilized the storage modulus in the magnetic field relative to an off-state value, and it is denoted as parameter Σ :

$$\Sigma = \frac{G'_H}{G'_0} \tag{1}$$

where G'_H represents the elastic modulus in a certain measured magnetic field, and G'_0 represents the elastic modulus in the absence of a magnetic field. Expressing Σ as a function of magnetic field intensity H (Figure 13C) gives a clear comparison of MRE in various hydrogels, since the slope of the curve is proportional to the magnitude of magnetically induced strengthening. Σ is expressed in logarithmic scale for clarity. The examined CIPs-filled hydrogels show substantial strengthening in magnetic fields (10^1 – 10^3 -times increase of storage modulus compared to the off-state value). The magnitude of the MR response is inversely proportional to hydrogel viscosity in the off state (Figures 12 and 13C). Therefore, the MRE is more pronounced in a softer gel E-CIP, as highly viscous materials restrict the

particles' ability to move through their structure, thus preventing the formation of the chain clusters necessary for MRE [15].

Furthermore, cyclic switching of the magnetic field proved the response of all examined hydrogels to a magnetic field occurring within a few seconds and capable of fully recovering to their respective baseline states (Figure 13D). This offers an opportunity to control their mechanical properties in real time, and to potentially create a variable stimulus during cell cultivation [88].

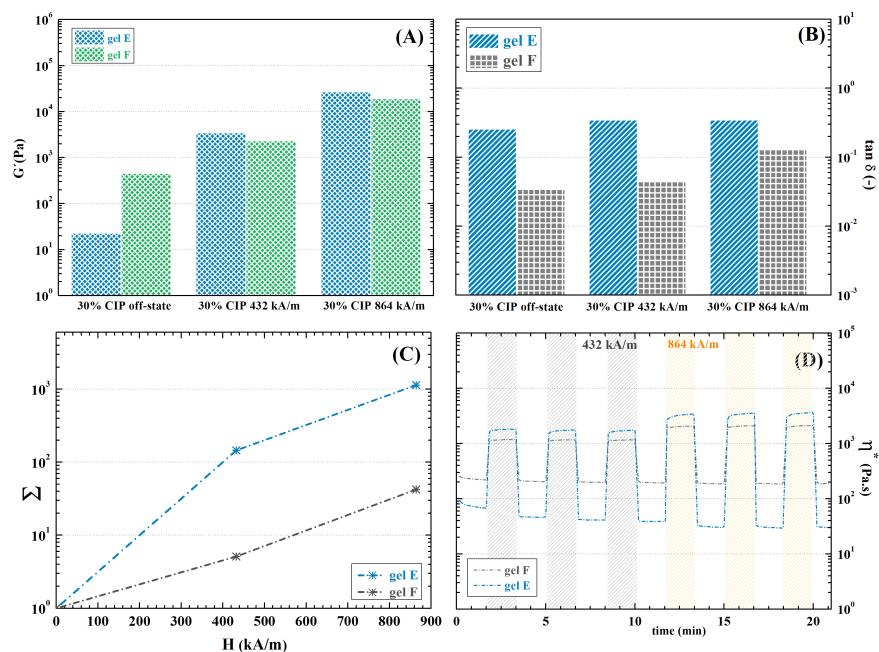


Figure 13. Mechanical characteristics obtained from rheological measurements of CIP-filled Schiff-base cross-linked hydrogels in an external magnetic field: (A) storage modulus; (B) damping factor; (C) intensity of MRE expressed as increase in storage modulus related to magnetic field intensity; (D) cyclic magnetic field exposure.

2.9.2. Dually Cross-Linked Hydrogels

Stabilization increased hydrogel stiffness significantly in the off-state (See Figure 14A) and hindered the viscous response, as is especially evident in gel E-CIP- Fe^{3+} (Figure 14B) as a consequence of additional cross-linking introduced by ionic bonds. Naturally, diminished the MR influence on the hydrogel's mechanical properties (Figure 14C). Notably, the MR behaviour of gel F-CIP- Fe^{3+} stayed almost the same as before stabilization, while gel E-CIP- Fe^{3+} experienced a dramatic increase in stiffness as well as a significant decrease in MRE. These results further support the hypothesis of low efficiency of applied ionic stabilization in DEX-OX DO 49 hydrogel. Despite the decrease in MRE, a 25-times increase was induced in the $862 \text{ kA} \cdot \text{m}^{-1}$ magnetic field in gel E-CIP- Fe^{3+} . This increase is sufficient to provide the desired response in cells [29]; thus, the hydrogels have potential for active cellular scaffold fabrication, e.g., in muscle regeneration. Myocytes positively react to dynamic mechanical stimuli due to their functional predispositions [89]. Additionally the absolute storage modulus of the hydrogels exceeded 10^4 Pa , which is the reported strength of some skeletal muscles [90]. Therefore, the presented materials may be particularly useful in this application.

Furthermore, the hydrogels retained the rapid responsiveness to magnetic field changes, which was observed in non-stabilized samples. The change in mechanical properties is instant, making the material suitable for fabrication of on-demand controlled scaffolds (see Figure 14D).

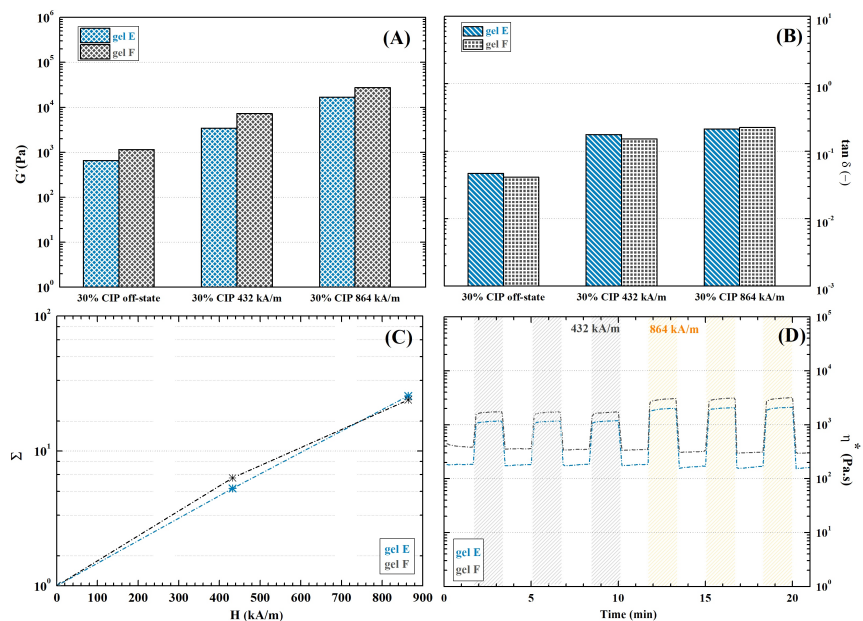


Figure 14. Mechanical characteristics obtained from rheological measurements of CIP-filled dually cross-linked hydrogels in an external magnetic field: (A) storage modulus; (B) damping factor; (C) intensity of MRE expressed as increase in storage modulus related to magnetic field intensity; (D) cyclic magnetic field exposure.

2.10. Porosity and Inner Morphology

SEM micrographs (Figure 15) of freeze-dried dually cross-linked gels with CIPs show porous structures in both samples. The average porosity is between 30–45%, and the average pore size is between $1000 \mu\text{m}^2$ and $2000 \mu\text{m}^2$. However, the variance of values is very broad, with the minimum value as low as $50 \mu\text{m}^2$, and the maximum reaching almost 1mm^2 . There is no significant influence of oxidized polysaccharide characteristics on porosity or average pore size of hydrogels.

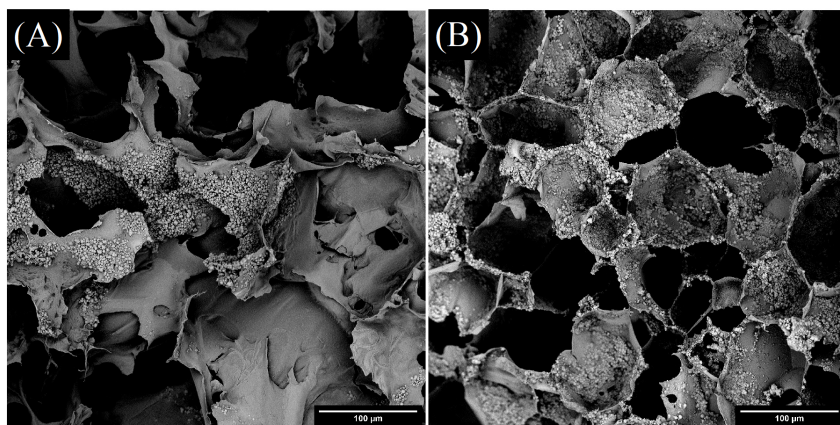


Figure 15. SEM micrographs of freeze-dried CIP-filled hydrogels: (A) gel E; (B) gel F.

3. Materials and Methods

3.1. Chemicals

HA of the following molecular weights: 243 kDa, 1.18 MDa, and 1.5 MDa, was obtained from Contipro Inc., Dolni Dobrouc, Czech Republic.

Dextran from *Leuconstoc* spp. $70,000 \text{ g}\cdot\text{mol}^{-1}$ was obtained from Roth s.r.o., Trebarov, Czech Republic.

Ultrapure water (UPW) was prepared using a Milipore-Q system (Merck KGaA, Darmstadt, Germany).

Dimethyl sulfoxide (DMSO) $\geq 98\%$ and NaHCO_3 , ACS reagent were obtained from VWR International, LLC., Radnor, PA, USA.

ADH $\geq 98\%$ and phosphate buffered saline (PBS), 1X, pH 7.4, sterile were obtained from Thermo Fisher Scientific, Waltham, MA, USA.

EDC $\geq 99\%$ was obtained from Roth s.r.o., Trebarov, Czech Republic.

HOBT $\geq 97\%$; DMTMM $\geq 96\%$, and NaIO_4 , ACS reagent for analysis were obtained from Merck KGaA, Darmstadt, Germany.

NaOH, p.a. was obtained from IPL, Uherský Brod, Czech Republic.

NaCl $\geq 99.5\%$ and HCl 35% were obtained from Lach-ner, s.r.o., Neratovice, Czech Republic.

Fe_3O_4 $\geq 98\%$ was obtained from PENTA s.r.o., Prague, Czech Republic.

A 3-(4,5-Dimethylthiazol-2-yl)-2,5-Diphenyltetrazolium bromide (MTT) cell proliferation assay kit was obtained from Duchefa Biochemie, Haarlem, The Netherlands.

Pentacarbonyl iron particles (i.e., CIPs), iron content over 97%, were obtained from BASF, Ludwigshafen, Germany.

3.2. Modification of HA

HA was grafted by ADH following two slightly modified respective reaction protocols utilizing either EDC [67] or DMTMM [91] as the HA carboxyl group activator.

3.2.1. EDC-Mediated Reaction

First, HA (1 g, 2.5 mmol, 243 kDa) was dissolved in UPW in 50°C while stirring overnight to obtain 0.3 wt.% solution. When the HA solution was cooled to 25°C , ADH (13 g, 75 mmol) was added, followed by pH adjustment to 6.8 with 0.1 M NaOH solution. Then, EDC (1.9 g, 10 mmol) and HoBt (1.4 g, 10 mmol) dissolved in 6 mL of DMSO/UPW (1/1, v/v) were added to the reaction mixture. The pH of the reaction decreased gradually and had to be continuously adjusted to 6.8 during the first hour of the reaction. After that, the reaction proceeded under stirring at 25°C for 22 h. The reaction mixture was

then transferred into dialysis tubes (cut-off 12,000 Da) and dialysed against salt solution (12.5 g NaHCO₃ and 12.5 g NaCl per 10 L) for one day, then against UPW for two days. ADH-modified HA (HA-ADH) was obtained after freeze-drying to yield 1.0 g (94%) with DS 22%. ¹H NMR (D₂O, 400 MHz) δ : 4.53–4.44 (2H, HA anomeric, CH), 3.82–3.32 (10H, HA skeletal, CH), 2.88 (4H, urea, NCH₂), 2.37 (2H, ADH, CH₂NHNHCO), 2.23 (2H, ADH, CH₂NHNH₂), 2.00 (3H, HA, NHCOCH₃), 1.65 (4H, ADH, CH₂CH₂) ppm.

3.2.2. DMTMM-Mediated Reaction

The 1% HA (5 g, 12.5 mmol, 243 kDa) solution in UPW was prepared in the same manner as described previously. Initially, ADH dissolved in 4.5 mL UPW was added to this HA solution. The pH of the reaction mixture was adjusted to 6.5 using HCl or NaOH solution. After that, DMTMM (865 mg, 3.1 mmol) was added, and the reaction was left to proceed for 24 h under stirring at 25 °C. Purification and product isolation followed the same manner as the previous case. HA-ADH with DS 12% and a yield of 2.9 g (53%) was obtained. ¹H NMR (D₂O, 400 MHz) δ : 4.52–4.43 (2H, HA anomeric, CH), 3.82–3.31 (10H, HA skeletal, CH), 2.37 (2H, ADH, CH₂NHNHCO), 2.23 (2H, ADH, CH₂NHNH₂), 2.00 (3H, HA, NHCOCH₃), 1.65 (4H, ADH, CH₂CH₂) ppm.

3.3. Oxidation of HA and Dextran

Polysaccharide polyaldehydes were obtained by periodate oxidation according to published procedures [67,68]. Specifically, the respective polysaccharide was dissolved in UPW overnight at 50 °C under stirring. Afterwards, the appropriate amount of sodium periodate dissolved in water was added to the polysaccharide solution under vigorous stirring at 25 °C. The reactions were carried out in the dark at 25 °C for a given time (Table 2) under stirring. The reaction mixtures were then placed into dialysis tubes (cut-off 3000 Da) and dialysed against UPW for three days. After that, the purified product was obtained by freeze-drying (Table 3).

Table 2. Specification of polysaccharide oxidation conditions.

	Initial Molecular Weight (kDa)	Mass of HA (g)	Molar Amount of HA (mmol)	Weight Fraction of HA (wt.%)	Mass of NaIO ₄ (g)	Molar Amount of NaIO ₄ (mmol)	Time (hours)
HA-OX A	1500	1.5	3.8	1	0.88	4.1	10
HA-OX B	1180	1.5	3.8	1	0.88	4.1	10
DEX-OX	70	3	18.5	13	1.58	7.4	4

Table 3. Characterisation of oxidized polysaccharides.

	Yield (g)	Yield (%)	DO	Final Molecular Weight (kDa)
HA-OX A	0.55	36	62	7.6
HA-OX B	0.78	51	35	8.4
DEX-OX	2.66	89	49	8.8

3.4. Schiff Base Linkage Formation

Hydrogel precursors, i.e., HA-ADH and polysaccharide polyaldehyde, were dissolved separately in PBS overnight at room temperature to obtain 2 wt.% solutions. Then, the solutions were mixed in a 1:1 volume ratio, and gelation occurred spontaneously. This procedure yielded Schiff-base cross-linked hydrogels.

For MR hydrogel preparation, 60 wt./vol.% of CIPs was added to the polysaccharide polyaldehyde solution and vortexed thoroughly to obtain homogeneous dispersion. Due to the fast sedimentation of CIPs, it was necessary to ensure immediate mixing with HA-ADH solution to induce gelation via Schiff base formation.

3.5. Dual Cross-Linking of Hydrogels

The covalently cross-linked hydrogels with and without CIPs were submerged in a 2 wt.% aqueous solution of FeCl_3 for 1 h at 25 °C. After removal from the Fe^{3+} bath, the samples were placed in a large amount of UPW for three days at 25 °C, with the water changed three times a day. To confirm that the excessive Fe^{3+} had been washed out, conductivity of the water was measured before each change. This procedure was unchanged regardless of CIP presence.

The stability of dually cross-linked hydrogels during cell cultivation was established in simulated cultivation conditions, i.e., shaking while submerged in a cultivation medium at 37 °C. The state of the hydrogel samples was checked daily, and the cultivation medium was changed every day as well.

3.6. Determining DO

The number of aldehyde groups per 100 saccharide subunits, i.e., the DO, was established using the hydroxylamine hydrochloride method [92]. The measurements were performed using an automatic titrator T50 (Metler Toledo, Greifensee, Switzerland).

3.7. Nuclear Magnetic Resonance

Proton nuclear magnetic resonance (^1H NMR) spectra were recorded on a JEOL ECZ 400 (JEOL Ltd., Tokyo, Japan) operating at a ^1H frequency of 399.78 MHz at 60 °C. The samples were dissolved in D_2O at concentrations of $10 \text{ mg}\cdot\text{mL}^{-1}$ for the analysis. Water was used as a reference signal and was set at 4.75 ppm. The DS of HA-ADH was calculated by comparing a molar ratio (integral) of the peaks assigned to an HA N-acetyl group (3H) at 2.00 ppm and two methylene groups of ADH (4H) at 1.65 ppm.

3.8. Molecular Weight Determination

The average molecular weight and distribution curve of oxidized polysaccharides (HA, dextran) were determined by gel permeation chromatography performed on a high-performance liquid chromatograph system equipped with a refractive index (RI) detector (Shimadzu Prominence, LC-20 series, Shimadzu Corporation, Kyoto, Japan) with the following parameters: 0.1 M PBS solution at 7.4 pH, flow $0.8 \text{ mL}\cdot\text{min}^{-1}$, oven temperature 30 °C, columns PL aquagel-OH 60 $8 \mu\text{m}$, $300 \times 7.5 \text{ mm}$ and PL aquagel-OH 40, $8 \mu\text{m}$, $300 \times 7.5 \text{ mm}$ were connected in series. Pullulan standards were used for molecular weight calibration; analyses were based on RI data.

3.9. Dynamic Light-Scattering Measurement

Hydrodynamic diameters of HA-OX and DEX-OX solutions were determined by dynamic light scattering on a Zetasizer Nano ZS90 (Malvern Instruments, Malvern, UK). The results were expressed as intensity-weighted z-average diameter. Measurements of all diluted samples (concentration 2 wt.%) were carried out at a scattering angle of 173° with a 4 mW He-Ne laser operating at 633 nm and 25 °C. Before the measurements, all samples were filtered through a $0.45 \mu\text{m}$ pore-size polytetrafluoro ethylene syringe filter (Millipore, UK). Each sample was measured in triplicate.

3.10. Particle Size Analysis

Particle size analysis of CIPs was done on a laser diffraction particle sizing instrument (Mastersizer 3000, Malvern Instruments Ltd., Malvern, UK). The results were expressed as volume distribution. The laser diffractive method provides the standard percentile readings $D_v 50$, $D_v 10$, and $D_v 90$. Each sample was measured five times, and the mean and standard deviation were subsequently calculated.

3.11. Magnetometry

The bare CIPs and the magneto-responsive hydrogels were characterized according to their magnetization with a vibrating sample magnetometer Lake Shore 7404 (Lake Shore

Cryotronics Inc., Westerville, OH, USA) at room temperature in room air in a magnetic field of up to 10 kOe. The amplitude and the frequency of the vibration were 1.5 mm and 82 Hz, respectively.

3.12. Rheology and Magnetorheology

All measurements were performed using a rotational rheometer, Anton-Paar MCR 502 (Anton Paar, Graz, Austria) at 25 °C under normal pressure in room air.

Time dependence of fresh polymer solution (2 mL) viscosity was measured using a double-gap measuring system DG26.7/T200/SS oscillating at constant 10% deformation with a constant angular frequency of 10 rad·s⁻¹. Changes in rheological behaviour were followed over a 14 h time sweep. The gelation point was defined as the crossover between storage and loss moduli. It ought to be noted that sample preparation caused an approximately 1 min delay between the reaction start and obtainment of the first datum.

On the other hand, the rheology of Schiff base and dual cross-linked hydrogels was performed using a Peltier measuring system P-PTD200/62/TG with PP/25 in oscillation at constant 1% deformation with angular frequency sweep increasing from 0.1 to 100 rad·s⁻¹. The hydrogel samples were prepared 12 h in advance for Schiff-base cross-linking, or 4 days in advance for dual cross-linking in order to satisfy the necessity to wash out excessive Fe³⁺ ions. The samples were in the form of circular plates with a diameter of 30 mm and a thickness of 2 mm.

Furthermore, CIP-filled hydrogels were subjected to magnetorheological measurement in a homogeneous magnetic field. For magnetorheological investigations, an MRD 180/1T measuring cell with PP 20/MRD/TI measuring geometry, and a Julabo temperating unit ensured that all investigation were performed at room temperature. The parallel-plate measuring system diameter was 20 mm. The magnetic field strength was consecutively set to 0 kA·m⁻¹, 432 kA·m⁻¹, and 862 kA·m⁻¹. Additionally, a time sweep measurement while periodically switching the magnetic field between on and off states with an interval of 30 s was done.

Viscosity and shear strain are shown with respect to shear rate in the measured range, i.e., from 0.001 s⁻¹ to 1 s⁻¹. Storage modulus and damping factor, on the hand, are expressed as the mean value measured in the range 0.01 s⁻¹ to 0.1 s⁻¹.

3.13. Morphological Analysis

CIP morphology and the inner morphology of the material was observed using scanning electron microscope (SEM) imaging of freeze-dried samples in vertical sections using a Phenom Pro (Thermo Fisher Scientific, Waltham, MA, USA) at an accelerating voltage of 5 kV. The samples were sputtered with a gold–palladium layer prior to imaging. Image processing was performed with the aid of ImageJ software.

3.14. Swelling

Gravimetric measurement protocol was used to determine the swelling behaviour of dually cross-linked hydrogels. Specifically, freeze-dried samples of known mass were immersed in PBS (0.1 M, pH 7.4). The equilibrium buffer uptake, S(e) (%), of hydrogels was determined by weighing the swollen samples at selected time intervals of 1, 2, 6, 15, 30, 60, 120, 240, 360 and 1440 min. The presented results are the average of 3 measurements. The samples were maintained at 37 °C throughout the measurement. The buffer and temperature were chosen with respect to biological testing requirements.

3.15. Cytotoxicity Testing

Cytotoxicity testing was done according to ISO standard 10993 using the NIH/3 T3 cell line. Sterilization was done prior to cytotoxicity testing by shaking samples in 70% ethanol for 1 h at laboratory temperature. Elution of the ethanol from samples was done by aspiration, a short rinsing in PBS, and then by shaking the samples in UPW for 48 h at laboratory temperature. After UPW aspiration, extracts were created. Extracts were

prepared according to ISO standard 10993-12 (100 mg of hydrogel/1 mL of media). The tested material was incubated in a cultivation medium for 24 h at 37 °C with stirring. The parent extracts (100%) were then diluted in medium to obtain a series of dilutions with concentrations of 75 vol.% and 50 vol.%. All extracts were used for up to 24 h. The cells were seeded at a concentration of 10^5 per well in 96-well plates. After the pre/incubation period (24 h), the extracts were filtered using a syringe filter with membrane pore size of 0.22 μm (TPP, Trasadingen, Switzerland) in order to ensure that no residual hydrogel was present. The filtered extracts in required dilutions were added to the cells and incubated for 24 h. Subsequently, tetrazolium salt was used to determine cell viability. Absorbance was measured using a microplate reader, Infinite M200 PRO (Tecan, Männedorf, Switzerland) at 570 nm, and the reference wavelength was adjusted to 690 nm. The results are presented as the percent reduction of cell viability when compared to cells cultivated in medium without the extracts of tested materials. Morphology of cells from the culture plates was observed using an inverted Olympus phase-contrast microscope (IX 81).

4. Conclusions

In this research paper, we have described synthesis of HA-based polysaccharide hydrogels utilizing dual cross-linking. Furthermore, the hydrogels were given magneto-responsiveness through incorporating CIPs in their structure in a simple and straightforward manner, maintaining low toxicity of the production process. In order to produce hydrogels, a reaction between HA-ADH and polysaccharide polyaldehydes yielding Schiff-base linkages was used. EDC and DMTMM carboxyl group activating agent respectively were employed for HA-ADH preparation, and the products were compared and evaluated. Despite DMTMM providing a product with lower DS, we proved that the DMTMM-mediated reaction led to pure HA-ADH without by-products. Moreover, product purity had a positive effect on cytocompatibility of resulting hydrogels compared to EDC. Therefore, it may be more suitable for application in cell cultivation.

We found that even though the DO of oxidized polysaccharides is a non-negligible factor in hydrogel mechanical performance, it is necessary to consider the specifics of polysaccharide chains, such as the hydrodynamic radius. The small size of DEX-OX with DO 49 polymer coils caused rapid gelation (less than 30 min) compared to HA-OX with DO 62, which, despite the higher quantity of available reactive sites, reached gelation in 50 min or 3 h depending on the DS of HA-ADH. Similarly, a disproportion in storage modulus was observed, as DEX-OX hydrogels were twice as strong as HA-OX with DO 62 due to more-compact structure provided by the lower hydrodynamic radius of its polymer coils.

Ionic cross-linking additionally increased the storage modulus of presented hydrogels as much as 10^2 times compared to sole Schiff base cross-linking. The effect of Fe^{3+} ions was more pronounced in hydrogels containing only HA in the polymer matrix. The use of CIPs as magneto-responsive filler substantially increased hydrogel mechanical performance in an external magnetic field. The magnitude of the MRE was inversely proportional to hydrogel off-state viscosity. Overall storage modulus of the hydrogels reached 10^4 Pa, and the maximum change induced by MRE was 10^3 higher than the off-state value of Schiff-base cross-linked hydrogels, and 25 times the value without the magnetic field for dually cross-linked hydrogels. This substantial increase promises opportunities for mechanical stimulation of cells such as myocytes.

To summarize, the current work demonstrates successful preparation of HA-based MR hydrogels utilizing CIPs as an active filler. To the best of our knowledge, this is the first time an HA-based material has been used as a matrix for CIPs to secure rapid and reversible stiffening through MRE. Their cytocompatibility encourages further research of these hydrogels in terms of tissue engineering, especially in skeletal muscle regeneration applications. These qualities promise the presented materials to be useful in biological applications, specifically scaffold fabrication as injectable or 3D printable hydrogels.

Author Contributions: Conceptualization, E.A., M.M. and A.M.; methodology, L.M. (Lenka Musilová), E.A., R.K., M.M. and Z.C.; validation L.V., L.M. (Lenka Musilová), E.A., R.K., M.M., K.K., L.M. (Leona Mahelová), Z.C. and A.M.; formal analysis, L.M. (Lenka Musilová) and R.K.; investigation, L.V., E.A., K.K. and L.M. (Leona Mahelová); writing—original draft preparation, L.V., L.M. (Lenka Musilová) and E.A.; writing—review and editing, R.K., M.M., Z.C. and A.M.; visualisation, L.M. (Lenka Musilová); supervision, M.M., Z.C. and A.M.; project administration, L.V. and E.A.; funding acquisition, M.M., Z.C. and A.M. All authors have read and agreed to the published version of the manuscript.

Funding: The research of L.V. was funded by the project OP RDE Junior Grants of TBU in Zlín, Reg. No. CZ.02.2.69/0.0/0.0/19_073/0016941. L.M. (Leona Mahelová) is grateful to TBU in Zlín for the internal grant IGA/CPS/2022/001 funded from the resources of specific academic research. Authors M.M., L.M. (Lenka Musilová), A.M. and R.K. were financially supported by the Ministry of Education, Youth and Sports of the Czech Republic—DKRVO (RP/CPS/2022/003). Author Z.C. would like to express her gratitude to the Ministry of Education, Youth and Sports of the Czech Republic project—DKRVO (RP/CPS/2022/001).

Institutional Review Board Statement: Not applicable.

Informed Consent Statement: Not applicable.

Data Availability Statement: Not applicable.

Conflicts of Interest: The authors declare no conflict of interest.

Abbreviations

The following abbreviations are used in this manuscript:

ADH	adipic acid dihydrazide
CIP	carbonyl iron particle
DEX-OX	oxidized dextran
DMSO	dimethyl sulfoxide
DMTMM	4-(4,6-Dimethoxy-1,3,5-triazin-2-yl)-4-methylmorpholinium chloride
DO	degree of oxidation
DS	degree of substitution
ECM	extracellular matrix
EDC	1-ethyl-3-(3-dimethylaminopropyl)carbodiimide hydrochloride
GAG	glycosaminoglycan
HA	hyaluronan
HA-ADH	adipic acid dihydrazide-modified hyaluronan
HA-OX	oxidized hyaluronan
HoBt	1-hydroxybenzotriazole hydrate
MR	magnetorheological
MRE	magnetorheological effect
MTT	3-(4,5-dimethylthiazol-2-yl)-2,5-diphenyltetrazolium Bromide
PBS	phosphate buffered saline
RI	refractive index
SPION	superparamagnetic iron-oxide particle
UPW	ultrapure water

References

1. Vasile, C.; Pamfil, D.; Stoleru, E.; Baican, M. New Developments in Medical Applications of Hybrid Hydrogels Containing Natural Polymers. *Molecules* **2020**, *25*, 1539. [[CrossRef](#)] [[PubMed](#)]
2. Zhang, G.; Wang, Z.; Han, F.; Jin, G.; Xu, L.; Xu, H.; Su, H.; Wang, H.; Le, Y.; Fu, Y.; et al. Mechano-regulation of vascular network formation without branches in 3D bioprinted cell-laden hydrogel constructs. *Biotechnol. Bioeng.* **2021**, *118*, 3787–3798. [[CrossRef](#)] [[PubMed](#)]
3. Cui, P.; Qin, P.P.L.; Wang, X.; Chen, X.; Deng, Y.; Zhang, X. Nanoengineered hydrogels as 3D biomimetic extracellular matrix with injectable and sustained delivery capability for cartilage regeneration. *Bioact. Mater.* **2022**, *19*, 487–498. [[CrossRef](#)] [[PubMed](#)]
4. Dangi, D.; Mattoo, M.; Kumar, V.; Sharma, P. Synthesis and characterization of galactomannan polymer hydrogel and sustained drug delivery. *Carbohydr. Polym. Technol. Appl.* **2022**, *4*, 100230. [[CrossRef](#)]

5. Razali, N.A.M.; Lin, W.C. Accelerating the excisional wound closure by using the patterned microstructural nanofibrous mats/gentamicin-loaded hydrogel composite scaffold. *Mater. Today Bio* **2022**, *16*, 100347. [[CrossRef](#)] [[PubMed](#)]
6. Huang, X.; Wang, L.; Shen, Z.; Ren, J.; Chen, G.; Li, Q.; Zhou, Z. Super-Stretchable and Self-Healing hydrogel with a Three-Dimensional silver nanowires network structure for wearable sensor and electromagnetic interference shielding. *Chem. Eng. J.* **2022**, *446*, 137136. [[CrossRef](#)]
7. Yin, X.; Wu, J.; Zhao, H.; Zhou, L.; He, T.; Fan, Y.; Chen, L.; Wang, K.; He, Y. A microgel-structured cellulose nanofibril coating with robust antifouling performance for highly efficient oil/water and immiscible organic solvent separation. *Colloids Surfaces A Physicochem. Eng. Asp.* **2022**, *647*, 128875. [[CrossRef](#)]
8. Ren, J.; Li, R.; Wang, X.; Li, M.; Yang, W. A superabsorbent hydrogel for removal of dyes from aqueous solution. *J. Polym. Environ.* **2022**, *30*, 3327–3339. [[CrossRef](#)]
9. Lu, H.; Li, X.; Yang, H.; Wu, J.; Zhang, Y.; Huang, H. Preparation and properties of riboflavin-loaded sanxan microcapsules. *Food Hydrocoll.* **2022**, *129*, 107641. [[CrossRef](#)]
10. Lopes, P.M.P.; Moldovan, D.; Moldovan, M.; Carpa, R.; Saroși, C.; Pășcuță, P.; Moldovan, A.M.; Fecete, R.; Popescu, V. New Composite Hydrogel Based on Whey and Gelatin Crosslinked with Copper Sulphate. *Materials* **2022**, *15*, 2611. [[CrossRef](#)]
11. Cvek, M.; Zahoranova, A.; Mrlík, M.; Sramkova, P.; Minarik, A.; Sedlacik, M. Poly(2-oxazoline)-based magnetic hydrogels: Synthesis, performance and cytotoxicity. *Colloids Surfaces B Biointerfaces* **2020**, *190*, 110912. [[CrossRef](#)]
12. Zhang, S.D.; Zhai, Y.C.; Zhang, Z.F. Study on Polyvinyl-Alcohol(PVA)/ Iron Oxide Black(Fe₃O₄) and Polyvinlyl-Alcohol(PVA)/ Iron Oxide Red(Fe₂O₃) Magnetic Sensitive Hydrogel. *Adv. Mater. Res.* **2011**, *287–290*, 2032–2035. [[CrossRef](#)]
13. Bardajee, G.R.; Hooshyar, Z. One-pot synthesis of biocompatible superparamagnetic iron oxide nanoparticles/hydrogel based on salver: Characterization and drug delivery. *Carbohydr. Polym.* **2014**, *101*, 741–751. [[CrossRef](#)]
14. Alveroğlu, E.; Sözeri, H.; Kurtan, U.; Şenel, M.; Baykal, A. Magnetic and spectroscopic properties of Polyacrylamide-CoFe₂O₄ magnetic hydrogel. *J. Mol. Struct.* **2013**, *1036*, 386–391. [[CrossRef](#)]
15. Morillas, J.; de Vicente, J. Magnetorheology: A review. *Soft Matter* **2020**, *16*, 9614–9642. [[CrossRef](#)] [[PubMed](#)]
16. Levy, M.; Luciani, N.; Alloyeau, D.; Elgrabli, D.; Deveaux, V.; Pechoux, C.; Chat, S.; Wang, G.; Vats, N.; Gendron, F.; et al. Long term in vivo biotransformation of iron oxide nanoparticles. *Biomaterials* **2011**, *32*, 3988–3999. [[CrossRef](#)]
17. Jingli, G.; Haifei, X.; Yehua, H.; Wei, D.; Wei, H.; Chunyu, W.; Ning, G.; Haiyan, X.; Jimin, C. The internalization pathway, metabolic fate and biological effect of superparamagnetic iron oxide nanoparticles in the macrophage-like RAW264.7 cell. *Sci. China Life Sci. Vol.* **2011**, *54*, 793–805. [[CrossRef](#)]
18. Mrlík, M.; Ilčíková, M.; Cvek, M.; Pavlínek, V.; Zahoranová, A.; Kroneková, Z.; Kasak, P. Carbonyl iron coated with a sulfobetaine moiety as a biocompatible system and the magnetorheological performance of its silicone oil suspensions. *RSC Adv.* **2016**, *6*, 32823–32830. [[CrossRef](#)]
19. Cvek, M.; Mrlík, M.; Ilčíková, M.; Mosnáček, J.; Babayan, V.; Kuceková, Z.; Humpolíček, P.; Pavlínek, V. The chemical stability and cytotoxicity of carbonyl iron particles grafted with poly(glycidyl methacrylate) and the magnetorheological activity of their suspensions. *RSC Adv.* **2015**, *5*, 72816–72824. [[CrossRef](#)]
20. Bossis, G.; Volkova, O.; Laci, S.; Meunier, A. Magnetorheology: Fluids, Structures and Rheology. In *Ferrofluids. Lecture Notes in Physics*; Springer: Berlin, Germany, 2002. [[CrossRef](#)]
21. Ruiz-López, J.A.; Hidalgo-Alvarez, R.; de Vicente, J. Towards a universal master curve in magnetorheology. *Smart Mater. Struct.* **2017**, *26*, 054001. [[CrossRef](#)]
22. Gila-Vilchez, C.; Bonhome-Espinosa, A.B.; Kuzhir, P.; Zubarev, A.; Duran, J.D.G.; Lopez-Lopez, M.T. Rheology of magnetic alginate hydrogels. *J. Rheol.* **2018**, *62*, 1083–1096. [[CrossRef](#)]
23. Bin, L.; Xu, C.; Wang, S.D.X. Alignment of magnetic particles in hydrogel matrix: A novel anisotropic magnetic hydrogels for soft robotics. *J. Intell. Mater. Syst. Struct.* **2021**, *32*, 1432–1440. [[CrossRef](#)]
24. Galindo-Gonzalez, C.; Gantz, S.; Ourry, L.; Mammeri, F.; Ammar-Merah, S.; Ponton, A. Elaboration and Rheological Investigation of Magnetic Sensitive Nanocomposite Biopolymer Networks. *Macromolecules* **2014**, *47*, 3136–3144. [[CrossRef](#)]
25. Borin, D.; Stepanov, G.; Musikhin, A.; Zubarev, A.; Bakhtiarov, A.; Storozhenko, P. Magnetorheological Effect of Magnetoactive Elastomer with a Permalloy Filler. *Polymers* **2020**, *12*, 2371. [[CrossRef](#)]
26. Rich, J.P.; McKinley, G.H.; Doyle, P.S. Arrested Chain Growth During Magnetic Directed Particle Assembly in Yield Stress Matrix Fluids. *Langmuir* **2012**, *28*, 3683–3689. [[CrossRef](#)]
27. Liu, J.; Flores, G.A.; Sheng, R. In-vitro investigation of blood embolization in cancer treatment using magnetorheological fluids. *J. Magn. Magn. Mater.* **2001**, *225*, 209–217. [[CrossRef](#)]
28. Zhang, Y.; Li, D.; Chen, Y.; Li, Z. A Comparative Study of Ferrofluid Seal and Magnetorheological Fluid Seal. *IEEE Trans. Magn.* **2018**, *54*, 4601207. [[CrossRef](#)]
29. Nardecchia, S.; Chocarro-Wrona, C.; Sánchez-Moreno, P.; Zambrano-Marín, J.R.; Marchal, J.A.; de Vicente, J. Living magnetorheological composites: From the synthesis to the in vitro characterization. *Smart Mater. Struct.* **2021**, *30*, 065015. [[CrossRef](#)]
30. Fang, Y.; Yang, X.; Lin, Y.; Shi, J.; Prominski, A.; Clayton, C.; Ostroff, E.; Tian, B. Dissecting Biological and Synthetic Soft–Hard Interfaces for Tissue-Like Systems. *Chem. Rev.* **2022**, *122*, 5233–5276. [[CrossRef](#)]
31. de Moraes Porto, I.C.C. Polymer Biocompatibility. In *Polymerization*; InTech: London, UK, 2012. [[CrossRef](#)]
32. Tibbitt, M.W.; Anseth, K.S. Hydrogels as extracellular matrix mimics for 3D cell culture. *Biotechnol. Bioeng.* **2009**, *103*, 655–663. [[CrossRef](#)]

33. Sigleitmeier, M.; Wu, B.; Kollmann, T.; Neubauer, M.; Nagy, G.; Schwahn, D.; Pipich, V.; Faivre, D.; Zahn, D.; Fery, A.; et al. Multifunctional layered magnetic composites. *Beilstein J. Nanotechnol.* **2015**, *6*, 134–148. [[CrossRef](#)] [[PubMed](#)]
34. de Marco, C.; Alcántara, C.C.J.; Kim, S.; Briatico, F.; Kadioglu, A.; de Bernardis, G.; Chen, X.; Marano, C.; Nelson, B.J.; Pané, S. Indirect 3D and 4D Printing of Soft Robotic Microstructures. *Adv. Mater. Technol.* **2019**, *4*, 1900332. [[CrossRef](#)]
35. Tognato, R.; Armiento, A.R.; Bonfrate, V.; Levato, R.; Malda, J.; Alini, M.; Eglín, D.; Giancane, G.; Serra, T. A Stimuli-Responsive Nanocomposite for 3D Anisotropic Cell-Guidance and Magnetic Soft Robotics. *Adv. Funct. Mater.* **2019**, *29*, 1804647. [[CrossRef](#)]
36. Löwik, D.W.P.M.; Shklyarevskiy, I.O.; Ruizendaal, L.; Christianen, P.C.M.; Maan, J.C.; van Hest, J.C.M. A Highly Ordered Material from Magnetically Aligned Peptide Amphiphile Nanofiber Assemblies. *Adv. Mater.* **2007**, *19*, 1191–1195. [[CrossRef](#)]
37. Lopez-Lopez, M.T.; Rodriguez, I.A.; Rodriguez-Arco, L.; Carriel, V.; Bonhome-Espinosa, A.B.; Campos, F.; Zubarev, A.; Duran, J.D.G. Synthesis, characterization and in vivo evaluation of biocompatible ferrogels. *J. Magn. Magn. Mater.* **2017**, *431*, 110–114. [[CrossRef](#)]
38. Akama, S.; Ikeda, J.; Kawai, M.; Mitsumata, T. A Feature in Magnetorheological Effect for Polysaccharide Magnetic Hydrogels. *Chem. Lett.* **2018**, *47*, 1240–1242. [[CrossRef](#)]
39. Abrougui, M.M.; Lopez-Lopez, M.T.; Duran, J.D.G. Mechanical properties of magnetic gels containing rod-like composite particles. *Philos. Trans. R. Soc. A Math. Phys. Eng. Sci.* **2019**, *377*. [[CrossRef](#)]
40. Abrougui, M.M.; Srasra, E.; Lopez-Lopez, M.T.; Duran, J.D.G. Rheology of magnetic colloids containing clusters of particle platelets and polymer nanofibres. *Philos. Trans. R. Soc. A Math. Phys. Eng. Sci.* **2020**, *378*. [[CrossRef](#)]
41. Zhao, X.; Kim, J.; Cezar, C.A.; Huebsch, N.; Lee, K.; Bouhadir, K.; Mooney, D.J. Active scaffolds for on-demand drug and cell delivery. *Proc. Natl. Acad. Sci. USA* **2011**, *108*, 67–72. [[CrossRef](#)]
42. Popa, E.; Santo, V.; Rodrigues, M.; Gomes, M. Magnetically-Responsive Hydrogels for Modulation of Chondrogenic Commitment of Human Adipose-Derived Stem Cells. *Polymers* **2016**, *8*, 28. [[CrossRef](#)]
43. Ikeda, J.; Takahashi, D.; Watanabe, M.; Kawai, M.; Mitsumata, T. Particle Size in Secondary Particle and Magnetic Response for Carrageenan Magnetic Hydrogels. *Gels* **2019**, *5*, 39. [[CrossRef](#)] [[PubMed](#)]
44. Amorim, S.; Reis, C.A.; Reis, R.L.; Pires, R.A. Extracellular Matrix Mimics Using Hyaluronan-Based Biomaterials. *Trends Biotechnol.* **2021**, *39*, 90–104. [[CrossRef](#)] [[PubMed](#)]
45. Jongprakitkul, H.; Turunen, S.; Parihar, V.S.; Annurakshita, S.; Kellomäki, M. Photocross-linkable Methacrylated Polypeptides and Polysaccharides for Casting, Injecting, and 3D Fabrication. *Biomacromolecules* **2021**, *22*, 481–493. [[CrossRef](#)] [[PubMed](#)]
46. Teong, B.; Wu, S.C.; Chang, C.M.; Chen, J.W.; Chen, H.T.; Chen, C.H.; Chang, J.K.; Ho, M.L. The stiffness of a crosslinked hyaluronan hydrogel affects its chondro-induction activity on hADSCs. *J. Biomed. Mater. Res. Part B Appl. Biomater.* **2018**, *106*, 808–816. [[CrossRef](#)] [[PubMed](#)]
47. Bobula, T.; Buffa, R.; Hermannová, M.; Kohutová, L.; Procházková, P.; Vágnerová, H.; Čepa, M.; Wolfová, L.; Židek, O.; Velebný, V. A novel photopolymerizable derivative of hyaluronan for designed hydrogel formation. *Carbohydr. Polym.* **2017**, *161*, 277–285. [[CrossRef](#)]
48. Staubli, F.; Stoddart, M.J.; D’Este, M.; Schwab, A. Pre-culture of human mesenchymal stromal cells in spheroids facilitates chondrogenesis at a low total cell count upon embedding in biomaterials to generate cartilage microtissues. *Acta Biomater.* **2022**, *143*, 253–265. [[CrossRef](#)]
49. Santhanam, S.; Liang, J.; Baid, R.; Ravi, N. Investigating thiol-modification on hyaluronan via carbodiimide chemistry using response surface methodology. *J. Biomed. Mater. Res. Part A* **2015**, *103*, 2300–2308. [[CrossRef](#)]
50. Köwitsch, A.; Niepel, M.S.; Michanetzis, G.P.A.; Missirlis, Y.F.; Groth, T. Effect of Immobilized Thiolated Glycosaminoglycans on Fibronectin Adsorption and Behavior of Fibroblasts. *Macromol. Biosci.* **2016**, *16*, 381–394. [[CrossRef](#)]
51. Barthold, J.E.; McCreery, K.P.; Martinez, J.; Bellerjeau, C.; Ding, Y.; Bryant, S.J.; Whiting, G.L.; Neu, C.P. Particulate ECM biomaterial ink is 3D printed and naturally crosslinked to form structurally-layered and lubricated cartilage tissue mimics. *Biofabrication* **2022**, *14*, 025021. [[CrossRef](#)]
52. Buffa, R.; Odstrčilová, L.; Šedová, P.; Basarabová, I.; Novotný, J.; Velebný, V. Conjugates of modified hyaluronic acid with amino compounds for biomedical applications. *Carbohydr. Polym.* **2018**, *189*, 273–279. [[CrossRef](#)]
53. Uman, S.; Dhand, A.; Burdick, J.A. Recent advances in shear-thinning and self-healing hydrogels for biomedical applications. *J. Appl. Polym. Sci.* **2020**, *137*, 48668. [[CrossRef](#)]
54. Wang, L.L.; Highley, C.B.; Yeh, Y.C.; Galarraga, J.H.; Uman, S.; Burdick, J.A. Three-dimensional extrusion bioprinting of single- and double-network hydrogels containing dynamic covalent crosslinks. *J. Biomed. Mater. Res. Part A* **2018**, *106*, 865–875. [[CrossRef](#)] [[PubMed](#)]
55. Shi, W.; Huang, J.; Fang, R.; Mingjie, M. Imparting Functionality to the Hydrogel by Magnetic-Field-Induced Nano-assembly and Macro-response. *Appl. Mater. Interfaces* **2020**, *12*, 5177–5194. [[CrossRef](#)] [[PubMed](#)]
56. Shi, L.; Zeng, Y.; Zhao, Y.; Yang, B.; Ossipov, D.; Tai, C.W.; Dai, J.W.; Xu, C.G. Biocompatible Injectable Magnetic Hydrogel Formed by Dynamic Coordination Network. *Appl. Mater. Interfaces* **2019**, *11*, 46233–46240. [[CrossRef](#)]
57. Zhang, Y.; Sun, Y.; Yang, X.; Hilbornand, J.; Heerschapand, A.; Ossipov, D.A. Injectable in situ forming hybrid iron oxide-hyaluronic acid hydrogel for magnetic resonance imaging and drug delivery. *Macromol. Biosci.* **2014**, *14*, 1249–1259. [[CrossRef](#)]
58. Tay, A.; Sohrabi, A.; Poole, K.; Seidlits, S.; Carlo, D.D. A 3D magnetic hyaluronic acid hydrogel for magnetomechanical neuromodulation of primary dorsal root ganglion neurons. *Adv. Mater.* **2018**, *30*, 1800927. [[CrossRef](#)]

59. Barbucci, R.; Giani, G.; Fedi, S.; Bottari, S.; Casolaro, M. Biohydrogels with magnetic nanoparticles as crosslinker: Characteristics and potential use for controlled antitumor drug-delivery. *Acta Biomater.* **2012**, *8*, 4244–4252. [[CrossRef](#)]
60. Tran, K.A.; Kraus, E.; Clark, A.T.; Bennett, A.; Pogoda, K.; Cheng, X.; Cebers, A.; Janmey, P.; Galie, P.A. Dynamic Tuning of Viscoelastic Hydrogels with Carbonyl Iron Microparticles Reveals the Rapid Response of Cells to Three-Dimensional Substrate Mechanics. *ACS Appl. Mater. Interfaces* **2021**, *13*, 20947–20959. [[CrossRef](#)]
61. Koand, E.S.; Kimand, C.; Choi, Y.; Lee, K.Y. 3D printing of self-healing ferrogel prepared from glycol chitosan, oxidized hyaluronate, and iron oxide nanoparticles. *Carbohydr. Polym.* **2020**, *245*, 116496. [[CrossRef](#)]
62. Choi, Y.; Kim, C.; Kim, H.S.; Moon, C.; Lee, K.Y. 3D Printing of dynamic tissue scaffold by combining self-healing hydrogel and self-healing ferrogel. *Colloids Surfaces B Biointerfaces* **2021**, *208*, 112108. [[CrossRef](#)]
63. Mo, C.; Xiang, L.; Chen, Y. Advances in Injectable and Self-healing Polysaccharide Hydrogel Based on the Schiff Base Reaction. *Macromol. Rapid Commun.* **2021**, *42*, 2100025. [[CrossRef](#)]
64. Townsend, J.M.; Beck, C.E.; Gehrke, S.H.; Berkland, C.J.; Detamore, M.S. Flow behavior prior to crosslinking: The need for precursor rheology for placement of hydrogels in medical applications and for 3D bioprinting. *Prog. Polym. Sci.* **2019**, *91*, 126–140. [[CrossRef](#)] [[PubMed](#)]
65. Zuo, X.; Tang, H.; Zhu, X.; Zhang, D.; Gao, W. Injectable magnetic hydrogels for self-regulating magnetic hyperthermia and drug release. *Mod. Phys. Lett. B* **2021**, *35*. [[CrossRef](#)]
66. Jahanban-Esfahlan, R.; Derakhshankhah, H.; Haghshenas, B.; Massoumi, B.; Abbasian, M.; Jaymand, M. A bio-inspired magnetic natural hydrogel containing gelatin and alginate as a drug delivery system for cancer chemotherapy. *Int. J. Biol. Macromol.* **2020**, *156*, 438–445. [[CrossRef](#)] [[PubMed](#)]
67. Bulpitt, P.; Aeschlimann, D. New strategy for chemical modification of hyaluronic acid: Preparation of functionalized derivatives and their use in the formation of novel biocompatible hydrogels. *J. Biomed. Mater. Res.* **1999**, *47*, 152–169. [[CrossRef](#)]
68. Maia, J.; Carvalho, R.A.; Coelho, J.F.J.; Simões, P.N.; Gil, M.H. Insight on the periodate oxidation of dextran and its structural vicissitudes. *Polymer* **2011**, *52*, 258–265. [[CrossRef](#)]
69. Nonsuwan, P.; Matsugami, A.; Hayashi, F.; Hyon, S.H.; Matsumura, K. Controlling the degradation of an oxidized dextran-based hydrogel independent of the mechanical properties. *Carbohydr. Polym.* **2019**, *204*, 131–141. [[CrossRef](#)]
70. Mendichi, R.; Soltés, L.; Schieroni, A.G. Evaluation of Radius of Gyration and Intrinsic Viscosity Molar Mass Dependence and Stiffness of Hyaluronan. *Biomacromolecules* **2004**, *4*, 1805–1810. [[CrossRef](#)]
71. Hersloef, A.; Sundeloef, L.O.; Edsman, K. Interaction between polyelectrolyte and surfactant of opposite charge: Hydrodynamic effects in the sodium hyaluronate/tetradecyltrimethylammonium bromide/sodium chloride/water system. *J. Phys. Chem.* **1992**, *96*, 2345–2348. [[CrossRef](#)]
72. Kok, C.M.; Rudin, A. Relationship between the hydrodynamic radius and the radius of gyration of a polymer in solution. *Die Makromol. Chemie Rapid Commun.* **1981**, *2*, 655–659. [[CrossRef](#)]
73. Zhou, H.X.; Szabo, A. Theory and simulation of the time-dependent rate coefficients of diffusion-influenced reactions. *Biophys. J.* **1996**, *71*, 2440–2457. [[CrossRef](#)]
74. Zellermann, A.M.; Bergmann, D.; Mayer, C. Cation induced conformation changes in hyaluronate solution. *Eur. Polym. J.* **2013**, *49*, 70–79. [[CrossRef](#)]
75. Xu, C.; Hung, C.; Cao, Y.; Liu, H.H. Tunable Crosslinking, Reversible Phase Transition, and 3D Printing of Hyaluronic Acid Hydrogels via Dynamic Coordination of Innate Carboxyl Groups and Metallic Ions. *ACS Appl. Bio Mater.* **2021**, *4*, 2408–2428. [[CrossRef](#)] [[PubMed](#)]
76. Radhakrishnan, J.; Subramanian, A.; Krishnan, U.M.; Sethuraman, S. Injectable and 3D Bioprinted Polysaccharide Hydrogels: From Cartilage to Osteochondral Tissue Engineering. *Biomacromolecules* **2017**, *18*, 1–26. [[CrossRef](#)] [[PubMed](#)]
77. Chang, C.; Lue, A.; Zhang, L. Effects of Crosslinking Methods on Structure and Properties of Cellulose/PVA Hydrogels. *Macromol. Chem. Phys.* **2008**, *209*, 1266–1273. [[CrossRef](#)]
78. Radulescu, D.M.; Neacsu, I.A.; Grumezescu, A.M.; Andronescu, E. New Insights of Scaffolds Based on Hydrogels in Tissue Engineering. *Polymers* **2022**, *14*, 799. [[CrossRef](#)]
79. Hölzl, K.; Lin, S.; Tytgat, L.; Vlierberghe, S.V.; Gu, L.; Ovsianikov, A. Bioink properties before, during and after 3D bioprinting. *Biofabrication* **2016**, *8*, 032002. [[CrossRef](#)]
80. Wang, B.; Moura, A.G.; Chen, J.; Erturk, A.; Hu, Y. Characterization of hydrogel structural damping. *Extrem. Mech.* **2020**, *40*, 100841. [[CrossRef](#)]
81. LoPachin, R.M.; Gavin, T. Molecular Mechanisms of Aldehyde Toxicity: A Chemical Perspective. *Chem. Res. Toxicol.* **2014**, *27*, 1081–1091. [[CrossRef](#)]
82. Gründelová, L.; Gregorova, A.; Mráček, A.; Vícha, R.; Smolka, P.; Minařík, A. Viscoelastic and mechanical properties of hyaluronan films and hydrogels modified by carbodiimide. *Carbohydr. Polym.* **2015**, *119*, 142–148. [[CrossRef](#)]
83. Tumanski, S. Chapter Magnetic Materials. In *Handbook of Magnetic Measurements*; CRC Press: Boca Raton, FL, USA, 2011. [[CrossRef](#)]
84. Genovese, D.B. Shear rheology of hard-sphere, dispersed, and aggregated suspensions, and filler-matrix composites. *Adv. Colloid Interface Sci.* **2012**, *171*, 1–16. [[CrossRef](#)] [[PubMed](#)]
85. Gila-Vilchez, C.; Duran, J.D.G.; Gonzalez-Caballero, F.; Zubarev, A.; Lopez-Lopez, M.T. Magnetorheology of alginate ferrogels. *Smart Mater. Struct.* **2019**, *28*, 035018. [[CrossRef](#)]

86. Sözeri, H.; Alveroğlu, E.; Kurtan, U.; Şenel, M.; Baykal, A. Magnetic hydrogel with high coercivity. *Mater. Res. Bull.* **2013**, *48*, 2751–2757. [[CrossRef](#)]
87. Cox, J.S.G.; Kennedy, G.R.; King, J.; Marshall, P.R.; Rutherford, D. Structure of and Iron-Dextran Complex. *J. Pharm. Sci.* **1972**, *24*, 513–517. [[CrossRef](#)] [[PubMed](#)]
88. Bendix, P.M.; Koenderink, G.H.; Cuvelier, D.; Dogic, Z.; Koeleman, B.N.; Briehar, W.M.; Field, C.M.; Mahadevan, L.; Weitz, D.A. A Quantitative Analysis of Contractility in Active Cytoskeletal Protein Networks. *Biophys. J.* **2008**, *94*, 3126–3136. [[CrossRef](#)]
89. Laskin, G.S.; Gordon, B.S. Changes to the Skeletal Muscle Gene Expression Signature in Response to Nutrient and/or Mechanical Stimuli. *FASEB J.* **2022**, *36*, R3761. [[CrossRef](#)]
90. Singh, G.; Chanda, A. Mechanical properties of whole-body soft human tissues: A review. *Biomed. Mater.* **2021**, *16*. [[CrossRef](#)]
91. D'Este, M.; Eglin, D.; Alimi, M. A systematic analysis of DMTMM vs EDC/NHS for ligation of amines to Hyaluronan in water. *Carbohydr. Polym.* **2014**, *108*, 239–246. [[CrossRef](#)]
92. Huiru, Z.; Heindel, N.D. Determination of Degree of Substitution of Formyl Groups in Polyaldehyde Dextran by the Hydroxylamine Hydrochloride Method. *Pharm. Res.* **1991**, *8*, 400–402. [[CrossRef](#)]

Magneto-responsive hyaluronan hydrogel for hyperthermia and bioprinting: magnetic, rheological properties and biocompatibility

L. Vítková,^{1,2} I. Smolková,^{1,2} N. Kazantseva,^{1,2} L. Musilová,^{1,2} P. Smolka,^{1,2} K. Valášková,² K. Kocourková,^{1,2} M. Humeník,³ A. Minařík,^{1,2} P. Humpolíček,^{1,2} and A. Mráček^{1,2}

¹*Faculty of Technology, Tomas Bata University in Zlín, Vavrečkova 5669, 76001 Zlín, Czech Republic*

²*Centre of Polymer Systems, Tomas Bata University in Zlín, tř. Tomáše Bati 5678, 76001 Zlín, Czech Republic*

³*Department of Biomaterials, Faculty of Engineering Science, Universität Bayreuth, Prof.-Rüdiger-Bormann-Str. 1, 95447 Bayreuth, Germany*

(*Electronic mail: smolka@utb.cz)

(Dated: 6 June 2023)

Magneto-responsive soft hydrogels are used for a number of biomedical applications, e.g., magnetic hyperthermia, drug delivery, tissue engineering, and neuromodulation. In this work, this type of hydrogel has been fabricated from hyaluronan (HA) filled with a binary system of Al₂O₃ nanoparticles (NPs) and multicore magnetic particles (MCPs) which were obtained by clustering of superparamagnetic iron oxide FeO_x NPs. It was established that the presence of diamagnetic Al₂O₃ has several positive effects: it enhances the hydrogel storage modulus and long-term stability in the cell cultivation medium; prevents the magnetic interaction among the MCPs. The HA hydrogel provides rapid heating of 0.3 °C per min under exposure to low amplitude radiofrequency alternating magnetic field (AMF). Furthermore, the magneto-responsive hydrogel was successfully used to encapsulate cells and extrusion-based 3D printing with 87±6 % cell viability, thus providing a bio-ink. The combination of high heating efficiency, softness, cytocompatibility, and 3D printability of magnetic HA hydrogel leads to a material suitable for biomedical applications.

I. INTRODUCTION

Magnetic hydrogels are promising materials for biomedical applications due to their ability to mimic the microstructure of extracellular matrix and strong response to external magnetic stimulus¹. Magnetic iron oxides (FeO_x), magnetite and maghemite, are well-recognized magnetic components of magnetically responsive hydrogels². Additionally, these materials are non-toxic and degradable *in vivo* through a biotransformation mechanism, producing non-toxic side products³⁻⁵. FeO_x are found to have the ability to produce significant heat in an alternating magnetic field (AMF) due to magnetization reversal⁶. Thus, FeO_x have been examined as potential materials for thermosensitive biological applications, controlled drug delivery⁷, thermal neuromodulation⁸, or magnetic hyperthermia⁹. Controlled drug delivery typically benefits from including the magnetic material as a specific polymer matrix filler, demonstrating self-healing or thermoresponsive character^{10,11}. The use of magnetic heating for neuromodulation was pioneered by Chen et al., 2015, by triggering the heat-sensitive receptors of TRPV1 ion channel¹². This study prompted wide research of wireless neuromodulation via magnetic heating¹³⁻¹⁷, and has found use in regenerative medicine and tissue engineering research^{18,19}. Inductive heating of the magnetic particles is also utilized in hyperthermia, a selective cancer treatment method in which the magnetic material is embedded in the tumor and is heated by exposure to the external AMF. Cancer cells are selectively damaged or killed at temperatures between 42°C-45°C due to apoptosis and necrosis^{6,20}. However, there are strict limitations on the frequency and amplitude of AMF due to patients' safety concerns. Currently, clinically relevant AMF parameters in hyperthermia are the frequencies within 0.05 – 1 MHz and

amplitudes $\leq 15 \text{ kA}\cdot\text{m}^{-121}$, considered safe for medical applications.

The potential of FeO_x largely depends on the particle size. The bulk material exhibits so-called hard magnetism and large coercivity. Lowering the material's size leads to the multidomain structure's collapse, resulting in superparamagnetic behavior at the size below 20 nm⁶. At this state, the magnetic particles show zero coercivity and remanence magnetization due to the very low energy barrier of magnetization reversal. Therefore, a magnetic moment in superparamagnetic NPs can rotate freely toward the direction of the magnetic field without energy loss. However, superparamagnetic FeO_x NPs tend to aggregate due to interparticle magnetic interactions, leading to the so-called multicore particles (MCPs)^{22,23}. These MCPs exhibit an effective magnetic moment, a combination of individual magnetic moments of the superparamagnetic NPs cores, appearing as a ferromagnetic material and producing energy loss upon magnetization reversal in AMF²⁴.

One of the significant drawbacks of using single FeO_x NPs and MCPs is their tendency to aggregate and sediment in neutral pH⁶. A possible way to enhance the particle's stability is the addition of highly charged Al₂O₃ NPs, increasing the system stability upon strong electrostatic repulsion²⁵. This so-called nanoparticle haloing was first described by Tohver et al., 2001 for mixtures of silica microspheres and hydrous zirconia NPs²⁶. Zubir et al., 2015 demonstrated that Al₂O₃ NPs ensure the stability of the binary system containing commercial magnetite NPs of the size 50-100 nm and Al₂O₃ NPs at pH of 6.5⁵¹. Nevertheless, utilizing this approach to stabilize magnetic MCPs is uncommon so far. This methodology appears promising to stabilize the dispersions of monodisperse magnetic MCPs in physiological pH 7.4, although the isoelectric point of FeO_x is between pH 4-5²⁷.

In magnetic hyperthermia, thermally triggered drug delivery, as well as in thermal neuromodulation, the magnetic material (heat mediator), in the form of magnetic fluid or composite, should fulfill several requirements, such as biocompatibility, possibility to be delivered to the desired site, homogeneous distribution of the magnetic particles, long term retention and high heating rate in the clinically approved AMF^{6–8}. The methods of the material administration include (a) arterial injection, (b) direct injection, (c) surgical implantation, and (d) active targeting by site-specific antibodies^{28–31}. Therefore, the matrix encapsulating the magnetic material requires specific mechanical and rheological properties. The injectability of the material allows for omitting surgical procedures, lowering the potential risks and patients' discomfort³². However, utilization of the water dispersions of magnetic particles in practical medical applications revealed several drawbacks, namely the difficulty of securing the liquid system in the desired location, uniform distribution, and long-term retention⁹. Therefore, embedding the magnetic particles in a hydrogel matrix is a favorable strategy^{33,34}. Hyaluronan (HA) based hydrogels cross-linked via Schiff base formation represent a suitable carrier^{35,36}. They are biocompatible and biodegradable due to the natural origin of HA. Moreover, the dynamic character of Schiff base cross-links allows injectability and fast recovery even in a fully cross-linked state³⁷. The material's relatively low storage modulus and high water content resemble some human soft tissue types, such as breast fat tissue³⁸, or spinal cord neural tissue³⁹.

In particular, regenerative medicine and tissue engineering can benefit from precise tissue constructs providing optimal mechanical, electrochemical, and biological environments during cell cultivation and tissue growth^{40,41}. To this end, 3D printing techniques are used with increasing popularity due to unprecedented precision⁴². Regarding tissue engineering, bioprinting appears to be a promising approach, as it involves living cells encapsulated in the printing material during the printing process. This technique can thus provide a highly uniform distribution of cells throughout the whole material⁴⁴, while post-printing cell seeding may often result in increased cell density on the surface of the scaffold, which needs to be addressed through complicated manipulation of the printed scaffold geometry⁴⁵. The use of magneto-responsive hydrogels in the 3D printing of scaffolds has been reported previously^{36,43}, whereas their incorporation in a bioprinting process enabled thermally triggered neuromodulation⁴⁶.

In the presented work, we studied the effects of diamagnetic Al₂O₃ NPs on the magneto-structural properties of FeO_x MCPs dispersions. It was found that the Al₂O₃ NPs enhance the heating efficiency of the MCPs in the AMF. MCPs and MCPs with Al₂O₃ NPs were used to prepare the magnetic HA hydrogel that was examined as a potential mediator of inductive heating in medical applications. The effect of the Al₂O₃ NPs on the heating efficiency was also confirmed in the hydrogel. The favorable rheological profile of the magneto-responsive HA hydrogel allowed extrusion-based bioprinting to be performed and thus confirmed the material's potential to develop magneto-responsive bio-ink. Therefore, the elab-

orated HA hydrogel filled with iron oxide MCPs and Al₂O₃ NPs can provide cytocompatible material capable of rapid heating in AMF while securing precise scaffold engineering through additive manufacturing technologies – 3D printing and bioprinting.

II. MATERIALS AND METHODS

A. MCPs synthesis

FeO_x NPs were prepared by co-precipitation of FeCl₂ (in the form of FeCl₂·2 H₂O, Merck KGaA, Germany) and FeCl₃ (in the form of FeCl₃·6 H₂O, Merck KGaA, Germany) in alkaline solution according to the procedure described previously²⁴. Briefly, the respective salts in Fe²⁺:Fe³⁺ 1:2 molar ratio were dissolved in demineralized water (Millipore Q System, Millipore, UK), and added dropwise to 0.38 M NH₃ solution (diluted from NH₃ 30%, Penta, Czechia) at 70°C. The reaction was carried on for 1 hour under vigorous stirring, 700 rpm. After that, a dark brown precipitate was obtained, containing FeO_x NPs of 13 nm and polydispersity 0.3 according to transmission electron microscopy (TEM)²⁴.

To achieve peptization and size separation of the FeO_x MCPs, a procedure described in Smolkova et al., 2017⁴⁷ was followed. The procedure requires washing of the FeO_x NPs precipitate 3 times with demineralized water, followed by acidification with 1 mM HCl (diluted from 35% HCl, Penta, Czechia) to pH 2,5 and ultrasonication for 20 minutes. After that, the dispersion was let to sediment on a strong permanent magnet for 30 minutes, and the brown supernatant was collected. The dispersion of particles collected at pH 2,5 with the average particle size 85 nm and zeta potential 45–55 mV⁴⁷ was used in the study. The concentration of FeO_x in the dispersion was determined by X-ray fluorescence spectroscopy using ARL Quant'X EDXRF Analyzer (Thermo Scientific, MA, USA). The Al₂O₃ nanopowder (13 nm primary particle size, 99.8% trace metal basis; Merck KGaA, Germany) was mixed with FeO_x by adding the appropriate amount of Al₂O₃ powder to the FeO_x dispersion to obtain weight ratios of FeO_x:Al₂O₃ 4:1, 3:1, 2:1, 1:1, and 1:2 respectively. Then, the mixtures were sonicated for 20 minutes.

B. Particle size and zeta potential analysis

The hydrodynamic size of MCPs and zeta potential were measured by dynamic light scattering (DLS) and laser Doppler velocimetry on Zetasizer Nano ZS (Malvern Panalytical, UK). The hydrodynamic radii of particles, expressed as z-average particle diameters, were measured at 25°C at a scattering angle of 173°. The polydispersity index (PDI) describing the width of the particle size distribution in a given sample was also determined. The measurements were performed in triplicates, and an arithmetic average of the results is presented.

C. HA hydrogels preparation

HA cross-linking via Schiff base formation was performed with two polysaccharide derivatives – adipic acid dihydrazide (ADH) grafted HA (HA-ADH), and oxidized dextran (DEX-OX). The derivatization and hydrogel formation is thoroughly described in Vítková et al., 2022³⁷ and Musilová et al., 2022⁴⁸. Briefly, HA-ADH was prepared by 4-(4,6-Dimethoxy-1,3,5-triazin-2-yl)-4-methylmorpholinium chloride (DMTMM; Merck KGaA, Germany) mediated reaction. HA (243 kDa; Contipro, Czechia) 1 wt.% solution was obtained by dissolving the polymer in demineralized water at 50°C. After cooling to room temperature, DMTMM and ADH (Merck KGaA, Germany) was added to the reaction mixture. The molar ratio of the reactants HA:DMTMM:ADH was 4:1:4. The reaction proceeded for 24 hours at 25°C under constant stirring. DEX-OX was, on the other hand, prepared by periodate oxidation. The procedure was derived from Maia et al., 2011⁴⁹. Dextran (40 kDa, Merck KGaA, Germany) was dissolved in demineralized water by mixing at 50°C overnight to obtain a 13 wt.% solution. After cooling the solution to room temperature, sodium periodate (Merck, NJ, USA) was added in a 5:2 molar ratio of dextran:NaIO₄. The reaction was left to proceed under constant mixing for 4 hours at 25°C in the dark. In both cases, the products were purified by dialysis against distilled water for three days (cut-off 5000 Da) and subsequently frozen and lyophilized.

To produce hydrogels, HA-ADH and DEX-OX were dissolved in MCPs dispersions (without or with Al₂O₃) by shaking overnight and at 25°C to obtain 2 wt.% of modified polymer in the solution. Afterward, the solutions of HA-ADH and HA-OX were mixed by vortex, and Schiff-base formation occurred spontaneously. The gelation process was finished within 30 minutes after the mixing.

D. Induction heating in AMF

The heating efficiency of the prepared MCPs in three different forms was determined: water dispersions, high-viscosity agar dispersions, and Schiff base cross-linked HA hydrogels. To obtain the dispersions of MCPs in the agar matrix, 3.4 wt% of agarose (Merck KGaA, Germany) was added to the water dispersion of MCPs and heated under continuous stirring to 70°C. After this, the mixture was placed in a fridge, where the solid matrix was quickly formed. The samples of HA hydrogel were prepared as described in IIC, and left to gelate at 25°C for at least 1 hour to ensure full cross-linking of the mixture.

A homemade AMF generator was used to determine the heating efficiency of the samples. It consisted of a signal generator Agilent 33521A (Agilent Technologies, CA, USA), RF broadband amplifier AR RF/Microwave Instrumentation 800A3A, induction coil (90 mm diameter), interchangeable capacitors, and magnetic field sensor. The measurements were carried out at AMF of 525 kHz frequency and amplitude range 5.4 mT to 9.4 mT, or 1050 kHz frequency and am-

plitude range 5.4 mT to 7.4 mT, respectively. The temperature was measured with monitoring system ReFlex 4, Neoptix (Qualitrol, NY, USA), and fiber optic temperature sensor TIS-03-PT06 inserted directly in the sample.

E. Morphological and elemental analysis

The inner morphology of the hydrogels was examined by scanning electron microscopy (SEM) of cross-sections of lyophilized samples of hydrogels using Phenom XL G2 instrument (Thermo Scientific, MA, USA). The 3D printed hydrogel samples were frozen first at -18 °C for 24 h, followed by freeze drying in a freeze-dryer (ALPHA1-2 LD plus, M. Christ, Osterode am Harz, Germany). Additionally, Phenom XL G2 instrument (Thermo Scientific, MA, USA) was used for elemental analysis by energy-dispersive X-ray spectroscopy (EDX). The accelerating voltage used for analysis was 15 kV. The samples were sputtered with a gold/palladium layer before measurement.

F. Rheological analysis

Rheological measurements were performed using a rotational rheometer, Anton Paar MCR 502 (Anton Paar, Austria), at human body temperature (37°C) and hyperthermia temperature (42°C) under normal pressure in air, using an MRD 180/1T measuring cell with parallel plate 20/MRD/TI measuring geometry in oscillation at constant deformation (varying to attribute to the linear region) with shear rate increasing from 0.001 s⁻¹ to 1 s⁻¹. The hydrogel samples were prepared 1 hour in advance in the form of circular plates with a diameter of 25 mm and a thickness of 1.5 mm. Viscosity is shown with respect to the shear rate in the measured range, i.e., from 0.001 s⁻¹ to 1 s⁻¹. On the other hand, storage modulus (G') is expressed as the mean value measured in the range 0.01 rad·s⁻¹ to 0.1 rad·s⁻¹, which corresponds to the linear region with a constant value of G'. Additionally, cyclic oscillatory shear stress was applied to the samples in the following specifications: constant low (0.03 s⁻¹) and high shear rate (0.8 s⁻¹) were applied for 50 s. The low-high shear rate cycle was repeated 3 times. The deformation was kept constant throughout this measurement.

G. Long-term stability and *in vitro* cytotoxicity

To assess the long-term stability of the hydrogels, the samples were placed in perforated sample holders and submerged in desired medium and conditions, either demineralized water at 25°C or Dulbecco's Modified Eagle's Medium (PAA Laboratories GmbH, Austria) containing 10 % bovine calf serum (BioSera, France) and 1 % of Penicillin/Streptomycin (GE Healthcare HyClone, United Kingdom), hereinafter denoted "complete DMEM" for simplification, at 37°C. The samples were weighted once every 24 hours. The results are expressed as the relative changes in weight, where the original sample

weight is considered 100%. The measurement was performed in triplicate, and the average results are given here.

Cytotoxicity testing was done according to ISO standard 10993 using a mouse embryonic fibroblast cell line (ATCC CRL-1658 NIH/3T3, USA). The complete DMEM was used as a cultivation medium. The cell line was incubated at 37°C in 5% CO₂ in humidified air. The relative humidity value during the cell line incubation was 95%. Sterilization of hydrogels was done before cytotoxicity testing by shaking samples in 70% ethanol for 1 hour at laboratory temperature. Elution of the ethanol from samples was done by aspiration, a short rinsing in PBS, and then by shaking the samples in ultrapure water for 48 hours at laboratory temperature. After ultrapure water aspiration, extracts were created. Extracts were prepared according to ISO standard 10993-12 (100 mg of hydrogel per 1 mL of media). The tested material was incubated in a cultivation medium for 24 hours at 37°C with stirring. The parent extracts (100 vol%) were then diluted in a medium to obtain a series of dilutions with concentrations of 75, 50, 25, 10, and 1 vol%. All extracts were used for up to 24 hours. The cells were seeded at a concentration of 10⁵ per well in 96-well plates (TPP, Switzerland). After the pre-incubation period (24 hours), the extracts were filtered using a syringe filter with a membrane pore size of 0.22 μm (TPP, Switzerland) to ensure that no residual hydrogel was present. The filtered extracts in required dilutions were added to the cells and incubated for 24 hours. Subsequently, tetrazolium salt (MTT cell proliferation assay kit, Duchefa Biochemie, Netherlands) was used to determine cell viability. Absorbance was measured using a microplate reader Infinite M200 PRO (Tecan, Switzerland) at 570 nm, and the reference wavelength was adjusted to 690 nm. The results are presented as the percent reduction of cell viability when compared to cells cultivated in a medium without the extracts of tested materials. The morphology of cells from the culture plates was observed using an inverted Olympus IX 81 phase-contrast microscope (Olympus, Japan).

H. Bioprinting

Bioprinting was done with BALB/3T3 mouse fibroblasts cell line. The cells were cultivated in complete DMEM at 37°C in a humidified incubator (95% relative humidity, 5% CO₂, HeraCell, Germany). The cells were split using 0.05% trypsin (Merck KGaA, Germany).

Bioinks were obtained by adding 100 μL of cell suspension in PBS (total amount of BALB/3T3 was 3·10⁶) into 1 mL of immediately mixed HA-ADH and DEX-OX solutions in FeO_x:Al₂O₃ dispersion. The encapsulation of the cells within the bio-ink matrix was achieved by rapid gelation of the polymer precursors. The bio-inks were loaded into cartridges and printed by pneumatic extrusion printhead. To this end, 3D Discovery Bioplotter (RegenHU, Switzerland) was used. The printing was done through a cylindrical needle of 0.52 mm inner diameter. The printing model was chosen as a simple 1 cm x 1 cm grid. The thickness of each layer was 0.5 mm. The scaffold consisted of two layers and had a thickness of 1 mm. The printing pressure was 2.078·10⁵ Pa.

Fluorescence imaging of the distribution of the cells through the material was done by means of Laser Scanning Confocal Microscopy (LSCM) using the Olympus FLU-OVIEW FV3000 (Olympus, Japan) device. The Plan-Apochromat objective with magnification 10x and numerical aperture NA=0.8, or 4x and NA=0.4 respectively were used for analysis. The figures were obtained as three-dimensional reconstructions from confocal images in the z-axis. The cell-loaded samples were fixed and fluorescence stained following this protocol: The staining solution containing Phalloidin DyLight 488 (Thermo Fisher Scientific, Germany) and DAPI (Thermo Fisher Scientific, Germany), each in 1:1000 dilution in PBS, was prepared immediately before fixing and kept in the dark. The samples were washed 3 times with PBS. After that, the cells were fixed with 3.7% formaldehyde (Thermo Fisher Scientific, Germany) solution for 25 minutes at room temperature. The fixative solution was aspirated, and the samples were washed once with PBS. The samples were then submerged in 0.1% Triton X-100 (Thermo Fisher Scientific, Germany) solution for 30 minutes to permeabilize cell membranes. After aspiration of permeabilization solution and washing samples once with PBS, the samples were submerged in the staining solution for 1 hour. Finally, the samples were washed twice with PBS and kept in a dark, cold, and humid environment before fluorescence imaging.

Directly following 3D bioprinting, live/dead staining was performed. The staining solution was prepared as follows: 2 μL of ethidium homodimer I (dead stain; Thermo Fisher Scientific, Germany) and 2 μL calcein acetoxyethyl ester (live stain; Thermo Fisher Scientific, Germany) were diluted in 10 mL of PBS. The staining solution was poured over the prints in sufficient amount, and left in an incubator for 1 hour to allow full diffusion of the staining solution through the material. The stained cells were observed in a LifeCell fluorescence microscope (DMI6000, Leica, Wetzlar, Germany). The percentage of live cells was determined as an average of images obtained from 3 different spots in the sample.

I. Statistical evaluation

Where appropriate, respective standard deviations of the arithmetic mean for the 68.3% confidence interval are presented along with the arithmetic mean value. The p-value of 0.05 was used when appropriate.

III. RESULTS AND DISCUSSION

A. Characterization of MCPs dispersions

Water dispersions of the magnetic MCPs with low polydispersity were prepared as we described previously^{24,47}. The MCPs represent dense aggregates composed of bare magnetic iron oxide NPs of 13 nm determined by TEM. The average particle size of the MCP is 85 nm at pH 2.5 determined by DLS. With the increase of pH the MCPs size increases and zeta-potential decreases, leading to the sedimentation of the

particles at around pH 4.5²⁷. The stability of the dispersion in the acidic medium is ensured solely due to the electrostatic repulsion between positively charged MCPs, zeta potential 45 - 55 mV. In order to increase the stability at higher pH Al₂O₃ NPs were added to the dispersion of MCPs^{51,52}. Commercially available Al₂O₃ NPs are of 13 nm size and form aggregates of about 250 nm average particle size^{50,51}. Therefore, a binary system composed of magnetic MCPs of 85 nm and Al₂O₃ aggregates of 250 nm was obtained. Al₂O₃ aggregates ensure the electrostatic repulsion between magnetic MCPs, preventing them from sedimentation at higher pH⁵¹. MCPs being clusters of superparamagnetic particles present a unique magnetic entity, in which each core displays a magnetic moment, but the MCP behaves as if it had one collective magnetic moment. Apparently, the presence of diamagnetic Al₂O₃ NPs aggregates equally distributed in between the MCPs shield the magnetic interaction among the MCPs. Thus, the stability of the MCPs dispersion increases, as their tendency to aggregate is diminished.

B. The effect of Al₂O₃ on induction heating of MCPs dispersions

The heating efficiency of both single MCPs and MCPs with Al₂O₃ aggregates was characterized by the specific loss power (SLP), i.e. the measure of the temperature change in time as referred to the mass of magnetic material. AMF of 1050 kHz, 7.4 mT was applied to the dispersions. A substantial increase from 40 W·g⁻¹ for single MCPs to almost 60 W·g⁻¹ for MCPs with Al₂O₃ aggregates was observed (Figure 1). Due to their diamagnetic character (see Figure S2), a direct contribution of Al₂O₃ NPs aggregates to the SLP is of low probability, and the increase of SLP is apparently attributed to the changes in the magnetic interactions between the MCPs.

In general, inductive heating of the magnetic particles is the result of two relaxation processes – Brown relaxation and Néel relaxation⁵³. Brown relaxation is the process of particle rotation in the direction of the magnetic field (Figure 2(A))⁵⁴. Therefore, this type of relaxation is particularly dependent on the magnetic particles volume, and on the viscosity of the dispersion medium.

$$\tau_B = \frac{3V_h\eta}{k_B T} \quad (1)$$

Equation 1 defines the Brown relaxation time, i.e. the time necessary for the relaxation mechanism to align the magnetic moment with the direction a magnetic field. V_h denotes particle hydrodynamically effective volume, η is the dynamic viscosity of the dispersion medium, k_B stands for the Boltzmann constant and T is the temperature^{6,54}.

Néel relaxation, on the other hand, is related to the rotation of magnetic moment within the particle, and the heating is facilitated by energy release due to the change of magnetic state of the particle. The characteristic Néel relaxation time can be found as:

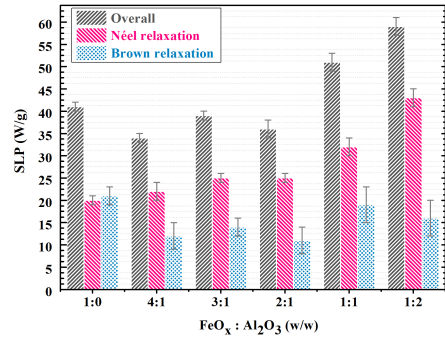


FIG. 1. SLP of FeO_x dispersions with the increasing amount of Al₂O₃; Overall denotes the SLP results for water dispersions, where both Brown and Néel relaxation are present; Néel relaxation denotes values obtained by measurement in agar gel, where Brown relaxation is suppressed and heating is facilitated only by Néel relaxation; Brown relaxation is the difference between overall SLP (measured in water dispersion), and Néel relaxation induced SLP (measured in agar gel)

$$\tau_N = \tau_0 e^{\frac{KV}{k_B T}} \quad (2)$$

where K is the magnetic anisotropy, V is the particle volume, k_B stands for the Boltzmann constant, T is the temperature and τ_0 is the factor approximately equal to 10^{-9} s^{6,54}. It is apparent, that Néel relaxation depends only on the intrinsic properties of the magnetic particles, while Brown relaxation is largely affected by the viscosity of the used medium⁵⁵. In order to understand the effect of Al₂O₃ aggregates shielding on the induction heating behavior of the MCPs, the contributions of the two types of relaxation were examined separately. To achieve that, the SLP measurements were conducted in two dispersion media – low viscosity (demineralized water), and high viscosity (agar gel). In low viscosity medium, both relaxation mechanisms are contributing to the induction heating. However, the high viscosity of the medium restricts Brown relaxation, allowing solely the Néel relaxation⁵⁶. Therefore, it is possible to distinguish the contribution of Brown relaxation to the overall SLP by subtracting the Néel relaxation contribution obtained from measurement in high viscosity medium⁵³. Agar gel was chosen in this case due to exceptionally high viscosity among water-based gels (10^4 - 10^5 Pa·s depending on the concentration and shear rate⁵⁷) that remains stable in the temperature range of the measurement (25°C-45°C) in order to ensure complete prevention of the Brown relaxation driven heating⁵⁸.

As for the Brown relaxation, the increase of Al₂O₃ content did not provide any significant change. Néel relaxation, on the other hand, follows the trend of overall SLP and increases with the increase of Al₂O₃ content. Therefore, Al₂O₃ shielding apparently leads to the weakening of the magnetic interactions among MCPs (Figure 2).

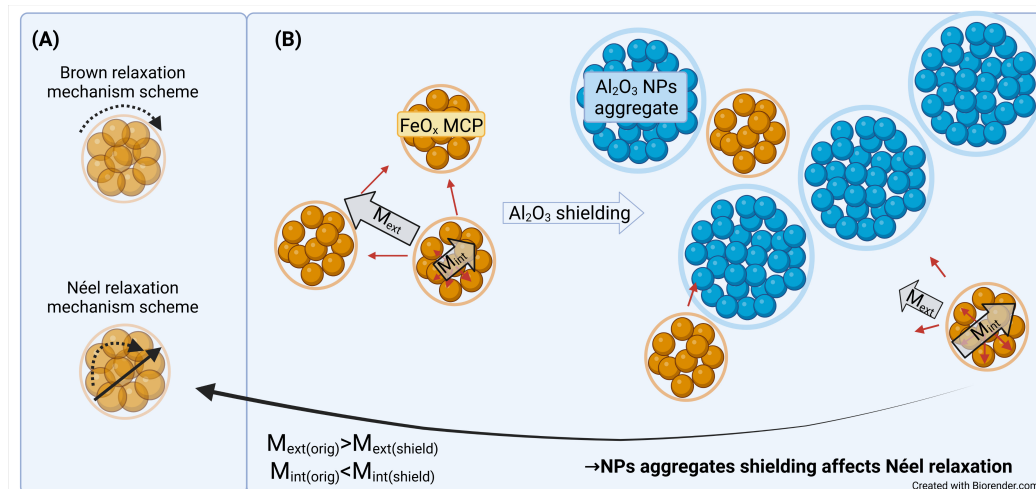


FIG. 2. (A) Schematic representation of the relaxation mechanisms of the MCPs; (B) Schematic representation of the Al_2O_3 shielding effect on the magneto-structural properties of the MCPs, where M_{ext} and M_{int} represent extrinsic and intrinsic magnetic interactions of MCPs respectively

C. Morphological analysis of the hydrogels

In order to be used as a selective heating agent the magnetic material should allow precise localization and uniform distribution within the desired tissue. In the current study, HA hydrogel was chosen as the matrix for MCPs due to its biocompatibility and ease of preparation³⁷ and high porosity, as shown in the present case (see Figure 3). This highly porous structure allows free diffusion of substances, thus creating an environment suitable for applications such as drug delivery (controlled release of therapeutics)⁵⁹ or tissue engineering (exchange of nutrients and waste among the cells)^{60,61}.

EDX analysis confirmed uniform distribution of Fe in the case of the MCPs filled HA hydrogels (Figure 3). This is a necessary condition for reproducibility of results obtained with the described material, and its subsequent applicability in medical field. In case of the addition of Al_2O_3 NPs to the MCPs dispersion, the EDX again showed the respective elements (Fe and Al) uniformly distributed throughout the material.

D. Assessment of HA hydrogels as mediators of induction heating

The solid character of hydrogels is bound to restrain Brown relaxation and thus decreased SLP in a wide range of amplitudes of AMF (see Figure 4). The hydrogels reached $25 \text{ W}\cdot\text{g}^{-1}$ as compared to aqueous dispersion reaching $40\text{--}60 \text{ W}\cdot\text{g}^{-1}$ in AMF of the frequency 1050 kHz and amplitude 7.4 mT. However, the SLP values in HA hydrogels are still higher compared to the values obtained in agar ($15 \text{ W}\cdot\text{g}^{-1}$).

Therefore, it is possible to assume that a certain portion of the heating is facilitated by Brown relaxation due to the softness of HA hydrogels allowing particle movement to some extent⁵⁶.

The heating efficiency of the HA hydrogels filled with single MCPs or MCPs with Al_2O_3 NPs aggregates was determined in two frequencies of the AMF (525 kHz and 1050 kHz) and the amplitudes ranging from 5.4 mT to 9.4 mT (Figure 4). As can be seen, the hydrogels filled with MCPs and Al_2O_3 aggregates displayed higher heating ability regardless of the AMF parameters. This is in correspondence with the previously described experiments and confirms that Al_2O_3 shielding facilitates the Néel relaxation. The experimental results demonstrated that at AMF, 1050 kHz, 7.4 mT, considered safe for use in medicine²¹, the samples heated at the rate of 0.3°C per minute. Therefore, the hyperthermia temperature range could be reached within 16.7 minutes. Thus, the investigated magnetic HA hydrogels are promising materials for magnetic hyperthermia treatment, as well as other thermally triggered therapies.

E. Rheology of the magneto-responsive hydrogel

The mechanical investigation of the hydrogels shows that increasing temperature from 37°C (body temperature) to 42°C (hyperthermia treatment) did not have any significant effect on hydrogels viscosity, or storage modulus (Figure 5 (A) - (C)). The hydrogels showed distinct shear thinning behavior, as their viscosity changes in the range of $10^2 \text{ Pa}\cdot\text{s}$ in the shear rate range of 10^2 s^{-1} (Figure 5 (A)). The individual differences between the curves in Figure 5 (A) measured at different temperatures fall within the measurement error. Generally,

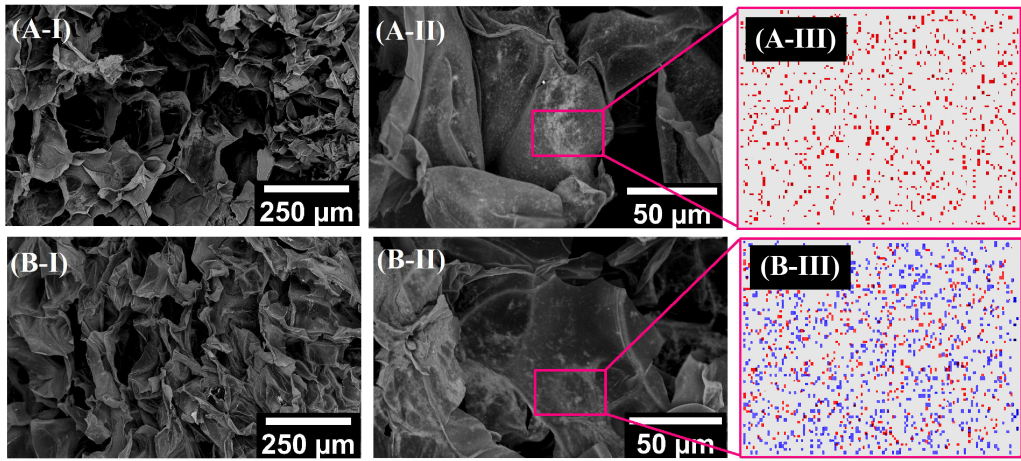


FIG. 3. SEM micrographs and EDX mapping of lyophilized hydrogel samples: A - FeO_x filled HA hydrogel; B - $\text{FeO}_x:\text{Al}_2\text{O}_3$ 1:1 filled HA hydrogel; I, II - SEM micrographs with different magnification; III - EDX mapping, red and blue dots denote Fe and Al, respectively

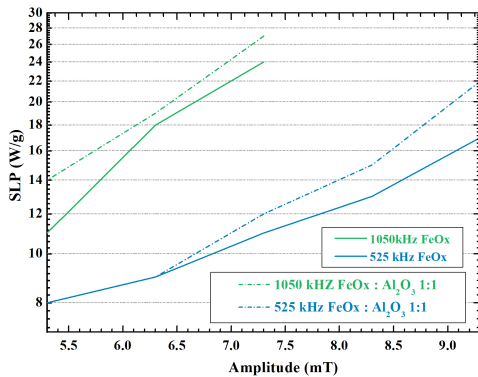


FIG. 4. SLP of magneto-responsive HA hydrogel as a function of AMF amplitude

shear-thinning hydrogels may find use as injectable, extrudable, and 3D printable materials⁶². At the low shear rate the hydrogels demonstrate the solid-like behavior, i.e. the loss modulus does not exceed storage modulus, $\tan \delta$ is lower than 1 (Figure S1 (A, B)).

Both hydrogels filled with MCPs and the mixture of MCPs and Al_2O_3 NPs aggregates displayed the storage modulus between 100-300 Pa (Figure 5 (C)), which corresponds to the values reported for normal fat tissue and spinal cord neural tissue^{38,39}. Therefore, the developed hydrogels can be for example useful in breast cancer treatment, as they would lower the discomfort of patients due to the close resemblance of the natural tissue.

The rheological measurements in the external magnetic field showed that the mechanical properties of the hydrogel are unaffected by the magnetic field, as the magneto-rheological effect (MRE) is less than 8% (Figure 5 (D)). This is apparently due to the low size of magnetic MCPs (85 nm), as well as due to the low particle concentration (0.3 wt.%). This is another factor contributing to diminishing the patient's discomfort.

3D printing applications, in particular, require not only shear thinning behavior but also fast recovery due to the nature of the process, in which the high shear stress in the print-head is suddenly lifted upon placing on the printbed⁶². As can be seen from Figure 5 (B), the hydrogels are capable of rapid change of rheological behavior in correspondence to the applied shear rate regardless of the temperature in the chosen temperature range. Additionally, the presence of Al_2O_3 has no observable impact on the reversibility of hydrogels' rheological behavior.

The cyclic shear stress testing proved the reversibility of Schiff base bonds forming the hydrogel. The material was able to return to the original viscosity and storage modulus from the fluid state within 30 s, as listed in Table I. These results make the proposed hydrogels promising materials for applications in extrusion-based 3D printing⁶³.

F. Stability during cultivation and *in vitro* cytotoxicity of the hydrogels

The proposed biomedical applications of the hydrogels, namely magnetic hyperthermia, and neuromodulation, as well as tissue engineering, require stability of the hydrogel structure over the course of several days. Long-term stability of the HA hydrogels was tested in mild conditions (water at 25°C),

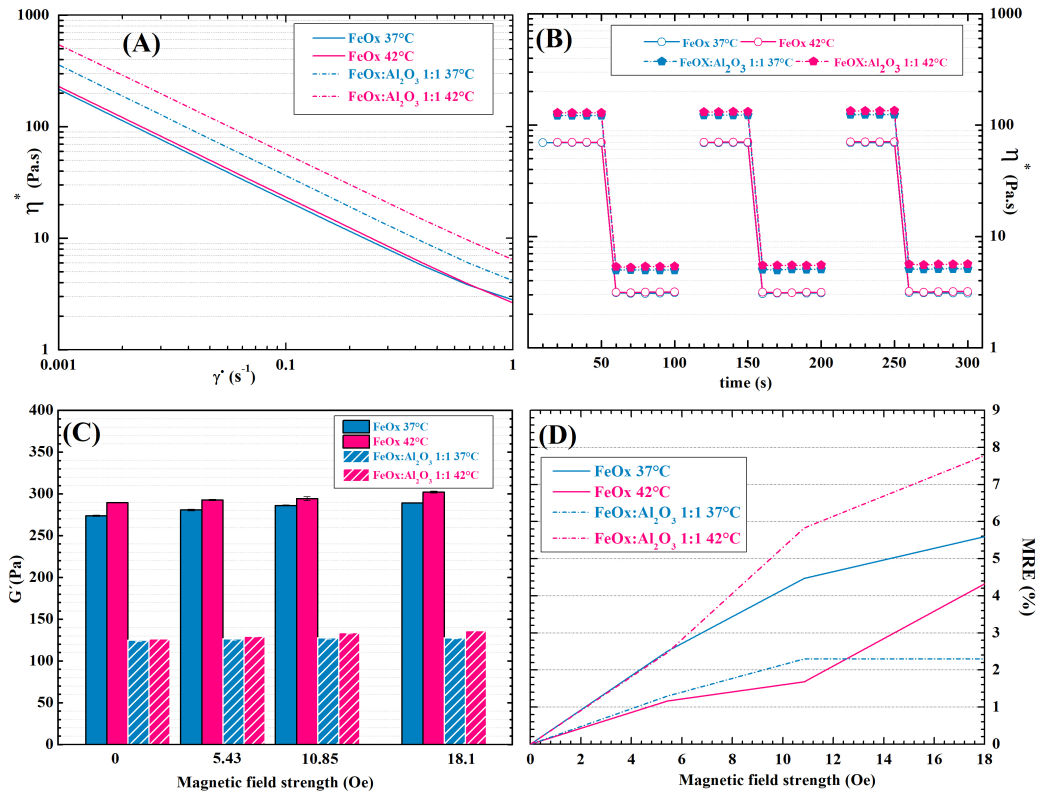


FIG. 5. Rheological characterization of the magneto-responsive HA hydrogels: (A) Dependence of magneto-responsive HA hydrogels viscosity on shear rate at body temperature (37°C) and hyperthermia temperature (42°); (B) Cyclic shear stress applied to hydrogels filled with FeO_x or FeO_x:Al₂O₃ 1:1 at normal body temperature (37°C) and at hyperthermia temperature (42°C) respectively; (C) Storage moduli of magneto-responsive HA hydrogels at different temperatures in increasing external magnetic field; (D) MRE induced in the magneto-responsive hydrogels by the external magnetic field.

and in simulated cell cultivation conditions (complete DMEM at 37°C) Figure 6 (A). The hydrogels were prone to significant solvent intake in water, reaching approximately 400 % of their weight after 3 days in the case of Al₂O₃-containing samples, or 6 days for samples without Al₂O₃. Additionally, the hydrogels did not lose their structural integrity even after 7 days in water. In simulated cultivation conditions, the sample solvent intake is more rapid (approximately 400 % with the relative deviation of 25 % was reached in 1 or 2 days for samples without and with Al₂O₃, respectively). The stability is significantly decreased in the cell cultivation medium and increased temperature. The hydrogel containing only FeO_x was completely disintegrated within 3 days. However, the presence of Al₂O₃ in the hydrogel provided a stable structure for 6 days. Though there is a decrease of the relative mass for the hydrogel with Al₂O₃ after day 2, the experimental observations revealed that the hydrogel structure was kept until the 7th day. It is known that HA chains are greatly affected by

the charges and ionic strength of their surrounding environment due to polyelectrolyte character⁶⁴. Thus, the particles' surface charge may significantly influence HA structures' stability. However, this effect would require further investigation in future studies. The long-term stability results revealed that the hydrogels containing Al₂O₃ are more suitable for biomedical applications.

The cytocompatibility of the HA hydrogel containing the MCPs and Al₂O₃ aggregates was examined by an indirect *in vitro* cytotoxicity test applying extract method (see Figure 6 (B)). This method is useful for preliminary cytotoxicity screening. The hydrogel components are generally considered non-toxic. However, it is important to test their cumulative effect on cell viability as well. Extracts not causing a cell viability decrease below 70% are considered non-cytotoxic, as described in the standard ISO 10993-5. The relative cell viability increased slightly with the increase of the extract concentration. For all the extract concentrations it exceeds the

	FeO _x (37°C)		FeO _x (42°C)	
	Recovery		Recovery	
	complex viscosity (%)		complex viscosity (%)	
	Low shear	High shear	Low shear	High shear
	rate	rate	rate	rate
1. cycle	100	100	100	100
2. cycle	99.8	99.9	100.1	99.5
3. cycle	99.4	100.3	101	101.1

	FeO _x :Al ₂ O ₃ 1:1 (37°C)		FeO _x :Al ₂ O ₃ 1:1 (42°C)	
	Recovery		Recovery	
	Storage modulus (%)		Storage modulus (%)	
	Low shear	High shear	Low shear	High shear
	rate	rate	rate	rate
1. cycle	100	/	100	/
2. cycle	99.7	/	100.2	/
3. cycle	99.7	/	101.1	/

	FeO _x :Al ₂ O ₃ 1:1 (37°C)		FeO _x :Al ₂ O ₃ 1:1 (42°C)	
	Recovery		Recovery	
	complex viscosity (%)		complex viscosity (%)	
	Low shear	High shear	Low shear	High shear
	rate	rate	rate	rate
1. cycle	100	100	100	100
2. cycle	100.8	101.1	101.9	102.9
3. cycle	101.6	102.2	104.1	105.1

	FeO _x :Al ₂ O ₃ 1:1 (37°C)		FeO _x :Al ₂ O ₃ 1:1 (42°C)	
	Recovery		Recovery	
	Storage modulus (%)		Storage modulus (%)	
	Low shear	High shear	Low shear	High shear
	rate	rate	rate	rate
1. cycle	100	/	100	/
2. cycle	100.8	/	101.7	/
3. cycle	101.8	/	103.9	/

TABLE I. Recovery of complex viscosity and storage modulus respectively during cyclic shear stress testing of magneto-responsive HA hydrogels

0.70 threshold value, thus proving the hydrogel cytocompatibility.

G. Bioprinting

Bioprinting, i.e., 3D printing of material including living cells, allows a homogeneous distribution of cells throughout the construct, increasing the usability in tissue engineering⁴⁵. Nevertheless, using the bioprinting technique in hyperthermia research would provide an opportunity to fabricate precise tumor tissue analogs and potentially aid the research and use of hyperthermia as a complementary therapeutic procedure in clinical practice^{65,66}. The selected polymer matrix, HA, with a molecular weight below 10⁶ Da, was observed to promote tumorigenesis in breast cancer, which is further advantageous in cultivating artificial tumor tissue⁶⁷.

Materials for bioprinting, commonly known as bio-inks, need to be carefully tailored to facilitate sufficient printability on the one hand and cell viability and biological functionality on the other. The bioprinting process exposes the printed material to significant shear stress due to forced flow through a narrow needle⁶⁸. The bio-ink matrix should therefore undergo the transition from high viscosity to low viscosity in the range of shear rate exposed in typical extrusion-based 3D printing

to minimize the shear stress imposed on cells encapsulated in the material and simultaneously maximize the cell viability⁶⁹. The shear thinning behavior of the proposed hydrogels, as was demonstrated earlier in III E, clearly shows that the material complies with the first condition for viable bio-ink.

The requirement of low shear stress during extrusion would encourage using low-viscosity materials in general. However, such materials fail to provide sufficient printing precision and shape fidelity due to the spreading of the material upon placing it on the printbed⁶². Therefore, rapid recovery of the material, as was demonstrated by cyclic shear stress measurement (Figure 5 (B)), is necessary to facilitate sufficient precision of the printed structure.

The biological functionality condition mainly depends on the desired tissue type in terms of mechanical, chemical, and morphological points of view. The soft and pliable materials developed in this study are mechanically in the range of soft tissue types, typically adipose tissue³⁸ or spinal cord neural tissue³⁹. Furthermore, the magnetic heating ability provided by the MCPs would enable heat-triggered neuromodulation, making the material promising beyond the scope of hyperthermia, advancing toward tissue engineering and regenerative medicine of neural tissue.

The bioprinting of the bio-inks prepared by encapsulation of BALB/3T3 mouse fibroblasts in HA hydrogels containing FeO_x MCPs with Al₂O₃ aggregates was done with sufficient printing precision and cell distribution homogeneity (Figure 7 (A - E)). Additionally, the live/dead staining proves that the cells retained their metabolic activity after printing (Figure 7 (F) and (G)), and there was no detectable damage to the cell membranes, as 87±6 % cell viability was achieved. Therefore, the materials reported here have been successfully tested as bio-inks for extrusion-based 3D bioprinting.

IV. CONCLUSION

The magneto-responsive hydrogel composed of HA matrix cross-linked via Schiff base formation, magnetic MCPs, and aluminum oxide NPs aggregates was elaborated. The MCPs ensure the hydrogel heating under exposure to an AMF with parameters approved for medicine. It was shown that the presence of Al₂O₃ NPs aggregates primarily influenced the Néel relaxation of the MCPs, while the Brown relaxation remained intact. On the base of the experimental findings, it can be concluded that the diamagnetic Al₂O₃ NPs aggregates apparently, shield the magnetic interactions among the MCPs, causing the increase in Néel relaxation and heating efficiency. A heating rate of 0.3 °C per minute was observed. The rheological measurements of the HA hydrogel confirmed the shear-thinning behavior and fast recovery after high shear stress. Additionally, the presence of Al₂O₃ NPs aggregates increases the long-term stability of the hydrogel at cell cultivation conditions, making them more suitable for tissue engineering-related applications. The hydrogel was proven to be cytocompatible. Moreover, it was demonstrated that viscoelastic properties of the hydrogel allowed extrusion-based 3D bioprinting with BALB/3T3 mouse fibroblasts. Self-supported multi-

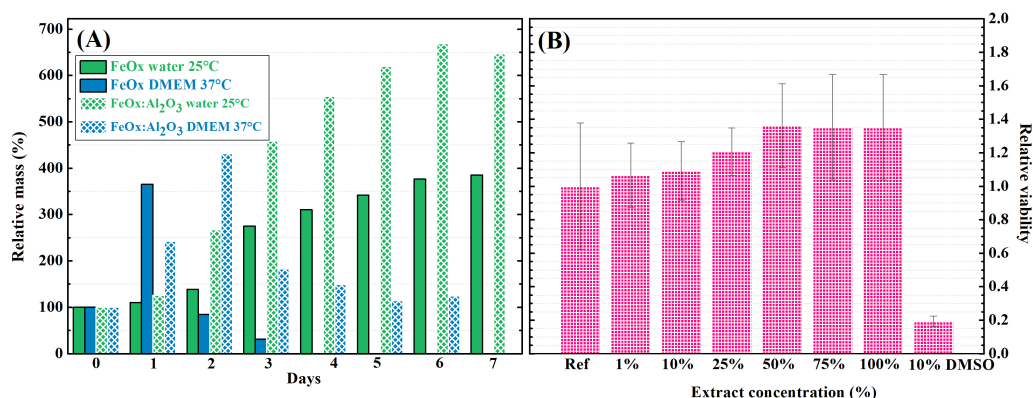


FIG. 6. (A) Long-term stability of magneto-responsive HA hydrogels in water and simulated cultivation conditions; (B) *in vitro* cytotoxicity evaluation of the hydrogels via extract method.

layered uniformly porous structure was formed with homogeneous cell distribution and high cell viability. The combination of high heating efficiency, softness, biocompatibility, and 3D printability of magnetic HA hydrogel allows to consider it a multifunctional material suitable for AMF induced heating in biomedical applications such as magnetic hyperthermia, wireless thermal brain stimulation, thermally triggered drug delivery as well as for precise scaffold engineering and bioprinting.

SUPPLEMENTARY MATERIAL

Supplementary material includes the rheological properties of HA hydrogels, namely, the dependence of the storage modulus and loss modulus on the shear rate, and the dependence of $\tan \delta$ on the shear rate (Figure S1), as well as the magnetization curves of FeO_x MCPs powder and Al₂O₃ NPs (Figure S2).

AUTHOR CONTRIBUTIONS

Conceptualization, PS, NK, AM (Aleš Mráček); methodology, LV, IS, LM, PS, MH; validation LV, IS, PS, LM, KV; formal analysis, LV, LM, KV, KK; investigation, LV, KV, KK; writing-original draft preparation, LV, IS, NK, LM; writing-review and editing, LV, IS, NK, PS, LM, KV, MH, AM (Antonín Minařík), PH, AM (Aleš Mráček); visualization, LV, IS, LM, KK; supervision, IS, NK, PS, MH, AM (Antonín Minařík), PH, AM (Aleš Mráček); project administration, PS, NK, AM (Antonín Minařík), AM (Aleš Mráček); funding acquisition, MH, PH, AM (Aleš Mráček).

DECLARATION OF COMPETING INTEREST

Authors declare no competing interest.

ACKNOWLEDGMENTS

Authors LV and KV are grateful to the "Junior Grant of TBU in Zlín", OP RDE Reg. No. CZ.02.2.69/0.0/0.0/19_073/0016941 provided by European Structural and Investment Funds and Ministry of Education, Youth and Sports of the Czech Republic. Authors LM and AM (Aleš Mráček) work was financially supported by the Ministry of Education, Youth and Sports of the Czech Republic - DKRVO (RP/CPS/2022/003). Author NK is grateful to the Ministry of Education, Youth and Sports of the Czech Republic – DKRVO (RP/CPS/2022/005), Program Multilateral Scientific and Technological Cooperation in the Danube Region (8X20041). Author KK would like to acknowledge the TBU grant No. IGA/FT/2023/006 for support. Authors PS, MH and AM (Antonín Minařík) are grateful to the project No. 22-33307S of Czech Science Foundation. Author PH acknowledges the project DKRVO (RP/CPS/2022/001) provided by the Ministry of Education, Youth and Sports of the Czech Republic. We thank Prof. Thomas Scheibel, Department of Biomaterials, University Bayreuth, for providing the facility for 3D printing on the RegenHU instrument.

DATA AVAILABILITY STATEMENT

The data that support the findings of this study are available from the corresponding author Petr Smolka (smolka@utb.cz) upon reasonable request.

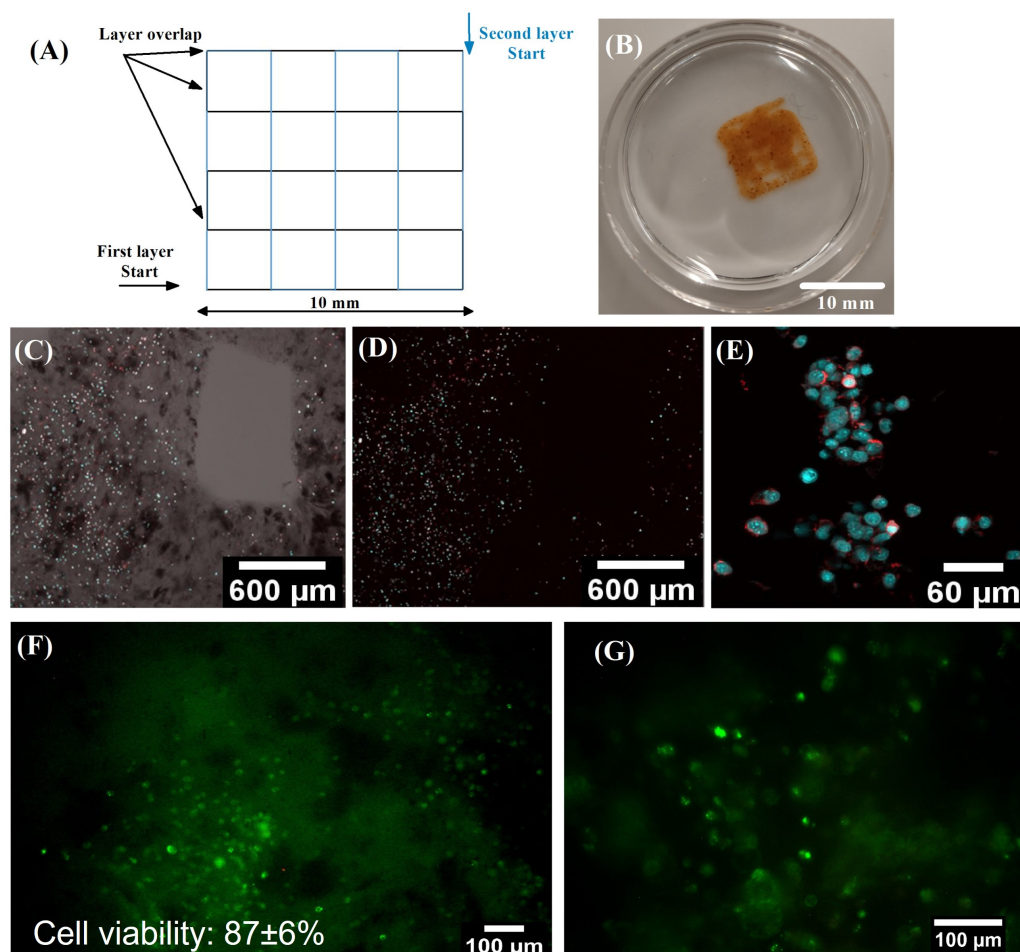


FIG. 7. Bioprinting of BALB/3T3 mouse fibroblasts encapsulated in magneto-responsive HA hydrogel: (A) Printing model; (B) Printed grid photography taken on the 8th day after printing; (C), (D), (E) Confocal imaging of cells distribution within the scaffold in bright field (C) and fluorescence channel (C-E). Cells were stained for cytoskeleton (red) and nucleus (blue); (F), (G) Live/Dead assay of BALB/3T3 fibroblasts. The cells were visualized in fluorescence immediately after the microextrusion.

REFERENCES

- ¹Z. Liu et al. "Recent Advances on Magnetic Sensitive Hydrogels in Tissue Engineering," *Frontiers in Chemistry*, 8, 2020, DOI: 10.3389/fchem.2020.00124.
- ²P.I.P Soares et al. "Thermal and magnetic properties of iron oxide colloids: influence of surfactants," *Nanotechnology*, 26, 2015, DOI: 10.1088/0957-4484/26/42/425704.
- ³M. Levy et al. "Long term *in vivo* biotransformation of iron oxide nanoparticles," *Biomaterials*, 32, 2011, DOI: 10.1016/j.biomaterials.2011.02.031.
- ⁴J. Gu et al. "The internalization pathway, metabolic fate and biological effect of superparamagnetic iron oxide nanoparticles in the macrophage-like RAW264.7 cell," *Science China Life Sciences*, 54, 2011, DOI: 10.1007/s11427-011-4215-5.
- ⁵M. Mahmoudi et al. "Assessing the *In Vitro* and *In Vivo* Toxicity of Superparamagnetic Iron Oxide Nanoparticles," *Chemical Reviews*, 112, 2012, DOI: 10.1021/cr2002596.
- ⁶S. Dutz and R. Hergt "Magnetic particle hyperthermia—a promising tumour therapy?," *Nanotechnology*, 25, 2014, DOI: 10.1088/0957-4484/25/45/452001.
- ⁷T. Vangijzegem, D. Stanicki and S. Laurent "Magnetic iron oxide nanoparticles for drug delivery: applications and characteristics," *Expert Opinion on Drug Delivery*, 16, 2019, DOI: 10.1080/17425247.2019.1554647.
- ⁸M. Roet et al. "Progress in neuromodulation of the brain: A role for magnetic nanoparticles?," *Progress in Neurobiology*, 177, 2019, DOI: 10.1016/j.pneurobio.2019.03.002.

- ⁹S. Laurent et al., "Magnetic fluid hyperthermia: Focus on superparamagnetic iron oxide nanoparticles," *Advances in Colloid and Interface Science*, 2011, DOI: 10.1016/j.cis.2011.04.003.
- ¹⁰C. Benwood et al. "Biohydrogels with magnetic nanoparticles as crosslinker: Characteristics and potential use for controlled antitumor drug-delivery," *Acta Biomaterialia*, 8, 2012, DOI: 10.1016/j.actbio.2012.09.006.
- ¹¹R.T. Guntur et al. "On-Demand Chemomagnetic Modulation of Striatal Neurons Facilitated by Hybrid Magnetic Nanoparticles," *Advanced Functional Materials*, 2022, DOI: 10.1002/adfm.202204732.
- ¹²R. Chen et al. "Wireless magnetothermal deep brain stimulation," *Science*, 347, 2015, DOI: 10.1126/science.1261821.
- ¹³Y. Liu et al. "Noninvasive Manipulation of Ion Channels for Neuromodulation and Therapeutics," *Accounts of Materials Research*, 3, 2022, DOI: 10.1021/acountsmr.1c00251.
- ¹⁴S.A. Hescham et al. "Magneto-thermal nanoparticle technology alleviates parkinsonian-like symptoms in mice," *Nature Communications*, 12, 2021, DOI: 10.1038/s41467-021-25837-4.
- ¹⁵K.L. Kozlowski et al. "Nonresonant powering of injectable nanoelectrodes enables wireless deep brain stimulation in freely moving mice," *Science Advances*, 7, 2021, DOI: 10.1126/sciadv.abc4189.
- ¹⁶Z. Chen et al. "Wireless Optogenetic Modulation of Cortical Neurons Enabled by Radioluminescent Nanoparticles," *ACS Nano*, 15, 2021, DOI: 10.1021/acsnano.0c10436.
- ¹⁷S. Wu et al. "Genetically magnetic control of neural system via TRPV4 activation with magnetic nanoparticles," *Nano Today*, 39, 2021, DOI: 10.1016/j.nantod.2021.101187.
- ¹⁸A. Tay et al. "A 3D Magnetic Hyaluronic Acid Hydrogel for Magnetomechanical Neuromodulation of Primary Dorsal Root Ganglion Neurons," *Advanced Materials*, 2018, DOI: 10.1002/adma.201800927.
- ¹⁹D. Rosenfeld et al. "Magnetothermal Modulation of Calcium-Dependent Nerve Growth," *Advanced Functional Materials*, 32, 2022, DOI: 10.1002/adfm.202204558.
- ²⁰R. Gilchrist et al. "Selective Inductive Heating of Lymph Nodes," *Annals of Surgery*, 4, 1957, DOI: 10.1097/00000658-195710000-00007.
- ²¹J. Wells et al., "Challenges and recommendations for magnetic hyperthermia characterization measurements," *International Journal of Hyperthermia*, 38, 2021, DOI: 10.1080/02656736.2021.1892837.
- ²²P. Bender et al. "Influence of clustering on the magnetic properties and hyperthermia performance of iron oxide nanoparticles," *Nanotechnology*, 42, 2018, DOI: 10.1088/1361-6528/aad67d.
- ²³S. Pourmiri et al. "Magnetic properties and hyperthermia behavior of iron oxide nanoparticle clusters," *AIP Advances*, 12, 2019, DOI: 10.1063/1.5130425.
- ²⁴I.S. Smolková et al. "Correlation between coprecipitation reaction course and magneto-structural properties of iron oxide nanoparticles," *Materials Chemistry and Physics*, 155, 2015, DOI: 10.1016/j.matchemphys.2015.02.022.
- ²⁵M. Moradi, Q. He and G. Willing "Tuning the stabilization mechanism of nanoparticle-regulated complex fluids," *Colloids and Surfaces A: Physicochemical and Engineering Aspects*, 2019, DOI: 10.1016/j.colsurfa.2019.06.021.
- ²⁶V. Tohver et al. "Nanoparticle halos: A new colloid stabilization mechanism," *Proceedings of the National Academy of Sciences*, 98, 2001, DOI: 10.1073/pnas.151063098.
- ²⁷A.E. Goldt et al. "Humic acid-stabilized superparamagnetic maghemite nanoparticles: surface charge and embryotoxicity evaluation," *Nanosystems-Physics Chemistry Mathematics*, 10, 2019, DOI: 10.17586/2220-8054-2019-10-2-184-189.
- ²⁸P. Moroz, S.K. Jones and B.N. Gray "Magnetically mediated hyperthermia: current status and future directions," *International Journal of Hyperthermia*, 18, 2002, DOI: 10.1080/02656730110108785.
- ²⁹A. Jordan et al., "Presentation of a new magnetic field therapy system for the treatment of human solid tumors with magnetic fluid hyperthermia," *Journal of Magnetism and Magnetic Materials*, 225, 2001, DOI: 10.1016/S0304-8853(00)01239-7.
- ³⁰P. Le Renard et al., "The *in vivo* performance of magnetic particle-loaded injectable, *in situ* gelling, carriers for the delivery of local hyperthermia," *Biomaterials*, 31, 2010, DOI: 10.1016/j.biomaterials.2009.09.091.
- ³¹A. Ito et al., "Medical application of functionalized magnetic nanoparticles," *Journal of Bioscience and Bioengineering*, 100, 2005, DOI: 10.1263/jbb.100.1.
- ³²L. Shi et al. "Biocompatible Injectable Magnetic Hydrogel Formed by Dynamic Coordination Network," *Applied Materials & Interfaces*, 11, 2019, DOI: 10.1021/acsmi.9b17627.
- ³³N.E. Kazantseva et al. "Magnetic Nanomaterials for Arterial Embolization and Hyperthermia of Parenchymal Organs Tumors: A Review," *Nanomaterials*, 11, 2021, DOI: 10.3390/nano11123402.
- ³⁴I.S. Smolková et al. "Maghemite based silicone composite for arterial embolization hyperthermia," *Materials Science and Engineering: C*, 48, 2015, DOI: 10.1016/j.msec.2014.12.046.
- ³⁵S. Li et al. "Self-healing hyaluronic acid hydrogels based on dynamic Schiff base linkages as biomaterials," *Carbohydrate Polymers*, 2020, DOI: 10.1016/j.carbpol.2020.116922.
- ³⁶Y. Choi et al. "3D Printing of dynamic tissue scaffold by combining self-healing hydrogel and self-healing ferrogel," *Colloids and Surfaces B: Biointerfaces*, 208, 2021, DOI: 10.1016/j.colsurfb.2021.112108.
- ³⁷L. Vítková et al. "Formulation of Magneto-Responsive Hydrogels from Dually Cross-Linked Polysaccharides: Synthesis, Tuning and Evaluation of Rheological Properties," *International Journal of Molecular Sciences*, 23, 2022, DOI: 10.3390/ijms23179633.
- ³⁸T.A. Krouskop et al. "Elastic Moduli of Breast and Prostate Tissues under Compression," *Ultrasonic Imaging*, 20, 1998, DOI: 10.1177/016173469802000403.
- ³⁹R.D. Bartlett et al. "Mechanical properties of the spinal cord and brain: Comparison with clinical-grade biomaterials for tissue engineering and regenerative medicine," *Biomaterials*, 258, 2020, DOI: 10.1016/j.biomaterials.2020.120303.
- ⁴⁰W.C. Xu et al., "Engineering the biomechanical microenvironment of chondrocytes towards articular cartilage tissue engineering," *Life Sciences*, 309, 2022, DOI: 10.1016/j.lfs.2022.121043.
- ⁴¹D. Warren et al., "Engineering *in vitro* human neural tissue analogs by 3D bioprinting and electrostimulation," *APL Bioengineering*, 5, 2021, DOI: 10.1063/5.0032196.
- ⁴²M.E. Prendergast and J.A. Burdick "Recent Advances in Enabling Technologies in 3D Printing for Precision Medicine," *Advanced Materials*, 32, 2020, DOI: 10.1002/adma.201902516.
- ⁴³E.S. Ko et al. "3D printing of self-healing ferrogel prepared from glycol chitosan, oxidized hyaluronate, and iron oxide nanoparticles," *Carbohydrate Polymers*, 245, 2020, DOI: 10.1016/j.carbpol.2020.116496.
- ⁴⁴W. Zhu et al., "Direct 3D bioprinting of prevascularized tissue constructs with complex microarchitecture," *Biomaterials*, 124, 2017, DOI: 10.1016/j.biomaterials.2017.01.042.
- ⁴⁵V.L. Mainardi et al., "Improving cell seeding efficiency through modification of fiber geometry in 3D printed scaffolds," *Biofabrication*, 13, 2021, DOI: 10.1088/1758-5090/abe5b4.
- ⁴⁶A. Pardo et al. "Magnetically-Assisted 3D Bioprinting of Anisotropic Tissue-Mimetic Constructs," *Advanced Functional Materials*, 2022, DOI: 10.1002/adfm.202208940.
- ⁴⁷I.S. Smolková et al. "Size Dependent Heating Efficiency of Multicore Iron Oxide Particles in Low-Power Alternating Magnetic Fields," *Acta Physica Polonica A*, 6, 2016, DOI: 10.12693/APhysPolA.131.663.
- ⁴⁸L. Musilová et al. "Cross-linked Gelatine by Modified Dextran as a Potential Bioink Prepared by a Simple and Non-toxic Process," *Polymers*, 14, 2022, DOI: 10.3390/polym14030391.
- ⁴⁹J. Maia et al. "Insight on the periodate oxidation of dextran and its structural vicissitudes," *Polymer*, 52, 2011, DOI: 10.1016/j.polymer.2010.11.058.
- ⁵⁰J. Mui, J. Ngo and B. Kim. "Aggregation and Colloidal Stability of Commercially Available Al₂O₃ Nanoparticles in Aqueous Environments," *Nanomaterials*, 6, 2016, DOI: 10.3390/nano6050090.
- ⁵¹M.N.M. Zubir et al. "Experimental investigation on the use of highly charged nanoparticles to improve the stability of weakly charged colloidal system," *Journal of Colloid and Interface Science*, 454, 2015, DOI: 10.1016/j.jcis.2015.05.019.
- ⁵²H. Karimian and A.A. Babaluo. "Halos mechanism in stabilizing of colloidal suspensions: Nanoparticle weight fraction and pH effects," *Journal of the European Ceramic Society*, 27, 2007, DOI: 10.1016/j.jeurceramsoc.2006.05.109.
- ⁵³S. Ota and Y. Takemura "Characterization of Néel and Brownian Relaxations Isolated from Complex Dynamics Influenced by Dipole Interactions in Magnetic Nanoparticles," *The Journal of Physical Chemistry C*, 123,

- 2019, DOI: 10.1021/acs.jpcc.9b06790.
- ⁵⁴I. Obaidat, B. Issa and Y. Haik "Magnetic Properties of Magnetic Nanoparticles for Efficient Hyperthermia," *Nanomaterials*, 5, 2015, DOI: 10.3390/nano5010063.
- ⁵⁵I.S. Smolkova et al. "Alternating magnetic field energy absorption in the dispersion of iron oxide nanoparticles in a viscous medium," *Journal of Magnetism and Magnetic Materials*, 374, 2015, DOI: 10.1016/j.jmmm.2014.08.096.
- ⁵⁶U. Engelmann et al. "Heating efficiency of magnetic nanoparticles decreases with gradual immobilization in hydrogels," *Journal of Magnetism and Magnetic Materials*, 471, 2019, DOI: 10.1016/j.jmmm.2018.09.113.
- ⁵⁷M. Ghebremedhin, S. Seiffert and T.A. Vilgis "Physics of agarose fluid gels: Rheological properties and microstructure," *Current Research in Food Science*, 4, 2021, DOI: 10.1016/j.crfs.2021.06.003.
- ⁵⁸E. Fernández et al. "Rheological and thermal properties of agarose aqueous solutions and hydrogels," *Journal of Polymer Science Part B: Polymer Physics*, 46, 2008, DOI: 10.1002/polb.21370.
- ⁵⁹I.S. Raja and N.N. Fathima "Porosity and dielectric properties as tools to predict drug release trends from hydrogels," *SpringerPLUS*, 3, 2014, DOI: 10.1186/2193-1801-3-393.
- ⁶⁰F. Zamani, M.A. Tehran and A. Abbasi "Fabrication of PCL nanofibrous scaffold with tuned porosity for neural cell culture," *Progress in Biomaterials*, 10, 2021, DOI: 10.1007/s40204-021-00159-2.
- ⁶¹F. Causa, P.A. Netti and L. Ambrosio, "A multi-functional scaffold for tissue regeneration: The need to engineer a tissue analogue," *Biomaterials*, 28, 2007, DOI: 10.1016/j.biomaterials.2007.07.030.
- ⁶²K. Hölzl et al. "Bioink properties before, during and after 3D bioprinting," *Biofabrication*, 3, 2016, DOI: 10.1088/1758-5090/8/3/032002.
- ⁶³M.M. Lübtow et al., "Temperature-Dependent Rheological and Viscoelastic Investigation of a Poly(2-methyl-2-oxazoline)-b-poly(2-iso-butyl-2-oxazoline)-b-poly(2-methyl-2-oxazoline)-Based Thermogelling Hydrogel," *Journal of Functional Biomaterials*, 10, 2019, DOI: 10.3390/jfb10030036.
- ⁶⁴A. Mracek et al. "The influence of Hofmeister series ions on hyaluronan swelling and viscosity," *Molecules*, 13, 2008, DOI: 10.3390/molecules13051025.
- ⁶⁵P. Sethi et al., "3D tumor tissue analogs and their orthotopic implants for understanding tumor-targeting of microenvironment-responsive nanosized chemotherapy and radiation," *Nanomedicine-Nanotechnology Biology and Medicine*, 11, 2015, DOI: 10.1016/j.nano.2015.07.013.
- ⁶⁶M. Upreti, "Tumor Tissue Analogs for the Assessment of Radioresistance in Cancer Stem Cells," *Cancer Stem Cells: Methods and Protocols*, 2018, DOI: 10.1007/978-1-4939-7401-6_11.
- ⁶⁷J.M. Louderbough and J.A. Schroeder. "Understanding the dual nature of CD44 in breast cancer progression," *Molecular Cancer Research*, 9, 2011, DOI: 10.1158/1541-7786.MCR-11-0156.
- ⁶⁸A. Blaeser et al. "Controlling Shear Stress in 3D Bioprinting is a Key Factor to Balance Printing Resolution and Stem Cell Integrity," *Advanced Healthcare Materials*, 5, 2015, DOI: 10.1002/adhm.201500677.
- ⁶⁹L. Ouyang et al. "Effect of bioink properties on printability and cell viability for 3D bioplotting of embryonic stem cells," *Biofabrication*, 8, 2016, DOI: 10.1088/1758-5090/8/3/035020.

Synthesis and Exfoliation of Calcium Organophosphonates for Tailoring Rheological Properties of Sodium Alginate Solutions: A Path toward Polysaccharide-Based Bioink

Kateřina Kopecká, Lenka Vítková,* Zuzana Kroneková, Lenka Musilová, Petr Smolka, Filip Mikulka, Klára Melánová, Petr Knotek, Martin Humeník, Antonín Minařík, and Aleš Mráček*



Cite This: <https://doi.org/10.1021/acs.biomac.3c00081>



Read Online

ACCESS |



Metrics & More

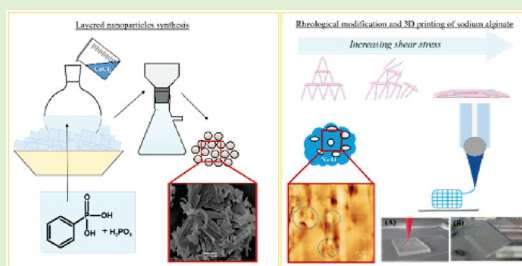


Article Recommendations



Supporting Information

ABSTRACT: Layered nanoparticles with surface charge are explored as rheological modifiers for extrudable materials, utilizing their ability to induce electrostatic repulsion and create a house-of-cards structure. These nanoparticles provide mechanical support to the polymer matrix, resulting in increased viscosity and storage modulus. Moreover, their advantageous aspect ratio allows for shear-induced orientation and decreased viscosity during flow. In this work, we present a synthesis and liquid-based exfoliation procedure of phenylphosphonate–phosphate particles with enhanced ability to be intercalated by hydrophilic polymers. These layered nanoparticles are then tested as rheological modifiers of sodium alginate. The effective rheological modification is proved as the viscosity increases from 10^1 up to 10^3 Pa·s in steady state. Also, shear-thinning behavior is observed. The resulting nanocomposite hydrogels show potential as an extrudable bioink for 3D printing in tissue engineering and other biomedical applications, with good shape fidelity, nontoxicity, and satisfactory cell viability confirmed through encapsulation and printing of mouse fibroblasts.



INTRODUCTION

3D printing has drawn a lot of attention due to the potential for precisely fabricating complex structures with minimal waste. Biocompatible materials are suggested for applications in the pharmaceutical and biomedical field, e.g., as drug delivery systems, tissue analogues for specialized *in vitro* testing, wound healing, and tissue engineering.¹ Cell cultivation and tissue engineering, in particular, require a porous matrix with high water content in order to achieve close resemblance to the extracellular matrix and, thus, sustain cell functionality.² To this end, natural polymer-based hydrogels—i.e., weakly cross-linked polymer networks capable of retaining large amounts of water³—appear as promising candidates in many of the suggested applications.

There have been recent developments in the processing of natural polymer-based hydrogels, which would allow additive manufacturing by means of extrusion 3D printing.^{4,5} The most established polymers include collagen,^{6,7} gelatin,^{8–12} hyaluronan,^{12–14} and sodium alginate (NaAlg).^{8,10,14–16} The wide usage of NaAlg is related to the possibility of mild cross-linking with multivalent cations.¹⁷ Furthermore, as a natural polysaccharide, NaAlg has been shown to be highly biocompatible and, thus, suitable for medical applications.¹⁸ However, it can be rather difficult to achieve the desired rheological behavior in solutions based solely on the NaAlg

matrix, which leads to the development of combined polymer matrices.

A less common approach to enhancing hydrogel printability involves the use of nanostructured fillers.¹⁹ This possibility was first described for Laponite, a charged discotic nanoclay, dispersed in poly(ethylene glycol) (PEG) solution.²⁰ In an exfoliated state these particles spontaneously form a house-of-cards structure.^{21,22} Laponite, in association with PEG and alginate, provided improved printability and, at higher clay concentrations, elevated recovery after shear.²³ High shape fidelity of construct was achieved by dÁvila et al., when Laponite–alginate hydrogels were printed.²⁴ The capacity to provide rheological tuning to NaAlg solution has also been demonstrated for montmorillonite discotic clay.²⁵ Consequently, the principle appears not to be limited to Laponite, but to be a common feature of charged discotic nanoparticles (NPs) suspended in a polymer solution.²² The functionality of

Received: January 23, 2023

Revised: May 12, 2023

NPs is largely dependent on their chemical nature, size, aspect ratio, and volume fraction.²⁶ Unlike traditional fillers, NPs are capable of inducing significant changes in material properties even at very low concentrations, owing to their large specific surface.²⁷ The potential to minimize their presence without compromising the desired effect is particularly advantageous in consideration of medical applications as the risk of immunogenicity is diminished.^{4,25,28–31} The presence of calcium and phosphate ions in scaffolds improves osteoblast adhesion, migration, and differentiation.^{32,33} Additionally, the presence of calcium cations is associated with a decrease of shear stress-induced damage to the cells during bioprinting.³⁴

Herein, we focus on the rheological modification of NaAlg solutions via the incorporation of nanoparticulate fillers. We hypothesize that exfoliated layered NPs can serve as efficient rheological modifiers through the formation of a house-of-cards structure. In order to test this hypothesis, layered calcium phenylphosphonate (CaPhP) particles are compared to spherical calcium phosphonate NPs (nanoAp) in terms of rheological modification. Additionally, we address the hydrophobicity of CaPhP with presumed limitation in NaAlg chain intercalation by developing a novel material in which part of the phenyl group is replaced by phosphate. These mixed calcium phenylphosphonate–phosphate (Ca3.1, where 3.1 stand for the ration of reactants during NPs synthesis) nanoplatelets are synthesized, characterized, and exfoliated. This material synthesis is reported here, to the best of our knowledge, for the first time. The rheological and printing evaluation describes the effects of nanofiller shape and chemical composition. Furthermore, the effect of Ca²⁺ dissociation from the NPs is outlined. The printable NaAlg nanocomposites are subsequently used as precursors of hydrogels, which are obtained by ionic cross-linking. Because of the potential to significantly decrease the number of NPs in the material, the hydrogels may find versatile application as 3D printable materials based on natural components. Finally, the materials introduced in this work are proposed and tested as biopolymer-based nanocomposite bioinks.

MATERIALS AND METHODS

Synthesis of Layered Materials. CaPhP: A solution of phenylphosphonic acid (Sigma-Aldrich, St. Louis, MO, p.a., 1.976 g, 1.2×10^{-2} mol in 50 mL of distilled water, conductivity $<2 \mu\text{S cm}^{-1}$) was brought to pH 9 by adding concentrated ammonia solution (Honeywell Fluka, Charlotte, NC, p.a., 32%) and then mixed with a solution of CaCl₂ (Penta, Chrudim, Czechia, p.a.) (1.381 g, 1.2×10^{-2} mol in 25 mL of distilled water). The reaction mixture was stirred for 30 min at 25 °C. A white precipitate formed and was collected by filtration, washed with distilled water until neutral pH, and dried in an oven at 80 °C.

Ca3.1: Phenylphosphonic acid (0.79 g, 0.5×10^{-2} mol) was dissolved in 50 mL of distilled water (conductivity $<2 \mu\text{S cm}^{-1}$) and mixed with 15 mL of 1 M H₃PO₄ (Sigma-Aldrich, St. Louis, MO, p.a., 1.5×10^{-2} mol). The pH of the reaction mixture was increased to 9 by a concentrated aqueous ammonia solution. Then 25 mL of CaCl₂ solution (2.21 g, 2×10^{-2} mol) was added under stirring by a magnetic stirrer. The reaction mixture was stirred for 1 h (a) at 25 °C, (b) in an oil bath at 50 °C, and (c) in an ice bath. A white precipitate formed and was collected by filtration, washed with distilled water, and dried in an oven at 80 °C. Other samples were prepared by the same procedure, varying the molar ratio of acids H₂PhP:H₃PO₄ (1:3, 1:1, 3:1, and 0:1), while the molar ratio of P:Ca remained constant (1:1).

Sample characterization: Powder X-ray diffraction (XRD) data were obtained with a D8 Advance diffractometer (Bruker AXS,

Karlsruhe, Germany) with Bragg–Brentano θ – θ geometry (40 kV, 30 mA), using Cu K α radiation, and equipped with a LynxEye detector with a Ni-beta filter. The scan was performed at room temperature from 4° to 90° (2 θ) in 0.01° steps with a counting time of 10 s per step.

Energy-dispersive X-ray (EDX) analysis was performed using a JSM-5500LV electron scanning microscope (JEOL, Tokyo, Japan) equipped with an EDX microanalyzer (detector GRESHAM Sirius 10, IXRF Systems, Austin, TX). The accelerating voltage of the primary electron beam was 20 kV.

Organic elemental analysis (C, H) was performed on a Flash 2000 CHNS elemental analyzer (Thermo Fisher Scientific, Waltham, MA).

Liquid-Based Exfoliation of Particles. Selection of suitable solvent: 10 mg of powder material was dissolved in 5 mL of solvent (water, isopropyl alcohol, ethylene glycol, or glycerol, all Sigma-Aldrich, St. Louis, MO, p.a.) in a glass vial. The obtained dispersions were treated by ultrasound in an ultrasound bath with frequency 37 kHz for 1 h. Then the sedimentation and presence of Tyndall scattering were evaluated 1 and 24 h after the end of ultrasound treatment.

Preparation of stock dispersions: 200 mg of powder material (CaPhP or Ca3.1) was dispersed in 40 mL of ethylene glycol and treated by a T10 Standard Ultra-Turrax high-shear homogenizer (IKA, Staufen, Germany) equipped with a dispersing tool (S10 D-7G-KS-65) at 13000 rpm for 5 min.

Ink Preparation for 3D Printing. The proposed 3D printing inks were based on a 3 wt % solution of NaAlg (medium viscosity, Sigma-Aldrich, St. Louis, MO) dissolved in demineralized (DEMI) water (Millipore Q system, Merck, Rathway, NJ). The solutions were prepared by adding the appropriate amount of polymer to DEMI water and dissolving at 50 °C for 18 h in an oven without mixing. This procedure provided a viscous solution, which was mixed with further components.

Layered CaPhP and Ca3.1 particles as well as spherical nanoapatite (nanoAp) particles (<150 nm particle size, Sigma-Aldrich, St. Louis, MO) were used in the form of ethylene glycol dispersions. The concentration of particles in such dispersions was 5 g L^{-1} . Also, CaCl₂ was dissolved in ethylene glycol to provide a solution of the same concentration, i.e., 5 g L^{-1} .

The previously described dispersions, as well CaCl₂ solution, were added to NaAlg solution in concentration of 2×10^{-6} particles/CaCl₂ per 1 mL of NaAlg. The resulting solution was then stirred vigorously with a glass rod in order to obtain a homogeneous mixture. The mixing was typically accompanied by an increase in viscosity and resulted in the pastelike appearance of the materials. Both components were kept at room temperature during the process. These materials were subjected to tests designed to establish 3D printing. In the following text, this stage of materials preparation will be termed “pre-cross-linked inks”.

Rheological Characterization. Rheological characterization of the pre-cross-linked inks was performed on an MCR 502 rotational rheometer (Anton-Paar, Graz, Austria) at 25 °C, using 25 mm parallel plate geometry. The shear flow behavior measurement occurred when the system was oscillating at constant 10% deformation with angular frequency sweep increasing from 0.1 to 630 rad s⁻¹.

Additionally, the inks were subjected to cyclic shear stress in order to characterize them from the 3D printing point of view. The measurement was conducted in oscillation mode, switching between low (3 rad s⁻¹) and high (100 rad s⁻¹) angular frequency. Both low and high angular frequencies were always held for 50 s, and the transition was instant.

3D Printing Experiments. Microextrusion 3D printing experiments were performed on pre-cross-linked inks with a BioX bioprinter (Cellink, Gothenburg, Sweden) with the following specifications: polypropylene conical nozzle of 0.41 mm inlet diameter and 0.26 mm outlet diameter, 3 mL polypropylene syringe, microextrusion syringe pump printhead, and microscope glass slide printed. The printhead speed was 2 mm s^{-1} , and the extrusion rate was varied between 1 and $1.5 \mu\text{L s}^{-1}$ according to each material's specific behavior. During printing, both printhead and printed bed were kept at 25 °C.

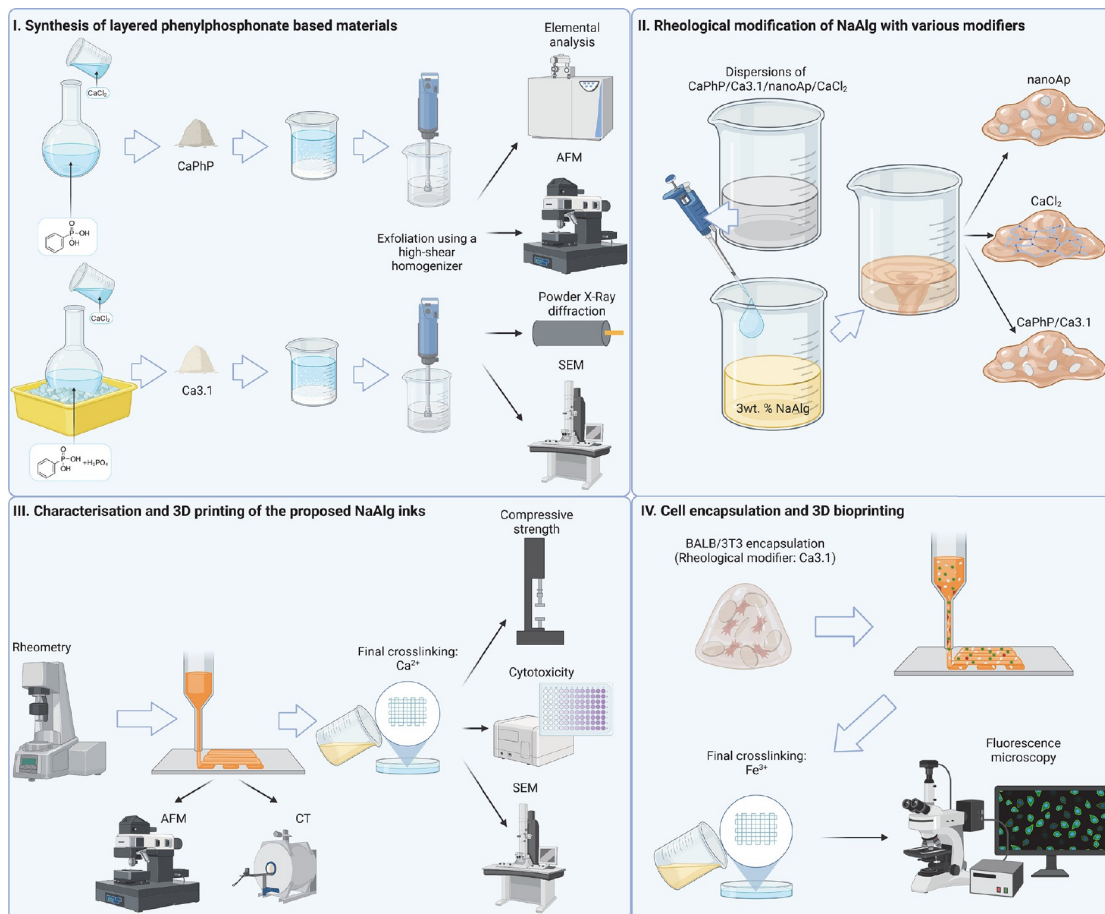


Figure 1. Schematic representation of the experimental workflow (created with BioRender.com).

The printing ability of the pre-cross-linked inks was evaluated by a method derived from the filament fusion test.³⁵ A zigzag pattern was printed, with the distance between the strands increasing at increments of 0.1 mm. This increment was chosen with consideration for the high swelling of the inks during microextrusion. Images of the printed patterns were taken using a Dino-Lite AM4815ZT optical microscope (AnMo Electronics Corporation, Taipei, Taiwan) and evaluated with the aid of the ImageJ software (v1.5, Wayne Rasband, National Institutes of Health, Bethesda, MD). Three characteristics were obtained from the test: strand thickness, partial fusion distance, and complete separation distance.

Compressive Strength Testing. Young's modulus in compression was measured on 3D printed cylinders (10 mm × 10 mm). Prior to compression testing, stabilization of the materials was performed in the following way: The structures obtained from pre-cross-linked inks were immersed in a 2 wt % aqueous solution of CaCl₂ for 30 min. The CaCl₂ solution was kept at 25 °C, and no mixing was applied during the final cross-linking. The samples subjected to this treatment will be termed "fully cross-linked hydrogels" in the following text. An Instron 3345 device (Instron, Norwood, MA) with a 100 N force transducer was used for compressive strength analysis. The measurement occurred at constant deformation rate of 1 mm min⁻¹.

Morphological Analysis. Scanning electron microscopy (SEM) imaging was used for observation of the composite hydrogels. Vertical sections of freeze-dried samples of the fully cross-linked hydrogels

were observed. The SEM analysis was done using the Phenom Pro instrument (Thermo Fisher Scientific, Waltham, MA) at an accelerating voltage 10 kV. The samples were sputtered with a gold/palladium layer prior to imaging.

Atomic force microscopy (AFM) was used to measure the topological profile of the exfoliated NPs and to determine the structure and morphology of the hydrogel samples. Measurement was performed at room temperature on a Dimension ICON atomic force microscope (Bruker, Karlsruhe, Germany) in peak force mode with a ScanAsyst tip. Samples of exfoliated particles were centrifuged for 5 min at 6000 rpm, spin-coated on atomically flat mica substrate, and dried at 60 °C. The morphology of the hydrogels was measured in sections of native hydrogel samples. The samples were prepared by cryomicrotome cutting by a diamond knife (Micro Star) at -80 °C. The primary particle size distribution was analyzed by the SW³⁶ in accordance with refs 37–39. The sizes are presented as the histograms of the equivalent circles' diameters.

X-ray computed microtomography (CT) analysis of the printed structures and their porosity was performed with the help of the SkyScan 1174 device (Bruker, New York, NY). The device used an X-ray source (voltage 20–50 kV, maximum power of 40 W) and an X-ray detector. The CCD 1.3 Mpix was coupled to a scintillator by a lens with 1:6 zoom range. The projection images were recorded at angular increments of 0.5° or 1° using tube voltage and tube current of 35 kV and 585 μA, respectively. The exposure time was set to 15 s,

Table 1. Influence of the Molar Ratio of Acids on the Obtained Phases

sample	molar ratio $\text{H}_2\text{PhP}:\text{H}_3\text{PO}_4$	basal spacing (Å)	composition
CaPhP	1:0	15.0	$\text{Ca}(\text{C}_6\text{H}_5\text{PO}_4) \cdot 2\text{H}_2\text{O}$
Ca3.1	3:1	15.0	$\text{Ca}(\text{C}_6\text{H}_5\text{PO}_3)_{0.62}(\text{HPO}_4)_{0.38} \cdot 1.18\text{H}_2\text{O}$
Ca1.1	1:1	15.2	contains $\text{Ca}_5(\text{PO}_4)_3(\text{OH})$
Ca1.3	1:3	7.6	$\text{HCA}(\text{PO}_4)(\text{H}_2\text{O})_2$
Ca0.1	0:1	7.6	$\text{HCA}(\text{PO}_4)(\text{H}_2\text{O})_2$

and no filter was used. The 3D reconstructions and the analysis of the surface, volume, and porosity of the structures were performed via built-in CT image analysis software (v1.16.4.1, Bruker). The results, in terms of images with different X-ray adsorption, and 3D models were exported from Data Viewer and CTVox v1.16.4.1 software (Bruker). Prior to CT characterization, the printed hydrogels were placed in a closed sample holder with increased humidity in order to prevent drying out during the measurement process. The porosity was calculated only for a central part of the sample (a cylindrical area of 500 mm × 400 mm) in order to exclude the irregularities of the 3D surface from CT.

In Vitro Cytotoxicity Testing. For the cytotoxicity study, 3T3 fibroblasts (DSMZ, Braunschweig, Germany) were used. These were cultured in a CO_2 incubator in Dulbecco's Modified Eagle Medium (DMEM) containing 10% fetal bovine serum (FBS), streptomycin, penicillin, and L-glutamine, which were all purchased from Gibco (Life Technologies, Grand Island, NY).

An MTT assay was performed using 3-(4,5-dimethylthiazol-2-yl)-2,5-diphenyltetrazolium bromide (MTT) purchased from Merck (Rahway, NJ). MTT at concentration 0.5 mg mL^{-1} was diluted in full growth media and sterile filtered through a 0.22 μm filter (TPP Techno Plastic Products AG, Trasadingen, Switzerland). After 24 h incubation of cells with testing samples, the medium in 96-well TC plates was replaced with 100 μL of MTT solution and incubated for 3 h. Then the MTT solution was removed, and 100 μL of dimethyl sulfoxide was added to the wells. Absorbance was determined at 595 nm using a Multiskan FC photometer (Thermo Fisher Scientific, Waltham, MA).

NPs for MTT cytotoxicity assay were prepared as follows: 10 mg mL^{-1} of NPs was resuspended in ethylene glycol, and ultrasound was applied for 1 h. Then the full growth medium (DMEM, 10% FBS) was used to prepare NP dilutions in the range 10^{-2} – 10^{-9} mg mL^{-1} . 3T3 fibroblasts were seeded on 96-well TC plates at a density of 5000 cells per well and incubated overnight before NPs were applied to the cells. The cells were treated with NPs for 24 h. Afterward, the MTT assay was performed as described above.

The cytotoxicity of hydrogels was determined using hydrogel extracts and direct contact according to ISO10993-12.

Bioprinting. Bioprinting was performed with BALB mouse fibroblast cell lines. The cells were cultivated in DMEM (Sigma-Aldrich, St. Louis, MO) containing 10% fetal calf serum (FCS, Biosell, Nuremberg, Germany), 1% GlutaMAX (Gibco, Life Technologies, Grand Island, NY), and 0.1% gentamycin sulfate (Sigma-Aldrich) at 37 °C in a humidified incubator (95% relative humidity, 5% CO_2 ; Thermo Fisher Scientific, Waltham, MA). The cells were split using 0.05% trypsin (Sigma-Aldrich).

Bioinks were obtained by preparing pre-cross-linked inks containing either CaPhP or Ca3.1 according to the procedure described in the section [Ink Preparation for 3D Printing](#) and adding the cell suspension in phosphate buffered saline (PBS, pH 7.4) in 100 $\mu\text{L}/1$ mL v/v ratio, followed by thorough stirring. The bioinks were loaded into cartridges and printed by pneumatic extrusion printhead, using the 3D Discovery Bioplotter (RegenHU, Villaz-Saint-Pierre, Switzerland). The printing was done through conical nozzles or cylindrical needles of 0.52, 0.41, or 0.21 mm diameter. A printing model of a simple 1 cm × 1 cm grid was chosen. The printing pressure varied according to the bioink's properties.

Stabilization of the inks was done by immersing the prints in 0.1 wt % FeCl_3 solution in PBS for 2 h. Following this, live/dead staining was performed. The staining solution was prepared as follows: 2 μL of

ethidium homodimer 1 (dead stain) and 2 μL of calcein acetoxymethyl ester (live stain) were diluted in 10 mL of PBS. The staining solution was poured over the prints in a sufficient amount and left in an incubator for 1 h to allow full diffusion of the staining solution through the material. The stained cells were visualized in a DMI6000 fluorescence microscope (Leica, Wetzlar, Germany). The percentage of living cells was determined in three different places in the printed structure, and the results were averaged.

RESULTS AND DISCUSSION

Synthesis and Characterization of New Calcium Phenylphosphonate–Phosphate. The synthesis and exfoliation of CaPhP, as well as its use for preparation of polymer–inorganic nanocomposites, were described in our previous work.⁴¹ To increase possible interactions and compatibility with water-based systems, such as hydrogels, new material was synthesized where part of the phenyl groups was replaced by phosphate, followed by characterization, exfoliation, and optimization of the nanocomposites with NaAlG solution for 3D printing.

The synthesis of mixed calcium phosphonate–phosphate follows the same route as preparation of CaPhP which has been described in our previous works.^{40,41} Whereas for obtaining pure CaPhP, keeping the pH > 9 is the only necessary condition, for material with combined phosphonate and phosphate groups there are other important factors influencing the properties of the final product. The molar ratio of the reacting acids determines not only the composition but also the basal spacing of the final product. Different molar ratios were tested (see [Table 1](#)). Despite the high affinity of phosphonate moieties to Ca^{2+} ions,⁴² it was observed that phosphoric acid forms structures with Ca^{2+} more easily than phosphonate acid. Where H_3PO_4 excess occurs in the reaction mixture ($\text{H}_2\text{PhP}:\text{H}_3\text{PO}_4$ ratio 1:3), only the layered structure of brushite is formed, which does not contain any phenylphosphonate anions (see [Figure S1](#) in the [Supporting Information](#)). When the $\text{H}_2\text{PhP}:\text{H}_3\text{PO}_4$ ratios 1:1 or 3:1 were used, layered phases with a basal spacing of about 15 Å were formed, together with some hydroxylapatite. The amount of hydroxylapatite was lower for the 3:1 acid ratio. As temperature plays a significant role in hydroxylapatite formation,⁴³ change of reaction temperature, either heating to 50 °C or cooling in an ice bath, was proposed to support phenylphosphonate–phosphate formation over hydroxylapatite precipitation. It was observed that both heating and cooling of the reaction can successfully suppress hydroxylapatite formation, leading to pure Ca3.1 in the case of acid ratio 3:1 (see [Figure S2](#)). However, in the case of acid ratio 1:1, hydroxylapatite forms in significant quantities regardless of the reaction temperature. Additionally, the reaction mixture tends to thicken while heating, which causes difficulties with stirring. This problem is not present in cooled reaction conditions. Thus, the sample (Ca3.1) prepared from a reaction mixture of 3:1 acid ratio, which was cooled in an ice bath, was selected for exfoliation and application in 3D printing ink. The purity of

the product was determined by XRD as well as by basal spacing, which is given in Table 1. The diffraction pattern of this compound can be indexed (see Table S1) in a monoclinic system with lattice parameters shown in Table 2. Its chemical

Table 2. Crystallographic Data of the Prepared Ca3.1 Material

material	Ca3.1
crystal system	monoclinic
<i>a</i>	19.3258 ± 0.0003 Å
<i>b</i>	11.0287 ± 0.0003 Å
<i>c</i>	5.7158 ± 0.0001 Å
β	129.055 ± 0.004°

composition was verified by elemental analysis (found: C = 22.47%, H = 2.92%; calculated: C = 22.96%, H = 3.02%), and the molar ratio P:Ca 1:1 was confirmed by EDX. The morphology of the resulting particles was determined by SEM imaging (see Figure S3).

Liquid-Based Exfoliation of Particles. Successful liquid-based exfoliation depends on suitable solvent selection. An appropriate solvent that possesses good compatibility with the material submitted to exfoliation can act as an exfoliating as well as a stabilizing agent for nanoplatelets formed during the process.⁴⁴ The suitability of the combination of material and solvent can be tested by the simple procedure described by Kopecká et al.,⁴¹ in which a small amount of material in solvent is treated by ultrasound for 1 h. The stability of the obtained dispersion is observed and the presence of NPs is verified by Tyndall scattering.⁴⁵ In the present work, four solvents were tested: water, isopropyl alcohol, ethylene glycol, and glycerol. These solvents were chosen with respect to their polarity, promising good compatibility with Ca3.1 nanoplatelets. The second parameter in selection of a solvent was its miscibility with water, as the dispersions of exfoliated particles are intended as components of hydrogel-based 3D printing ink.

The best results were obtained for isopropyl alcohol, where no sedimentation occurred. Ethylene glycol dispersions also showed good stability, with only small amounts of material, which settled down. In the case of glycerol, significant sedimentation was observed, although Tyndall scattering was still present. Distilled water did not facilitate any stability in the dispersion, as no Tyndall scattering could be observed after 1 day of sedimentation. This means that the initial assumption that the presence of phosphate groups enhances compatibility with water was not confirmed. However, the potential to

perform liquid-based exfoliation in ethylene glycol provides a material highly miscible with water-based systems, with low cytotoxicity.⁴⁶ Therefore, we have successfully obtained a material suitable for mixing with aqueous biopolymer solution.

Furthermore, the morphology of the Ca3.1 nanoplatelets was characterized and compared to previously synthesized CaPhP.⁴⁰ When liquid-based exfoliation was performed by high shear homogenizer in the same conditions for CaPhP and Ca3.1, the mixed structure resulted in nanoplatelets with larger lateral dimensions, as determined by AFM (Figure 2), which showed Ca3.1 particles typically in the range of 3.2–3.6 nm thickness with lateral dimensions varying from 2 to 10 μm after the exfoliation process. It is assumed that the overlaps are created upon drying, but in the dispersion the individual lamellae are available.⁴⁵ The number-based histograms illustrate the decrease of the lateral size for CaPhP nanoplates (the most-populated equivalent diameter ca. 200 nm) in comparison to Ca3.1 (1300 nm) (Figure S4).

Rheological Characterization of NaAlg Nanocomposites. 3D printing via microextrusion is a technological process, typically requiring non-Newtonian liquids to achieve the desired results. In general, low viscosity is advantageous during extrusion in order to minimize energy consumption and the mechanical stress applied to the material. However, as the material is placed freely on the printed bed, high viscosity is required in order to maintain the cylindrical shape of the filament. Hence, the ideal rheological behavior of a 3D ink is shear thinning.⁴⁷ Here, we compare the ability of layered calcium phosphate particles to rheologically tune NaAlg solutions with that of spherical nanoAp particles.

The pre-cross-linked inks displayed clear shear thinning in the range of 10^{-1} – 10^2 rad s^{-1} (see Figure 3A). The microextrusion process typically corresponds to angular frequencies of 10^2 rad s^{-1} ; therefore, the selected range is sufficient to satisfy characterization requirements.⁴⁷ Three of the assessed inks showed initial viscosity in the range of 10^3 – 10^4 Pa·s, while all the compositions reached viscosities of 10^1 Pa·s upon approaching angular frequencies of 10^2 rad s^{-1} . The spherical nanoAp made virtually no difference to a pure 3% solution of NaAlg. Therefore, these particles are not suitable as a viscosity-modifying additive. Furthermore, the non-Newtonian tendency is rather weak in the case of these two compositions, and the initial viscosity is in the range of 10^1 Pa·s, which would presumably lead to high spreading of the filament upon deposition during printing.

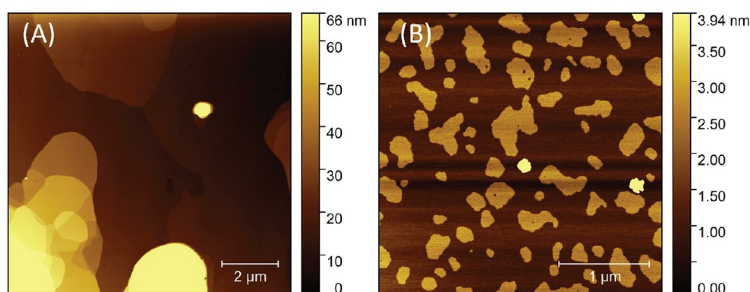


Figure 2. Atomic force microscopy scans of exfoliated particles. Nanoplatelets of (A) Ca3.1 exhibit greater lateral dimensions than nanoplatelets of (B) CaPhP.

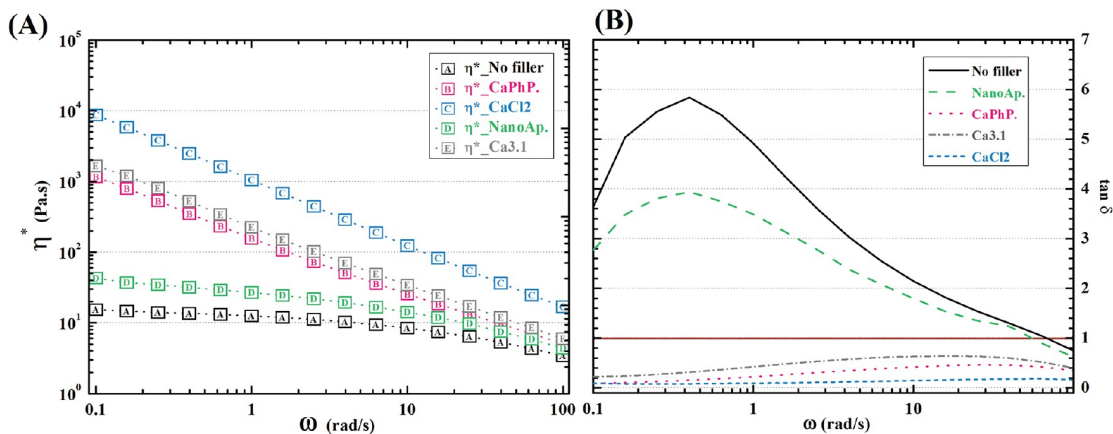


Figure 3. Dependence of (A) viscosity and (B) damping factor of pre-cross-linked inks on angular frequency.

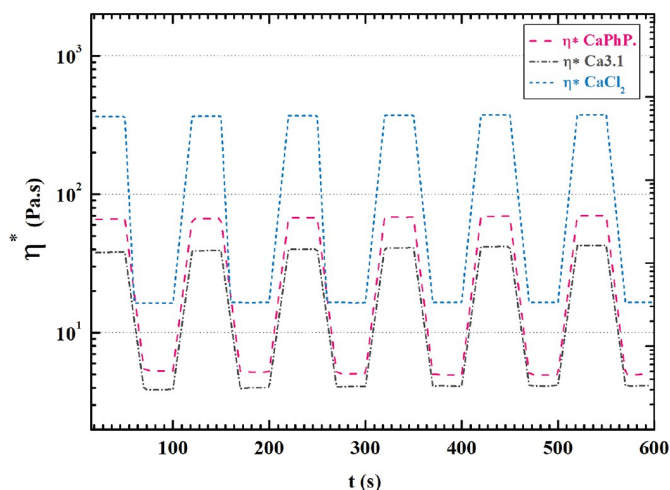


Figure 4. Cyclic shearing simulation of the microextrusion process.

This assumption is further supported by the damping factor, i.e., loss-to-storage modulus ratio (Figure 3B). Where the viscous response prevails, the material appears to be liquid; otherwise, the material is solid. Therefore, the damping factor gives an overall idea of the material's apparent behavior. A damping factor above 1, which was measured in the case of pure NaAlg as well as in nanoAp-modified NaAlg, determined these inks' behavior as liquidlike in the whole range of angular frequencies studied here. Conversely, the other viscosity-modifying additives caused the NaAlg to appear as a solid throughout the measurement. It can be assumed that the nanofillers dissociate some Ca^{2+} ions, which are known to cross-link polyanionic polymers, such as NaAlg.⁴⁸ In order to assess the influence of the free calcium ions on the rheology of NaAlg solution, one sample contained no nanoparticulate fillers, but only free Ca^{2+} ions. This sample displayed the lowest damping factor, determining that the presence of multivalent ions is a significant factor in the thickening of NaAlg solution. However, the high prevalence of storage over

loss modulus in this case may cause further problems in 3D printing accuracy due to the phenomenon of overgelation.⁴⁹

3D printing via microextrusion involves two main shear states of the material: (a) extrusion, during which the material is subjected to shear rates of 10^2 rad s^{-1} and (b) deposition, upon which the shear stress suddenly drops to zero. In order to more closely assess the suitability of the nanocomposite hydrogels for microextrusion 3D printing, the three selected inks were subjected to cyclic shear stress rapidly oscillating between high (extrusion) and low (deposition) shear stress. Figure 4 clearly shows that the rapid change in shear stress induces a change of viscosity which occurs within 10 s for any given rheological modifier. Furthermore, the hysteresis between cycles is minimal. These qualities are essential for a successful microextrusion process.⁵⁰

It is also clear that there is a large difference in the magnitude of the change, with the largest occurring with addition of CaCl_2 , followed by CaPhP, and Ca3.1. While a large difference in viscosity is generally beneficial to microextrusion printing, the viscosity values in the case of high shear

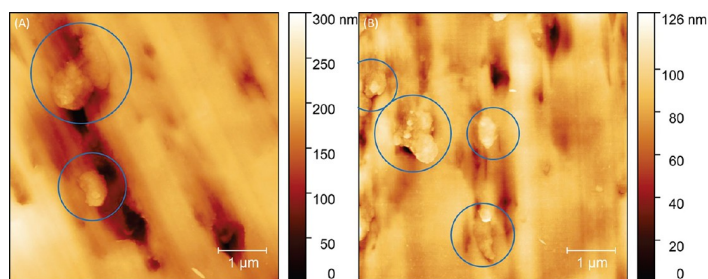


Figure 5. Atomic force microscopy topography scans of the section of the modified NaAlg hydrogel samples by (A) Ca3.1 and (B) CaPhP, where randomly oriented aggregates of nanoplatelets are observed.

stress should be noted. In that situation it is clear that CaPhP and Ca3.1 containing NaAlg inks reach the same orders of magnitude of viscosity as pure NaAlg solution (Figure 3A) at 10^2 rad s^{-1} , while the viscosity of CaCl_2 is 1 order higher in comparison. This may suggest a certain percentage of permanent cross-linking being present in the latter case. This would result in high irregularity of the printed strand during microextrusion.^{49,51} It could lead to higher occurrence of defects and result in overall mechanical weakening of the printed object. However, the shear-thinning behavior of the CaPhP- and Ca3.1-modified NaAlg pre-cross-linked inks could be the result of a flow-induced orientation of NPs. This phenomenon has been reported for Laponite filler.^{23,50} Due to the presence of ionic moieties on the surface of the particles, it is reasonable to assume the occurrence of a house-of-cards structure due to the particles' surface saturation by guluronic acid units of NaAlg. Thus, the rheological behavior of the presented pre-cross-linked inks could be the result of analogous phenomena.²³ Additionally, it was attempted to observe the nanoplatelets positioning in the pre-cross-linked inks by AFM. As can be seen in Figure 5, it was possible to observe randomly arranged particles in the cross section, which is in agreement with the hypothesis of the house-of-cards structure formation. However, it should be noted that AFM is in principle a surface measurement technique, and it may not reflect the positioning of the platelets in the bulk. Furthermore, the dimensions of the observed particles are larger compared to Figure 2, possibly suggesting incomplete exfoliation of the nanoplatelets. Despite this drawback, the CaPhP and Ca3.1 fillers facilitate significant rheological modification of the NaAlg solution.

When all the parameters are taken into account, the rheological evaluation favors the additive as the most suitable for 3D printing via microextrusion, in terms of viscosity modification of NaAlg. These assumptions are further tested by experimental microextrusion.

3D Printing. The main advantage of manufacturing via 3D printing is the ability to accurately place the material and all its components in the desired shape and, thus, form highly homogeneous and precise structures. Printing precision depends on material characteristics as well as processing parameters.⁵² It has been shown above that the inks tested display similar rheological behavior at high shear rate 4. Therefore, it is possible to obtain good printing results, as demonstrated by the printing of several structures, which can be seen in Figure 6.

The assessment of shape fidelity proposed by Ribeiro et al.³⁵ describes a filament fusion test method. This method makes

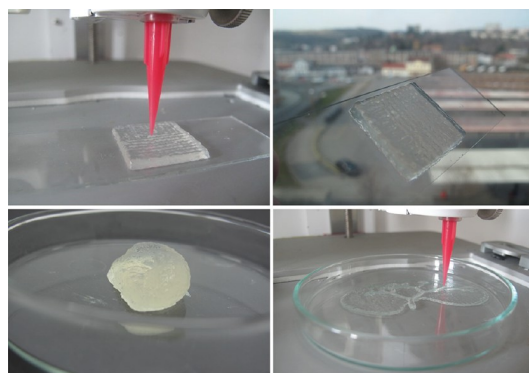


Figure 6. Structures obtained by 3D printing using either CaPhP- or Ca3.1-modified NaAlg.

readily available three parameters connected to printing precision. The current study is focused on strand thickness, partial fusion distance, and complete separation distance. The evaluation methodology is schematically described in Figure 7. Table 3 presents the obtained data.

In an ideal 3D printing ink, the strand thickness matches the nozzle diameter. However, hydrogel inks typically provide thicker strands than the ideal case. In order to provide complex characterization of the proposed inks, the die swell of material suspended from the nozzle and the strand thickness obtained on the printbed were measured. The strand thickness can be easily related to the ideal ink by the so-called swelling ratio, or the ratio of strand diameter to nozzle diameter. A decrease in nozzle diameter increases the shear stress placed upon the material during flow. Die swell, i.e., the ratio of real strand diameter of suspended material at the exit of the nozzle to the nominal nozzle diameter, is in direct connection to the normal stresses induced during shear flow of the material.⁵³ It is clear from the data in Table 3 that lower nozzle diameter induces higher normal stresses, causing more significant die swell. Furthermore, the pre-cross-linked ink containing Ca3.1 particles appears to be the least susceptible to the influence of normal stresses. The presence of fillers influences the rheological behavior of polymeric systems. There are several characteristics that need to be taken into account, mainly the concentration and geometry of the filler.⁵⁴ It has been found that the addition of solid particles in low concentrations generally decreases die swell. This effect is the most pronounced for fibers and flakes.⁵⁵ This is consistent with

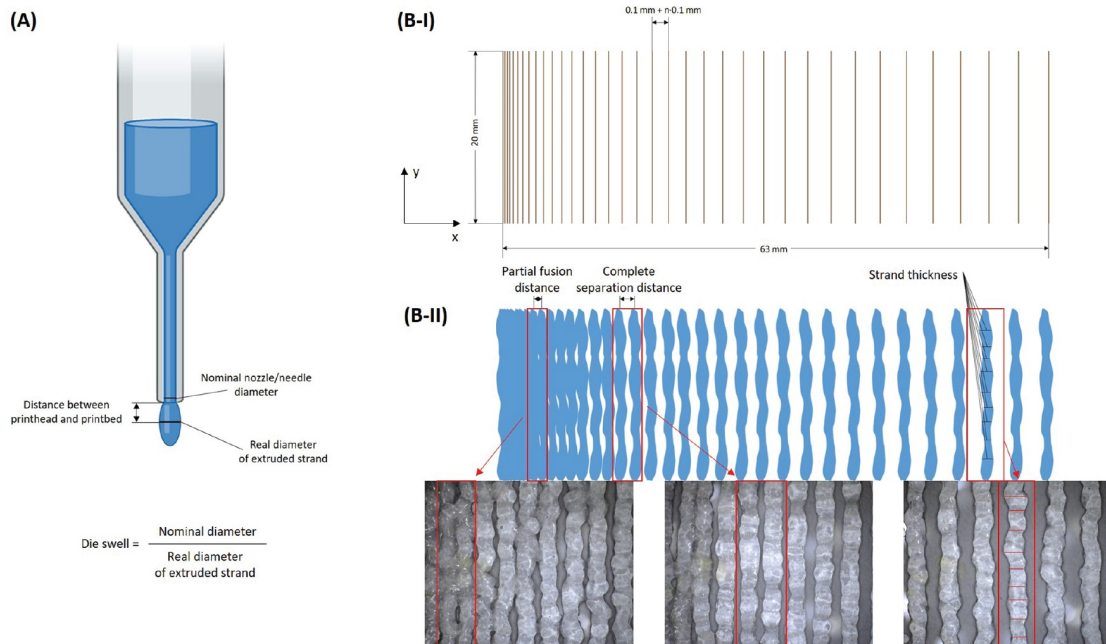


Figure 7. Schematic representation of evaluation of printing precision characteristics: (A) die swell, (B-I) filament fusion test printing model, and (B-II) example of filament fusion test evaluation.

Table 3. Printing Precision Characteristics of the Examined Pre-Cross-Linked Inks

	type of filler	die swell	strand thickness (mm)	partial fusion distance (mm)	complete separation distance (mm)
nozzle diameter 0.26 mm	CaCl ₂	3.0 ± 0.5	0.33 ± 0.08	1.7	1.9
	nanoAp	3.2 ± 0.2	0.56 ± 0.09	2.2	2.5
	Ca3.1	1.4 ± 0.2	0.45 ± 0.05	1.4	1.8
	CaPhP	2.3 ± 0.2	0.39 ± 0.06	1.4	1.8
nozzle diameter 0.42 mm	CaCl ₂	2.2 ± 0.4	0.6 ± 0.1	1.7	1.9
	nanoAp	2.2 ± 0.4	0.8 ± 0.1	2.5	2.9
	Ca3.1	1.42 ± 0.12	0.51 ± 0.07	1.5	1.9
	CaPhP	2.0 ± 0.2	0.45 ± 0.08	1.5	1.9

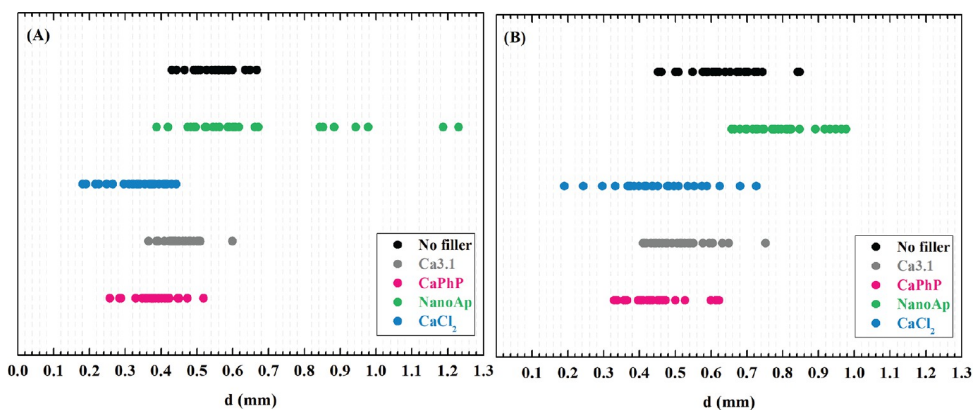


Figure 8. Strand diameter variation diagram: (A) 0.21 mm nozzle; (B) 0.42 mm nozzle.

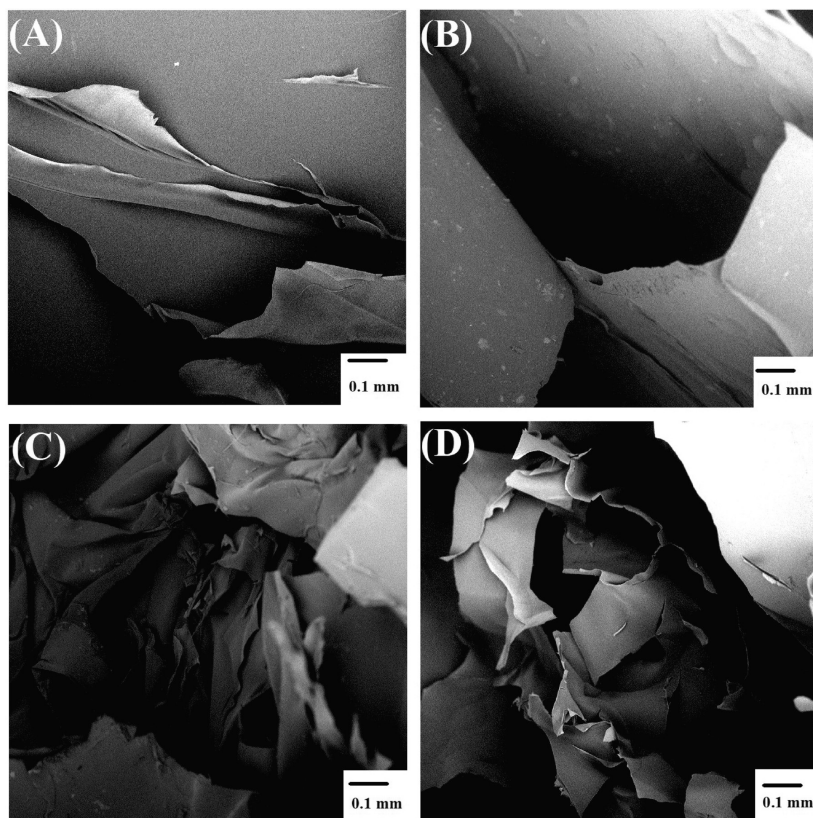


Figure 9. Scanning electron microscopy micrographs of cross-section cuts of freeze-dried hydrogels: (A) pure NaAlg, (B) nanoAp filler, (C) Ca3.1 filler, and (D) CaPhP filler.

the findings of the current study, as the lowest die swell was observed for layered nanofillers—CaPhP and Ca3.1—compared to using spherical nanoAp or no filler.

However, strand thickness does not follow the same trend as die swell. As is apparent from Table 3, Ca3.1 filler leads to higher strand thickness than CaPhP, despite lower die swell. It is possible to conclude that material spreading due to lower viscosity in the steady state (see Figure 4) plays a considerable role. The results for NaAlg pre-cross-linked ink containing only CaCl_2 (Figure 8) suggest even thinning of the material upon its placement on the printbed. This can be caused by the elongation of the material due to the constant movement of the printhead. The high viscosity of this ink at steady state prevents any material spreading.

The partial fusion distance and complete separation distance are parameters characterizing the nonideality of an ink by taking into account not only the mean strand thickness but also its fluctuations throughout the printing process. Under the assumption of well-designed process parameters in terms of avoiding turbulent flows in the channel, these fluctuations may be caused by the accumulation of stress due to the need to overcome material adhesion to the flow channel walls and also by inhomogeneities, such as improperly dispersed modifier particles and air bubbles. The fluctuations typically occur in the case of overgelation,⁴⁹ when the extreme rigidity of the

material prevents smooth flow. It is evident that though a thinner nozzle leads to higher swelling of the strand, the strand thickness distribution is narrower than in the case of a thicker nozzle (Figure 8). The large variations in strand diameter are particularly prominent when CaCl_2 is incorporated, on account of the overgelation phenomenon. Also, the liquid character of nanoAp-modified pre-cross-linked ink causes high spreading of the material, leading to great unevenness in the strand, which is intensified by greater die swell when a narrow nozzle is used. It can be assumed that the higher shear stress induced by a lower diameter of flow geometry contributes to the elimination of fluctuations in the flow of the material. It is therefore possible to obtain more precise structures with narrow nozzles than with wide ones when die swell is taken into account.

Morphology of Hydrogels. The advantageous rheological characteristics obtained by the incorporation of layered CaPhP and Ca3.1 in NaAlg solution and satisfactory printing precision allow the printing of constructs consisting of several layers of material (up to 25 layers). However, in order to achieve sufficient long-term stability of the hydrogel and increase its usability in further applications, a secondary form of cross-linking is needed. Because of the polyanionic character of NaAlg, it is readily cross-linkable by the simple addition of multivalent ions. In order to maintain the nontoxicity of the scaffold as well as the process, a 2 wt % solution of CaCl_2 was

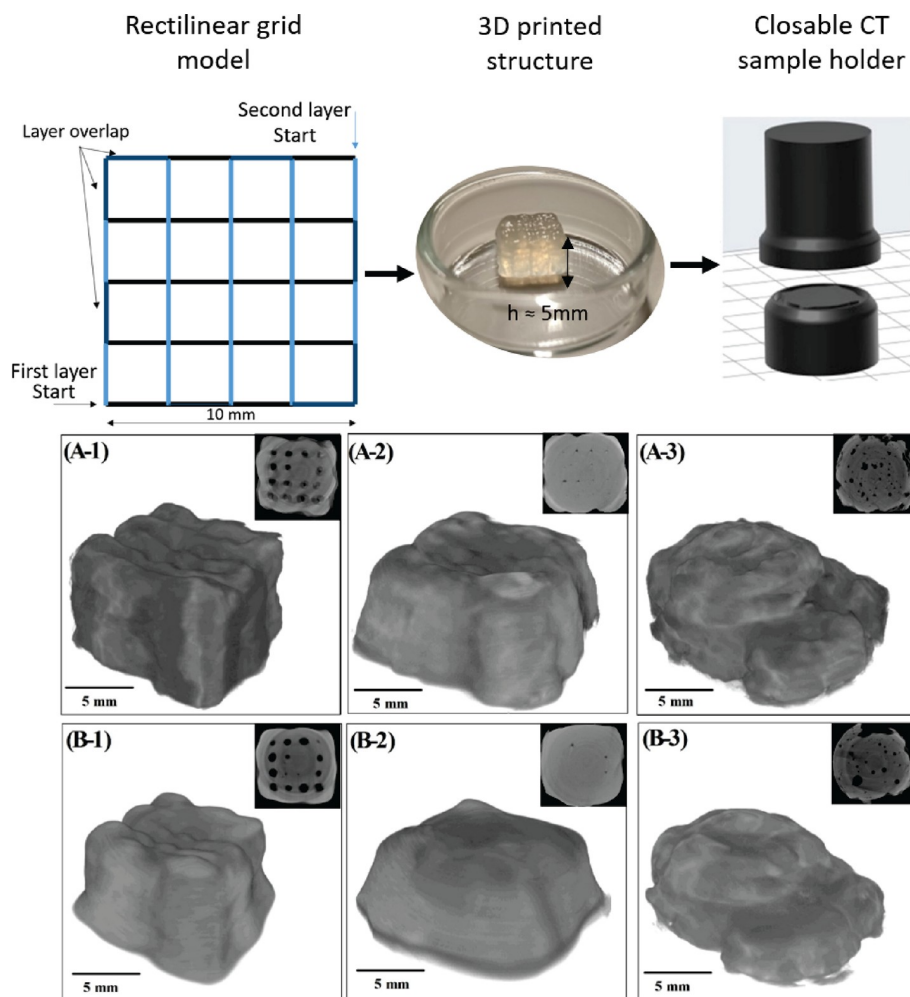


Figure 10. X-ray computed microtomography reconstruction of 3D printed NaAlg structures: (A) pre-cross-linked ink structures, (B) fully cross-linked hydrogel structures, (1) CaPhP filler, (2) Ca3.1 filler, and (3) CaCl₂ substitute for filler.

chosen as the source of multivalent ions. To assess the influence of ionic cross-linking on the morphology of printed constructs, SEM and CT analyses were applied.

Scanning electron microscopy imaging of freeze-dried hydrogels provided an insight into their inner structure. The hydrogels contained large pores, and their structure appeared to consist of laminated layers (see Figure 9).

CT measurement was used to characterize the overall shape and porosity of the printed constructs (multilayered grids). As seen in Figure 10, the best printing precision was achieved with CaPhP rheological modifier. Furthermore, it is apparent that the printed structures lose some shape fidelity and shrink in volume when ionic cross-linking is applied. The porosity present in the 3D structure due to fabrication by micro-extrusion was also evaluated from CT data. While CaPhP and CaCl₂ resulted in open porosity of approximately 25%, Ca3.1 provided open porosity below 0.2% and no closed porosity (see Table 4). This is consistent with the comparatively higher

Table 4. Analysis of Printing Induced Porosity of Hydrogel Scaffolds before and after Ionic Cross-Linking

ionic cross-linking	open porosity (%)		closed porosity (%)		number of pores	
	before	after	before	after	before	after
CaPhP	25.43	25.85	0.61	0.10	25	22
Ca3.1	0.13	0.01	0.01	0.01	5	3
CaCl ₂	23.89	25.85	0.01	0.12	35	22

spreading of the material during printing, which was discussed earlier. In all cases, the number of pores slightly decreased with the application of ionic cross-linking. Additionally, open porosity increased in the case of CaPhP- and CaCl₂-modified NaAlg samples. It can be assumed that the cross-linking causes the structure to collapse, leading to overall shrinkage, partial collapse of the structure, and the joining of pores in close proximity. This results in fewer pores with larger areas,

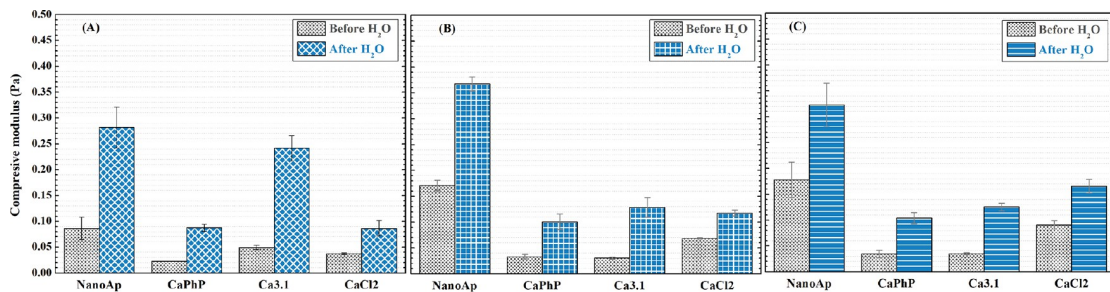


Figure 11. Comparison of Young's modulus of printed samples before and after washing with respect to printing density: (A) 10% infill density, (B) 20% infill density, and (C) 30% infill density.

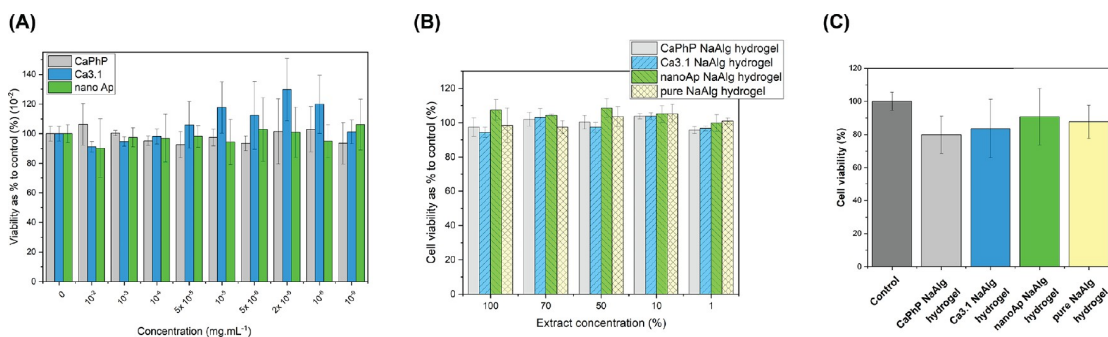


Figure 12. *In vitro* cytotoxicity test of (A) ethylene glycol dispersions of nanofillers after 24 h treatment of 3T3 fibroblasts, (B) extracts of NaAlg hydrogels, and (C) NaAlg hydrogels in direct contact developed in the study using 3T3 fibroblasts.

increasing porosity. It can be speculated that the described differences between agents for rheological modification result from their different chemical natures. These nuances ought to alter the material's surface energy, for both the organophosphonate particles and the composite ink. The higher surface energy of Ca3.1 containing NaAlg may explain part of the discrepancy in the behavior of CaPhP- and Ca3.1-filled hydrogels. However, this assumption needs further evaluation.

Compressive Strength. In order to increase the stability of the printed structures, ionic cross-linking was applied to them. The mechanical stability of hydrogels results from a variety of factors, both intrinsic (such as polymer M_w or cross-linking density) and extrinsic (shape and construction of the sample, temperature, etc.). Furthermore, fillers play a crucial role in guiding the mechanical performance. They can work as reinforcement, increasing the strength of a material, or as plasticizers. Hard inorganic particles, such as those present in the current study, generally work as reinforcing fillers due to their restricted ability to compress. Figure 11 shows the compressive moduli of NaAlg with various fillers. Nanoparticles of nanoAp failed to provide sufficient strength to the ink, and the structure collapsed during printing. Therefore, these hydrogels are excluded from the mechanical analysis.

The different infill density refers to the volume of free space in the printed cylinder. There is no distinct trend indicating correlation between infill density and compressive modulus of the hydrogels. However, there is a sharp increase of modulus (2 times or more) when the hydrogel is washed in DEMI water for several days. The values of the moduli are consistent with results published elsewhere.^{48,56,57} This treatment ensures the

diffusion of excessive ions out of the hydrogel. This phenomenon is likely caused by a difference in swelling behavior with respect to the environment. The polyelectrolytic nature of NaAlg causes higher swelling in ion-rich environments. Indeed, swelling has been reported to be lower in water than in salt solutions.⁵⁸ Also, the equilibrium swelling in CaCl₂ solutions is dependent on their concentration, peaking at 2 wt %, ^{59,60} the concentration used for the cross-linker in this study. Furthermore, the concentration of Ca²⁺ in the hydrogels is likely to induce conjugation of junction zones of α -L-galuronic acid and β -D-mannuronic acid. These junctions lead to the collapse of the polymer network, which results in a decrease of Young's modulus.⁶¹ The washed samples are more suitable for mechanically demanding applications. Additionally, it is possible to assume that high salt concentration may be harmful to cells.⁶² Therefore, the highly concentrated CaCl₂ solution is unsuitable for applications involving direct contact with living cells, specifically bioprinting, as washing is necessary from both a mechanical and a cytocompatibility point of view.

***In Vitro* Cytotoxicity.** The potential application of the new hydrogels prepared in this study is as scaffolds in regenerative medicine. In this respect, the cytotoxicity of pure NPs and of fully cross-linked hydrogel formulations was assessed according to ISO norm 10993-12 using 3T3 fibroblasts and MTT assay. Three types of NPs were tested in the concentration range 10^{-2} – 10^{-9} mg mL⁻¹. As can be seen from Figure 12A, the NPs were found to be nontoxic up to a concentration of 10^{-2} mg mL⁻¹, which is 10000 times higher than the concentration necessary for rheological modification. It can be concluded that

Table 5. Bioprinting Conditions

printhead tip	cylindrical needle			conical nozzle		
diameter (mm)	0.52	0.41	0.21	0.52	0.41	0.21
printing pressure (kPa)	46.9	51.9	82.6	88.7	119.7	178.0
stabilization with Fe ³⁺	stable	stable	unstable	stable	stable	unstable

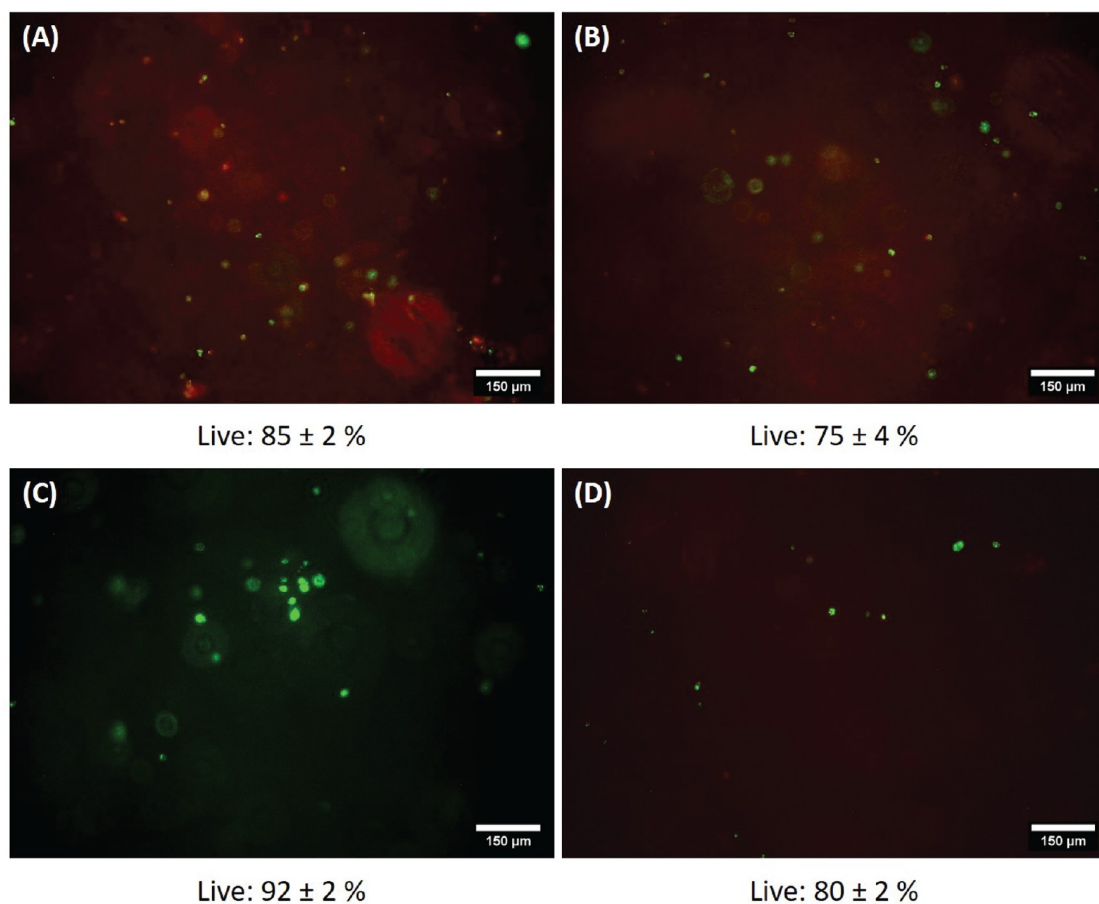


Figure 13. Live/dead staining of bioinks after 3D printing: (A) 0.52 mm diameter nozzle, (B) 0.52 mm diameter needle, (C) 0.42 mm diameter nozzle, and (D) 0.42 mm diameter needle.

the use of all three types of NPs is safe from the cytocompatibility point of view.

Further, the cytotoxicity of different hydrogel formulations was tested after direct contact with hydrogels and as hydrogel extracts (Figure 12B,C). All prepared hydrogels were non-cytotoxic. Thus, the presented materials have potential in biological applications, including scaffold fabrication and cell cultivation.

Bioprinting. The simple usage of the bioink was possible due to the highly shear-thinning character of the pre-cross-linked inks, which imposes minimum stress on the cells during rapid mechanical mixing. The Ca3.1 nanofiller was chosen as the most suitable option due to its higher damping factor compared to CaPhP-formed pre-cross-linked ink, which is presumed to be beneficial to protecting the encapsulated cells

during microextrusion 3D printing.⁶³ In order to map the effect of printhead shape and size on cells, the experimental 3D bioprinting was conducted with two types of printhead tips—cylindrical needle and conical nozzle—of three different sizes: 0.52, 0.41, and 0.21 mm. It is expected that a narrower printhead causes higher shear stress and will result in lower cell viability.⁶⁴ Additionally, the cylindrical needle imposes constant high shear stress on the material, including the cells, whereas the shear stress increases gradually with the conical nozzle.⁶⁵ In fact, printing pressure increases with the decrease of tip diameter, as well as between nozzle and needle, which is in agreement with theory (see Table 5).

Stabilization of the NaAlg pre-cross-linked inks with 2 wt % CaCl₂ solution is incompatible with living cells, as the high salt concentration is cytotoxic.⁶² Therefore, an alternative final

cross-linking method was proposed: 0.1% MCl_x solution in PBS, where M stands for a metal cation: Zn^{2+} , Mg^{2+} , or Fe^{3+} . The results can be found in the [Supporting Information](#) (Figure S5). Because of good long-term stability, $FeCl_3$ was chosen for the stabilization of the bioprinted structures. The significant decrease of salt concentration would allow the washing out step described earlier to be omitted, enabling (a) the achievement of maximum mechanical strength in one step and (b) the immediate cultivation of cells placed on the surface of the printed structures or encapsulated in the printing material itself. In other words, the alteration of the full cross-linking procedure is a step toward preparation of a bioink. Additionally, Fe^{3+} appears more advantageous than Ca^{2+} on account of its improved mechanical stability, stimuli-responsiveness, and redox properties.⁶⁶ However, the need to significantly reduce the concentration of multivalent ions in the cross-linking solution leads to a lower rate of final cross-linking and a 4-fold increase of cross-linking time from 30 min to 2 h. This prolonged exposure to a high-water-content environment caused dissolution of the pre-cross-linked inks in some cases (see [Table 5](#)).

It was observed that printed strands of lower dimensions disintegrate faster than bulky structures, and the prints obtained by a 0.21 mm diameter tip all dissolved before live/dead assay could be performed. Previously, it was found that porous structures formed of Ca3.1-modified materials tend to collapse during the final cross-linking (see [Table 4](#)). This led to the creation of bulkier printed structures, decreasing the disintegration rate.

Live/dead staining was used as a qualitative assessment of the materials' usability as bioink. Ethidium homodimer, a DNA stain, cannot penetrate an intact cell membrane;⁶⁸ thus, it can be used as an efficient means to detect mechanical damage resulting from microextrusion.⁶⁹ It can be seen that extrusion printing with BALB/3T3 cells sustains 70–90% cell viability ([Figure 13](#)). Therefore, BALB cells can be safely encapsulated in Ca3.1-modified NaAlg, forming a bioink for printing via microextrusion.

CONCLUSION

The current study aimed to employ layered nanoparticulate organophosphonate-based fillers in order to achieve rheological modification of NaAlg solution through the formation of a house-of-cards structure. In order to increase the hydrophilicity of NPs, enhancing the interactions in aqueous NaAlg solution, a novel material, Ca3.1, was synthesized. Its ability to modify the flow behavior of the polymer solution was compared to that of previously developed layered CaPhP NPs as well as to spherical nanoAp. Furthermore, the effect of Ca^{2+} dissociation was assessed by omitting the nanofiller carrier and using free Ca^{2+} ions in solution.

It was found that spherical nanoAp does not have any effect on NaAlg rheology as it is incapable of spontaneously creating the desired random arrangement. Free Ca^{2+} ions, however, lead to significant stiffening of the polymer, which causes overgelation and loss of printing precision. Therefore, the use of layered nanofillers—CaPhP and Ca3.1—shows potential to create highly precise constructs by microextrusion 3D printing.

In order to maintain the long term stability of the hydrogels, a secondary cross-linking using multivalent ions (Ca^{2+} or Fe^{3+} , respective of a single-step or multistep cell cultivation procedure) was used. This cross-linking led to a certain

shrinkage of the hydrogel and the loss of a portion of printing-induced porosity. It also led to a decreasing of stiffness in compression. However, this loss of stiffness was reversible by extracting the excess Ca^{2+} ions.

In summary, we have described the synthesis of novel layered organophosphonate NPs, as well as their use as rheological modifiers for biopolymer-based hydrogels. We have shown that these layered organophosphonates provide high printing precision in microextrusion experiments. Furthermore, we have used the NaAlg-based matrices modified with Ca3.1 for the encapsulation of BALB/3T3 cells and experimental microextrusion bioprinting. This process was proved to be nonharmful. Thus, the potential to use the materials described in this study for bioprinting is proved.

ASSOCIATED CONTENT

Supporting Information

The Supporting Information is available free of charge at <https://pubs.acs.org/doi/10.1021/acs.biomac.3c00081>.

Figures S1–S5 and Table S1 (PDF)

AUTHOR INFORMATION

Corresponding Authors

Lenka Vítková – Department of Physics and Materials Engineering, Faculty of Technology, Tomas Bata University in Zlin, 76001 Zlin, Czech Republic; orcid.org/0000-0002-6747-1785; Email: vitkova@utb.cz

Alěš Mráček – Department of Physics and Materials Engineering, Faculty of Technology, Tomas Bata University in Zlin, 76001 Zlin, Czech Republic; Centre of Polymer Systems, Tomas Bata University in Zlin, 76001 Zlin, Czech Republic; orcid.org/0000-0003-4387-5627; Email: mracek@utb.cz

Authors

Kateřina Kopecká – SYNPO, 532 07 Pardubice, Czech Republic; Department of General and Inorganic Chemistry, Faculty of Chemical Technology, University of Pardubice, 53210 Pardubice, Czech Republic; Joint Laboratory of Solid State Chemistry, Faculty of Chemical Technology, University of Pardubice, 53210 Pardubice, Czech Republic; orcid.org/0000-0002-5628-7595

Zuzana Kroneková – Polymer Institute of Slovak academy of Sciences, 84541 Bratislava, Slovak Republic; National Institute of Rheumatic Diseases, 921 12 Piestany, Slovak Republic

Lenka Musilová – Department of Physics and Materials Engineering, Faculty of Technology, Tomas Bata University in Zlin, 76001 Zlin, Czech Republic; Centre of Polymer Systems, Tomas Bata University in Zlin, 76001 Zlin, Czech Republic

Petr Smolka – Department of Physics and Materials Engineering, Faculty of Technology, Tomas Bata University in Zlin, 76001 Zlin, Czech Republic; Centre of Polymer Systems, Tomas Bata University in Zlin, 76001 Zlin, Czech Republic

Filip Mikulka – Department of Physics and Materials Engineering, Faculty of Technology, Tomas Bata University in Zlin, 76001 Zlin, Czech Republic; Centre of Polymer Systems, Tomas Bata University in Zlin, 76001 Zlin, Czech Republic

Klára Melánová – Joint Laboratory of Solid State Chemistry, Faculty of Chemical Technology, University of Pardubice, 53210 Pardubice, Czech Republic; orcid.org/0000-0001-7163-2476

Petr Knotek – Department of General and Inorganic Chemistry, Faculty of Chemical Technology, University of Pardubice, 53210 Pardubice, Czech Republic; orcid.org/0000-0003-2407-4947

Martin Humeník – Lehrstuhl Biomaterialien, Universität Bayreuth, 95447 Bayreuth, Germany; orcid.org/0000-0002-2097-8941

Antonín Minařík – Department of Physics and Materials Engineering, Faculty of Technology, Tomas Bata University in Zlín, 76001 Zlín, Czech Republic; Centre of Polymer Systems, Tomas Bata University in Zlín, 76001 Zlín, Czech Republic; orcid.org/0000-0002-0055-675X

Complete contact information is available at:

<https://pubs.acs.org/10.1021/acs.biomac.3c00081>

Author Contributions

Author contributions to the present study according to CRediT taxonomy, are as follows. Conceptualization: K.K., L.V., A.M. (Antonín Minařík), A.M. (Aleš Mráček). Formal analysis: Z.K., L.M., P.K. Funding acquisition: K.K., Z.K., A.M., M.H. Investigation: K.K., L.V., Z.K., F.M., K.M., P.K.. Methodology: L.M., P.S., K.M., M.H.. Project administration: K.K.; Z.K.; A.M. Supervision: L.M., P.K., A.M., M.H. (Antonín Minařík), A.M. (Aleš Mráček). Validation: K.K., L.V., Z.K.; Visualization: K.K., Z.K., L.M. Writing—original draft: K.K., L.V., Z.K., F.M. Writing—review and editing: K.K., L.V., Z.K., L.M., P.S., F.M., K.M., P.K., M.H., A.M.

Notes

The authors declare no competing financial interest.

ACKNOWLEDGMENTS

K.K. is grateful for the support of Grant TH02020201 of the Technology Agency of the Czech Republic. L.V. acknowledges the support of OP RDE Junior Grants of TBU in Zlín, Reg. No. CZ.02.2.69/0.0/0.0/19_073/0016941. Z.K. gratefully acknowledges the support of Advanced bioactive hydrogel scaffolds for regenerative medicine, ITMS 2014+: 313011BWL6 of the Operational Programme Integrated Infrastructure, funded by the European Regional Development Fund. L.M. and A.M. (Aleš Mráček) express their gratitude to project DKRVO (RP/CPS/2022/003). F.M. is thankful to TBU Grant IGA/FT/2023/006. P.S., M.H., and A.M. (Antonín Minařík) are grateful to Project No. 22-33307S of the Czech Science Foundation. The authors thank Prof. Thomas Scheibel, Department of Biomaterials, University of Bayreuth, for providing them with the facility for 3D printing on a RegenHU instrument.

REFERENCES

- (1) Li, J.; Wu, C. T.; Chu, P. K.; Gelinsky, M. 3D printing of hydrogels: Rational design strategies and emerging biomedical applications. *Mater. Sci. Eng. R Rep.* **2020**, *140*, 100543.
- (2) Benwood, C.; Chrenek, J.; Kirsch, R. L.; Masri, N. Z.; Richards, H.; Teetzen, K.; Willerth, S. M. Natural Biomaterials and Their Use as Bioinks for Printing Tissues. *Bioeng.* **2021**, *8* (2), 27.
- (3) Wu, X.; Li, W.; Chen, K.; Zhang, D. K.; Xu, L. M.; Yang, X. H. A tough PVA/HA/COL composite hydrogel with simple process and excellent mechanical properties. *Mater. Today Commun.* **2019**, *21*, 100702.

- (4) Zhu, H.; Monavari, M.; Zheng, K.; Distler, T.; Ouyang, L. L.; Heid, S.; Jin, Z. R.; He, J. K.; Li, D. C.; Boccaccini, A. R. 3D Bioprinting of Multifunctional Dynamic Nanocomposite Bioinks Incorporating Cu-Doped Mesoporous Bioactive Glass Nanoparticles for Bone Tissue Engineering. *Small* **2022**, *18* (12), 2104996.

- (5) Karis, D.; Nelson, A. Time-dependent covalent network formation in extrudable hydrogels. *Polym. Chem.* **2020**, *11* (43), 6910–6918.

- (6) Li, Z. W.; Du, T. M.; Ruan, C. S.; Niu, X. F. Bioinspired mineralized collagen scaffolds for bone tissue engineering. *Bioact. Mater.* **2021**, *6* (5), 1491–1511.

- (7) Lee, A.; Hudson, A. R.; Shiwarski, D. J.; Tashman, J. W.; Hinton, T. J.; Yerneni, S.; Bliley, J. M.; Campbell, P. G.; Feinberg, A. W. 3D bioprinting of collagen to rebuild components of the human heart. *Science* **2019**, *365* (6452), 482.

- (8) Dutta, S. D.; Hexiu, J.; Patel, D. K.; Ganguly, K.; Lim, K. T. 3D-printed bioactive and biodegradable hydrogel scaffolds of alginate-gelatin/cellulose nanocrystals for tissue engineering. *Int. J. Biol. Macromol.* **2021**, *167*, 644–658.

- (9) Gao, F.; Xu, Z. Y.; Liang, Q. F.; Li, H. F.; Peng, L. Q.; Wu, M. M.; Zhao, X. L.; Cui, X.; Ruan, C. S.; Liu, W. G. Osteochondral Regeneration with 3D-Printed Biodegradable High-Strength Supramolecular Polymer Reinforced-Gelatin Hydrogel Scaffolds. *Adv. Sci.* **2019**, *6* (15), 1900867.

- (10) Sultan, S.; Mathew, A. P. 3D printed scaffolds with gradient porosity based on a cellulose nanocrystal hydrogel. *Nanoscale* **2018**, *10* (9), 4421–4431.

- (11) Bello, A. B.; Kim, D.; Kim, D.; Park, H.; Lee, S. H. Engineering and Functionalization of Gelatin Biomaterials: From Cell Culture to Medical Applications. *Tissue Eng. Part B Rev.* **2020**, *26* (2), 164–180.

- (12) Anand, R.; Amoli, M. S.; Huysecom, A. S.; Amorim, P. A.; Ageton, H.; Geris, L.; Bloemen, V. A tunable gelatin-hyaluronan dialdehyde/methacryloyl gelatin interpenetrating polymer network hydrogel for additive tissue manufacturing. *Biomed. Mater.* **2022**, *17* (4), 045027.

- (13) Kim, H. S.; Kim, C.; Lee, K. Y. Three-dimensional bioprinting of polysaccharide-based self-healing hydrogels with dual cross-linking. *J. Biomed. Mater. Res, Part A* **2022**, *110* (4), 761–772.

- (14) Roh, H. K.; Kim, H. S.; Kim, C.; Lee, K. Y. 3D Printing of Polysaccharide-Based Self-Healing Hydrogel Reinforced with Alginate for Secondary Cross-Linking. *Biomedicines* **2021**, *9* (9), 1224.

- (15) Rastogi, P.; Kandasubramanian, B. Review of alginate-based hydrogel bioprinting for application in tissue engineering. *Biofabrication* **2019**, *11* (4), 042001.

- (16) Raus, R. A.; Nawawi, W. M. F. W.; Nasaruddin, R. R. Alginate and alginate composites for biomedical applications. *Asian J. Pharm. Sci.* **2021**, *16* (3), 280–306.

- (17) Jejurikar, A.; Lawrie, G.; Martin, D.; Grondahl, L. A novel strategy for preparing mechanically robust ionically cross-linked alginate hydrogels. *Biomed. Mater.* **2011**, *6* (2), 025010.

- (18) Tam, S. K.; Dusseault, J.; Bilodeau, S.; Langlois, G.; Halle, J. P.; Yahia, L. Factors influencing alginate gel biocompatibility. *J. Biomed. Mater. Res, Part A* **2011**, *98A* (1), 40–52.

- (19) Cross, L. M.; Shah, K.; Palani, S.; Peak, C. W.; Gaharwar, A. K. Gradient nanocomposite hydrogels for interface tissue engineering. *Nanomedicine: NBM* **2018**, *14* (7), 2465–2474.

- (20) Plaizier-Vercammen, J. Rheological properties of Laponite® XLG, a synthetic purified hectorite. *Pharmazie* **1992**, *47* (11), 856–861.

- (21) Afghah, F.; Altunbek, M.; Dikyol, C.; Koc, B. Preparation and characterization of nanoclay-hydrogel composite support-bath for bioprinting of complex structures. *Sci. Rep.* **2020**, *10* (1), 5257.

- (22) Reich, H.; Dijkstra, M.; van Rooij, R.; Schmidt, M. Entropic Wetting and the Free Isotropic-Nematic Interface of Hard Colloidal Platelets. *J. Phys. Chem. B* **2007**, *111* (27), 7825–7835.

- (23) Davila, J. L.; d'Ávila, M. A. Laponite® as a rheology modifier of alginate solutions: Physical gelation and aging evolution. *Carbohydr. Polym.* **2017**, *157*, 1–8.

- (24) Davila, J. L.; d'Ávila, M. A. Rheological evaluation of Laponite®/alginate inks for 3D extrusion-based printing. *J. Adv. Manuf. Technol.* **2019**, *101*, 675–686.
- (25) Leu, A. R.; Cucuruz, A.; Ghitulica, C. D.; Voicu, G.; Stamati, L. R.; Dinescu, S.; Vlasceanu, G. M.; Stavarache, C.; Ianchis, R.; Iovu, H. 3D Printable Composite Biomaterials Based on GelMA and Hydroxyapatite Powders Doped with Cerium Ions for Bone Tissue Regeneration. *Int. J. Mol. Sci.* **2022**, *23* (3), 1841.
- (26) Teepakakorn, A.; Ogawa, M. Interactions of layered clay minerals with water-soluble polymers; structural design and functions. *Appl. Clay Sci.* **2022**, *222*, 106487.
- (27) Haraguchi, K.; Farnworth, R.; Ohbayashi, A.; Takehisa, T. Compositional Effects on Mechanical Properties of Nanocomposite Hydrogels Composed of Poly(N, N-dimethylacrylamide) and Clay. *Macromolecules* **2003**, *36* (15), 5732–5741.
- (28) Patarroyo, J. L.; Cifuentes, J.; Munoz, L. N.; Cruz, J. C.; Reyes, L. H. Novel antibacterial hydrogels based on gelatin/polyvinyl-alcohol and graphene oxide/silver nanoconjugates: formulation, characterization, and preliminary biocompatibility evaluation. *Heliyon* **2022**, *8* (3), e09145.
- (29) Paydayesh, A.; Heleil, L.; Sh, A. D. Preparation and application of poly(hydroxyl ethyl methacrylate) nanocomposite hydrogels containing iron oxide nanoparticles as wound dressing. *Polym. Polym. Compos.* **2022**, *30*, 09673911211063106.
- (30) Fang, Z.; Qiao, K.; Wang, Y. S.; Zheng, Y. D.; He, W.; Xie, Y. J.; Yang, H. Y. Injectable and biodegradable double-network nanocomposite hydrogel with regulable sol-gel transition process and mechanical properties. *Polym. Test.* **2022**, *106*, 107452.
- (31) Saglam-Metiner, P.; Gulce-Iz, S.; Biray-Avci, C. Bioengineering-inspired three-dimensional culture systems: Organoids to create tumor microenvironment. *Gene* **2019**, *686*, 203–212.
- (32) Jung, G. Y.; Park, Y. J.; Han, J. S. Effects of HA released calcium ion on osteoblast differentiation. *J. Mater. Sci.: Mater. Med.* **2010**, *21* (5), 1649–1654.
- (33) Beck, G. Inorganic phosphate regulates multiple genes during osteoblast differentiation, including Nr2f. *Exp. Cell Res.* **2003**, *288* (2), 288–300.
- (34) Fischer, L.; Nosratlo, M.; Hast, K.; Karakaya, E.; Strohlein, N.; Esser, T. U.; Gerum, R.; Richter, S.; Engel, F. B.; Detsch, R.; Fabry, B.; Thievensen, I. Calcium supplementation of bioinks reduces shear stress-induced cell damage during bioprinting. *Biofabrication* **2022**, *14* (4), 045005.
- (35) Ribeiro, A.; Blokzijl, M. M.; Levato, R.; Visser, C. W.; Castilho, M.; Hennink, W. E.; Vermonden, T.; Malda, J. Assessing bioink shape fidelity to aid material development in 3D bioprinting. *Biofabrication* **2018**, *10* (1), 014102.
- (36) Klapetek, P.; Necas, D.; Anderson, C. “Gwyddion - Free SPM data analysis software”, v. 2.53, 2019.
- (37) Sahoo, P. K.; Soltani, S.; Wong, A. K. C. A survey of thresholding techniques. *Comput. graph. image process.* **1988**, *41* (2), 233–260.
- (38) Knotek, P.; Vlcek, M.; Kincl, M.; Tichy, L. On the ultraviolet light induced oxidation of amorphous As₂S₃ film. *Thin Solid Films* **2012**, *520* (16), 5472–5478.
- (39) Knotek, P.; Tichy, L. Atomic force microscopy and atomic force acoustic microscopy characterization of photo-induced changes in some Ge-As-S amorphous films. *Thin Solid Films* **2009**, *517* (5), 1837–1840.
- (40) Svoboda, J.; Zima, V.; Benes, L.; Melanova, K.; Vlcek, M. Synthesis and Characterization of New Calcium Phenylphosphonates and 4-Carboxyphenylphosphonates. *Inorg. Chem.* **2005**, *44* (26), 9968–9976.
- (41) Kopecka, K.; Benes, L.; Melanova, K.; Zima, V.; Knotek, P.; Zetkova, K. Layered calcium phenylphosphonate: a hybrid material for a new generation of nanofillers. *Beilstein J. Nanotechnol.* **2018**, *9*, 2906–2915.
- (42) Sevrain, C. M.; Berchel, M.; Couthon, H.; Jaffres, P. A. Phosphonic acid: preparation and applications. *Beilstein J. Org. Chem.* **2017**, *13*, 2186–2213.
- (43) Vandecandelaere, N.; Rey, C.; Drouet, C. Biomimetic apatite-based biomaterials: on the critical impact of synthesis and post-synthesis parameters. *J. Mater. Sci.: Mater. Med.* **2012**, *23* (11), 2593–2606.
- (44) Niu, L.; Coleman, J. N.; Zhang, H.; Shin, H.; Chhowalla, M.; Zheng, Z. J. Production of Two-Dimensional Nanomaterials via Liquid-Based Direct Exfoliation. *Small* **2016**, *12* (3), 272–293.
- (45) Coleman, J. N.; Lotya, M.; O'Neill, A.; Bergin, S. D.; King, P. J.; Khan, U.; Young, K.; Gaucher, A.; De, S.; Smith, R. J.; Shvets, I. V.; Arora, S. K.; Stanton, G.; Kim, H.-Y.; Lee, K.; Kim, G. T.; Duesberg, G. S.; Hallam, T.; Boland, J. J.; Wang, J. J.; Donegan, J. F.; Grunlan, J. C.; Moriarty, G.; Shmeliov, A.; Nicholls, R. J.; Perkins, J. M.; Grievson, E. M.; Theuwissen, K.; McComb, D. W.; Nellist, P. D.; Nicolosi, V. Two-Dimensional Nanosheets Produced by Liquid Exfoliation of Layered Materials. *Science* **2011**, *331* (6017), 568–571.
- (46) McMartin, K. E.; Cenac, T. A. Toxicity of Ethylene Glycol Metabolites in Normal Human Kidney Cells. *Ann. N. Y. Acad. Sci.* **2000**, *919* (1), 315–317.
- (47) Fu, Z. Q.; Naghie, S.; Xu, C. C.; Wang, C. J.; Sun, W.; Chen, X. B. Printability in extrusion bioprinting. *Biofabrication* **2021**, *13* (3), 033001.
- (48) Voo, V. P.; Ooi, C. W.; Islam, A.; Tey, B. T.; Chan, E. S. Calcium alginate hydrogel beads with high stiffness and extended dissolution behaviour. *Eur. Polym. J.* **2016**, *75*, 343–353.
- (49) Ouyang, L.; Yao, R.; Zhao, Y.; Sun, W. Effect of bioink properties on printability and cell viability for 3D bioplotting of embryonic stem cells. *Biofabrication* **2016**, *8* (3), 035020.
- (50) Zhang, M.; Vora, A.; Han, W.; Wojtecki, R. J.; Maune, H.; Le, A. B. A.; Thompson, L. E.; McClelland, G. M.; Ribet, F.; Engler, A. C.; Nelson, A. Dual-Responsive Hydrogels for Direct-Write 3D Printing. *Macromolecules* **2015**, *48* (18), 6482–6488.
- (51) Hölzl, K.; Lin, S. M.; Tytgat, L.; Van Vlierberghe, S.; Gu, L. X.; Ovsianikov, A. Bioink properties before, during and after 3D bioprinting. *Biofabrication* **2016**, *8* (3), 032002.
- (52) Gillispie, G.; Prim, P.; Copus, J.; Fisher, J.; Mikos, A. G.; Yoo, J. J.; Atala, A.; Lee, S. J. Assessment methodologies for extrusion-based bioink printability. *Biofabrication* **2020**, *12* (2), 022003.
- (53) Wang, K. 4. Die Swell of Complex Polymeric Systems. In *Viscoelasticity - From Theory to Biological Applications*; De Vicente, J., Ed.; InTechOpen: 2012.
- (54) Metzner, A. B. Rheology of Suspensions in Polymeric Liquids. *J. Rheol.* **1985**, *29* (6), 739–775.
- (55) Stabik, J. Influence of Filler Particle Geometry on Die Swell. *Int. Polym. Process.* **2004**, *19* (4), 350–355.
- (56) Olderoy, M. Ø.; Xie, M.; Andreassen, J.-P.; Strand, B. L.; Zhang, Z.; Sikorski, P. Viscoelastic properties of mineralized alginate hydrogel beads. *J. Mater. Sci.: Mater. Med.* **2012**, *23* (7), 1619–1627.
- (57) Serrano-Aroca, A.; Ruiz-Pividal, J. F.; Llorens-Gámez, M. Enhancement of water diffusion and compression performance of crosslinked alginate films with a minuscule amount of graphene oxide. *Sci. Rep.* **2017**, *7*, 11684.
- (58) Qin, Y. Gel swelling properties of alginate fibers. *J. Appl. Polym. Sci.* **2004**, *91* (3), 1641–1645.
- (59) Bajpai, S.K.; Sharma, S. Investigation of swelling/degradation behaviour of alginate beads crosslinked with Ca²⁺ and Ba²⁺ ions. *React. Funct. Polym.* **2004**, *59* (2), 129–140.
- (60) Matyash, M.; Despang, F.; Ikonomidou, C.; Gelinsky, M. Swelling and Mechanical Properties of Alginate Hydrogels with Respect to Promotion of Neural Growth. *Tissue Eng., Part C* **2014**, *20* (5), 401–411.
- (61) Donati, I.; et al. New Hypothesis on the Role of Alternating Sequences in Calcium-Alginate Gels. *Biomacromolecules* **2005**, *6* (2), 1031–1040.
- (62) Garland, E. M.; Parr, J. M.; Williamson, D. S.; Cohen, S. M. In vitro cytotoxicity of the sodium, potassium and calcium salts of saccharin, sodium ascorbate, sodium citrate and sodium chloride. *Toxicol. In Vitro* **1989**, *3* (3), 201–205.
- (63) Soltan, N.; Ning, L. Q.; Mohabatpour, F.; Papagerakis, P.; Chen, X. B. Printability and Cell Viability in Bioprinting Alginate

Dialdehyde-Gelatin Scaffolds. *ACS Biomater. Sci. Eng.* **2019**, *5* (6), 2976–2987.

(64) Blaeser, A.; Duarte Campos, D. F.; Puster, U.; Richtering, W.; Stevens, M. M.; Fischer, H. Controlling Shear Stress in 3D Bioprinting is a Key Factor to Balance Printing Resolution and Stem Cell Integrity. *Adv. Healthcare Mater.* **2016**, *5* (3), 326–333.

(65) Lemarié, L.; Anandan, A.; Petiot, E.; Marquette, C.; Courtial, E. J. Rheology, simulation and data analysis toward bioprinting cell viability awareness. *Bioprinting* **2021**, *21*, e00119.

(66) Roquero, D. M.; Othman, A.; Melman, A.; Katz, E. Iron (III)-cross-linked alginate hydrogels: a critical review. *Mater. Adv.* **2022**, *3* (4), 1849–1873.

(67) Hotchkiss, P. J.; Jones, S. C.; Paniagua, S. A.; Sharma, A.; Kippelen, B.; Armstrong, N. R.; Marder, S. R. The Modification of Indium Tin Oxide with Phosphonic Acids: Mechanism of Binding, Tuning of Surface Properties, and Potential for Use in Organic Electronic Applications. *Acc. Chem. Res.* **2012**, *45* (3), 337–346.

(68) Kato, M.; Makino, S.; Kimura, H.; Ota, T.; Furuhashi, T.; Nagamura, Y. Evaluation of mitochondrial function and membrane integrity by dual fluorescent staining for assessment of sperm status in rats. *J. Toxicol. Sci.* **2002**, *27* (1), 11–19.

(69) Lechner, A.; Trossmann, V. T.; Scheibel, T. Impact of Cell Loading of Recombinant Spider Silk Based Bioinks on Gelation and Printability. *Macromol. Biosci.* **2022**, *22* (3), 2100390.

Article

Electrospinning of Hyaluronan Using Polymer Coelectrospinning and Intermediate Solvent

Lenka Vítková¹, Lenka Musilová^{1,2}, Eva Achbergerová³, Antonín Minařík^{1,2},
Petr Smolka^{1,2}, Erik Wrzeczionko^{1,2} and Aleš Mráček^{1,2,*}

¹ Department of Physics and Materials Engineering, Faculty of Technology, Thomas Bata University in Zlín, Vavrečkova 275, 760 01 Zlín, Czech Republic; l_davidova@utb.cz (L.V.); lmusilova@utb.cz (L.M.); minarik@utb.cz (A.M.); smolka@utb.cz (P.S.); wrzeczionko@utb.cz (E.W.)

² Center of Polymer Systems, Thomas Bata University in Zlín, tř. Tomáše Bati 5678, 760 01 Zlín, Czech Republic

³ CEBIA-Tech, Faculty of Applied Informatics, Thomas Bata University in Zlín, Nad Stráněmi 4511, 760 05 Zlín, Czech Republic; achbergerova@utb.cz

* Correspondence: mracek@utb.cz; Tel.: +420-733-690-668

Received: 9 August 2019; Accepted: 8 September 2019; Published: 18 September 2019



Abstract: In the current study, we present methods of sodium hyaluronate, also denoted as hyaluronan (HA), nanofiber fabrication using a direct-current (DC) electric field. HA was spun in combination with poly(vinyl alcohol) (PVA) and polyethylene oxide (PEO) and as a pure polymer. Nonaggressive solvents were used due to the possible use of the fibers in life sciences. The influences of polymer concentration, average molecular weight (M_w), viscosity, and solution surface tension were analyzed. HA and PVA were fluorescent-labeled in order to examine the electrospun structures using fluorescence confocal microscopy. In this study, two intermediate solvent mixtures that facilitate HA electrospinning were found. In the case of polymer co-electrospinning, the effect of the surfactant content on the HA/PVA electrospinning process, and the effect of HA M_w on HA/PEO nanofiber morphology, were examined, respectively.

Keywords: electrospinning; hyaluronan; poly(vinyl alcohol); polyethylene oxide; nanofibers; intermediate solvent; fluorescence confocal microscopy

1. Introduction

Electrospinning, nowadays a well-established fiber-fabrication method first described in 1902 by Cooley and Morton [1,2], is based on several electrohydrodynamic phenomena [3]. The method utilizes Taylor cones, the product of electric field-induced instabilities in liquid bodies stabilized by capillary forces. However, if electric forces overcome capillary forces, a liquid jet is ejected, which is then subjected to elongation at high rates, causing a decrease in diameter up to micron fractions. Due to the large specific surface of the polymer jet, rapid evaporation of the solvent occurs, leading to the solidification of the polymer jet in the form of a nanofiber. Several instabilities may occur and disrupt the electrospinning process, causing particle formation (so-called electrospraying), bead-on-string structure formation, or branching. The preliminary cause of these phenomena is Rayleigh instability, which is surface tension-driven and electrostatically hindered. Similarly to Taylor cone formation prior to electrospinning, cone-shaped undulations may be formed on the cylindrical jet, leading to jet collapse if the charge per unit area is small, providing electrospraying or bead-on-string structured fibers, or undulation stabilization and elongation, giving branched fibers [3,4]. This technique inherently gives nonwoven mats composed of infinite fibers. In practice, DC electric fields of up to tens of kilovolts magnitude are used in most cases.

Nanofibrous materials have uses in many industry fields, for example, in porous materials [5–7], the fuel cell industry [8,9], petroleum engineering [10,11], and particularly biomedical applications such as wound dressing [12,13], drug delivery, [14,15], or tissue engineering [16,17]. The most popular synthetic polymers for electrospinning include polyethylene oxide (PEO), poly(lactide), and polyethyleneimine [4,18,19]. Regarding natural polymers, proteins, such as silk fibroin [20], or polysaccharides, such as alginate, cellulose, or chitosan, can be used [14]. The presence of a nanostructure was proven to enhance cell proliferation [21], which is why combined 3D printing and electrospinning techniques are widely studied for potential uses in tissue engineering (see, e.g., Mori et al. (2018) [22]).

Hyaluronan (HA) is a polysaccharide abundant in the extracellular matrix of living organisms. Its primary structure is linear, and its secondary structure is typically a twisted ribbon. Due to a rather stiff backbone chain caused by the disaccharide structure, internal hydrogen bonds, and interactions with solvents, the tertiary structure is an expanded random coil [23,24]. It was experimentally proven that the presence of ions can influence coil diameter [25]. The coil structure is capable of absorbing approximately 1000 times its weight of water [26]. This provides solutions of HA with extraordinarily high viscosity at low concentrations, as well as shear-thinning behavior. Its excellent biocompatibility and solubility in water makes it a popular choice in biomedical applications [27]. HA melt processing is impossible due to its instability at high temperatures [28].

The main complications in HA solution electrospinning are the high surface tension of HA aqueous solutions, extremely high viscosity at low concentrations, preventing the formation of highly concentrated solutions, and the low evaporation rate of water. Attempts to fabricate HA nanofibers using electrospinning have been made by many researchers. A common approach to electrospinning of polymers with low spinnability is the use of a highly spinnable polymer that then serves as a dragging polymer [20,29]. Under certain conditions, this approach provides core-shell nanofibers, as was demonstrated by Ma et al. (2017) [30] using chitosan and an HA solution. To overcome the problem of high surface tension, the use of surfactants [31] or a different solvent choice is possible [27,32,33]. According to Malkin et al. (2017), a change in solvent also has a positive effect on spinnability due to introducing a polymer-solvent demixing solidification mechanism [34]. Previously, it was assumed that electrospinning is only possible above critical concentration, i.e., polymer concentration corresponding to one entanglement per chain [3]. However, using solutions of PEO and polyethylene glycol (PEG), Yu et al. (2006) demonstrated that electrospinning is possible below critical concentration [35]. It was argued that the ability to form smooth fibers via electrospinning is governed by solution elasticity [36–38]. On the other hand, Shenoy et al. (2005) performed electrospinning experiments on several polymer solutions, and concluded that complete stabilization of the electrospinning process is provided by a minimum of 2.5 entanglements per chain [39]. Malkin et al. (2017) argued that stabilization of the electrospinning process can be achieved at concentrations below critical if an intermediate solvent is used [34]. Experiment evidence suggests great contribution of solution elasticity, interaction parameters, surface tension, and conductivity to the electrospinning process. Ambient parameters, such as temperature and humidity, need to be taken into account as well [40]. Although there have been attempts for analysis of electrospinning jet behavior [4,41], so far none are comprehensive enough to account for all influence.

In the current study, nanofibrous mats containing HA were obtained using electrospinning. Two approaches were employed: HA co-electrospinning in a blend with highly spinnable polymers PVA and PEO, respectively, and the use of an intermediate solvent. As intermediate solvents, mixtures containing water and isopropanol (IPA), and water, ethanol EtOH, and methanol (MeOH) were used. The solvent mixtures were found with the aid of a Teas graph, incorporating the method described in Luo et al. (2010) [42]. We attempted to offer insight on the influence of shear viscosity and polymer-chain conformation in the solution on the electrospinning process. Furthermore, HA and PVA were fluorescent-labeled, which allowed the products to be observed by fluorescence confocal microscopy.

2. Materials and Methods

2.1. Materials and Chemicals

HA of M_w 243 kDa, 370 kDa, 600 kDa, and 1180 kDa was purchased from Contipro a.s. Demineralized (DEMI) water was prepared using the Milipore Direct-Q 3UV system. PVA of M_w 89–98 kDa, 99+% hydrolyzed, PEO of M_w 300 and 600 kDa, respectively, EtOH absolute Spectranal, IPA puriss p.a., ACS reagent, disodium hydrogen phosphate dodecahydrate $\geq 99\%$, 4-acetamido-TEMPO free radical, 97%, dimethyl sulfoxide (DMSO) ACS reagent, $\geq 99,9\%$, Nile Blue A, dye content $\geq 75\%$, NaBH_3CN reagent grade, 95%, pyridine anhydrous 99.8%, dibutyltin dilaurate, 95%, fluorescein isothiocyanate isomer (FITC), $\geq 90\%$ and benzethonium chloride (BEC), $\geq 97\%$ were purchased from Sigma Aldrich. MeOH p.a. was purchased from Lach:NER. Sodium bromide pure was purchased from Lachema a.s. Sodium hypochlorite solution pure was purchased from Penta. NaCl PharmaGrade was purchased from SAFC. NaHCO_3 ACS Grade was purchased from VWR.

2.2. HA Fluorescent Labeling

In order to prepare Nile Blue A labeled-HA (600 kDa), HA was initially oxidized according to a previously published method, Huerta-Angeles et al. (2012) [43], followed by fluorescent labeling described in Šmejkalová et al. (2017) [44].

Initially, HA (1 g) was dissolved in 10 mL of DEMI water. To the HA solution, sodium bromide (0.129 g) and disodium hydrogen phosphate (0.771 g) were added. The reaction mixture was cooled to 5 °C, followed by the addition of 4-acetamido-TEMPO (5 mg) and 450 μL of sodium hypochlorite. The reaction was carried out for 45 min under nitrogen atmosphere at 5 °C. The oxidized HA was dialyzed against DEMI water for 3 days and freeze-dried (yield: 96%). In the second step, an aqueous solution (2 wt.%) of oxidized HA (0.5 g) was stirred with Nile Blue A (92 mg) predissolved in DMSO (5 mL) for 5 h. Subsequently, NaBH_3CN (79 mg) was added to this reaction mixture which was then stirred over night at room temperature. The crude product was precipitated by NaCl solution and IPA, and the remaining Nile Blue A was washed out using IPA. The product was then dialyzed against 0.5 wt.% NaCl and 0.5 wt.% NaHCO_3 aqueous solutions for 2 days and against DEMI water for 3 days. The final product was obtained in a form of a blue lyophilisate (yield 78%).

2.3. PVA Fluorescent Labeling

PVA was labeled with FITC following the procedure published by Kaneo et al. (2005) [45]. Briefly, PVA (2.5 g) was dissolved in DMSO (66.6 mL) and pyridine (416.6 μL) under stirring at 80 °C for 24 h. FITC (83 mg) and dibutyltin dilaurate (31 μL) were added to the PVA solution and the reaction was carried out for 2 h at 95 °C in darkness. The crude product was precipitated and washed with IPA, followed by dialysis against DEMI water and lyophilization. The yield of the reaction was 88%.

2.4. Solutions Preparation

HA of respective M_w was dissolved in binary and ternary solvent mixtures at 50 °C under vigorous stirring for 48 h regardless the HA M_w and solvent mixture, to obtain completely homogenized solution. The solvent mixtures chosen for the experiments were H_2O :IPA in 10:7 weight ratio, and H_2O :EtOH:MeOH in 5:5:1 weight ratio.

HA/PVA blend solutions with BEC surfactant were prepared in the following way; 2 wt.% HA 600 kDa solution and 1 wt.% PVA 89–98 kDa solution were prepared separately by dissolving the respective polymers in DEMI water for 24 h at elevated temperature (50 °C for HA, and 80 °C for PVA). BEC aqueous solutions of the following concentrations: 1 wt.%, 2 wt.%, 5 wt.%, and 10 wt.% were prepared separately as well. The final solutions were prepared by mixing 2.5 g of HA solution with 2 g of PVA solution. After the components were properly mixed, 0.03 g of BEC solution of respective concentration was added and the solution was mixed properly. Slight turbidity appearance was

observed upon the surfactant addition. For the purpose of confocal microscopy, 4% of the respective polymer content was replaced by fluorescent labeled analogue.

HA/PEO 2 wt.% blend solutions were prepared by mixing the polymers at 1:1 weight ratio and dissolving them in DEMI water by stirring vigorously at room temperature for 48 h. HA M_w used were 243, 370, and 600 kDa. PEO M_w used were 300 and 600 kDa. For the purpose of confocal microscopy, 4% of HA content was replaced by Nile Blue A labeled HA.

2.5. Electrospinning Equipment

A homemade electrospinner consisting of high DC voltage power supply Spellman SL150, a grounded metal collector, 40.3 mm in diameter, and a simple metal rod spinneret, 8 mm in diameter, were used in the study (see Figure 1). The tip-to-collector distance was kept at 76 mm. Experiments were conducted in air atmosphere at room temperature and humidity, and normal pressure. The fibers were collected using a recycled paper substrate to ensure good adhesion.

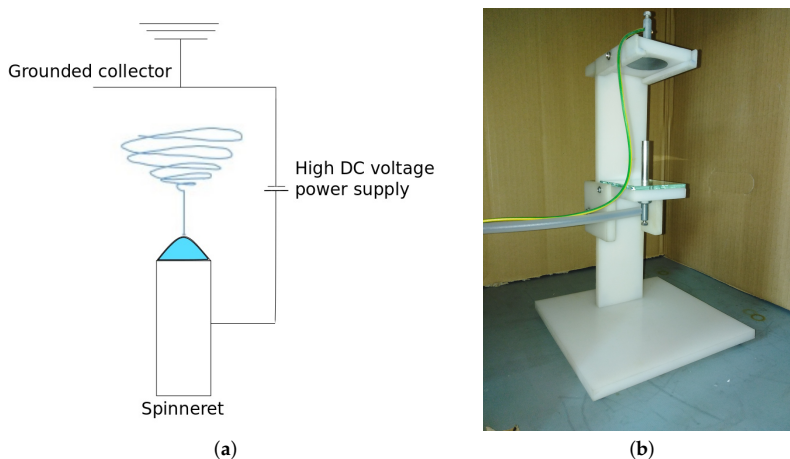


Figure 1. Electrospinning device: (a) device scheme and (b) device used in experiments.

2.6. Characterization

Dynamic viscosity was determined using a Malvern Kinexus Pro+ rotational rheometer with cup-and-bob geometry. The measurements were conducted at 25 °C at 11 different shear rates ranging from 0.1 to 10 s⁻¹.

Portable conductometer Mettler Toledo Seven2Go Pro was used to determine the conductivity of the solutions. Each solution was measured 3 times at room temperature.

Surface tension was determined by a pendant drop method using a Krüss Drop Shape Analyzer DSA 100. Three separate drops of each sample were measured. Each drop was measured 30 times with a 1 s delay between the measurements. Dixon's Q-test was used to exclude the outliers. The measurement was conducted at 25 °C in an air atmosphere.

The fiber morphology analysis was done using a Phenom Pro X Scanning Electron Microscope (SEM) in the backscattered electron mode. The samples were sputtered with a layer of gold prior to the analysis. Acceleration voltage was 10 kV. Optical analysis of the images was done using ImageJ software.

An Olympus FLUOVIEW FV3000 Laser Scanning Microscope was used for fluorescence confocal microscopy. Excitation wavelengths available were 405, 488, 561, and 640 nm. Wavelength ranges 600–640 nm and 450–520 nm were, respectively, used as emission spectra for HA labeled by Nile Blue A, and PVA labeled by FTIC. The immersion objective ($Z = 60$) with numerical aperture $A = 1.35$ was used for nanofibers observation.

3. Results and Discussion

The electrospinning process is highly dependent on the intrinsic properties of the spinning solution. The most prevalent were polymer M_w , concentration and polydispersity, all of which were reflected in viscosity, and also surface tension and conductivity [40]. Higher conductivity was presumed to facilitate stability in the spinning process [4], while high surface tension prevented electrospinning onset [3]. Measurement of shear viscosity was done at low shear rates in a narrow range, since the formation of a Taylor cone in sufficiently conductive fluids typically occurs without inducing high shear rates [46], and solutions are considered Newtonian liquids in this part of the process.

3.1. HA/PVA Blend Aqueous Solutions

In the past, electrospinning HA/PVA aqueous solutions was not possible without the addition of a small amount of surfactant. BEC was chosen due to the coil-shrinking effect on HA conformation [24], which we assumed to be beneficial in terms of electrospinning.

The surface tension of HA/PVA blend aqueous solutions was lower than the HA aqueous solutions (around $70 \text{ mN}\cdot\text{m}^{-1}$, see Jurošková (2017) [47]), which is likely the result of surfactant BEC addition. Surface tension decreases with increasing of BEC content. Solution conductivity was increased by the increase of BEC content as a result of BEC ionic nature (see Table 1).

Table 1. Characteristics of Hyaluronan (HA)/Poly(vinyl alcohol) (PVA) blend solution with benzethonium chloride (BEC).

BEC Content [wt.%]	Surface Tension [$\text{mN}\cdot\text{m}^{-1}$]	Conductivity [$\mu\text{S}\cdot\text{cm}^{-1}$]
0.006	43.7 ± 0.9	1473 ± 7
0.013	42.6 ± 0.2	1496 ± 2
0.033	41.4 ± 0.6	1513 ± 4
0.065	41.1 ± 0.2	1546 ± 4

HA/PVA blend aqueous solutions show the highest conductivity of the spinnable solutions used in the current study (see Tables 1 and 3–5). This is likely the synergic effect of dissociation of HA and PVA in water, and the addition of ionic surfactant to the solution.

Low polymer concentration causes the viscosity of the solutions to be low as well. As apparent from Figure 2, there was a quick drop of viscosity present upon addition of 0.065 wt.% of BEC.

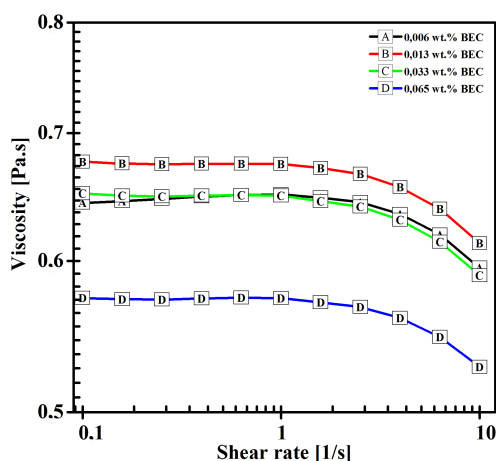


Figure 2. Viscosity of HA/PVA blend solutions with BEC as a function of shear rate.

0.065 wt.% of BEC was close to critical aggregation concentration [24] and HA coil shrinkage was expected, causing significant increase in turbidity of the solution, which was observed during the preparation, and it was in agreement with findings of Gřundělová et al. (2013) [24]. It is safe to assume that BEC effectively created an intermediate solvent to HA, and electrospinning HA is therefore encouraged not only by mixing with highly spinnable PVA, but also by the intermediate solvent effect. Due to HA precipitation, further increase of BEC content would be counterproductive.

The effect of surfactant content on electrospun-structure morphology and the electrospinning process was examined. As the BEC content increased, the minimum spinning voltage decreased (see Table 2) due to the decrease in surface tension.

Table 2. Morphology analysis of HA/PVA blend solutions with BEC electrospinning products.

BEC Content [wt.%]	Spinning Voltage [kV]	Product Form	Beads Diameter [μm]	Fibers Diameter [μm]
0.006	20.4	Elongated beads	0.1–0.5	/
0.013	18.8	Elongated beads	0.3–0.7	/
0.033	17.5	Bead-on-string	0.1–0.8	0.03–0.06
0.065	15.9	Bead-on-string	0.2–0.6	0.06–0.1

With the increase of BEC content, product morphology shifted from elongated beads to bead-on-string structured fibers (see Figure 3).

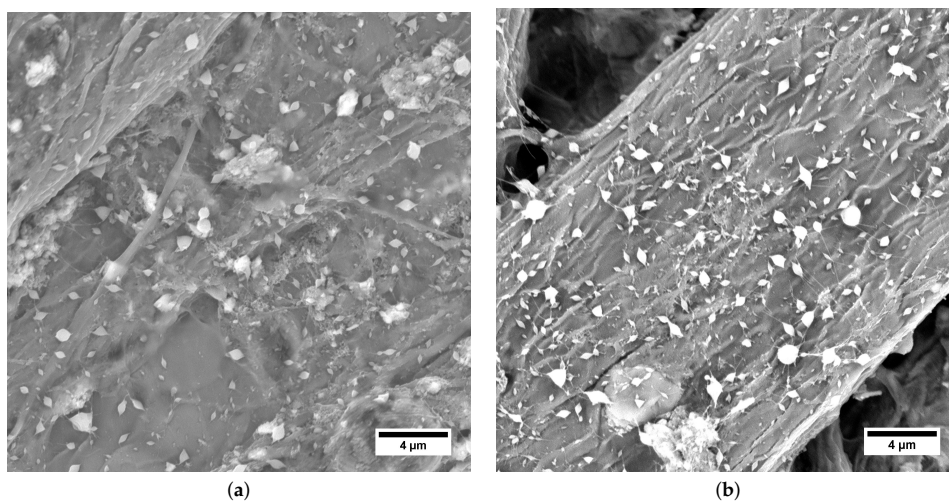
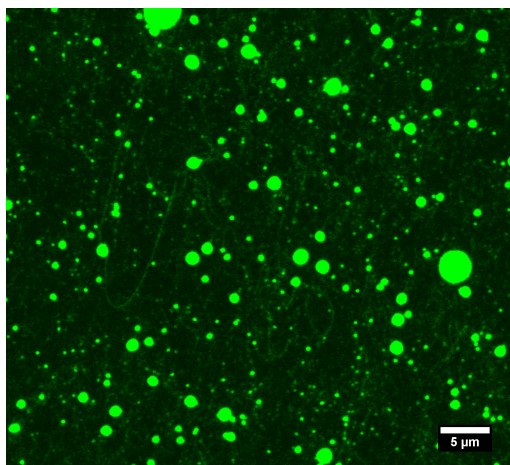


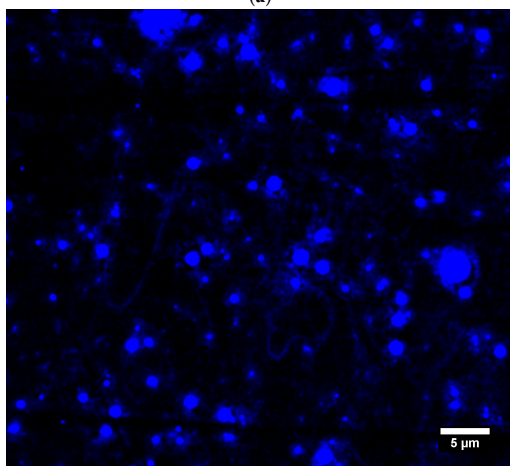
Figure 3. Scanning Electron Microscopy (SEM) micrographs of electrospun structures obtained from HA/PVA blend solutions with BEC. BEC content (a) 0.033 wt.% and (b) 0.065 wt.%.

The increase in stability may be the result of increased conductivity of the solution, as argued by Reneker and Yarin (2008) [4], or the increase in polymer–polymer interactions, i.e., lowering solvent quality, which would be in agreement with the findings of Malkin et al. (2017) [34]. However, electrospinning smooth fibers was not achieved by this method. There were multiple reasons, such as insufficient solution elasticity, difference in HA and PVA viscoelastic behavior, or uneven BEC distribution, leading to formation of clumps of the respective polymers. Higher BEC content also led to the formation of multiple Taylor cones, therefore increasing the yield of the process. To proceed on this subject, it would be possible to choose a different surfactant with higher critical aggregation concentration, or alter the HA/PVA ratio in the solution in a way to increase the elongation elasticity. Both approaches would certainly lead to a better understanding of the co-electrospinning phenomenon, and might lead to smooth nanofiber production. The electrospun structures did not exceed 1 μm in diameter (see Table 2).

Nile Blue A labeled HA 600 kDa and FITC labeled PVA 89–98 kDa blend aqueous solution containing 0.065 wt.% of BEC was electrospun, and the products were observed by fluorescence confocal microscopy. It is clear from Figure 4 that both polymers are present jointly in fibers, as well as beads. However, due to insufficient magnification it was not possible to determine the respective position of the polymers within the structures. The absence of some structures when illuminated by a different wavelength suggested fluctuation in the contents of the respective polymers throughout spinning.

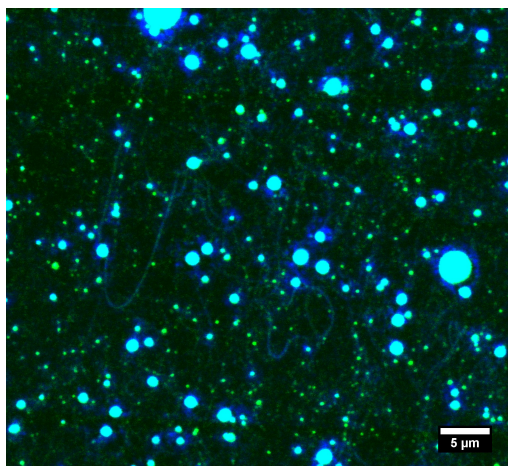


(a)



(b)

Figure 4. *Cont.*



(c)

Figure 4. Fluorescence confocal microscope micrographs of electrospun structures obtained from Nile Blue A labeled HA 600 kDa and FITC labeled PVA 89–98 kDa aqueous solution with BEC content 0.065 wt.%. (a) Nile Blue A labeled HA visible. Emission spectrum 600–640 nm. (b) FITC labeled PVA visible. Emission spectrum 450–520 nm. (c) Both fluorescent labeled polymers visible—combined emission spectra.

3.2. HA/PEO Blend Aqueous Solutions

HA/PEO blend solutions were spun in order to produce HA containing nanofibers from aqueous solutions without use of any additional substances, such as surfactants or salts. PEO served as elasticity and shear viscosity mediator, as well as a highly spinnable polymer for co-electrospinning. In order to examine the influence of HA M_w on the electrospinning process, PEO was used in such M_w and concentration that would facilitate the electrospinning of all HA M_w chosen. The PEO M_w and concentration were found experimentally.

Surface tension of HA/PEO blend aqueous solutions was significantly higher than the one of HA in intermediate solvents solutions (see Tables 3–5) due to use of water as a solvent, but still considerably lower than HA aqueous solutions [47], caused by the surface tension-enhancing effect of HA being hindered by the presence of PEO, which induced a decrease in surface tension of the aqueous solutions instead [48].

Table 3. Characteristics of HA/Polyethylene oxide (PEO) aqueous blend solutions.

PEO M_w [kDa]	HA M_w [kDa]	Surface Tension [$\text{mN}\cdot\text{m}^{-1}$]	Conductivity [$\mu\text{S}\cdot\text{cm}^{-1}$]
300	243	46 ± 2	1284 ± 8
	370	49.3 ± 0.2	1255 ± 7
	600	49 ± 2	1241 ± 6
600	243	51 ± 2	1312 ± 4
	370	52 ± 2	1258 ± 3
	600	54 ± 1	1213 ± 3

The effect of respective polymers M_w on the surface tension was inconclusive, as a result of the low polymer concentration used (2 wt.%). Conductivity of the solutions was significantly higher than that of the pure HA solutions (see Tables 3–5), despite the lower concentration of HA. This can be attributed to the higher dissociation of HA in water than in solvents containing alcohols. As a result of the increase in molar fraction with the decrease in M_w while the same weight fraction of a polymer was kept, solution conductivity slightly decreased with the increase of HA M_w . As the M_w decreased,

the effect of the end groups also gained significance and, in the case of HA and PEO, contributed to conductivity as well.

Table 4. Characteristics of HA solutions in H₂O:Isopropanol (IPA) in 10:7 weight ratio solvent mixtures.

M_w [kDa]	Concentration [wt.%]	Surface Tension [$\text{mN}\cdot\text{m}^{-1}$]	Conductivity [$\mu\text{S}\cdot\text{cm}^{-1}$]
600	3.2	27 ± 1	854 ± 2
	2.3	25 ± 0.5	568 ± 1
	1.3	26.2 ± 0.3	465 ± 1
1180	2.9	24 ± 3	682 ± 2
	1.2	28 ± 2	386 ± 2
	1.0	27.1 ± 0.5	343 ± 2

Table 5. Characteristics of HA solutions in H₂O:Ethanol (EtOH):Methanol (MeOH) in 5:5:1 weight ratio solvent mixtures.

M_w [kDa]	Concentration [wt.%]	Surface Tension [$\text{mN}\cdot\text{m}^{-1}$]	Conductivity [$\mu\text{S}\cdot\text{cm}^{-1}$]
600	2.8	32.3 ± 0.9	740 ± 8
	2.4	30.5 ± 0.5	748 ± 1
	0.7	30.2 ± 0.8	249 ± 1
1180	2.3	27.4 ± 0.8	704 ± 1
	2.2	28 ± 2	616 ± 1
	1.5	27.6 ± 0.9	459 ± 1

Solution viscosity dropped as the M_w of the respective polymers decreased (see Figure 5). Viscosity was significantly lower than that in the case of solutions of HA in intermediate solvents, which was one of the purposes of adding PEO into an HA aqueous solution.

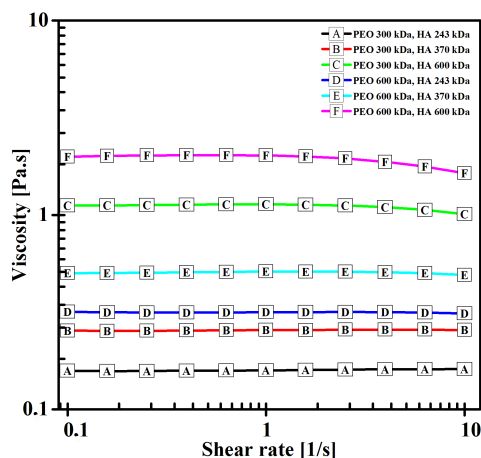


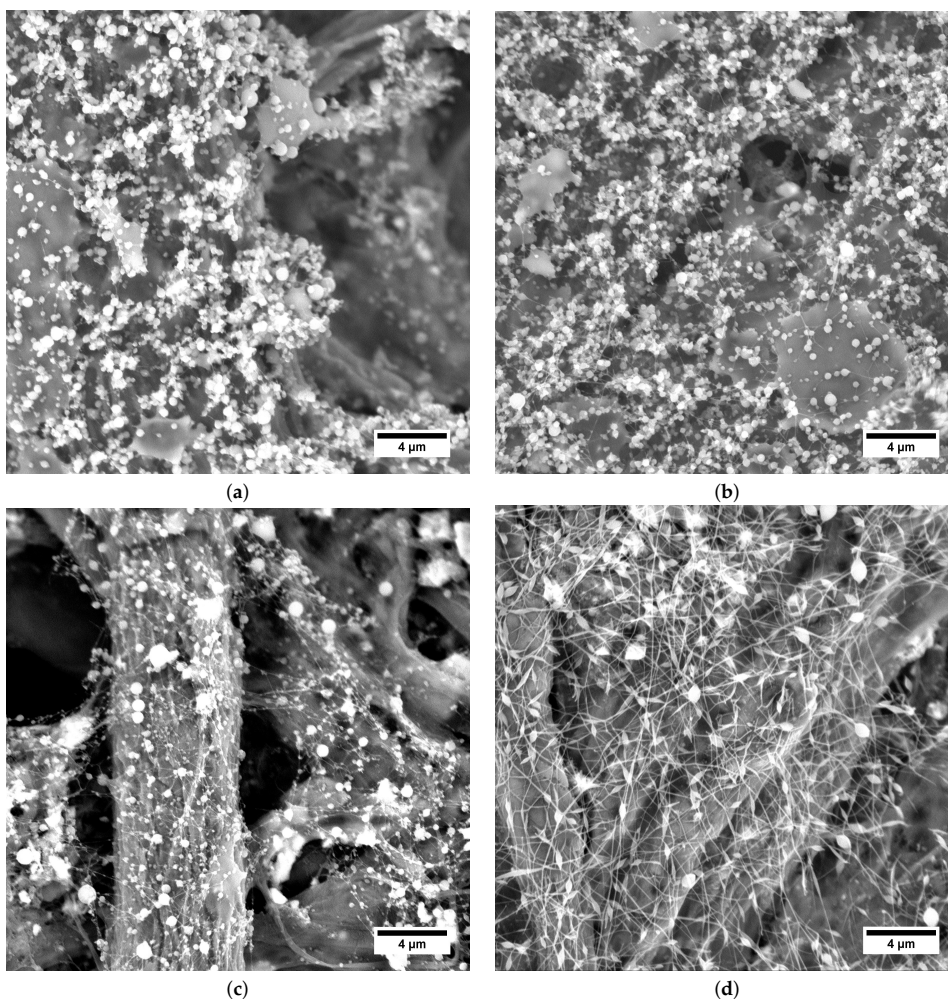
Figure 5. Viscosity of HA/PEO blend solutions as a function of shear rate.

In order to examine the effect of HA M_w on the morphology of structures electrospun from HA/PEO blend aqueous solutions, the processing parameters, i.e., tip-to-collector distance and spinning voltage, were kept constant for each series of samples. All of the solutions gave bead-on-string structured fibers, which was a result of Rayleigh instability acting on a conductive liquid jet in a strong electric field [4]. The structures did not exceed 1 μm in size (see Table 6).

Table 6. Morphology analysis of HA/PEO blend-solution electrospinning products.

PEO M_w	HA M_w	Spinning Voltage [kV]	Product Form	Beads Diameter [μm]	Fibers Diameter [μm]
300	243	18.2	Bead-on-string	0.25–0.5	0.02–0.05
	370	18.2	Bead-on-string	0.3–0.5	0.03–0.07
	600	18.2	Bead-on-string	0.2–0.6	0.04–0.1
600	243	24.5	Bead-on-string	0.2–0.7	0.05–0.1
	370	24.5	Bead-on-string	0.3–0.6	0.05–0.1
	600	24.5	Bead-on-string	0.3–0.6	0.03–0.09

As can be seen in Figure 6, the shape of the beads was influenced by the M_w of PEO. If PEO 300 kDa (Figure 6a–c) was used, the beads were almost spherical, while for PEO 600 kDa (Figure 6d–f) strong elongation of the beads was apparent.

**Figure 6.** *Cont.*

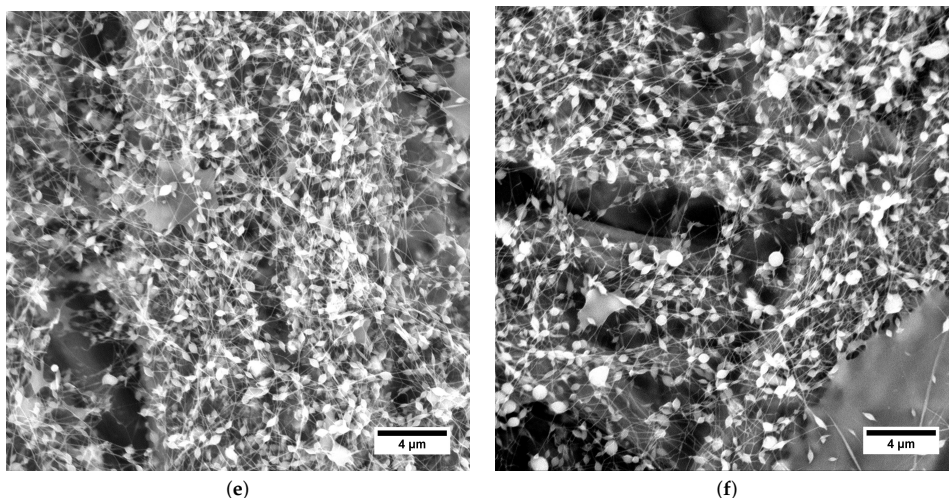


Figure 6. SEM micrographs of electrospun structures obtained from HA/PEO blend solutions. (a) HA 243 kDa, PEO 300 kDa. (b) HA 370 kDa, PEO 300 kDa. (c) HA 600 kDa, PEO 300 kDa. (d) HA 243 kDa, PEO 600 kDa. (e) HA 370 kDa, PEO 600 kDa. (f) HA 600 kDa, PEO 600 kDa.

The significance of morphology difference could even suggest different bead origin. Another explanation is a significant shift in solution elasticity induced by the different M_w of PEO. A great difference in viscoelasticity of the respective polymers also contributed to the uneven distribution of polymers throughout the spinning via a phenomenon known as polymer wrapping in coextrusion [49]. Further experimental examination of this phenomenon is needed in order to fully understand the causes. No effect of HA M_w on HA/PEO fiber morphology was found in the current study, as it was likely hindered by the significant PEO content in the used samples.

Electrospinning of HA/PEO blend solution containing Nile Blue A labeled HA 600 kDa and PEO 600 kDa allowed us to investigate the obtained structures by using fluorescence confocal microscopy. This technique proved the presence of HA in both fibers and beads (see Figure 7). On account of PEO's nonfluorescence, it is not visible in the figure.

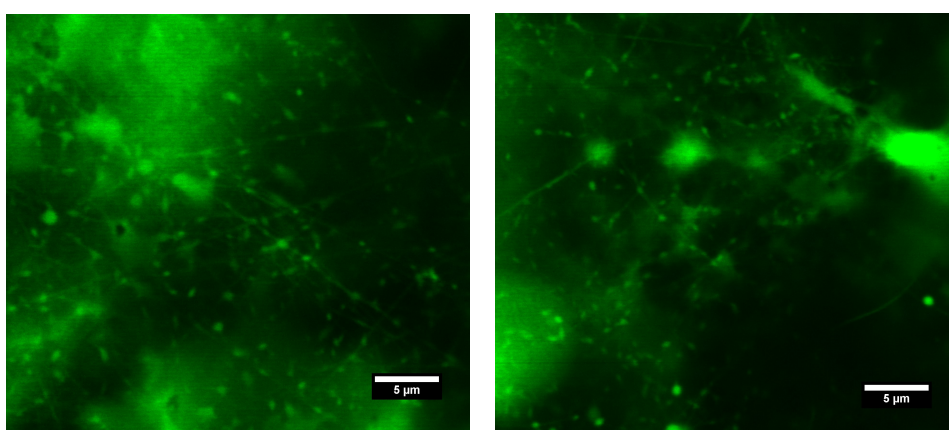


Figure 7. Fluorescence confocal microscope micrographs of electrospun structures obtained from the Nile Blue A Labeled HA 600 kDa and PEO 600 kDa aqueous solution. Emission spectrum: 600–640 nm.

3.3. HA Solutions in Intermediate Solvents

Two solvent mixture systems were chosen for the experiments: H₂O:IPA in 10:7 weight ratio and H₂O:EtOH:MeOH in 5:5:1 weight ratio. These were chosen with the aid of a Teas graph (see Figure 8) in such manner that they would lower the surface tension compared to water solutions, and encourage polymer–polymer interactions over polymer–solvent interactions, leading to smooth nanofiber production.

Electrospinning solutions of three different concentrations were considered for each solvent mixture and HA M_w , respectively, with the intention to find upper and lower limiting concentration for electrospinning.

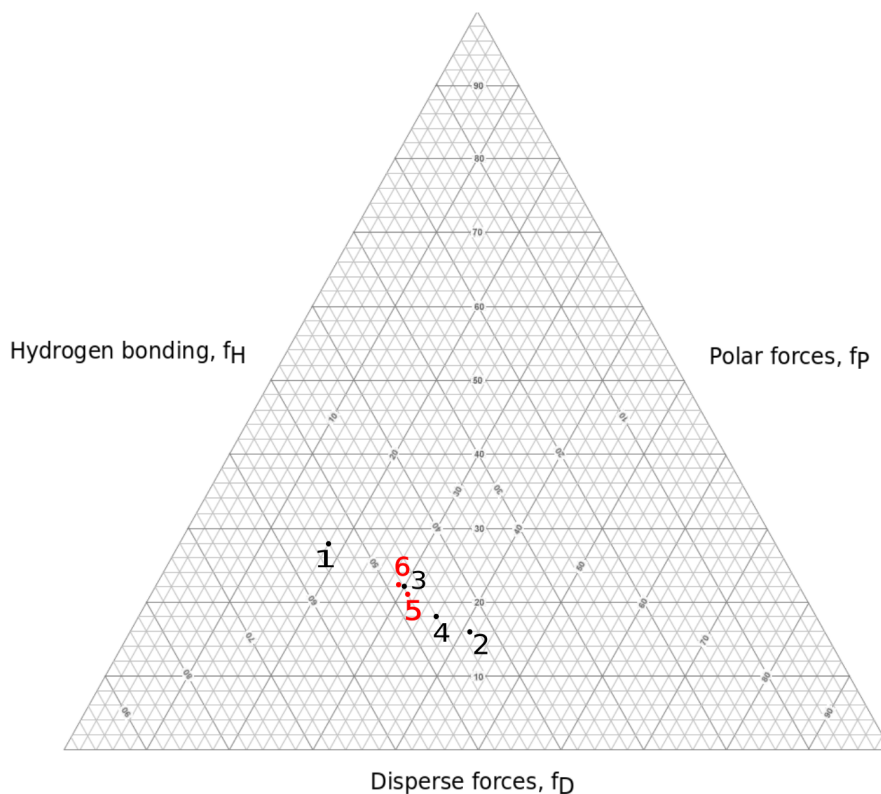
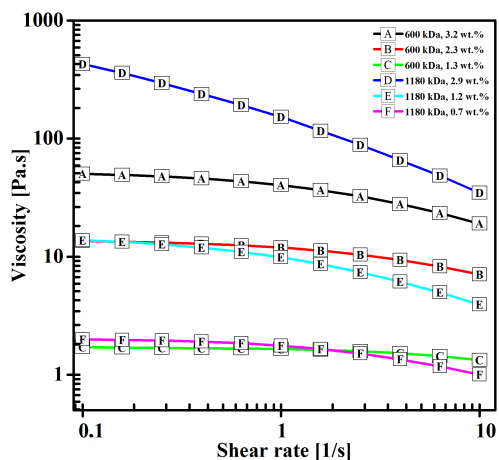


Figure 8. Solvent–mixture representation in Teas graph. 1: water; 2: IPA; 3: MeOH; 4: EtOH; 5: H₂O:IPA 10:7; 6: H₂O:EtOH:MeOH 5:5:1.

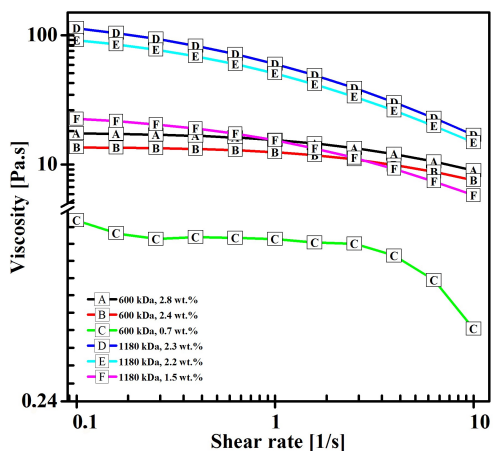
The use of H₂O:IPA and H₂O:EtOH:MeOH mixed solvents led to a significant reduction of surface tension compared to the aqueous HA solutions, see Tables 4 and 5 [47]. H₂O:EtOH:MeOH solutions showed slightly higher surface tension than that of the H₂O:IPA solutions.

No significant effect of HA concentration or M_w on surface tension was found in the current study, which was due to very low polymer concentrations and the narrow range of concentrations used. As a consequence of HA's ionic nature, solution conductivity was decreased as the concentration of the polymer was decreased. Electrospinning at very low concentration could therefore be hindered by two mechanisms—insufficient polymer chain entanglement, caused by low polymer concentration, and instability of the cylindrical jet, due to a decrease in conductivity.

The shear viscosity of the solutions decreased with the decrease in both concentration, and M_w of the polymer, with the difference being in the range of several orders of magnitude, as is evident from Figure 9.



(a)



(b)

Figure 9. Viscosity of HA solutions in intermediate solvents as a function of shear rate. (a) $H_2O:IPA$ in 10:7 weight ratio solvent mixture. (b) $H_2O:EtOH:MeOH$ in 5:5:1 weight ratio solvent mixture.

Viscosity is sometimes considered the determining parameter of spinnability via electrostatic force [18]. The findings of this study contradict such assumption as overly simplified, which is in agreement with Yarin et al. (2001) [46], who claimed that shear viscosity was insignificant in terms of Taylor cone formation. The maximum viscosity of a spinnable solution can differ as much as ten times if different M_w of the same polymer are used. We assumed that the determining parameter was polymer chain entanglement, which is affected by the polymer chain conformation in given solvent, the ionic strength of the solution, polymer concentration, and other parameters. Further investigation on this subject is necessary.

Regardless the solvent mixture, spinning voltage decreased with the decrease of concentration (see Tables 7 and 8), which can possibly be explained by a shift in solution viscoelasticity, causing the critical instability wavelength leading to Taylor cone formation to increase [3], thus consuming less energy and lowering spinning voltage. Since surface tension does not change with concentration, its effect on spinning voltage can be neglected.

Table 7. Morphology analysis of H₂O:IPA in 10:7 weight ratio HA solutions electrospinning products.

HA M _w [kDa]	Concentration [wt.%]	Spinning Voltage [kV]	Product Form	Particles Diameter [μm]	Fibers Diameter [μm]
600	3.2	20.5	Spherical Particles; Fibers	0.3–0.6	0.04–0.1
	2.3	20.0	Spherical Particles; Fibers	0.3–1.0	0.06–0.1
	1.3	16.2	Spherical Particles; Fibers	0.4–1.2	0.05–0.1
1180	2.9	24.0	Fibers	/	0.05–0.09
	1.2	16.3	Spherical Particles; Fibers	0.3–0.8	0.06–0.1
	1.0	19.0	Spherical Particles	0.7–1.1	/

Table 8. Morphology analysis of H₂O:EtOH:MeOH in 5:5:1 weight ratio HA solutions electrospinning products.

HA M _w [kDa]	Concentration [wt.%]	Spinning Voltage [kV]	Product Form	Particles Diameter [μm]	Fibers Diameter [μm]
600	2.8	19.1	Spherical Particles; Fibers	0.4–1.0	0.05–0.07
	2.4	16.5	Spherical Particles; Fibers	0.2–0.8	0.05–0.07
	0.7	14.9	Spherical Particles	0.3–1.2	/
1180	2.3	29.2	/	/	/
	2.2	22.9	Fibers	/	0.05–0.08
	1.5	19.2	Fibers	/	0.05–0.1

No influence of the concentration on the electrospun structure morphology was found, which was the result of little difference in the concentrations of the respective samples. However, the concentration clearly governed the transition between electrospinning and electrospaying, which is explained by polymer chain entanglement according to Shenoy et al. (2005) [39] or by polymer solution elasticity according to Yu et al. (2006) [35]. The mechanism could not clearly be determined from the experiments conducted in the current study. The obtained fibers did not exceed 100 nm in diameter in any of the cases, making them promising in terms of biomedicine. The spherical particle diameter was mostly in the 1 to 0.1 μm range.

In the case of each solvent mixture, HA 600 kDa showed more tendency to undergo instabilities, which resulted in a combination of electrospinning and electrospaying (Figures 10a–c and 11a–b), whereas HA 1180 kDa was able to provide smooth fibers (Figures 10d and 11c,d). It could be assumed that a higher HA M_w was more favorable in terms of electrospinning as a result of the higher elasticity of the solution.

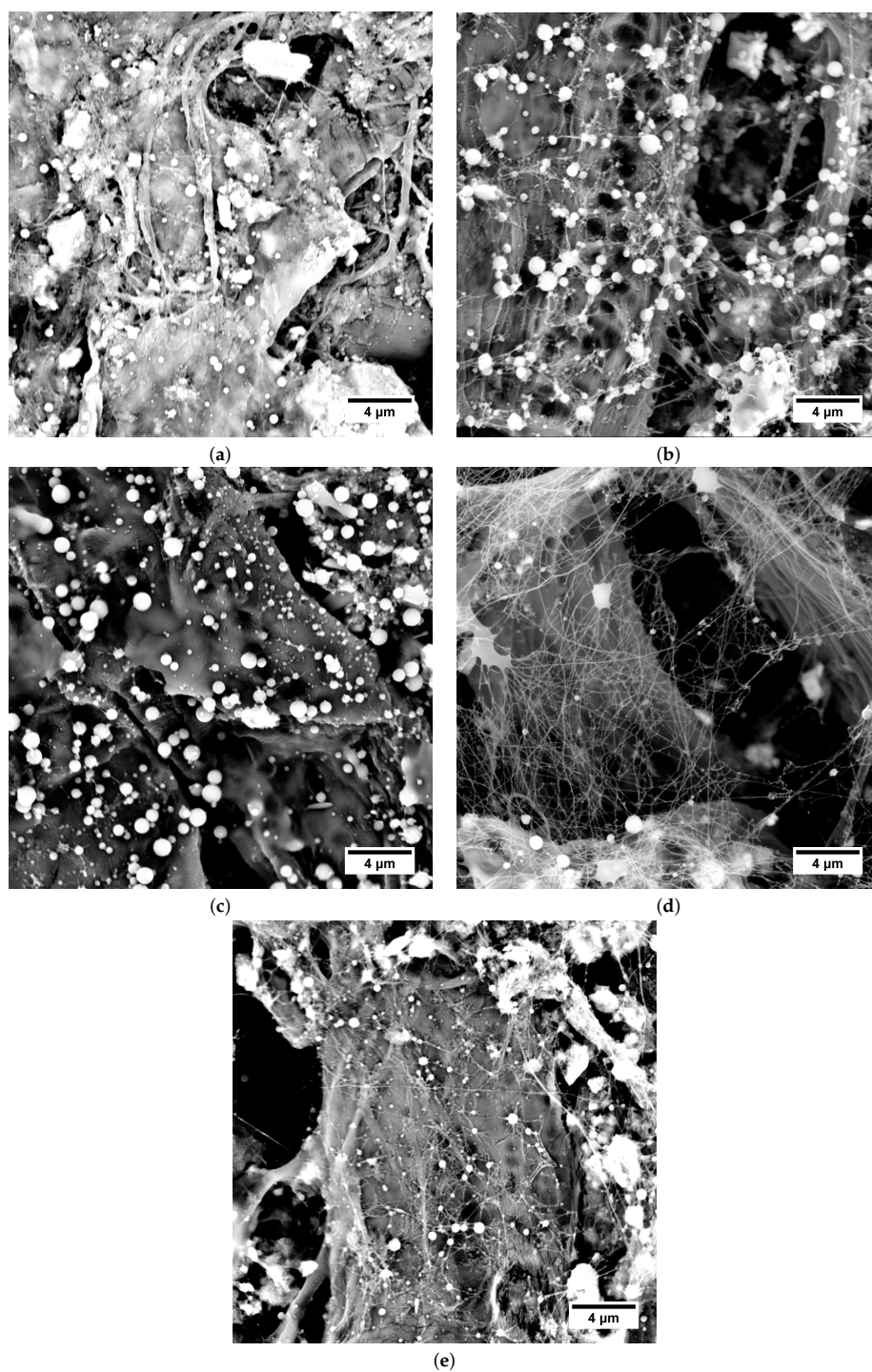


Figure 10. SEM micrographs of electrospun structures obtained from H₂O:IPA in 10:7 weight ratio solutions. (a) 3.2 wt.% HA M_w 600 kDa; (b) 2.3 wt.% HA M_w 600 kDa; (c) 1.3 wt.% HA M_w 600 kDa; (d) 2.9 wt.% HA M_w 1180 kDa; (e) 1.2 wt.% HA M_w 1180 kDa.

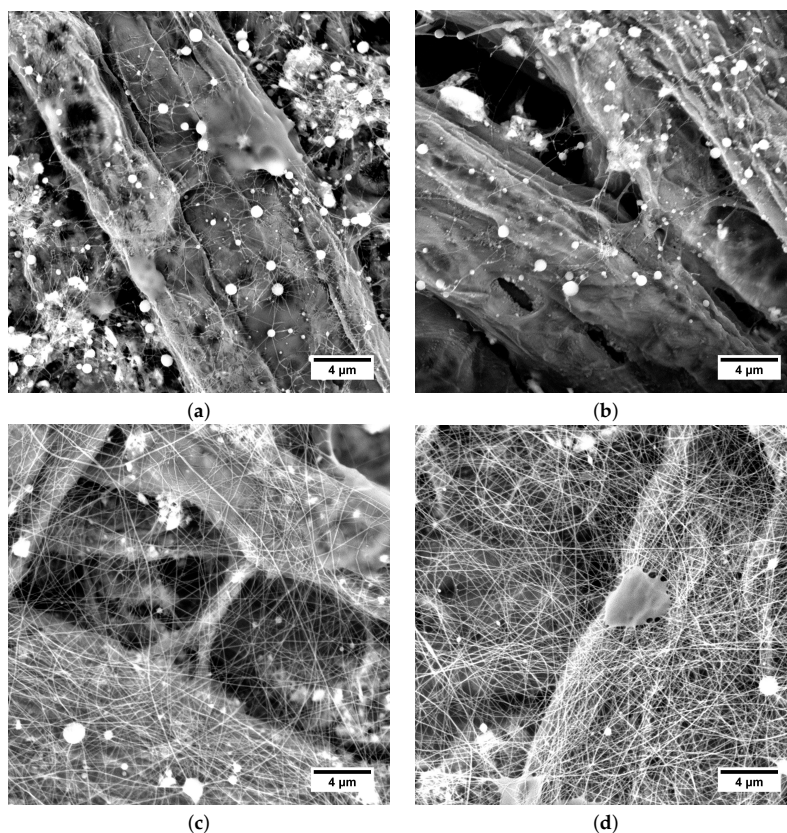


Figure 11. SEM micrographs of electrospun structures obtained from H₂O:EtOH:MeOH in 5:5:1 weight ratio solutions. (a) 2.8 wt.% HA M_w 600 kDa; (b) 2.4 wt.% HA M_w 600 kDa; (c) 2.2 wt.% HA M_w 1180 kDa; (d) 1.5 wt.% HA M_w 1180 kDa.

We can also see that instabilities in the form of electrospinning and branching were more frequent for solutions using H₂O:IPA in 10:7 weight ratio solvent mixture (Figure 10). Solvent mixture H₂O:EtOH:MeOH in 5:5:1 weight ratio provided higher stability to the electrospinning process. As the conductivity of the solutions using respective solvent mixtures was comparable (see Tables 4 and 5), the stabilization mechanism was presumably more complex than stabilization by charge density suggested by Reneker and Yarin (2008) [4]. Polymer chain conformation and interaction parameters can be expected to have a significant influence on electrospinning phenomena stabilization, but further investigation is necessary in order to fully understand the process.

Although the conductivity of HA solutions in intermediate solvents was significantly lower than those of aqueous blend solutions with PVA or PEO, smooth fibers were only obtained from a certain HA in intermediate solvent solutions. Our conclusion is that although conductivity does have a positive effect on electrospun jet stabilization, as stated by Reneker and Yarin (2008) [4], the influence of polymer viscoelasticity needs to be taken into account, as suggested by Stepanyan et al. (2014) and Palangetic et al. (2014) [36,37]. In the case of blend-solution electrospinning, the situation is complicated due to the difference in the viscoelastic properties of the polymers, which are simultaneously drawn at high elongation rates. A non-negligible effect of interaction parameters was present as well, because an intermediate solvent has a great influence on the solution behavior in a strong electric field, as was demonstrated in this study, as well as previously [34,39,42].

4. Conclusions

Electrospinning of biocompatible and biodegradable polymers is a desirable technique for use in biomedicine and life sciences. Production of HA nanofibers is a challenging task due to the extremely high viscosity and high surface tension of aqueous solutions.

In this study, nanofibers containing HA were obtained by solution electrospinning. Two approaches to the problem were chosen: co-electrospinning of aqueous blend solutions of HA/PVA and HA/PEO, respectively, and use of the intermediate solvent for pure HA solutions electrospinning. The choice of materials was done with regard to potential uses for cell cultivation. To facilitate fiber formation in HA/PVA blend solutions, the addition of BEC was necessary. Both HA/PEO and HA/PVA blend solutions provided bead-on-string structured fibers. As intermediate solvents, H₂O:IPA in a 10:7 weight ratio and H₂O:EtOH:MeOH in a 5:5:1 weight ratio were chosen. Both solvent mixtures facilitate the electrospinning of HA of M_w 600 and 1180 kDa. Lower M_w solutions had higher tendency to form spherical particles. There is clear correlation between the decrease in solution surface tension and the decrease in spinning voltage can be seen in the results, but no significant impact of these parameters on the fiber diameter was found. Variation in electrospun-structure dimensions and morphology was intensely associated with the change in M_w of the polymers. It was experimentally demonstrated that shear viscosity cannot be used as a sole determining parameter of solution spinnability, as there are differences as high as ten times the order of magnitude for spinnable solutions that differ only in polymer M_w .

The best results were achieved with the HA 1180 kDa solution in H₂O:EtOH:MeOH 5:5:1 at concentrations of 2.2 wt.% and 1.5 wt.%, as these provided smooth fibers. Fiber diameter did not exceed 100 nm for any sample that provided fibers, which makes them promising in terms of tissue engineering.

Author Contributions: Conceptualization, L.V. and A.M. (Aleš Mráček); methodology, L.V., L.M., E.A., P.S., E.W., and A.M. (Antonín Minařík); validation, L.V. and A.M. (Aleš Mráček); formal analysis, L.V.; investigation, L.V. and A.M. (Aleš Mráček); resources, L.V. and A.M. (Aleš Mráček); writing—original draft preparation, L.V.; writing—review and editing, L.V. and A.M. (Aleš Mráček); visualization, L.V. and A.M. (Aleš Mráček); supervision, A.M. (Aleš Mráček)

Funding: The research was funded by the Ministry of Education, Youth, and Sports of the Czech Republic, Program NPU I (LO1504); the European Regional Development Fund (No. CZ.1.05/2.1.00/19.0409); as well as by TBU (Nos. IGA/FT/2018/011 and IGA/FT/2019/012), funded from resources for specific university research. The work of author Eva Achbergerová was supported by the European Regional Development Fund under project CEBIA-Tech Instrumentation No. CZ.1.05/2.1.00/19.0376.

Conflicts of Interest: The authors declare no conflicts of interest.

Abbreviations

The following abbreviations are used in this manuscript:

HA	Hyaluronan
DC	Direct current
PVA	Poly(vinyl alcohol)
PEO	Polyethylene oxide
M_w	Average molecular weight
PEG	Polyethylene glycol
EtOH	Ethanol
IPA	Isopropanol
MeOH	Methanol
DEMI	Demineralized
DMSO	Dimethyl sulfoxide
FITC	Fluorescein isothiocyanate isomer
BEC	Benzethonium chloride
SEM	Scanning Electron Microscope/Scanning Electron Microscopy

References

1. Cooley, J. Apparatus for Electrically Dispersing Fluids. U.S. Patent 692631, 4 February 1902.
2. Morton, W. Method of Dispersing Fluids. U.S. Patent 705691, 29 July 1902.
3. Lukáš, D.; Sarkar, A.; Martinová, L.; Vodsed'álková, K.; Lubasová, D.; Chaloupek, J.; Pokorný, P.; Mikeš, P.; Chvojka, J.; Komárek, M. Physical principles of electrospinning (electrospinning as a nano-scale technology of the twenty-first century). *Text. Prog.* **2009**, *41*, 59–140, doi:10.1080/00405160902904641. [[CrossRef](#)]
4. Reneker, D.; Yarin, A. Electrospinning jets and polymer nanofibers. *Polymer* **2008**, *49*, 2387–2425, doi:10.1016/j.polymer.2008.02.002. [[CrossRef](#)]
5. Xiao, B.; Wang, W.; Zhiang, X.; Long, G.; Fan, J.; Chen, H.; Deng, L. A novel fractal solution for permeability and Kozeny–Carman constant of fibrous porous media made up of solid particles and porous fibers. *Powder Technol.* **2019**, *349*, 92–98, doi:10.1016/j.powtec.2019.03.028. [[CrossRef](#)]
6. Liang, M.; Fu, C.; Xiao, B.; Luo, L.; Wang, Z. A fractal study for the effective electrolyte diffusion through charged porous media. *Int. J. Heat Mass Transf.* **2019**, *137*, 365–371, doi:10.1016/j.ijheatmasstransfer.2019.03.141. [[CrossRef](#)]
7. Xiao, B.; Zhang, X.; Jiang, G.; Long, G.; Wang, W.; Zhang, Y.; Liu, G. Kozeny–Carman constant for gas flow through fibrous porous media by fractal–Monte Carlo simulations. *Fractals* **2019**, *27*, 1950062, doi:10.1142/S0218348X19500622. [[CrossRef](#)]
8. Xiao, B.; Wang, W.; Zhang, X.; Long, G.; Chen, H.; Deng, L. A novel fractal model for relative permeability of gas diffusion layer in proton exchange membrane fuel cell with capillary pressure effect. *Fractals* **2019**, *27*, 1950012, doi:10.1142/S0218348X19500129. [[CrossRef](#)]
9. Liang, M.; Liu, Y.; Xiao, B.; Yang, S.; Wang, Z.; Han, H. An analytical model for the transverse permeability of gas diffusion layer with electrical double layer effects in proton exchange membrane fuel cells. *Int. J. Hydrog. Energy* **2018**, *43*, 17880–17888, doi:10.1016/j.ijhydene.2018.07.186. [[CrossRef](#)]
10. Long, G.; Xu, G. The Effects of Perforation Erosion on Practical Hydraulic–Fracturing Applications. *SPE Prod. Oper.* **2017**, *22*, 645–659, doi:10.2118/185173-PA. [[CrossRef](#)]
11. Long, G.; Liu, S.; Xu, G.; Wong, S.; Chen, H.; Xiao, B. A Perforation–Erosion Model for Hydraulic–Fracturing Applications. *SPE Prod. Oper.* **2018**, *33*, 770–783, doi:10.2118/174959-PA. [[CrossRef](#)]
12. Sofi, H.; Akram, T.; Tamboli, A.; Majeed, A.; Shabir, N.; Sheikh, F. Novel lavender oil and silver nanoparticles simultaneously loaded onto polyurethane nanofibers for wound–healing applications. *Int. J. Pharm.* **2019**, *569*, 118590–118590, doi:10.1016/j.ijpharm.2019.118590. [[CrossRef](#)]
13. Afshar, S.; Rashedi, S.; Nazockdast, H.; Ghazalian, M. Preparation and characterization of electrospun poly(lactic acid)–chitosan core–shell nanofibers with a new solvent system. *Int. J. Biol. Macromol.* **2019**, *138*, 1130–1137, doi:10.1016/j.ijbiomac.2019.07.053. [[CrossRef](#)] [[PubMed](#)]
14. Lee, K.Y.; Jeong, L.; Kang, Y.O.; Lee, S.J.; Park, W.H. Electrospinning of polysaccharides for regenerative medicine. *Adv. Drug Deliv. Rev.* **2009**, *61*, 1020–1032, doi:10.1016/j.addr.2009.07.006. [[CrossRef](#)] [[PubMed](#)]
15. Hampejsova, Z.; Batek, J.; Sirc, J.; Hobzova, R.; Bosakova, Z. Polylactide/polyethylene glycol fibrous mats for local paclitaxel delivery: comparison of drug release into liquid medium and to HEMA-based hydrogel model. *Monatsh. Chem.* **2019**, doi:10.1007/s00706-019-02469-5. [[CrossRef](#)]
16. Yin, Y.; Zhao, X.; Xiong, J. Modeling Analysis of Silk Fibroin/Poly(ϵ -caprolactone) Nanofibrous Membrane under Uniaxial Tension. *Nanomaterials* **2019**, *9*. [[CrossRef](#)] [[PubMed](#)]
17. Mombini, S.; Mohammdnejad, J.; BakhsHandeh, B.; Narmani, A.; Nourmohammadi, J.; Vahdat, S.; Zirak, S. Chitosan–PVA–CNT nanofibers as electrically conductive scaffolds for cardiovascular tissue engineering. *Int. J. Biol. Macromol.* **2019**, *140*, 278–287, doi:10.1016/j.ijbiomac.2019.08.046. [[CrossRef](#)]
18. Agarwal, S.; Wendorff, J.; Greiner, A. Use of electrospinning technique for biomedical applications. *Polymer* **2008**, *49*, 5603–5621, doi:10.1016/j.polymer.2008.09.014. [[CrossRef](#)]
19. Son, W.; Youk, J.; Lee, T.; Park, W. The effects of solution properties and polyelectrolyte on electrospinning of ultrafine poly(ethylene oxide) fibers. *Polymer* **2004**, *45*, 2959–2966, doi:10.1016/j.polymer.2004.03.006. [[CrossRef](#)]
20. Jin, H.; Fridrikh, S.; Rutledge, G.; Kaplan, D. Electrospinning Bombyx mori Silk with Poly(ethylene oxide). *Biomacromolecules* **2002**, *3*, 1233–1239, doi:10.1021/bm025581u. [[CrossRef](#)] [[PubMed](#)]

21. Chung, S.; Son, S.; Min, J. The nanostructure effect on the adhesion and growth rates of epithelial cells with well-defined nanoporous alumina substrates. *Nanotechnology* **2010**, *21*, 1–7, doi:10.1088/0957-4484/21/12/125104. [[CrossRef](#)]
22. Mori, A.; Fernández, M.; Blunn, G.; Tozzi, G.; Roldo, M. 3D Printing and Electrospinning of Composite Hydrogels for Cartilage and Bone Tissue Engineering. *Polymers* **2018**, *10*, 285, doi:10.3390/polym10030285. [[CrossRef](#)]
23. Ingr, M.; Kutálková, E.; Hrnčířik, J. Hyaluronan random coils in electrolyte solutions—A molecular dynamics study. *Carbohydr. Polym.* **2017**, *170*, 289–295, doi:10.1016/j.carbpol.2017.04.054. [[CrossRef](#)] [[PubMed](#)]
24. Gřundělová, L.; Mráček, A.; Kašpárková, V.; Minařík, A.; Smolka, P. The influence of quarternary salt on hyaluronan conformation and particle size in solution. *Carbohydr. Polym.* **2013**, *98*, 1039–1044, doi:10.1016/j.carbpol.2013.06.057. [[CrossRef](#)] [[PubMed](#)]
25. Musilová, L.; Kašpárková, V.; Mráček, A.; Minařík, A.; Minařík, M. The behaviour of hyaluronan solutions in the presence of Hofmeister ions: A light scattering, viscometry and surface tension study. *Carbohydr. Polym.* **2019**, *212*, 395–402, doi:10.1016/j.carbpol.2019.02.032. [[CrossRef](#)] [[PubMed](#)]
26. Cowman, M.; Matsuoka, S. Experimental approaches to hyaluronan structure. *Carbohydr. Res.* **2005**, *340*, 791–809, doi:10.1016/j.carres.2005.01.022. [[CrossRef](#)] [[PubMed](#)]
27. Um, I.; Fang, D.; Hsiao, B.; Okamoto, A.; Chu, B. Electro-Spinning and Electro-Blowing of Hyaluronic Acid. *Biomacromolecules* **2004**, *5*, 1428–1436, doi:10.1021/bm034539b. [[CrossRef](#)] [[PubMed](#)]
28. Caspersen, M.; Roubroeks, J.; Qun, L.; Shan, H.; Fogh, J.; RuiDong, Z.; Tommeraas, K. Thermal degradation and stability of sodium hyaluronate in solid state. *Carbohydr. Polym.* **2014**, *107*, 25–30, doi:10.1016/j.carbpol.2014.02.005. [[CrossRef](#)]
29. Xie, J.; Hsieh, Y. Ultra-high surface fibrous membranes from electrospinning of natural proteins: casein and lipase enzyme. *J. Mater. Sci.* **2003**, *38*, 2125–2133, doi:10.1023/A:1023763727747. [[CrossRef](#)]
30. Ma, H.; Chen, G.; Zhang, J.; Liu, Y.; Nie, J.; Ma, G. Facile fabrication of core-shell polyelectrolyte complexes nanofibers based on electric field induced phase separation. *Polymer* **2017**, *110*, 80–86, doi:10.1016/j.polymer.2016.12.062. [[CrossRef](#)]
31. Uppal, R.; Ramaswamy, G.; Arnold, C.; Goodband, R.; Wang, Y. Hyaluronic acid nanofiber wound dressing-production, characterization, and in vivo behavior. *J. Biomed. Mater. Res.—Part B: Appl. Biomater.* **2011**, *97 B*, 20–29, doi:10.1002/jbm.b.31776. [[CrossRef](#)]
32. Liu, Y.; Ma, G.; Fang, D.; Xu, J.; Zhang, H.; Nie, J. Effects of solution properties and electric field on the electrospinning of hyaluronic acid. *Carbohydr. Polym.* **2011**, *83*, 1011–1015, doi:10.1016/j.carbpol.2010.08.061. [[CrossRef](#)]
33. Brenner, E.; Schiffman, J.; Thompson, E.; Toth, L.; Schauer, C. Electrospinning of hyaluronic acid nanofibers from aqueous ammonium solutions. *Carbohydr. Polym.* **2012**, *87*, 926–929, doi:10.1016/j.carbpol.2011.07.033. [[CrossRef](#)]
34. Malkin, A.; Semakov, A.; Skvortsov, I.; Zatonskikh, P.; Kulichikhin, V.; Subbotin, A.; Semenov, A. Spinnability of Dilute Polymer Solutions. *Macromolecules* **2017**, *50*, 8231–8244, doi:10.1021/acs.macromol.7b00687. [[CrossRef](#)]
35. Yu, J.H.; Fridrikh, S.V.; Rutledge, G.C. The role of elasticity in the formation of electrospun fibers. *Polymer* **2006**, *47*, 4789–4797, doi:10.1016/j.polymer.2006.04.050. [[CrossRef](#)]
36. Stepanyan, R.; Subbotin, A.; Cuperus, L.; Boonen, P.; Dorschu, M.; Oosterlinck, F.; Butlers, M. Fiber diameter control in electrospinning. *Appl. Phys. Lett.* **2014**, *105*, doi:10.1063/1.4900778. [[CrossRef](#)]
37. Palangetic, L.; Reddy, N.; Srinivasan, S.; Cohen, R.E.; McKinley, G.H.; Clasen, C. Dispersity and spinnability: Why highly polydisperse polymer solutions are desirable for electrospinning. *Polymer* **2014**, *55*, 4920–4931, doi:10.1016/j.polymer.2014.07.047. [[CrossRef](#)]
38. Stepanyan, R.; Subbotin, A.V.; Cuperus, L.; Boonen, P.; Dorschu, M.; Oosterlinck, F.; Butlers, M.J.H. Nanofiber diameter in electrospinning of polymer solutions: Model and experiment. *Polymer* **2016**, *97*, 428–439, doi:10.1016/j.polymer.2016.05.045. [[CrossRef](#)]
39. Shenoy, S.; Bates, W.; Frish, H.; Wnek, G. Role of chain entanglements on fiber formation during electrospinning of polymer solutions: good solvent, no-specific polymer-polymer interaction limit. *Polymer* **2005**, *46*, 3372–3384, doi:10.1016/j.polymer.2005.03.011. [[CrossRef](#)]

40. Rogina, A. Electrospinning process: Versatile preparation method for biodegradable and natural polymers and biocomposite systems applied in tissue engineering and drug delivery. *Appl. Surf. Sci.* **2014**, *296*, 221–230, doi:10.1016/j.apsusc.2014.01.098. [[CrossRef](#)]
41. Miloh, T.; Spivak, B.; Yarin, A. Needleless electrospinning: Electrically driven instability and multiple jetting from the free surface of a spherical liquid layer. *J. Appl. Phys.* **2009**, *106*, 114910, doi:10.1063/1.3264884. [[CrossRef](#)]
42. Luo, C.; Nangrejo, M.; Edirisinghe, M. A novel method of selecting solvents for polymer electrospinning. *Polymer* **2010**, *51*, 1654–1662, doi:10.1016/j.polymer.2010.01.031. [[CrossRef](#)]
43. Huerta-Angeles, G.; Němcová, M.; Příkopová, E.; Šmejkalová, D.; Pravda, M.; Velebný, V. Reductive alkylation of hyaluronic acid for the synthesis of biocompatible hydrogels by click chemistry. *Carbohydr. Polym.* **2012**, *90*, 1704–1711, doi:10.1016/j.carbpol.2012.07.054. [[CrossRef](#)] [[PubMed](#)]
44. Šmejkalová, D.; Muthný, T.; Nešporová, K.; Hermannová, M.; Achbergerová, E.; Huerta-Angeles, G.; Svoboda, M.; Čepa, M.; Machalová, V.; Luptáková, D.; et al. Hyaluronan polymeric micelles for topical drug delivery. *Carbohydr. Polym.* **2017**, *156*, 86–96, doi:10.1016/j.carbpol.2016.09.013. [[CrossRef](#)] [[PubMed](#)]
45. Kaneo, Y.; Hashihama, S.; Kakinoki, A.; Tanaka, T.; Nakano, T.; Ikeda, Y. Pharmacokinetics and Biodisposition of Poly(vinyl alcohol) in Rats and Mice. *Drug Metab. Pharmacokin.* **2005**, *20*, 435–442, doi:10.2133/dmpk.20.435. [[CrossRef](#)]
46. Yarin, A.; Koombhongse, S.; Reneker, D. Taylor cone and jetting from liquid droplets in electrospinning of nanofibers. *J. Appl. Phys.* **2001**, *90*, 4836–4846, doi:10.1063/1.1408260. [[CrossRef](#)]
47. Jurošková, D. *Charakterizace Hyaluronanu Sodného ve Vodných Roztocih a Na fázových Rozhraních*; Department of Physics and Materials Engineering, Thomas Bata University in Zlín: Zlín, Czech Republic, 2017.
48. Kim, M.; Cao, B. Additional Reduction of Surface Tension of Aqueous Polyethylene Oxide (PEO) Solution at High Polymer Concentration. *Europhys. Lett.* **1993**, *24*, 229–234, doi:10.1209/0295-5075/24/3/012. [[CrossRef](#)]
49. Han, C. A Study of Coextrusion in a Circular Die. *J. Appl. Polym. Sci.* **1975**, *19*, 1875–1883. [[CrossRef](#)]



© 2019 by the authors. Licensee MDPI, Basel, Switzerland. This article is an open access article distributed under the terms and conditions of the Creative Commons Attribution (CC BY) license (<http://creativecommons.org/licenses/by/4.0/>).